NATIONAL SCIENCE FOUNDATION

Print ISSN 1391-4588
E - ISSN 2362-0161
Volume 54 No. 3
September 2026

Journal of the National Science Foundation of Sri Lanka



www.nsf.gov.lk

NATIONAL SCIENCE FOUNDATION

JOURNAL OF THE NATIONAL SCIENCE FOUNDATION OF SRI LANKA

Editorial Board

Ajit Abeysekera (Editor in Chief)
Gayan Bowatte
Tushara Chaminda
Nelum Deshappriya
J.K.D.S. Jayanetti
Saroj Jayasinghe
P. Jayatissa
P. Prasad M. Jayaweera
Dushan Kumarathunge
Chandrika Perera
Jenifer Perera
S.S.N. Perera
Roshan G. Ragel
Punniamoorthy Ravirajan
S.A.H.A. Suraweera
Pushpa Wijekoon
M.J.S. Wijeyaratne
H.D. Yapa

Language Editor

R.D. Guneratne
M.C.M. Iqbal

Editorial Office

Nadeeja Wickramarachchi (Principal Scientific Officer)
Upuli Ratnayake (Scientific Officer)
Hasari Amaya (Intern)

Graphic Designing & Typesetting
Kanchana Sewwandi

International Editorial Advisory Board

I.M. Dharmadasa, UK
Shameen Jinadasa, Australia
Saman K. Halgamuge, Australia
Upali Samarajeewa, USA
Kirthi Tennakone, USA
Upul K.G. Wijayantha, UK

Contact details
Editorial Office, National Science Foundation,
47/5, Maitland Place, Colombo 07, Sri Lanka.

E-mail : jnsf@nsf.gov.lk
Phone : +94-11- 2696771
JNSF online submission portal :
https://jnsfsl.sljol.info/about/submissions
JNSF home page :
http://www.nsf.gov.lk/ index.php/nsfscience magazine

Publication : Published quarterly (March, June, September and December) by the National Science Foundation of Sri Lanka.

Manuscripts: Research Articles, Research Communications, Reviews and Correspondences in all fields of Science and Technology can be submitted for consideration for publication. A guide to the preparation of manuscripts is provided in each issue. The guidelines may also be obtained by visiting the NSF website or JNSF online submission portal.

Disclaimer: No responsibility is assumed by the National Science Foundation of Sri Lanka for statements and opinions expressed by contributors to this Journal.

Publication : free A publication fee of US$ 250 will be levied for each manuscript in two stages except, when the corresponding author is affiliated with a Sri Lankan institution.

- A processing fee of US$ 20 will be levied for each manuscript at peer-review stage.
- Remaining US$ 230 will be charged for accepted articles at the time of publication.

Copyright : © National Science Foundation of Sri Lanka

Articles in the Journal of the National Science Foundation of Sri Lanka are Open Access articles published under the Creative Commons CC-BY-ND License (http:// creative commons. org/licenses/by/4.0/). This license permits the use, distribution and reproduction, commercial and non-commercial, provided that the original work is properly cited and has not been changed anyway.

Indexing : **The JNSF is indexed in Science Citation Index Expanded, Journal Citation Reports/Science Edition, BIOSIS Previews, Zoological Record, Biological Abstracts, Chemical Abstracts, Scopus, DOAJ, TEEAL, Ulrich's, AGRICOLA and EBSCOhost, CAB Abstracts, SafetyLit, Journal TOCs, EBSCO Applied Science & Technology Source Ultimate**

JOURNAL OF THE
NATIONAL SCIENCE FOUNDATION
OF SRI LANKA

Volume 54 Number 3 September 2026

CONTENTS

EDITORIAL

285 **Why does human oversight remain essential in the age of AI?**
L.P. Jayatissa

REVIEW ARTICLE

287 **Exploring deep learning approaches for Tamil text processing: A comprehensive review and experimental comparison**
A Aravinthan and *EYA Charles*

RESEARCH ARTICLES (BIOLOGICAL SCIENCES)

305 **Optimizing drought stress to enhance root yield and secondary metabolites in Ashwagandha (*Withania somnifera* L. Dunal) under polyhouse conditions in Sri Lanka**
MS Jayathilaka, AAA Nishantha, S Subasinghe, KMW Rajawatta and *KHT Karunarathne*

317 **First insights into HLA-Cw6 in Sri Lankan paediatric psoriasis: A pilot study on genetic susceptibility and oxidative stress**
ND Wanniarachchi, S Samaraweera, J Seneviratne, HASG Dharmaratne and *ADDS Amarasekara*

325 **Adsorption characteristics and adsorption behavior of ammonium ions onto rice husk biochar pyrolyzed at different temperatures**
N Jayarathna, S Dharmakeerthi and *A Igalavithana*

RESEARCH ARTICLES (PHYSICAL SCIENCES)

339 **Eco-friendly electrodeposited SnO_2/Cu_2O thin-film heterojunction solar cells for low-cost photovoltaic applications**
BMUH Balasuriya, FSB Kafi, WTRS Fernando, KMDC Jayathilaka, LSR Kumara, T Nakatani RP Wijesundera and *W Siripala*

347 **Identification of rainfall and water level fluctuations and their relationships in the Kelani River Basin**
S Wijesekera, A Dewan and *M Khun*

369 **A hybrid adaptive artificial bee colony - liquid neural network scheduler for multi-objective task optimization in dynamic cloud environments**
NR Sabat, RR Sahoo and *S Radhakrishnan*

389 **Nerenchi Bot: A robotic system for playing the board game 'Nerenchi' against a human opponent**
MKMGPA Jayasinghe and *B Hettige*

407 **Robust quantile regression for improved population mean estimation under simple random sampling**
A Subhani, M Irfan, M Javed and *T Nawaz*

425 **Sensitivity analysis of the simulation of tropical cyclone Amphan using the WRF model**
TD Gamage, U Sonnadara, S Jayasinghe and *S Basnayake*

439 **On the (*k*,*c*) – Choosability of tri-partite graphs**
GGBR Jayawardhana, GS Wijesiri and *SVA Almeida*

Guidelines for Contributors

Cover page



Cover: Nerenchi Bot: A robotic system for playing the board game 'Nerenchi' against a human opponent
See J.Natn.Sci.Foundation Sri Lanka 2026 54(3): 389 - 406

J.Natn.Sci.Foundation Sri Lanka 2026 54 (3): 285
DOI: http://dx.doi.org/10.4038/jnsfsr.v54i3.13135

EDITORIAL

Why does human oversight remain essential in the age of AI?

Biological evolution required millions of years for primates to evolve into *Homo sapiens*, acquiring advanced cognitive abilities along the way. Among all species, humans stand out for their superior intelligence—specifically, the capacity to perceive information, store it as knowledge, and apply it adaptively within complex environments. Today, similar processes can be simulated artificially through Artificial Intelligence (AI) without direct human intervention. However, this raises a crucial question: as AI advances, can human input be discarded?

The answer is clearly no. Human intelligence encompasses another vital dimension: creative imagination, the ability to generate genuinely original and valuable ideas. While intelligence forms the foundation of creative thinking, true human creativity involves semantic understanding, intentionality, and contextual reasoning that current generative AI models lack.

A striking real-world case in academic publishing illustrates why uncritical reliance on AI is so problematic. In early 2024, a peer-reviewed research paper was published in the reputable journal *Surfaces and Interfaces* (Elsevier). The published paper's introduction opened with the literal sentence: *"Certainly, here is a possible introduction for your topic:"*—a standard conversational prefix generated by ChatGPT that the authors had blindly copied into their manuscript.

Despite passing through multiple rounds of author revisions, editorial screening, and expert peer review, this glaring artifact went completely undetected prior to publication.

This scenario highlights two critical issues in human–AI interaction:

- **Lack of 'Common-Sense Reasoning' in AI:** Generative language models process statistical patterns rather than true meaning. The AI could not evaluate the contextual impropriety of inserting conversational conversational metadata into a formal scientific manuscript.
- **Familiarity Blindness in Humans:** When AI-generated text appears highly fluent, structured, and articulate, human reviewers often lower their guard and unconsciously assume the underlying information and context are accurate.

This example serves as a stark reminder for academia and beyond. The ideal relationship between humans and AI is not one of passive reliance, but of intelligent, critical collaboration. While AI serves as a powerful accelerator for information processing, the human mind must remain the final judge of context, logic, and ultimate meaning.

Prof. L.P. Jayatissa

J.Natn.Sci.Foundation Sri Lanka 2026 54 (3): 287 - 303
DOI: http://dx.doi.org/10.4038/jnsfsr.v54i3.12728

REVIEW ARTICLE

Deep Learning

Exploring deep learning approaches for Tamil text processing: A comprehensive review and experimental comparison

A Aravinthan and EYA Charles*
Department of Computer Science, Faculty of Science, University of Jaffna, Jaffna, Sri Lanka.

Submitted: 03 July 2025; Revised: 13 May 2026; Accepted: 22 July 2026

Abstract: The integration of deep learning techniques into natural language processing (NLP) has led to significant advancements in language-based applications. However, these rapid developments present challenges for researchers, particularly in understanding their applicability to low-resource languages. Tamil, a morphologically rich Dravidian language, continues to face limitations in NLP due to resource scarcity and linguistic complexity. This study aims to investigate the applicability of various deep learning models for Tamil text processing and to identify effective, computationally efficient approaches suitable for low-resource language settings. To achieve this, the study first provides a focused review of recent deep learning approaches applied to NLP, with particular emphasis on Tamil language processing. It then presents a comparative experimental analysis of 20 deep learning models, including word embedding-based architectures (Word2Vec and FastText combined with ANN, CNN, RNN, LSTM, GRU, and Bi-GRU) and transformer-based models (such as mBERT, DistilBERT, and XLM-RoBERTa), evaluated across four Tamil NLP tasks using five datasets. The experimental results show that the FastText-based Bi-GRU model consistently outperforms other approaches across most tasks. Furthermore, word embedding methods demonstrate performance comparable to or better than transformer-based models while requiring significantly fewer computational resources. These findings highlight that efficient and well-designed models can achieve strong performance for Tamil NLP. The study also emphasizes the importance of improving language resources, such as large-scale corpora and annotated datasets, to further advance NLP research in low-resource languages.

Keywords: Deep learning, natural language processing, Tamil NLP applications, transfer learning, word embedding.

INTRODUCTION

The rapid advancement of deep learning has significantly transformed the field of natural language processing (NLP), leading to substantial improvements in tasks such as sentiment analysis, machine translation, and text classification. However, these advancements have primarily been driven by high-resource languages such as English, and their applicability to low-resource languages remains a challenge. Tamil, a morphologically rich Dravidian language with complex linguistic structures, continues to face limitations in NLP due to the scarcity of large-scale annotated datasets, standardized resources, and language-specific tools.

In recent years, deep learning approaches, particularly word embedding-based neural architectures and transformer-based pre-trained models, have demonstrated strong performance across a wide range of NLP tasks. Word embedding techniques such as Word2Vec and FastText, when combined with neural architectures including artificial neural networks (ANN), convolutional neural networks (CNN), and recurrent neural networks (RNN), are effective in capturing semantic and syntactic features of text. More recently, transformer-based

* Corresponding author (charles.ey@univ.jfn.ac.lk; https://orcid.org/0000-0002-0678-3486)

This article is published under the Creative Commons CC-BY-ND License (http://creativecommons.org/licenses/by-nd/4.0/). This license permits use, distribution and reproduction, commercial and non-commercial, provided that the original work is properly cited and is not changed in anyway.

models, including multilingual variants such as mBERT and XLM-RoBERTa, have enabled transfer learning across languages, offering promising solutions for low-resource settings. Nevertheless, these models often require substantial computational resources and may not consistently achieve strong performance across different tasks and domains in Tamil NLP.

Despite the growing body of research, several limitations remain. First, many studies focus on specific applications (e.g., sentiment analysis or hate speech detection) and evaluate only a limited number of models, making it difficult to generalize findings across tasks. Second, the existing literature often lacks critical synthesis, with studies presented in isolation rather than through systematic comparison. Third, there is limited empirical work that evaluates both word embedding–based approaches and transformer-based models within a unified experimental framework for Tamil NLP.

To address these gaps, this study investigates the effectiveness of various deep learning approaches for Tamil text processing and identifies computationally efficient models suitable for low-resource NLP settings. The study adopts a hybrid approach that combines a structured review of deep learning methods in Tamil NLP with a comprehensive experimental analysis. Specifically, twenty deep learning models are evaluated, including word embedding–enhanced neural network models (Word2Vec and FastText integrated with ANN, CNN, RNN, LSTM, GRU, and Bi-GRU) and transformer-based models (mBERT, DistilBERT, XLM-RoBERTa, IndicBERT, ELECTRA, LaBSE, and MuRIL). These models are assessed across four NLP tasks—domain classification, short text classification, sentiment analysis, and author identification—using five datasets.

The main contributions of this study are as follows:

- A critical synthesis of deep learning approaches for Tamil NLP, highlighting key trends and research gaps.
- A systematic comparative evaluation of twenty models across multiple tasks and datasets.
- An analysis of the trade-offs between model performance and computational efficiency, particularly in low-resource settings.
- Practical insights to support the selection of appropriate models for Tamil NLP applications.

The remainder of this paper is organized as follows. The Background and Literature Review section reviews the relevant background and related literature. The Methodology and Experimental Setup section describes the proposed methodology and the selected models. The Experimental Setup and Results section presents the experimental setup and results. The Discussion section discusses the findings and their implications. Finally, the Conclusion section concludes the paper and outlines directions for future research.

BACKGROUND AND LITERATURE REVIEW

Review Method

To ensure a structured and transparent review, relevant studies were identified from major academic databases including IEEE Xplore, ScienceDirect, SpringerLink, and Google Scholar. The search covered publications from 2015 to 2024 and used keywords such as "Tamil NLP," "deep learning," "word embeddings," "transformers," and "low-resource languages." Studies were included if they (1) focused on Tamil NLP or multilingual settings that include Tamil, (2) employed deep learning or embedding-based approaches, and (3) provided empirical evaluation on benchmark or publicly available datasets. After removing duplicates and excluding irrelevant works, the remaining studies were grouped into feature representation methods, neural architectures, and transformer-based approaches.

Evolution of NLP approaches

Early Tamil NLP research relied on rule-based and statistical methods, addressing tasks such as part-of-speech tagging, stemming, and morphological analysis (Ramachandran & Krishnamurthi, 2012; Rekha et al., 2010; Ram, 2010). While these approaches provided foundational contributions, they were limited in scalability and semantic understanding.

With the advancement of neural networks, representation learning emerged as a major breakthrough. Distributed representations (Bengio et al., 2001) and neural architectures (Collobert & Weston, 2008) enabled more effective language modeling. Subsequent developments such as RNNs, LSTMs, and GRUs improved sequence modeling, while attention mechanisms and transformers (Vaswani et al., 2017) significantly enhanced contextual understanding. Despite these advancements, Tamil NLP adopted these methods more gradually due to challenges associated with low-resource settings. Table 1 presents a comparative overview of existing deep learning–based studies in Tamil NLP, covering a range of tasks such as classification, sentiment analysis, named entity recognition, machine translation, and hate speech detection.

Table 1: Comparative summary of deep learning-based Tamil NLP studies

Study	Task	Dataset	Features	Model	Key Findings
Rajan et al. (2009)	Classification	CIIL	VSM	ANN	ANN improved accuracy
Nivedhitha et al. (2016)	Sentiment	SAIL	Word2Vec	Classifier	Improved performance
Seshadri et al. (2016)	Sentiment	SAIL	Embeddings	RNN	Strong performance
Devi et al. (2018)	NER	Twitter	GloVe	DL	GloVe better than Word2Vec
Thenmozhi et al. (2018)	Translation	FIRE	Seq2Seq	LSTM	Effective translation
Hariharan et al. (2019)	NER	FIRE	FastText	LSTM	FastText performed best
Ramraj et al. (2020)	Classification	News	Word2Vec	CNN	CNN + embeddings effective
Rajkumar et al. (2020)	Classification	Custom	TF-IDF	CNN	High accuracy achieved
Kalaivani & Thenmozhi (2020)	Sentiment	FIRE	Embeddings	AWD-LSTM	Moderate performance
Chakravarthi et al. (2021)	Code-mixed	FIRE	Embeddings	XLM-R	Transformer best
Vasantharajan & Thayasivam (2021)	Offensive	YouTube	Embeddings	mBERT	Strong performance
Hariprasad et al. (2022)	Meme Classification	Custom	Embeddings	XLNet	XLNet best
Kumar et al. (2023)	Hate Speech	Social	Word + Char	CNN + DNN	Ensemble improved results
Ratnavel Rajalakshmi et al. (2023)	Hate Speech	HASOC	Transformers	MuRIL	Best performance
Shibly et al. (2024)	Hate Speech	Custom	Mixed	Ensemble	Ensemble best
Krishnan et al. (2024)	Fake News	News	LLM	GPT-3.5	LLM outperformed others

Table 1 summarizes key aspects of each study, including the dataset used, feature representation techniques, model architectures, and principal findings. Overall, the comparison highlights the progression from traditional feature-based approaches to embedding-based methods and, more recently, transformer and large language model–based techniques, demonstrating consistent improvements in performance across tasks.

Feature representation in Tamil NLP

Feature representation has played a central role in Tamil NLP research. Early approaches such as Bag-of-Words and TF-IDF were widely used but lacked semantic understanding.

Word embedding techniques, including Word2Vec (Mikolov et al., 2013) and GloVe (Pennington et al., 2014), improved semantic representation. Studies such as Devi et al. (2018) and Nivedhitha et al. (2016) demonstrated improved performance using these methods.

FastText (Bojanowski et al., 2017), which incorporates subword information, has proven especially effective for Tamil due to its morphological richness. Several studies (Hariharan et al., 2019; Thavareesan & Mahesan, 2020) confirmed that FastText outperforms other embedding methods in handling rare and unseen words.

Critical observation: Although embeddings have become standard, most studies evaluate them in isolated settings, lacking systematic comparison across datasets and tasks.

Deep learning architectures for Tamil NLP

Deep learning models such as ANN, CNN, RNN, and LSTM have been widely applied to Tamil NLP tasks. CNN models are effective in extracting local patterns, while RNN and LSTM models are better suited for sequential data. Hybrid architectures combining multiple models have also shown improved performance.

However, the effectiveness of these models varies significantly depending on the dataset and preprocessing techniques, making direct comparison difficult.

Transformer models and large language models

Transformer-based models such as BERT and XLM-RoBERTa have significantly advanced Tamil NLP. Multilingual models including mBERT, IndicBERT, and MuRIL allow transfer learning for low-resource languages.

Although recent large language models such as GPT-3.5 and GPT-4 have shown promising results

in multilingual settings, they are not included in the experimental scope of this study. This decision reflects the study's focus on evaluating models that are more suitable for low-resource Tamil NLP, particularly in terms of computational requirements, Tamil-specific pretraining, and deployment in resource-constrained environments.

Review of deep learning-based Tamil NLP applications

Tamil NLP research has evolved considerably over the past decade, transitioning from traditional rule-based methods to sophisticated deep learning approaches. This progression can be broadly understood across three thematic strands: foundational neural approaches, embedding-driven architectures, and transformer-based models.

Foundational neural approaches: Early Tamil NLP studies began moving away from rule-based and statistical methods by incorporating neural networks. Rajan et al. (2009) demonstrated that combining a vector space model with an artificial neural network improved classification accuracy over conventional methods, laying the groundwork for neural adoption in Tamil NLP. Subsequent work by Seshadri et al. (2016) and Nivedhitha et al. (2016) introduced distributed word representations for sentiment analysis, with RNN-based models showing strong performance particularly for Tamil text. These studies established those neural architectures, even in their early forms, offered meaningful improvements over prior statistical approaches.

Embedding-driven architectures: As word embedding techniques matured, their integration with deeper neural architectures became a dominant research direction. Studies consistently demonstrated that embeddings such as Word2Vec, GloVe, and FastText, when combined with CNN or LSTM models, outperformed traditional classifiers such as SVM and Naïve Bayes across tasks including document classification, sentiment analysis, and named entity recognition (Ramraj et al., 2020; Rajkumar et al., 2020; Devi et al., 2018). Among these, FastText proved especially effective for Tamil due to its subword modeling capability, which handles the language's morphological richness and addresses out-of-vocabulary challenges (Hariharan et al., 2019; Thavareesan & Mahesan, 2020). In sequence modeling and machine translation, LSTM-based Seq2Seq architectures further demonstrated the utility of embedding-driven approaches, particularly when combined with techniques such as Byte Pair Encoding to manage vocabulary diversity (Thenmozhi et al., 2018; Choudhary et al., 2018).

Transformer-based and large language models: More recent research has shifted towards pretrained multilingual transformer models. Studies by Chakravarthi et al. (2020, 2021) and Vasantharajan and Thayasivam (2021) demonstrated that models such as mBERT, XLM-RoBERTa, and IndicBERT consistently outperform embedding-based approaches on tasks including hate speech detection, offensive language identification, and code-mixed text classification. Ensemble and hybrid strategies combining multiple transformer models have further improved performance, as reported by Kumar et al. (2023) and Kumaresan and Thangaraju (2023). Most recently, large language models such as GPT-3.5-turbo have shown promising results; Krishnan et al. (2024) found that GPT-3.5-turbo outperforms transformer-based models for Tamil fake news detection, particularly when Tamil text is paired with English translations. However, given their extremely high computational cost and limited Tamil-specific pretraining data, LLMs remain largely inaccessible for standard low-resource NLP settings and are therefore not included in the experimental scope of this study.

Overall trend: Across these three strands, a clear progression is evident — from early neural models to embedding-enhanced architectures and finally to transformer-based approaches. While transformer models achieve superior performance on benchmark tasks with sufficient data, embedding-based models, particularly FastText-based architectures, remain competitive and computationally efficient in low-resource settings. This observation directly informs the experimental design of the present study, which systematically evaluates both categories of models under a unified framework to assess their practical applicability for Tamil NLP.

Methodological comparison

A key observation across the literature is the trade-off between model complexity and computational efficiency. Word embedding-based models, such as FastText combined with LSTM or Bi-LSTM, are widely adopted due to their efficiency, lower data requirements, and robustness to out-of-vocabulary words. These models are particularly effective in low-resource settings and morphologically rich languages like Tamil. However, their main limitation lies in their relatively weak ability to capture deep contextual relationships within text.

In contrast, transformer-based models such as mBERT and XLM-RoBERTa offer strong contextual understanding and superior cross-lingual transfer capabilities. These models have demonstrated state-of-

the-art performance across various NLP tasks, but at the cost of higher computational complexity, greater data requirements, and reduced interpretability.

Empirical studies (e.g., Hariharan et al., 2019; Thavareesan & Mahesan, 2020) indicate that FastText-based approaches can achieve competitive performance, especially in morphologically rich and low-resource scenarios. However, other works (Chakravarthi et al., 2021) show that transformer-based models outperform traditional and embedding-based approaches on large-scale benchmark datasets. This suggests that model effectiveness is highly dependent on factors such as dataset size, task complexity, and domain characteristics, rather than a universally optimal approach.

Application domains

Tamil NLP research has predominantly focused on a limited set of application domains, including sentiment analysis and opinion mining, hate speech and offensive language detection, document and news classification, as well as machine translation and code-mixed text processing. These tasks have attracted significant attention due to their practical relevance and the availability of benchmark datasets and shared tasks.

However, comparatively fewer studies have explored emerging and complex areas such as low-resource domain adaptation, dialogue systems and conversational AI, multimodal NLP applications, and linguistically informed or hybrid modeling approaches. This indicates that current research is largely concentrated on classification-oriented tasks, with limited diversification into more advanced or interdisciplinary NLP applications.

Identified research gaps

Despite notable advancements, several critical research gaps remain in Tamil NLP. A major challenge is resource scarcity, particularly the lack of large-scale, high-quality annotated datasets. The growing prevalence of code-mixed Tamil-English text further complicates NLP tasks due to linguistic variability and informal usage patterns. Additionally, there is a limited availability of domain-specific corpora, which restricts the development of robust, domain-adaptive models.

Another important gap is the need for model efficiency, as many current approaches rely on computationally expensive architectures that are not well-suited for low-resource environments. Furthermore, there is a lack of standardized evaluation benchmarks across studies, making it difficult to compare results and draw consistent conclusions.

Most importantly, many existing studies evaluate models on isolated datasets, limiting their generalizability across tasks and domains. Addressing these challenges will be essential for advancing Tamil NLP and enabling the development of more robust, scalable, and generalizable solutions.

Discussion on review

The review highlights that Tamil NLP research has made steady progress, particularly with the adoption of deep learning techniques. Initially constrained by limited resources, the field has increasingly benefited from word embedding methods and, more recently, transformer-based transfer learning approaches. A key trend is the continued relevance of word embedding-based models, especially FastText, in low-resource contexts. These models offer a favorable balance between performance and computational efficiency, making them suitable for practical applications. At the same time, transformer-based models such as mBERT and XLM-RoBERTa have demonstrated strong performance in benchmark tasks, particularly when sufficient data and computational resources are available.

However, it is important to interpret performance comparisons cautiously. The effectiveness of embedding-based versus transformer-based models varies depending on dataset characteristics, task complexity, and experimental settings. Therefore, no single model can be considered universally superior across all Tamil NLP applications.

Another important observation is the narrow focus of existing research, with a heavy emphasis on classification tasks such as sentiment analysis and hate speech detection. Broader applications, including conversational systems, domain adaptation, and low-resource transfer learning, remain under explored. Furthermore, the review underscores the lack of standardized datasets and evaluation frameworks, which limits the comparability and reproducibility of results. Addressing these issues requires collaborative efforts to develop large-scale corpora, shared benchmarks, and open-source resources for Tamil NLP.

Finally, while recent advances in large language models (LLMs) show promising potential, their applicability to Tamil remains constrained by data availability, computational requirements, and linguistic

diversity. Future research should focus on developing efficient, scalable, and linguistically informed models tailored to low-resource languages.

These gaps directly motivate the present study, which aims to systematically investigate the applicability of various deep learning models for Tamil text processing under a unified experimental framework.

METHODOLOGY AND EXPERIMENTAL SETUP

Based on the literature review, this study identified a set of models that have demonstrated strong performance in prior NLP tasks. This section discusses these models in detail.

Overview of selected approaches

The majority of research on NLP for the Tamil language has traditionally emphasized specific applications, integrating additional features to augment the efficacy of those applications. However, these investigations commonly focus on a single or at most a couple of models that are custom-made for a particular application. To bridge this gap, an extensive analysis of the adaptability of the latest high-performing learning architectures across four distinct NLP tasks for the Tamil language has been conducted using performance evaluation as the measure. The purpose of this analysis is to provide guidance for future researchers who are keen on developing deep-learning models for Tamil NLP applications.

The models were selected based on an exhaustive literature review, paying special attention to their performance in NLP tasks in other languages. The analysis was done using two different strategies. In the first strategy, a set of word embedding enhanced neural network models were built and analysed. In the second strategy, the performance of cutting-edge transfer learning models was analysed.

NLP tasks and data sets for the analysis

The study considered Domain classification, short text classification, Sentiment analysis and Author identification NLP tasks and five different data sets to do the analysis. For the domain classification task, the TamilMurasu news articles data set (DC1) and Tamil news data set (DC2) were used. For Short text classification, a data set consisting of Tamil news headlines was used (STC). For the Sentiment analysis, a data set of Tamil movie reviews was used (SA). A data set (AI) of Tamil Novels was used for Author identification. Details about the data sets are given below:

- **DC1:** The study used a subset of the TamilMurasu news articles data set (Krishnaraj, 2020). This subset contains 67,259 samples in six domains, namely, World, Sports, India, Crime, Cinema, and District with 7477, 8230, 16,935, 16,290, 9248, and 9079 records, respectively.
- **DC2:** This data set has 10491 samples of Tamil news articles (Kunchukuttan et al., 2020). The data set has an equal number of samples in three classes, namely, Entertainment, Sports, and Politics.
- **STC:** This dataset consists of 13955 samples of Tamil news headlines from the Puthiyathalaimurai website (Rajkumar, n.d.). This contains six categories, namely, India, Tamil Nadu, Cinema, Politics, World, and Sports with 3337, 4807, 1937, 1172, 1045, and 1657 samples, respectively.
- **SA:** This dataset has 601 Tamil movie review (Rajkumar, n.d.) samples from online movie review websites. The study considered positive and negative sentiment classes, which contained 222 and 379 samples, respectively.
- **AI:** This dataset contains 5310 sample texts from books written by seven Tamil authors (Archchitha & Charles, 2022). The names of the authors are, Jeyakanthan, Puthumaipiththan, Kalki, Karthikesu, Annadurai, Varatharajan, Parthasarathi. Text selected from each author is considered as a class and contains 600, 1429, 1590, 291, 737, 497, and 166 samples, respectively.

Word embedding enhanced neural network models built for the analysis

As part of the analysis, Word2Vec and FastText embedding models were trained using a corpus containing approximately three million unique words compiled specifically for this study. These embeddings, together with the selected datasets, were used to train multiple neural network models for different NLP tasks, and their performance was subsequently evaluated.

Figure 1 illustrates the overall process followed in this analysis. To construct a word embedding enhanced neural network model, each input text is first tokenized and padded to ensure a uniform sequence length. Each token in the padded sequence is then represented using its corresponding word embedding from the pre-trained vectors. These embedded representations are provided as input to the neural network model, which learns task-specific features for classification.

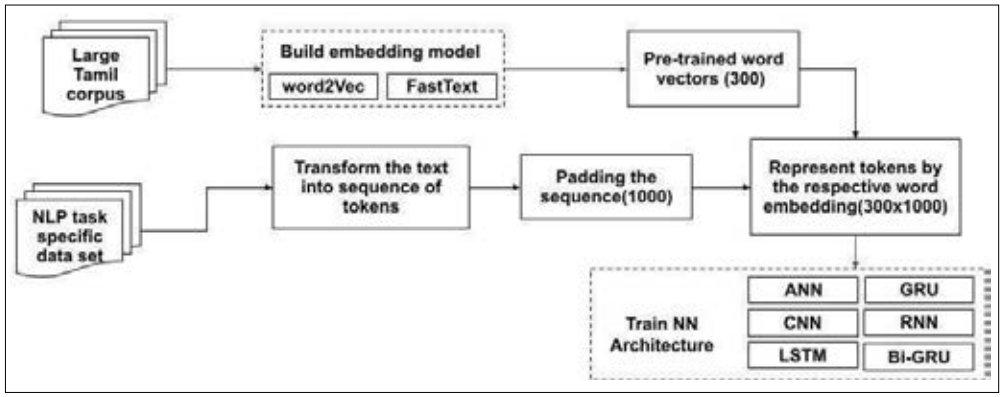

Figure 1: Process of constructing a word embedding enhanced neural network model.

The models developed and evaluated in this study are described below.

w2V + ANN: This model employs an Artificial Neural Network (ANN) architecture with Word2Vec embedding. The input text is represented using 300-dimensional Word2Vec vectors. The model consists of two dense layers that learn from the embedding features, followed by a softmax output layer for classification.

w2V + CNN: This model utilizes a Convolutional Neural Network (CNN) with 300-dimensional Word2Vec embeddings. It includes a one-dimensional convolutional layer followed by a max-pooling layer to capture local n-gram features. A softmax layer is used for the final prediction.

w2V + RNN: In these models, 300-dimensional Word2Vec embeddings are used as input features. Different recurrent architectures are employed to capture sequential dependencies, including simple RNN, Long Short-Term Memory (LSTM), Gated Recurrent Unit (GRU), and Bidirectional GRU (Bi-GRU). Each model includes a softmax output layer for classification. These variants are denoted as w2V + RNN, w2V + LSTM, w2V + GRU, and w2V + Bi-GRU, respectively.

FastText + ANN: This model is similar to the w2V + ANN model but uses 300-dimensional FastText embeddings as input features.

FastText+CNN: This model follows the same architecture as w2V + CNN but replaces Word2Vec embeddings with 300-dimensional FastText embeddings.

FastText + RNN: These models mirror the w2V + RNN variants but use FastText embeddings instead of Word2Vec embeddings for input representation.

Pre-trained transformer models for the analysis

To evaluate the applicability of transformer-based models for Tamil NLP tasks, this study considers several publicly available, high-performing pre-trained models. These models are fine-tuned on the selected Tamil datasets, and their performance is evaluated under a consistent experimental framework. The selected models are described below.

mBERT: Multilingual BERT (mBERT) is pre-trained on Wikipedia data from 102 languages (Devlin et al., 2018). This study uses both bert-base-multilingual-cased and bert-base-multilingual-uncased variants.

DistilBERT: DistilBERT is a compressed version of BERT that reduces model size while retaining much of its performance (Sanh et al., 2019). This study uses the multilingual distilled version trained on Wikipedia data across multiple languages.

XLM-RoBERTa: XLM-RoBERTa is a multilingual extension of RoBERTa, trained on 2.5 TB of filtered Common Crawl data covering 100 languages (Conneau et al., 2019). The xlm-roberta-base model is used in this study.

IndicBERT: IndicBERT is based on the ALBERT architecture (Lan et al., 2019) and is designed for Indian languages. It is trained on a large-scale corpus covering 12 major Indian languages, including Tamil, and aims to reduce computational requirements while maintaining performance.

ELECTRA: ELECTRA is a transformer model trained using a generator–discriminator framework (Clark et al., 2020). Instead of predicting masked tokens, the model learns to distinguish between original and replaced tokens. This study uses the Tamil-specific ELECTRA variant (monsoon-nlp/Tamillion), which is pre-trained on a large Tamil corpus.

LaBSE: The Language-agnostic BERT Sentence Encoder (LaBSE) is a multilingual model designed for sentence embeddings and trained on 109 languages (Feng et al., 2020).

MuRIL: MuRIL is a multilingual BERT-based model trained on 17 Indian languages, including Tamil, with a focus on improving performance for low-resource languages (Khanuja et al., 2021).

EXPERIMENTAL SETUP AND RESULTS

Experimental setup for Word embedding enhanced neural network models

The models considered in this study were implemented using the Keras library with TensorFlow as the backend. For the Convolutional Neural Network (CNN) architecture, one-dimensional convolution was applied with 128 filters and a kernel size of 5.

For the recurrent architectures, including RNN, Long Short-Term Memory (LSTM), Gated Recurrent Unit (GRU), and Bidirectional GRU (Bi-GRU), the number of hidden units was fixed at 100 to ensure consistency across models. The Rectified Linear Unit (ReLU) activation function was used in the CNN layers, while the hyperbolic tangent (tanh) activation function was applied in the recurrent layers.

The models were trained using the Adam optimizer with a learning rate of 0.001. A batch size of 32 was used for all experiments. The loss function was selected based on the task: binary cross-entropy for binary classification tasks and categorical cross-entropy for multi-class classification tasks. The number of training epochs ranged from 5 to 10, depending on the dataset and model configuration.

Results and analysis for Word embedding enhanced neural network models

The selected models were trained separately for each task using the corresponding datasets. For all experiments, each dataset was divided into training and testing subsets, with 70% of the data used for training and the remaining 30% reserved for testing.

Model performance was evaluated using accuracy as the primary metric, defined as the proportion of correctly classified samples relative to the total number of samples in the test set. While accuracy is widely used and facilitates comparison with prior Tamil NLP studies, it may not fully reflect model performance in the presence of class imbalance.

In particular, tasks such as sentiment analysis and author identification may involve skewed class distributions, where accuracy alone can yield an overly optimistic estimate of performance. Therefore, the reported results should be interpreted with this limitation in mind. Future work should incorporate additional evaluation metrics, such as precision, recall, and F1-score, to provide a more comprehensive assessment of model performance.

Table 2 presents the accuracy achieved by the neural network models enhanced with Word2Vec embeddings across the selected NLP tasks. The tasks considered in this study include document classification (datasets DC1 and DC2), short text classification (dataset STC), sentiment analysis (dataset SA), and author identification (dataset AI). The results indicate that the Bi-GRU model achieves the highest accuracy for document classification on DC1 and for the author identification task. The LSTM model shows comparatively better performance for short text classification. For sentiment analysis and document classification (DC2), the CNN model attains higher accuracy than the other models. In these tasks, the Bi-GRU model demonstrates slightly lower performance relative to the best-performing models.

Table 3 presents the accuracy achieved by the FastText-enhanced neural network models across the selected datasets. Consistent with the trends observed for the Word2Vec-based models, the Bi-GRU model achieves the highest accuracy across most tasks, including sentiment analysis. The remaining models generally exhibit slightly lower performance in comparison. Among the other architectures, the CNN model demonstrates higher accuracy than the ANN model, while the simple RNN shows comparatively lower performance on some datasets. Overall, the FastText-enhanced models provide consistent improvements across tasks. In addition, a similar pattern of performance is observed between the Word2Vec- and FastText-based models.

Table 2: Accuracy scores of the neural network models enhanced by Word2Vec Word embedding

Dataset	w2V+ANN	w2V+CNN	w2V+RNN	w2V+LSTM	w2V+GRU	w2V+Bi-GRU
DC1	0.8300	0.8698	0.8423	0.8504	0.8654	0.8701
STC	0.6126	0.6803	0.6806	0.7097	0.6868	0.7016
SA	0.6077	0.6733	0.5800	0.6500	0.6200	0.6000
AI	0.8168	0.7578	0.4749	0.8256	0.8206	0.8513
DC2	0.9145	0.9485	0.9158	0.9390	0.9409	0.9447

Table 3: Accuracy scores of the neural network models enhanced by FastText Word embedding

Dataset	FT+ANN	FT+CNN	FT+RNN	FT+LSTM	FT+GRU	FT+Bi-GRU
DC1	0.8368	0.9032	0.8513	0.8532	0.8856	0.9042
STC	0.6523	0.7392	0.6778	0.6956	0.7269	0.7397
SA	0.6077	0.6961	0.56	0.60	0.66	0.7293
AI	0.8394	0.8626	0.5226	0.8601	0.8526	0.8726
DC2	0.939	0.9684	0.8529	0.9479	0.9485	0.9718

Table 4: Parameter values for transformer models

Parameters	Settings
Number of training epochs	5
Maximum sequence length	128
Training batch size	32
Learning rate	3e-5
Threshold	0.5

Experimental setup for pre-trained transformer models

In this part of the analysis, transformer-based models were implemented using the Simple Transformers library, which is built on top of the Hugging Face Transformers framework. To ensure consistency and comparability, the same set of hyperparameters was applied across all models. The parameter settings used in the experiments are summarized in Table 4.

Results and analysis for pre-trained transformer models

Table 5 presents the accuracy achieved by the transformer-based models across the selected NLP tasks and datasets.

Among the multilingual BERT variants, the cased version of mBERT achieves higher accuracy than the uncased version for the domain classification datasets.

In contrast, the uncased variant shows comparatively better performance for sentiment analysis and author identification tasks.

Table 5: Accuracy score of transformer-based pre-trained models with Attention

Dataset	m-bert (cased)	m-bert (uncased)	DistilBERT	XLM-RoBERTa	ELECTRA	IndicBERT	LaBSE	MuRIL
DC1	0.8931	0.8279	0.8467	0.9052	0.8937	0.9013	0.8847	0.8566
STC	0.6704	0.4434	0.4655	0.6854	0.5431	0.6985	0.7244	0.5058
SA	0.62	0.6266	0.6666	0.6266	0.64	0.62	0.6206	0.62
AI	0.6011	0.7854	0.3809	0.5746	0.5305	0.4430	0.7140	0.7535
DC2	0.9631	0.9224	0.8853	0.9634	0.9456	0.9660	0.9688	0.9390

XLM-RoBERTa demonstrates strong performance across most datasets and generally achieves higher accuracy than the mBERT variants, except for author identification task. In addition, both XLM-RoBERTa and IndicBERT perform well on the domain classification datasets, while DistilBERT shows relatively better performance for sentiment analysis.

For the author identification task, the uncased mBERT, LaBSE, and MuRIL models achieve comparatively higher accuracy than the other models. Overall, the results indicate that model performance varies across tasks and datasets, and no single model consistently outperforms others across all settings.

The results obtained from the analysis do not indicate a single model that consistently achieves the highest performance across all datasets and tasks. The best-performing models from each category are summarized in Table 6.

Table 6: Summary of the highest accuracies obtained among each category of models

Dataset	Word2Vec (max)	Word2Vec model	FastText (max)	FastText model	Transformer (max)
DC1	0.8701	w2V + Bi-GRU	0.9042	FT + Bi-GRU	0.9052 (XLM-RoBERTa)
STC	0.7097	w2V + LSTM	0.7397	FT + Bi-GRU	0.7244 (LaBSE)
SA	0.6733	w2V + CNN	0.7293	FT + Bi-GRU	0.6666 (DistilBERT)
AI	0.8513	w2V + Bi-GRU	0.8726	FT + Bi-GRU	0.7854 (m-bert uncased)
DC2	0.9485	w2V + CNN	0.9718	FT + Bi-GRU	0.9688 (LaBSE)

Among the word embedding–enhanced models, the FastText + Bi-GRU model achieves the highest accuracy on most datasets, except for domain classification dataset DC1. In comparison, the pre-trained transformer models generally achieve lower or comparable accuracy for domain classification (DC1 and DC2) and short text classification (STC). For sentiment analysis (SA) and author identification (AI), the FastText + Bi-GRU model demonstrates higher accuracy than the transformer-based models.

In addition, the difference in performance between Word2Vec- and FastText-based models is relatively small compared to the gap observed between embedding-based models and transformer-based models for certain tasks. However, these differences vary across datasets and should be interpreted with caution.

The transformer models considered in this study are substantially larger than the word embedding–enhanced models in terms of training data, number of parameters, and computational requirements. Despite this, their performance in this experimental setting is comparable to, or in some cases lower than, that of the simpler models. It is important to note that the embedding models were trained on a corpus composed exclusively of Tamil text, and the datasets used in this study are relatively large. These factors may influence the observed performance. Therefore, the results suggest that model effectiveness depends not only on architectural complexity but also on the alignment between the training corpus and the target task.

Analysis of performance uncertainty

Figures 2, 3, and 4 present performance comparisons of Word2Vec-based, FastText-based, and transformer-based models, respectively, across the five NLP tasks (DC1, DC2, STC, SA, and AI). The height of each bar represents accuracy, and the error bars indicate 95% confidence intervals.

To quantify uncertainty in model performance, 95% confidence intervals were estimated using a binomial proportion approach based on test-set predictions. Since accuracy represents the proportion of correctly classified instances, it can be modeled as a binomial variable. The confidence intervals were computed using the normal approximation, which relies on the observed accuracy and test set size and does not require repeated model training. While this method provides a statistically grounded estimate of uncertainty, it reflects sampling variability rather than variability across multiple training runs.

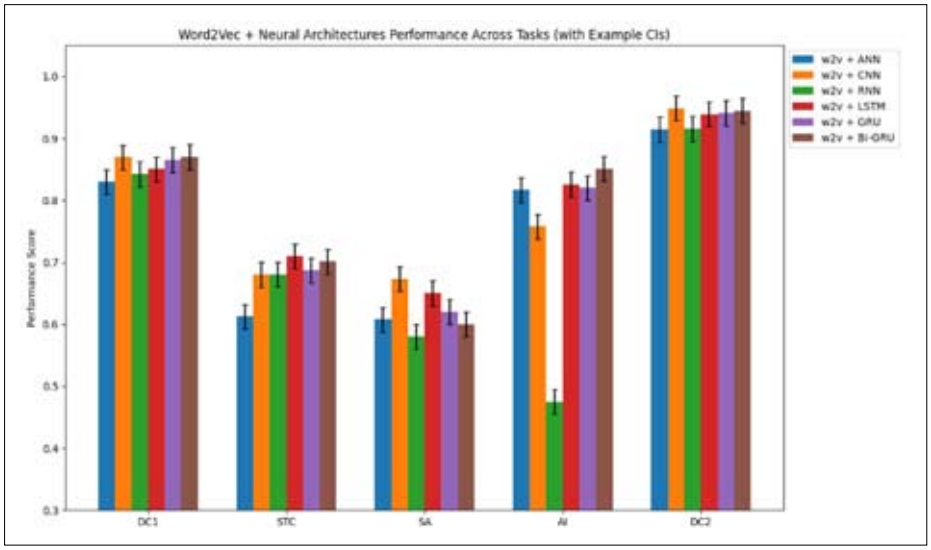

Figure 2: Performance comparison of Word2Vec-based neural network models across NLP tasks (DC1, DC2, STC, SA, and AI), with 95% confidence intervals.

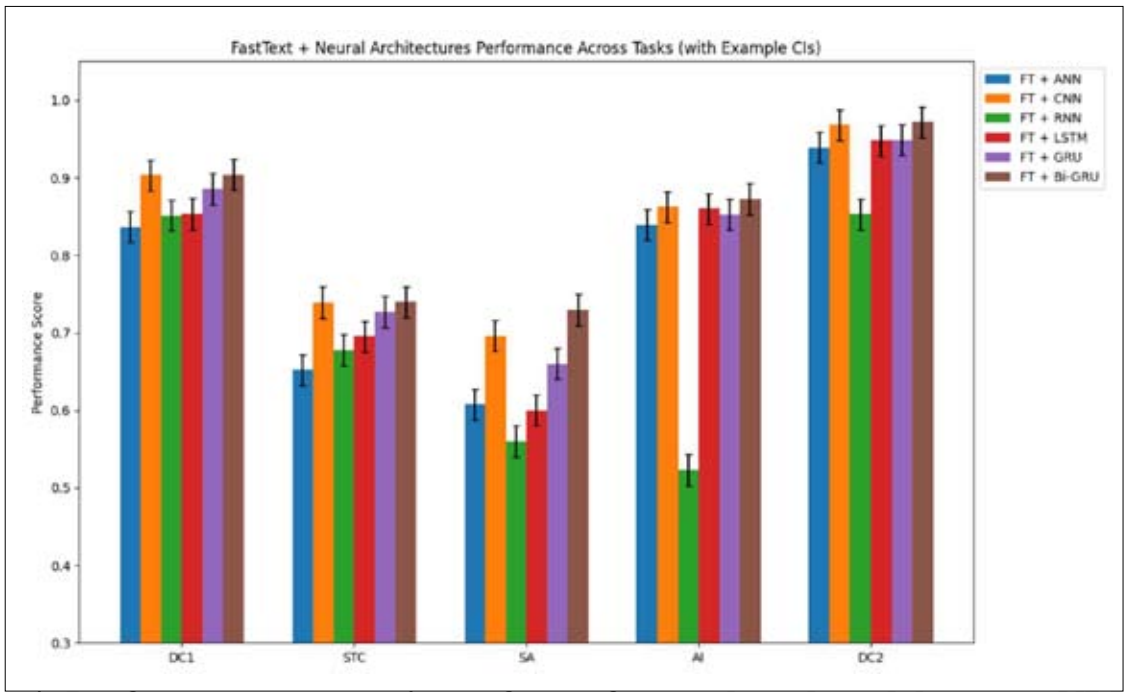

Figure 3: Performance comparison of FastText-based neural network models across NLP tasks (DC1, DC2, STC, SA, and AI), with 95% confidence intervals.

For transformer-based models (Figure 4), performance is generally strong on domain classification tasks (DC1 and DC2), with relatively narrow confidence intervals indicating stable predictions. However, greater uncertainty is observed for sentiment analysis (SA) and author identification (AI), where some models (e.g., mBERT uncased and MuRIL) exhibit wider confidence intervals.

The Word2Vec-based models (Figure 2) demonstrate competitive performance on domain classification tasks, although slightly lower accuracy and wider confidence intervals are observed for SA and AI, suggesting greater uncertainty in prediction accuracy. The FastText-based models (Figure 3) show a similar pattern but tend to achieve relatively higher accuracy and narrower confidence intervals for short text classification (STC) and sentiment analysis (SA), particularly when combined with CNN and Bi-GRU architectures.

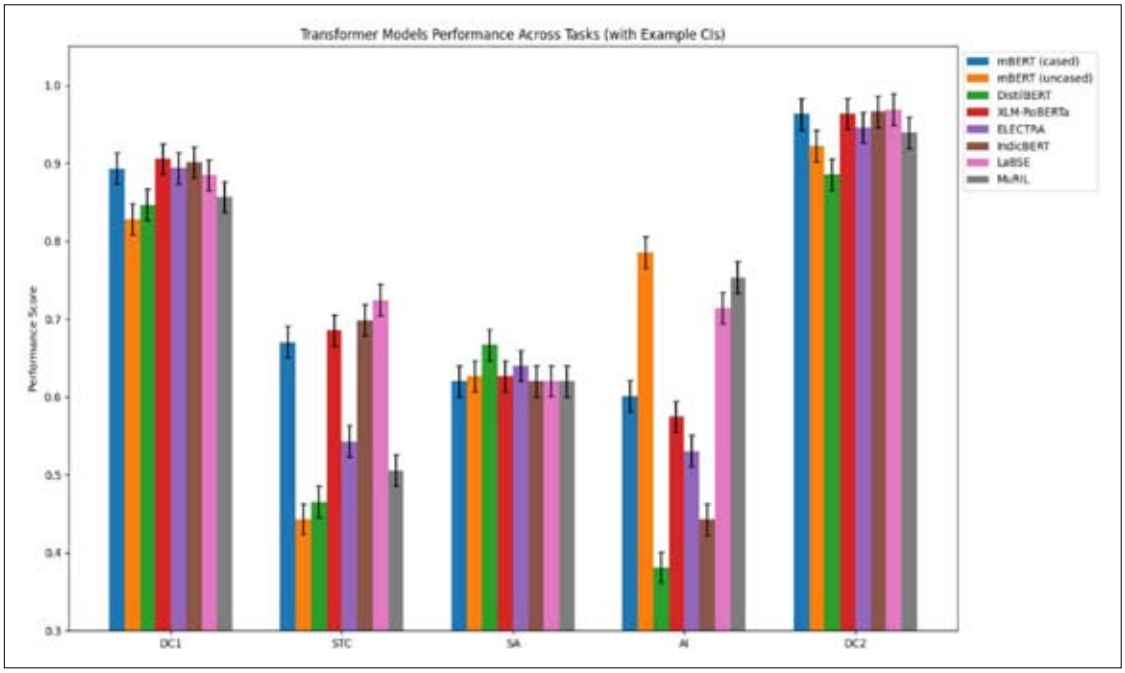

Figure 4: Performance comparison of transformer-based models across NLP tasks (DC1, DC2, STC, SA, and AI), with 95% confidence intervals.

Overall, the results indicate that transformer-based models perform strongly on domain-level tasks, while embedding-based hybrid models such as FastText + Bi-GRU are effective for tasks requiring finer-grained linguistic analysis, including sentiment analysis and author identification. The inclusion of confidence intervals supports a more cautious interpretation of these findings by highlighting the degree of uncertainty associated with each model's performance.

DISCUSSION

The comparative evaluation of Word2Vec-enhanced models, FastText-enhanced models, and pre-trained Transformer architectures reveals distinct performance patterns across the selected Tamil NLP tasks. Overall, FastText-enhanced Bi-GRU models demonstrate consistently strong performance across most datasets, achieving the highest accuracy in short text classification (STC: 0.7397), sentiment analysis (SA: 0.7293), author identification (AI: 0.8726), and DC2 document classification (0.9718). The only exception is the DC1 dataset, where the XLM-RoBERTa model slightly outperforms FastText-based Bi-GRU, achieving an accuracy of 0.9052 compared to 0.9042.

Word2Vec-enhanced models also show competitive performance, particularly when combined with Bi-GRU and CNN architectures. However, their overall performance is consistently lower than that of FastText-based models across all datasets. This indicates that subword-level representations provided by FastText are more effective in handling the morphological complexity of the Tamil language.

Transformer-based models exhibit more variable performance across tasks. Models such as XLM-

RoBERTa and LaBSE perform strongly in document classification and short text classification tasks, demonstrating their ability to capture contextual representations effectively. However, their performance does not consistently surpass that of FastText-enhanced models, particularly in sentiment analysis and author identification tasks. For instance, DistilBERT achieves an accuracy of 0.6666 in sentiment analysis, which remains below the corresponding FastText-BiGRU performance. Similarly, mBERT (uncased) performs reasonably well in author identification (0.7854) but does not exceed the performance of embedding-based neural architectures.

An important observation from the results is that increasing model complexity does not necessarily lead to improved performance in all low-resource NLP settings. Despite being pretrained on large multilingual corpora and containing significantly more parameters, Transformer-based models do not consistently outperform embedding-enhanced recurrent architectures. This may be attributed to domain mismatch, limited Tamil-specific pretraining data, and the relatively small size of task-specific datasets used in this study.

In contrast, FastText-based models trained on a dedicated Tamil corpus demonstrate strong and stable performance across multiple tasks. This suggests that domain-specific embeddings can be highly effective in low-resource language settings, particularly when combined with sequence modeling architectures such as Bi-GRU.

Another notable finding is the uncertainty in model performance across different NLP tasks. Document classification tasks (DC1 and DC2) generally yield higher and more stable accuracy across all model categories, while sentiment analysis and author identification tasks show greater uncertainty. This indicates that task complexity and linguistic uncertainty significantly influence model effectiveness. Although Transformer-based models are widely considered state-of-the-art in multilingual NLP, the results of this study suggest that their advantages are not always fully realized in low-resource settings such as Tamil. In particular, when high-quality domain-specific embeddings are available, simpler architectures can achieve comparable or even superior performance.

It is also important to note that the performance differences observed in this study should not be interpreted as universal superiority of one model type over another. Instead, model effectiveness is highly dependent on multiple factors, including dataset size, domain specificity, preprocessing strategy, and linguistic characteristics of the input text.

Overall, FastText-enhanced Bi-GRU emerges as the most consistently strong-performing model across the evaluated tasks, while Transformer-based models provide competitive but task-dependent performance. Word2Vec-based models remain comparatively less effective but still demonstrate reasonable performance in structured classification tasks.

CONCLUSION

This paper presented a combined structured review and experimental evaluation of deep learning approaches for Tamil Natural Language Processing (NLP), with a particular focus on low-resource language settings. A set of twenty representative models, including word embedding-enhanced neural architectures and transformer-based pre-trained models, were analyzed across four NLP tasks — domain classification, short text classification, sentiment analysis, and author identification — using five benchmark datasets.

The experimental results indicate that FastText-based Bi-GRU models consistently achieved strong and stable performance across most tasks, particularly in short text classification, sentiment analysis, and author identification. Transformer-based models, including XLM-RoBERTa, LaBSE, and mBERT variants, demonstrated competitive performance, especially in domain classification tasks, highlighting their effectiveness in leveraging multilingual contextual representations. However, the results also show that performance varies across tasks and datasets, and no single model uniformly outperforms others in all scenarios.

While embedding-based models exhibited comparable or, in some cases, superior performance relative to transformer-based models in this study, such findings should be interpreted with caution. The observed performance differences are influenced by several factors, including dataset size, domain specificity, preprocessing strategies, and the availability of language-specific corpora. In particular, the use of a dedicated Tamil corpus for training word embeddings may have contributed to the strong performance of embedding-based approaches. Therefore, the results do not suggest a general superiority of one class of models, but rather emphasize the importance of task-specific model selection and resource considerations.

From a review perspective, this study identifies several important research trends and gaps in Tamil NLP. Existing research has primarily focused on text classification tasks, particularly sentiment analysis and hate speech detection, whereas areas such as conversational AI, domain adaptation, and multimodal NLP remain underexplored. Furthermore, the limited availability of large-scale annotated datasets, standardized evaluation benchmarks, and publicly accessible resources continues to hinder reproducibility, fair model comparison, and the advancement of Tamil NLP research.

It should be noted that large language models such as GPT-3.5 and GPT-4 were not included in the experimental evaluation of this study. While recent studies have demonstrated their potential in multilingual and low-resource settings, their exclusion is justified by several practical considerations: their high computational demands, limited Tamil-specific pretraining data, and reduced suitability for resource-constrained deployment environments — all of which are central concerns in low-resource NLP research. Nonetheless, evaluating and comparing LLMs with traditional deep learning approaches represents a promising direction for future work.

This study makes several contributions to Tamil NLP research. First, it provides a critical synthesis of existing deep learning approaches, highlighting key methodological trends and research gaps in the field. Second, it presents a systematic comparative evaluation of twenty models across multiple tasks and datasets under a unified experimental framework, enabling more reliable and generalizable conclusions than isolated single-task studies. Third, it offers an empirical analysis of the trade-offs between model performance and computational efficiency, providing evidence-based insights for low-resource language settings. Finally, the study offers practical guidance for researchers in selecting appropriate models for Tamil NLP applications, particularly where computational resources are limited.

Future research should focus on: (i) developing comprehensive and diverse Tamil language resources, including annotated corpora and shared benchmarks; (ii) designing computationally efficient and scalable models suitable for low-resource environments; and (iii) extending research to broader and more complex NLP applications, including dialogue systems, cross-lingual transfer, and code-mixed language processing.

In summary, this study demonstrates that both transformer-based and embedding-based approaches have significant potential for Tamil NLP. However, sustained progress in this domain will depend not only on advances in model architectures but also on systematic resource development, rigorous evaluation practices, and a broader research scope. Overall, this study successfully investigated the applicability of various deep learning approaches for Tamil text processing, providing empirical evidence to guide model selection in low-resource NLP settings.

REFERENCES

Archchitha, A., & Charles, E. Y. A. (2022). Tamil author identification using convolutional neural network. In *2022 22nd International Conference on Advances in ICT for Emerging Regions* (ICTer) (pp. 1–6). https://doi.org/10.1109/ICTer58063.2022.10024098

Arora, G. (2020). *Gauravarora@HASOC-Dravidian-CodeMix-FIRE2020: Pre-training ULMFiT on synthetically generated code-mixed data for hate speech detection*. arXiv. https://arxiv.org/abs/2010.02094

Awatramani, V. (2021). No Offense@ DravidianLangTechEACL2021: Offensive Tamil identification and beyond the performance. In *Proceedings of the First Workshop on Speech and Language Technologies for Dravidian Languages.*

Bahdanau, D., Cho, K., & Bengio, Y. (2014). *Neural machine translation by jointly learning to align and translate.* ICLR.

Balaji, N. N. A., & Bharathi, B. (2020). SSNCSE_NLP@ HASOC-Dravidian-CodeMix-FIRE2020: Offensive language identification on multilingual code mixing text. In *FIRE 2020 Working Notes* (pp. 370–376).

Barathi Ganesh, H., Soman, K. P., Reshma, U., Kale, M., Mankame, P., Kulkarni, G., Kale, A., & Anand Kumar, M. (2018). Overview of Arnekt IECSIL at FIRE-2018 track on information extraction for conversational systems in Indian languages. In FIRE 2018.

Baruah, A., Das, K. A., Barbhuiya, F. A., & Dey, K. (2021). *IIITG-ADBU@HASOC-Dravidian-CodeMix-FIRE2020: Offensive content detection in code-mixed Dravidian text*. arXiv. https://arxiv.org/abs/2107.14336

Bengio, Y., Ducharme, R., & Vincent, P. (2001). A neural probabilistic language model. In *Advances in Neural Information Processing Systems* (pp. 932–938).

Bhargava, N., & Johari, A. (2023). Enhancing deep learning approach for Tamil English mixed text classification. In *Proceedings of the International Conference on Computational Intelligence and Data Science* (pp. 829–837). https://doi.org/10.2991/978-94-6463-136-4_73

Bhattu, S. N., Krishna, N. S., & Somayajulu, D. V. L. N. (2018). idrbt-team-a@ IECSIL-FIRE-2018: Named Entity Recognition of Indian Languages using bi-LSTM. In *FIRE 2018 Working Notes* (pp. 158–165).

Bojanowski, P., Grave, E., Joulin, A., & Mikolov, T. (2017). Enriching word vectors with subword information.

Transactions of the Association for Computational Linguistics, 5, 135–146. https://doi.org/10.1162/tacl_a_00051

Chakravarthi, B. R., Kumar, M., McCrae, J. P., Premjith, B., Soman, K. P., & Mandl, T. (2020). Overview of the track on HASOC-Offensive Language Identification-DravidianCodeMix. In *FIRE 2020 Working Notes* (pp. 112–120).

Chakravarthi, B. R., Priyadharshini, R., Jose, N., Mandl, T., Kumaresan, P. K., Ponnusamy, R., Hariharan, R. L., McCrae, J. P., Sherly, E., et al. (2021). Findings of the shared task on offensive language identification in Tamil, Malayalam, and Kannada. In *Proceedings of the First Workshop on Speech and Language Technologies for Dravidian Languages* (pp. 133–145).

Cho, K., Merrienboer, B., Bahdanau, D., & Bengio, Y. (2014). On the properties of neural machine translation: Encoder-decoder approaches. In *Proceedings of SSST-8, Eighth Workshop on Syntax, Semantics and Structure in Statistical Translation* (pp. 770). https://doi.org/10.3115/v1/W14-4012

Choudhary, H., Pathak, A., Saha, R., & Kumaraguru, P. (2018). Neural machine translation for English-Tamil. In *Proceedings of the 11th International Conference on Natural Language Processing* (pp. 770–775). https://doi.org/10.18653/v1/W18-6459

Clark, K., Luong, M.-T., Le, Q. V., & Manning, C. D. (2020). *ELECTRA: Pre-training text encoders as discriminators rather than generators*. arXiv. https://arxiv.org/abs/2003.10555

Collobert, R., & Weston, J. (2008). A unified architecture for natural language processing: Deep neural networks with multitask learning. In *Proceedings of the 25th International Conference on Machine Learning* (pp. 160–167). https://doi.org/10.1145/1390156.1390177

Conneau, A., Khandelwal, K., Goyal, N., Chaudhary, V., Wenzek, G., Guzmán, F., Grave, E., Ott, M., Zettlemoyer, L., & Stoyanov, V. (2019). *Unsupervised cross-lingual representation learning at scale*. arXiv. https://arxiv.org/abs/1911.02116

Dahl, G. E., Yu, D., Deng, L., & Acero, A. (2012). Context-dependent pre-trained deep neural networks for large-vocabulary speech recognition. *IEEE Transactions on Audio, Speech, and Language Processing, 20*(1), 30–42. https://doi.org/10.1109/TASL.2011.2134090

Dai, A. M., & Le, Q. V. (2015). *Semi-supervised sequence learning*. arXiv. https://arxiv.org/abs/1511.01432

Devi, R. G., Kumar, M., & Soman, K. P. (2018). Co-occurrence based word representation for extracting named entities in Tamil tweets. *Journal of Intelligent and Fuzzy Systems, 34*(4). https://doi.org/10.3233/JIFS-169439

Devi, R. G., Kumar, M., & Soman, K. P. (2019). Extraction of named entities from social media text in Tamil language using N-gram embedding for disaster management. In *Proceedings of the International Conference on Intelligent Computing and Applications* (pp. 207–223). https://doi.org/10.1007/978-3-030-28553-1_10

Devlin, J., Chang, M.-W., Lee, K., & Toutanova, K. (2018). *BERT: Pre-training of deep bidirectional transformers for language understanding*. arXiv. https://arxiv.org/abs/1810.04805

Fayaza, F., & Ranathunga, S. (2020). Tamil news clustering using word embeddings. In *2020 Moratuwa Engineering Research Conference (MERCon)* (pp. 277–282). https://doi.org/10.1109/MERCon50084.2020.9185282

Feng, F., Yang, Y., Cer, D., Arivazhagan, N., & Wang, W. (2020). Language-agnostic BERT sentence embedding. arXiv. https://arxiv.org/abs/2007.01852

Firth, J. R. (1957). A synopsis of linguistic theory. In *Studies in linguistic analysis* (pp. 1–31).

Hariprasad, S., Esackimuthu, S., Madhavan, S., Sivanaiah, R., & Angel, S. (2022). SSN_MLRG1@DravidianLangTech-ACL2022: Troll meme classification in Tamil using transformer models. In *Proceedings of the Second Workshop on Speech and Language Technologies for Dravidian Languages*. https://doi.org/10.18653/v1/2022.dravidianlangtech-1.21

Hochreiter, S., & Schmidhuber, J. (1997). Long short-term memory. *Neural Computation, 9*(8), 1735–1780. https://doi.org/10.1162/neco.1997.9.8.1735

Howard, J., & Ruder, S. (2018). Universal language model fine-tuning for text classification. In *Proceedings of the 56th Annual Meeting of the Association for Computational Linguistics (Volume 1: Long Papers)* (pp. 328–339). https://doi.org/10.18653/v1/P18-1031

Jayanthi, S. M., & Gupta, A. (2021). *SJ_AJ@DravidianLangTech-EACL2021: Task-adaptive pre-training of multilingual BERT models for offensive language identification*. arXiv. https://arxiv.org/abs/2102.01051

Joulin, A., Grave, E., Bojanowski, P., & Mikolov, T. (2016). *Bag of tricks for efficient text classification*. arXiv. https://arxiv.org/abs/1607.01759

Kalchbrenner, N., Grefenstette, E., & Blunsom, P. (2014). *A convolutional neural network for modelling sentences*. arXiv. https://arxiv.org/abs/1404.2188

Kaur, K. (2018). Khushleen@IECSIL-FIRE-2018: Indic language named entity recognition using bidirectional LSTMs with subword information. In *FIRE Working Notes* (pp. 153–157).

Khanuja, S., Bansal, D., Mehtani, S., Khosla, S., Dey, A., Gopalan, B., Margam, D. K., Aggarwal, P., Nagipogu, R. T., Dave, S., Gupta, S., Gali, S. C. B., Subramanian, V., & Talukdar, P. (2021). MuRIL: Multilingual representations for Indian languages. *arXiv*. https://arxiv.org/abs/2103.10730

Kim, Y. (2014). Convolutional neural networks for sentence classification. In *Proceedings of the 2014 Conference on Empirical Methods in Natural Language Processing (EMNLP)* (pp. 1746–1751). https://doi.org/10.3115/v1/D14-1181

Krishnaraj, J. (2020). *Tamil news classification* [Dataset]. Kaggle. https://www.kaggle.com/code/krishnarajj/tamil-news-classification/data?select=tamilmurasu_dataset.csv

Krishnan, A., Srikanth, M., & Shahina, A. (2024). Multilingual fake news detection in low-resource languages:

A comparative study using BERT and GPT-3.5. In *Proceedings of the International Conference on Artificial Intelligence and Data Science* (pp. 387–397). https://doi.org/10.1007/978-3-031-58495-4_28

Kumar, A., Irsoy, O., Su, J., Bradbury, J., English, R., Pierce, B., Ondruska, P., Gulrajani, I., & Socher, R. (2015). *Ask me anything: Dynamic memory networks for natural language processing*. arXiv. https://arxiv.org/abs/1506.07285

Kumar, A., Saumya, S., & Singh, A. (2023). Detecting Dravidian offensive posts in MIoT: A hybrid deep learning framework. *ACM Transactions on Asian and Low-Resource Language Information Processing*. https://doi.org/10.1145/3592602

Kumar, S., Kanojia, D., & Bhattacharyya, P. (2020). "A passage to India": Pre-trained word embeddings for Indian languages. In *Proceedings of the 1st Joint Workshop on Spoken Language Technologies for Under-resourced languages (SLTU) and Collaboration and Computing for Under-Resourced Languages (CCURL)* (pp. 352–357).

Kumaresan, C., & Thangaraju, P. (2023). ELSA: Ensemble learning based sentiment analysis for diversified text. *Measurement: Sensors, 25,* 100663. https://doi.org/10.1016/j.measen.2022.100663

Kunchukuttan, A., Kakwani, D., Golla, S., N. C., G., Bhattacharyya, A., Khapra, M. M., & Kumar, P. (2020). *AI4Bharat-IndicNLP corpus: Monolingual corpora and word embeddings for Indic languages*. arXiv. https://arxiv.org/abs/2005.00085

Lample, G., & Conneau, A. (2019). Cross-lingual language model pretraining. In *Advances in Neural Information Processing Systems*.

Lan, Z., Chen, M., Goodman, S., Gimpel, K., Sharma, P., & Soricut, R. (2019). *ALBERT: A lite BERT for self-supervised learning of language representations*. arXiv. https://arxiv.org/abs/1909.11942

Lebret, R., Grangier, D., & Auli, M. (2016). Neural text generation from structured data with application to the biography domain. In *Proceedings of the 2016 Conference on Empirical Methods in Natural Language Processing* (pp. 1203–1213). https://doi.org/10.18653/v1/D16-1128

Liu, Y., Ott, M., Goyal, N., Du, J., Joshi, M., Chen, D., Levy, O., Lewis, M., Zettlemoyer, L., & Stoyanov, V. (2019). *RoBERTa: A robustly optimized BERT pretraining approach*. arXiv. https://arxiv.org/abs/1907.11692

McCann, B., Bradbury, J., Xiong, C., & Socher, R. (2017). *Learned in translation: Contextualized word vectors*. arXiv. https://arxiv.org/abs/1708.00107

Merity, S., Keskar, N. S., & Socher, R. (2017). *Regularizing and optimizing LSTM language models*. arXiv. https://arxiv.org/abs/1708.02182

Mikolov, T., Chen, K., Corrado, G., & Dean, J. (2013). *Efficient estimation of word representations in vector space*. arXiv. https://arxiv.org/abs/1301.3781

Mikolov, T., Karafiát, M., Burget, L., Černocký, J., & Khudanpur, S. (2010). Recurrent neural network based language model. In *Proceedings of Interspeech 2010* (pp. 1045–1048). https://doi.org/10.21437/Interspeech.2010-343

Mikolov, T., Sutskever, I., Chen, K., Corrado, G. S., & Dean, J. (2013). Distributed representations of words and phrases and their compositionality. In *Advances in Neural Information Processing Systems*, 26.

Mishra, A., Mundotiya, R. K., & Pal, S. (2018). IIT (BHU)@ IECSIL-FIRE2018: Language independent automatic framework for entity extraction in Indian languages. In *FIRE 2018 Working Notes* (pp. 145–152).

Nivedhitha, E., Sanjay, S. P., Kumar, M., & Soman, K. P. (2016). Unsupervised word embedding based polarity detection for Tamil tweets. *Journal of Intelligent Systems, 9*(1), 4631–4638.

Pareed, A., & Idicula, S. (2019). A relation extraction system for Indian languages. *Advances in Science, Technology and Engineering Systems Journal, 4*(2). https://doi.org/10.25046/aj040208

Pennington, J., Socher, R., & Manning, C. D. (2014). GloVe: Global vectors for word representation. In *Proceedings of the 2014 Conference on Empirical Methods in Natural Language Processing (EMNLP)* (pp. 1532–1543). https://doi.org/10.3115/v1/D14-1162

Peters, M. E., Neumann, M., Iyyer, M., Gardner, M., Clark, C., Lee, K., & Zettlemoyer, L. (2018). Deep contextualized word representations. In *Proceedings of the 2018 Conference of the North American Chapter of the Association for Computational Linguistics: Human Language Technologies, Volume 1 (Long Papers)* (pp. 2227–2237). https://doi.org/10.18653/v1/N18-1202

Priyadharshan, T., & Sumathipala, S. (2018). Text summarization for Tamil online sports news using NLP. In *2018 International Conference on Information Technology Research (ICITR)* (pp. 1–5). https://doi.org/10.1109/ICITR.2018.8736154

Radford, A., Narasimhan, K., Salimans, T., & Sutskever, I. (2018). *Improving language understanding by generative pre-training*. OpenAI.

Rajalakshmi, R., Selvaraj, S., Mattins, F. R., Vasudevan, P., & Kumar, M. (2023). *HOTTEST: Hate and offensive content identification in Tamil using transformers and enhanced stemming*. https://doi.org/10.1016/j.csl.2022.101464

Rajan, K., Ramalingam, V., Ganesan, M., Palanivel, S., & Palaniappan, B. (2009). Automatic classification of Tamil documents using vector space model and artificial neural network. Expert Systems with Applications, 36(10), https://doi.org/10.1016/j.eswa.2009.02.010

Rajkumar, N., Subashini, T. S., Rajan, K., & Ramalingam, V. (2020). An ensemble of feature selection with deep learning based automated Tamil document classification models. *International Journal of Electrical Engineering and Technology, 11*(11), 70–91.

Rajkumar, S. (n.d.). *Tamil NLP* [Dataset]. Kaggle. https://www.kaggle.com/datasets/sudalairajkumar/tamil-nlp?select=tamil_movie_reviews_test.csv

Ramachandran, V., & Krishnamurthi, I. (2012). An iterative stemmer for Tamil language. In *Proceedings of the International Conference on Advances in Computing and Communications* (pp. 197–205). https://doi.org/10.1007/978-3-642-28493-9_22

Ramraj, S., Arthi, R., Murugan, S., & Julie, M. S. (2020). Topic categorization of Tamil news articles using pre-trained Word2Vec embeddings with convolutional neural network. In *2020 International Conference on Computational Intelligence for Smart Power System and Sustainable Energy (CISPSSE)* (pp. 1–4). https://doi.org/10.1109/CISPSSE49931.2020.9212248

Saha, D., Paharia, N., Chakraborty, D., Saha, P., & Mukherjee, A. (2021). *Hate-Alert@DravidianLangTech-EACL2021: Ensembling strategies for transformer-based offensive language detection*. arXiv. https://arxiv.org/abs/2102.10084

Sanh, V., Debut, L., Chaumond, J., & Wolf, T. (2019). *DistilBERT, a distilled version of BERT: Smaller, faster, cheaper and lighter*. arXiv. https://arxiv.org/abs/1910.01108

Sasidharan, T., E, S., B, V., M, V., & M, P. (2020). Code mixed question answering challenge using deep learning methods. In *2020 International Conference on Computer Communication and Informatics* (pp. 1331–1337). https://doi.org/10.1109/ICCES48766.2020.9137971

Schuster, M., & Paliwal, K. K. (1997). Bidirectional recurrent neural networks. *IEEE Transactions on Signal Processing, 45*(11), 2673–2681. https://doi.org/10.1109/78.650093

Seshadri, S., Kumar, M., & Soman, K. P. (2016). Analyzing sentiment in Indian languages micro text using recurrent neural network. *Journal of Intelligent Systems, 7*(1), 313–318.

Shibly, A., Sharma, U., & Naleer, H. (2024). An efficient method for detecting hate speech in Tamil tweets using an ensemble approach. In *Proceedings of the International Conference on Artificial Intelligence and Data Science* (pp. 19–26). https://doi.org/10.1007/978-981-99-4071-4_2

Subramanian, S., Trischler, A., Bengio, Y., & Pal, C. J. (2018). Learning general purpose distributed sentence representations via large scale multi-task learning. In *International Conference on Learning Representations*.

Sukhbaatar, S., Szlam, A., Weston, J., & Fergus, R. (2015). *End-to-end memory networks*. arXiv. https://arxiv.org/abs/1503.08895

Sundaram, M., Kumar, M., & Soman, K. P. (2015). A paraphrase detection for Twitter using unsupervised feature learning with recursive autoencoders. In *Proceedings of the 9th International Workshop on Semantic Evaluation (SemEval 2015)* (pp. 45–50). https://doi.org/10.18653/v1/S15-2008

Swamy, M., Hanumanthappa, P., & Mohan, J. (2014). Indian language text representation and categorization using supervised learning algorithm. In *2014 International Conference on Information Communication and Embedded Systems* (pp. 406–410). https://doi.org/10.1109/ICICA.2014.89

Thavareesan, S., & Mahesan, S. (2019). Sentiment analysis in Tamil texts: A study on machine learning techniques and feature representation. In *2019 14th Conference on Industrial and Information Systems (ICIIS)* (pp. 320–325). https://doi.org/10.1109/ICIIS47346.2019.9063341

Thavareesan, S., & Mahesan, S. (2020). Sentiment lexicon expansion using Word2Vec and fastText for sentiment prediction in Tamil texts. In *2020 Moratuwa Engineering Research Conference (MERCon)* (pp. 272–276). https://doi.org/10.1109/MERCon50084.2020.9185369

Thenmozhi, D., Kumar, B. S., & Aravindan, C. (2018). Deep learning approach to English-Tamil and Hindi-Tamil verb phrase translations. In *FIRE 2018*.

Thenmozhi, D., Kumar, S., & Aravindan, C. (2018). SSN_NLP@IECSIL-FIRE-2018: Deep learning approach to named entity recognition and relation extraction for conversational systems in Indian languages. In *FIRE 2018 Working Notes* (pp. 187–201).

Vasantharajan, C., & Thayasivam, U. (2021). *Towards offensive language identification for Tamil code-mixed YouTube comments and posts*. arXiv. https://doi.org/10.48550/arXiv.2108.10939

Vinyals, O., Toshev, A., Bengio, S., & Erhan, D. (2015). Show and tell: A neural image caption generator. In *2015 IEEE Conference on Computer Vision and Pattern Recognition (CVPR)* (pp. 3156–3164). https://doi.org/10.1109/CVPR.2015.7298935

Wang, J., Yu, L.-C., Lai, K. R., & Zhang, X. (2016). Dimensional sentiment analysis using a regional CNN-LSTM model. In *Proceedings of the 54th Annual Meeting of the Association for Computational Linguistics (Volume 2: Short Papers)* (pp. 225–230). https://doi.org/10.18653/v1/P16-2037

Weston, J., Chopra, S., & Bordes, A. (2014). *Memory networks*. arXiv. https://arxiv.org/abs/1410.3916

Zhang, X., Zhao, J., & LeCun, Y. (2015). Character-level convolutional networks for text classification. In *Advances in Neural Information Processing Systems, 28* (pp. 649–657).

Zhao, Y., & Tao, X. (2021). ZYJ123@DravidianLangTech-EACL2021: Offensive language identification based on XLM-RoBERTa with DPCNN. In *Proceedings of the First Workshop on Speech and Language Technologies for Dravidian Languages* (pp. 216–221).

Zhu, Y., & Dong, K. (2020). YUN111@Dravidian-CodeMix-FIRE2020: Sentiment analysis of Dravidian code mixed text. In *FIRE 2020 Working Notes* (pp. 628–634).

Zhu, Y., & Zhou, X. (2020). Zyy1510@HASOC-Dravidian-CodeMix-FIRE2020: An ensemble model for offensive language identification. In *FIRE 2020 Working Notes* (pp. 397–403).

J.Natn.Sci.Foundation Sri Lanka 2026 54 (3): 305 - 316
DOI: http://dx.doi.org/10.4038/jnsfsr.v54i3.12715

RESEARCH ARTICLE

Agriculture Technology

Optimizing drought stress to enhance root yield and secondary metabolites in Ashwagandha (*Withania somnifera* L. Dunal) under polyhouse conditions in Sri Lanka

MS Jayathilaka[1*], AAA Nishantha[2], S Subasinghe[2], KMW Rajawatta[1] and KHT Karunarathne[2]
[1] *Department of Biosystems Technology, Faculty of Technology, University of Ruhuna, Karagoda-Uyangoda, Kamburpitiya, Sri Lanka.*
[2] *Department of Crop Science, Faculty of Agriculture, University of Ruhuna,Mapalana,Sri Lanka.*

Submitted: 22 June 2025; Revised: 21 April 2026; Accepted: 18 May 2026

Abstract: Roots of Ashwagandha (*Withania somnifera* L. Dunal) are widely used in Sri Lankan herbal medicine, yet most roots are imported from India due to the low yields of local varieties and poor performance of Indian varieties under Sri Lankan conditions. Additionally, importation of Ashwagandha from India was halted in 2023 to support domestic agriculture. This study investigated whether moderate drought stress could enhance root yield and secondary metabolite content in locally grown Ashwagandha. A polyhouse experiment was conducted in the low-lying wet zone of Sri Lanka. Seven drought stress levels were maintained including 50–100 % Field capacity (control), 45–50 %, 40–45%, 35–40%, 30–35 %, 25–30 %, and 20–25%. There were five replicates per treatment, with one Ashwagandha plant grown in a sand filled pot considered as one experimental unit. Plant height, number of leaves, SPAD value, root dry matter content, total polyphenol content, flavonoid content, and DPPH (2, 2 - diphenyl -1- picrylhydrazyl) radical scavenging activity were measured. The highest shoot growth (plant height, number of leaves, SPAD value) was recorded in plants that received a drought stress of 50–100% FC. Root dry matter content, polyphenol content, and flavonoid content increased by 2.16-folds, 1.54-fold, and 1.40-folds, respectively, at 35–40% FC relative to the control. Therefore, a moisture stress level of 35–40% FC is recommended to improve root yield and secondary metabolite production in Ashwagandha roots. These findings suggest that moderate drought management can optimize both yield and medicinal value, of Ashwagandha roots, providing a practical approach to boost local production and reduce reliance on imports.

Keywords: Abiotic stress, Ashwagandha root, drought stress, moisture stress, secondary metabolite.

INTRODUCTION

Ashwagandha (*Withania somnifera* L. Dunal), which belongs to the family Solanaceae is a popular medicinal herb grown for its roots in the arid regions of India, Baluchistan, Pakistan, Afghanistan, Sri Lanka, Congo, South Africa, Egypt, Morocco, and Jordan. The plant is known globally as Indian ginseng, 'Amukkra', 'Punir' and 'Aksan' (Kulkarni & Dhir, 2008). The roots of the Ashwagandha plant are a key ingredient in many herbal medicine formulations used to treat the nervous system and musculoskeletal conditions, as well as serving as a general health tonic. Withanolides, which consist of steroidal alkaloids and lactones are the major active compounds present in Ashwagandha roots (Sanchita et al., 2014). Withanolides has different medicinal properties, including anti-inflammatory, anti-aging, immunomodulatory, anti-cancer, immunoprophylactic, and rejuvenating effects. There is a strong requirement to enhance production of secondary metabolites, since withanolides are formed in small quantities in the leaf and root tissues of plants (Singh et al., 2018). Despite the growing demand for Ashwagandha in Sri Lanka, domestic production

* Corresponding author (mevuni.jayathilaka@gmail.com; https://orcid.org/0000-0002-7674-7667)

This article is published under the Creative Commons CC-BY-ND License (http://creativecommons.org/licenses/by-nd/4.0/). This license permits use, distribution and reproduction, commercial and non-commercial, provided that the original work is properly cited and is not changed in anyway.

remains limited (Kaliyadasa et al., 2019). Most of the roots used by the local herbal medicine industry are imported from India, primarily due to the low root yields of locally cultivated varieties (Khabiya et al., 2024). Recent trade data indicate that Sri Lanka imported nearly 200 shipments of Ashwagandha products from India and other suppliers between October 2023 and September 2024, involving over 50 domestic buyers (VOLZA Grow Global, 2025). This reliance on imports stems from the low root yields and suboptimal performance of locally cultivated Ashwagandha varieties under Sri Lankan agro-climatic conditions (Khabiya et al., 2024). Improving local productivity and quality is therefore a national priority, offering the potential to reduce import dependency, strengthen domestic supply chains, and support the country's growing herbal medicine sector.

Water availability critically influences both plant growth and secondary metabolite production (Bistgani et al., 2024). While drought stress can act as a beneficial abiotic elicitor enhancing secondary metabolites such as polyphenols and flavonoids, it can also severely limit growth if unmanaged (Ramakrishna & Ravishankar, 2011). Drought stress, identified by low availability of moisture in the growth substrate and high plant evapotranspiration rates is one of the major causes for crop losses occurring worldwide (Kumar et al., 2019). The water deficient conditions in growth substrates results in a decrease of water potential in plants, inducing various physiological and biochemical processes (Shao et al., 2009). As an abiotic stress tolerance mechanism, the plant synthesizes and accumulates secondary metabolites (SMs) under drought and other environmental stress conditions. These secondary metabolites are not only essential for abiotic stress tolerance but also have an important role as pharmaceuticals and food additives due to their antioxidant, anti-inflammatory and anti-microbial properties (Bistgani et al., 2024). This signaling process of synthesizing phytochemicals or secondary metabolites in response to physical stimulants is known as abiotic elicitation (Ramakrishna & Ravishankar, 2011).

On the other hand, water scarcity is increasing with climate change, and drought stress has become one of the most influential factors determining crop yields in arid and semi-arid regions. Therefore, it is necessary to maximize the crop yield from available water to fulfill the medicinal demands of the escalating world population with limited land and water resources. Optimum irrigation management coupled with appropriate selection of crops with the potential of drought tolerance and economic importance, is an ideal alternative for climate change and dry lands (Farooq et al., 2009; Flexas et al., 2009).
Based on their chemical nature and biosynthetic pathways, secondary metabolites (SMs) are categorized into three main groups: (1) phenolic compounds (including phenolic acids, flavonoids, lignin, coumarins, stilbenes, tannins, and lignans), (2) terpenes (such as plant volatile compounds, sterols, carotenoids, and glycosides), and (3) nitrogen-containing compounds (alkaloids and glucosinolates) (Yadav et al., 2021). Other than the detrimental effects on primary metabolism and energy balance in plants, moisture stress also affects secondary metabolism and the accumulation of secondary metabolites in different plant parts (Naghizadeh et al., 2019). Other plant growth conditions, including light, temperature, and nutrient availability strongly influence the synthesis and accumulation of plant secondary metabolites (Pant et al., 2021). The complex nature of plant secondary metabolism, along with the wide array of secondary metabolites, necessitates a comprehensive approach that includes biochemical, molecular, cellular, and physiological perspectives to understand the occurrence and significance of these metabolites. The global demand for secondary metabolites is rapidly increasing as these compounds are widely used in various industries, including pharmaceuticals (antibiotic, antifungal, and antiviral), food additives, flavors, and pigments (Ozyigit et al., 2023). Therefore, understanding how drought stress affects growth, biomass partitioning, and secondary metabolite production plays a significant role in optimizing environmental conditions for enhancing production and recovery of phytochemicals.

Ashwagandha is cultivated under rain-fed conditions in many parts of South Asia. It thrives well in soils with residual moisture and requires only one or two supplementary irrigations throughout its growing season (Khabiya et al., 2024). Although Ashwagandha is a drought- tolerant plant, extended periods of substrate moisture deficiency hinders its growth and development, adversely affecting crop yield and plant productivity, and can ultimately lead to plant death.

Limited water availability leads to partial stomatal closure, resulting in reduced gas and water vapor exchange. This causes a decrease in intracellular CO_2 concentrations thereby diminishing the availability of ATP and $NADPH^{2+}$ essential for CO_2 fixation in the Calvin cycle (Selmar & Kleinwachter, 2013). Accordingly, the declining NADP+ concentration significantly reduces electron acceptors available for the electron transport chain. Drought stress induces the production of reactive oxygen species and enhances the $NADPH^{2+}/NADP^{+}$ ratio. According to the law of mass action, an increase in reductive power shifts reactions that consume $NADPH^{2+}$ toward the reduction side of equilibrium. This results in an enhancement of highly reduced secondary metabolites,

including alkaloids, monoterpenes, and aromatic amino acids (Yadav & Pandey, 2020).

The cultivation and management of medicinal plants under stressful conditions differs from those of other crops. This is because the cultivation of medicinal plants is not about increasing the yield of aboveground or belowground parts, but to increase the production of active ingredients, including essential oils (Bistgani et al., 2024). The synthesis of SMs (active ingredients), is directly influenced by the severity and intensity of drought. In most cases severe drought stress causes a significant reduction in the synthesis and accumulation of SMs, whereas moderate moisture stress conditions are reported to stimulate SM production (Isah, 2019). Therefore, it is crucial to investigate the optimal drought stress conditions that maximize SM production without compromising plant growth or yield.

Shah et al., (2011) recommended a moderate drought stress condition of two irrigations at 67 days after sowing (DAS), compared to severe water stress, (irrigations at 67 DAS and 114 DAS), moderate water stress, and control treatments (irrigations at 67 DAS, 114 DAS, 153 DAS, and 168 DAS). However, the results of this study cannot be fully interpreted since the soil moisture levels are not specified. In a previous study, where the impact of drought stress on Ashwagandha root yield was investigated, a moisture stress level of 50% field capacity (FC) was reported as the optimal drought stress level out of 50%, 60%, 80%, and 100% FC treatments (Jayathilaka et al., 2025). In a study conducted in India, the soil moisture level of 20 ± 5% total available water (TAW) with mulching was ideal for maximizing Ashwagandha root yield, compared to rainfed conditions and moisture levels of, 20 ± 5%, 40 ± 5% and 60 ± 5% of TAW (Absar et al., 2021). Therefore, more studies are needed to investigate the exact moisture stress level that maximizes the root yield of Ashwagandha to reduce water and land use in cultivation.

This study, therefore, investigated whether seven precisely defined drought stress levels, which are less than 50% FC, enhance plant growth, root biomass, and secondary metabolite content in locally grown Ashwagandha under polyhouse conditions in southern Sri Lanka.

The study hypothesized that moderate drought stress would significantly enhance both root yield and secondary metabolite production in Ashwagandha, compared to severe drought stress or well-watered conditions. While drought stress below 50% FC may reduce growth parameters including plant height and leaf number, the stress-adaptive mechanisms of the plant were likely to prioritize secondary metabolite production as a survival mechanism. This balance between growth reduction and enhanced secondary metabolite synthesis would determine the optimal moisture stress level for maximizing the medicinal properties of Ashwagandha roots.

The objectives of this study were to understand the response of field grown *W. somnifera* to soil moisture deficit, to evaluate changes in the productivity of root secondary metabolites, and to determine the optimal moisture stress level for maximizing root yield and secondary metabolite production in Ashwagandha roots.

MATERIALS AND METHODS

Experimental site

A polyhouse experiment was conducted in the Faculty of Agriculture, University of Ruhuna, Sri Lanka. This is a low-lying area in the WL_{2B} climate zone (60 06 ‘N 80022 ‘E). It is a modified top vent protected house with a floor area of 92 m^2 and covered with an insect screening net of 15.7 × 9.8 openings per cm^2 (40*25 squares/$inch^2$) and clear polyfilm of 1000 guage.

Experimental treatments

The seedlings were transplanted into sand-filled polybags (26 × 30 cm) after a nursery period of one month. Each bag was filled with 5 kg of well-washed river sand of particle sizes less than 2 mm. Sand was selected as the growth medium since its large pores facilitate rapid water drainage from the media, helping to maintain different moisture stress levels. The sand-filled polybags were saturated with water and allowed to drain for 24 hours to reach FC (evaporation was prevented). The sand-filled polybags were then exposed to evaporation, and soil moisture samples were taken to determine the different moisture levels. The weight of the sandbags was measured at each moisture level to monitor and maintain the different moisture levels. The moisture content (dry basis) at field capacity was determined by oven-drying the soil samples at 108 °C until a constant weight was reached.

This is the second experiment in a series. The first experiment, (Jayathilaka et al., 2025) reported that the root yield and polyphenol content were significantly higher under the interaction effect of 1 mM foliar salicylic acid application and a substrate drought stress level of

50% FC. Therefore, in this experiment, the moisture stress levels below 50% FC were selected to investigate the optimal moisture stress level for growth, yield, and secondary metabolite production in Ashwagandha. The goal is to reduce water consumption during growth while optimizing the root yield.

The drought stress levels maintained during the experiment (Table 1) were applied to 2-months-old plants with 50% to 100% FC serving as the control treatment. The experiment was conducted using a completely randomized design with five replications for each treatment. One Ashwagandha plant grown in a grow bag was considered as an experimental unit.

Table 1: Range of moisture content of each treatment in the experiment

Treatment	Moisture range	Percentage from field capacity	Weight range of water
T1	9.12 – 4.56%	100 – 50%	451– 225.5 g
T2	4.56 – 4.104%	45 – 50%	225.5 – 203 g
T3	4.104 – 3.648%	40 – 45%	203 – 180.45 g
T4	3.648 – 3.192%	35 – 40%	180.45 – 157.9 g
T5	3.192 – 2.736%	30 – 35%	157.9 – 135.35 g
T6	2.736 – 2.28%	25 – 30%	135.35 – 112.8 g
T7	2.28 – 1.824%	20 – 25%	112.8 – 90.25 g

The weight of each grow bag was measured daily, and water was supplied to maintain the upper moisture level for each treatment. The weights corresponding to each treatment were recalculated at two-week intervals by adding the average fresh weight of the plants to the weight range of the treatment. Separate sets of polybags with Ashwagandha plants were uprooted, and their fresh weights were measured at two-week intervals. The weights of the grow bags were measured consistently. A separate set of plants (with the same treatment) was maintained to measure the fresh weight at relevant growth stages. The recommended fertilizer schedule was followed according to Dmapr et al., (2015).

Data collection

Growth and yield parameters

The growth parameters, plant shoot height, leaf area, and number of leaves per plant, were recorded 45 days after the application of the water stress treatment. Plant shoot height was measured from the ground level to the tip of the highest fully expanded leaf using a meter scale. The number of leaves was counted manually. Leaf area was measured on the third fully expanded leaf from the top using the ADC BioScientific Leaf Area Meter AM350, Ver.1.00. After uprooting the plants, fresh shoot and root samples were oven-dried at 72 °C until a constant weight was reached to calculate the dry mass (Nazeri et al., 2018).

Physio-biochemical parameters

The physio-biochemical parameters of SPAD values, leaf relative water content (LRWC), and membrane stability index (MSI) were measured 45 days after the onset of drought stress. The SPAD value (leaf greenness) was recorded using a handheld SPAD meter (SPAD-502 Plus, Konica Minolta Corporation Ltd., Osaka, Japan) on the third fully expanded leaf from the top of each plant. The second fully expanded leaf was used to calculate the LRWC following the method of Udpuay et al., (2023). The fresh weight (FW) of the leaves was recorded before soaking in water for 24 hours to obtain the turgid weight (TW), which was measured after 24 hours. The samples were then oven-dried at 80 °C until the dry weight (DW) remained constant. LRWC (%) was calculated using the following equation:

$$LRWC = \frac{(FW - DW)}{(TW - DW)} \times 100$$

The membrane stability index (MSI) was measured using an electrical conductivity meter. Leaf samples were cut into discs of 1 cm diameter and placed in test tubes containing 20 ml of distilled water. The tubes were

incubated at 40 °C for 30 minutes in a water bath, and electrical conductivity (EC_1) was measured after cooling. Subsequently, the tubes with leaf discs were incubated at 100 °C for 15 minutes, and the electrical conductivity (EC_2) was measured.

$$MSI = \left[1 - \left(\frac{EC_1}{EC_2}\right)\right] \times 100$$

Free proline content

The free proline content, expressed in mg g^{-1} fresh weight, was measured from the second fully expanded mature leaf from the top of the plant following the method of Bates et al., (1973). Fresh leaf samples were ground using liquid nitrogen, and 100 mg of the sample was obtained. The sample was centrifuged with sulfosalicylic acid and 200 µL supernatant was collected. The supernatant was reacted with 200 µL glacial acetic acid and 200 µL of acid ninhydrin and mixed using a vortex mixer. The mixture was incubated in a 100 °C water bath for one hour and immediately transferred to an ice bath to stop the reaction. After cooling to room temperature, 400 µL of toluene was added to the sample and vortexed. After the mixture reached room temperature, 100 µL of the chromophore was diluted with 900 µL of toluene, and the absorbance of the upper layer was measured at 520 nm wavelength in a UV-Vis spectrophotometer using toluene as a blank (Alam et al., 2023).

Total polyphenol content -- Folin-Ciocalteu method (modified ISO 14502-1)

The total polyphenol content was analyzed using the Folin-Ciocalteu method (modified ISO 14502-1). Root samples were shade-dried and finely ground to obtain 0.2 g from each sample. To each sample, 5.00 ml of 70% methanol preheated to 70 °C was added, and the samples were heated at 70 °C for 10 minutes with intermittent mixing at 5-minute intervals. After cooling to room temperature, the samples were centrifuged at 3500 rpm for 10 minutes, and the supernatant was decanted. The extraction was repeated on the residual samples by adding fresh 5.00 ml of 70% methanol. Both extracts were mixed and diluted to a final volume of 10.00 ml by adding 70% methanol. A 5.00 ml aliquot of this solution was diluted to 25.00 ml with distilled water for further analysis. An anhydrous gallic acid standard series was prepared with concentrations of 10, 20, 30, 40 and 50 µg/ml. For this assay, 5 ml of 10% Folin-Ciocalteu phenol reagent and 1.00 ml of the gallic acid standard series were mixed with 1.00 ml of the sample. Within 3 to 8 minutes after the addition of the Folin-Ciocalteu phenol reagent, 4.00 ml of 7.5% sodium carbonate solution was added and mixed thoroughly. The mixtures were allowed to stand for 60 minutes at room temperature. The absorbance was measured against a blank using a UV-Vis spectrophotometer at 765 nm.

The total polyphenol content (TPC), expressed as a percentage by mass on a dry matter basis of the sample, is given by the formula:

$$TPC = \frac{(Optical\ density\ of\ sample - Optical\ density\ at\ intercept) * Sample\ volume(ml) * dilution\ factor\ * 100}{Slope\ of\ best\ fit\ linear\ calibration * mass\ of\ fresh\ sample\ (g) * 10000 * dry\ matter\ content\ of\ sample\ in\ mass\ (\%)}$$

Total flavonoids content (TFC) and 2, 2 - diphenyl -1-picrylhydrazyl (DPPH) scavenging activity

Ashwagandha root extract for flavonoid content and DPPH scavenging activity was prepared according to the method of Kähkönen et al., (1999). Shade-dried root samples (0.5 g) were added to test tubes followed by the addition of 80% methanol and the mixture was stirred. The mixture was sonicated for 5 minutes and centrifuged for 10 minutes to collect the supernatants. The extraction process was repeated, and the supernatant solutions were combined and the supernatant then evaporated to a volume of 1 ml . The extract was further lyophilized and weighed.

The aluminum chloride colorimetric method developed by Zhishen et al., (1999) was used to determine the flavonoid content in Ashwagandha roots. One mL (1mg/ml) of root extract was diluted with 4 mL of distilled water, and 0.3 mL of $NaNO_2$ (5% w/v) added. The sample was kept for 5 minutes and 0.3 mL of $AlCl_3$ (10% w/v) was added, and six minutes later 2 ml of 1M NaOH solution was added. The volume was adjusted to 10 mL by adding distilled water. After shaking the mixture, the absorbance was measured at 510 nm against a standard series of catechin (20, 40, 60, 80, and 100 µg/mL).

The DPPH scavenging activity was determined using the method described by Ferreira et al., (2009). One mL of

root extract (1mg/1ml) was added to 2.7 mL of methanolic solution containing DPPH radicals (0.024 mg /ml). The mixture was shaken and left to stand in the dark for 60 minutes. Absorbance was read at 517 nm to determine the reduction of DPPH radicals. The radical scavenging activity (RSA) was calculated as the percentage of DPPH discoloration using the formula:

$$RSA = [(ADPPH - AS)/ADPPH] \times 100$$

Where AS = absorbance of the solution with the extract, ADPPH = absorbance of the DPPH solution.

Data analysis

Data were analyzed by using one-way Anova and means were separated by Tukey's honest significant difference test at $P \leq 0.05$ in SAS® OnDemand for Academics platform.

RESULTS AND DISCUSSION

The results of this study showed that different drought stress levels significantly affected the growth, yield, and physio-biochemical parameters of secondary metabolite production in Ashwagandha.

Table 2: Effect of different drought stress levels on plant height, number of leaves, leaf area, and SPAD value of Ashwagandha plant

Drought stress level	Plant height (cm)	Number of leaves	Leaf area (mm ^{2})	SPAD value
100–50% FC (control)	43.67 ±2.68 a	38.34 ± 4.34 a	2183.33 ±44.09 a	51.13 ± 3.13 a
45–50% FC	43.34 ± 1.33 ab	32.67 ± 4.63 ab	2016.67 ± 109.29 ab	47.06 ± 1.29 a
40–45% FC	31.00 ± 1.52 ab	35.34 ± 4.04 ab	2067.67 ± 139.88 a	53.00 ± 0.85 a
35–40% FC	37.50 ± 3.81 ab	32.67 ± 8.17 ab	2016.67 ± 60.09 ab	46.67 ± 1.11 ab
30–35% FC	36.00 ± 2.64 ab	23.67 ± 3.38 ab	1883.33 ± 44.09 ab	45.36 ± 1.48 ab
25–30% FC	42.34 ± 3.38 ab	26.34 ± 1.45 ab	1600.00 ± 57.73 bc	40.67 ±2.74 b
20–25% FC	30.67 ± 2.33 b	19 ± 4.16 b	1266.67 ± 120.18 c	31.06 ± 1.68c

Means followed by the same letters within a column are statistically similar based on Tukey's honest significant difference test at $P \leq 0.05$; data are means of four replications ± standard errors. FC = Field Capacity

Table 2 presents the impact of different drought stress levels (measured as a percentage of FC) on the growth and yield parameters of Ashwagandha. It shows the variation of plant height, number of leaves, and SPAD values across various drought stress levels, ranging from 100–50% FC (control) to 20–25% FC. A consistent trend of higher plant growth was observed with the highest plant height, number of leaves, leaf area, and SPAD value recorded in the control (50–100% FC). In contrast, the significantly lowest plant growth with the lowest plant height, number of leaves, and leaf area was reported in plants subjected to the highest drought stress level (20–25% FC). When compared to the control, plant height, number of leaves and leaf area decreased by 29.76%, 50.44%, and 41.98%, respectively, under severe drought stress (20–25 % FC). The highest SPAD values were observed in the control (50–100% FC), 45–50% FC and 40–45% FC treatments while the lowest values were recorded at 20–25% FC. Root dry matter was significantly higher (0.59 g) in plants subjected to 35–40% FC while the lowest root dry matter content (0.15 g) was found in plants subjected to 20–25% FC (Figure 1 a). Application of moderate drought stress (35–40% FC) increased the root dry matter content by 293% relative to the control, which is the irrigation level used by farmers at present (Figure 1). These results are supported by a drought study conducted on Mexican marigold (*Tagetes minuta* L.) (Babaei et al., 2021).

With the increase of drought stress, leaf area decreased, although new leaves emerged at a severe stress level of 20–25% FC. Under severe water stress, leaves showed symptoms of withering, rolling, and falling followed by accelerated leaf senescence. These symptoms can be identified as morphological adaptations by plants to withstand drought stress by reducing water loss through transpiration (Shah et al., 2011). Accelerated senescence of older leaves is considered an adaptation shown by plants to direct translocation of nutrients to growing tissues to sustain growth and development under severe moisture stress (Thakur et al., 2016). Shah et al., (2011)

reported reductions in leaf area by 72.6% and 65.6%, under severe (one irrigation after sowing), and mild water stress (two irrigations after sowing), respectively, relative to the control (four irrigations after sowing), indicating that leaf area is the most sensitive growth parameter to variations in substrate moisture. During the present study, plant growth which indicated by leaf area, number of leaves, and plant height increased with drought stress. This observation is in agreement with previous studies as discussed above. Plant physiological responses, including stomatal closure, reduced photosynthesis, cell turgidity, and impaired nutrient uptake by roots, causes these morphological changes under drought stress (Babaei et al., 2021).

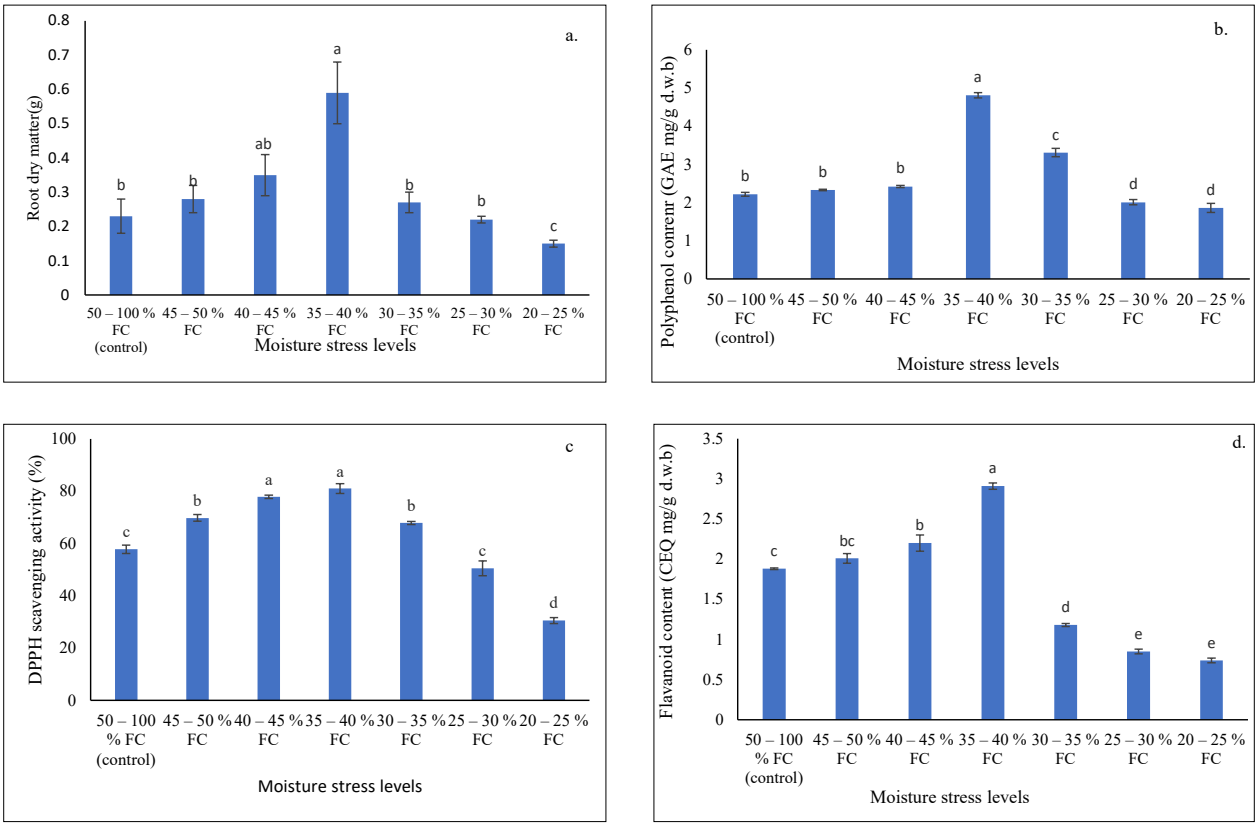

Figure 1: Effect of different moisture stress levels on (a) root dry matter, (b) polyphenol content, (c) DPPH scavenging activity, and (d) flavonoid content. GAE = (gallic acid equivalents) QE = (quercetin equivalents) d.w.b. = dry weight basis. Different lowercase letters above the bars indicate significant differences among treatments at $p < 0.05$.

Table 3 presents the effects of different drought stress levels on several physio-biochemical parameters, including leaf relative water content (LRWC), membrane stability index (MSI), and free proline content. Leaf relative water content showed a decreasing trend with increasing drought stress, with plants in the control treatment (50–100 % FC) having the highest LRWC (90.91 %), while the lowest LRWC was under severe drought stress conditions of 25–30% and 20–25% FC. Similarly, MSI decreased significantly as the drought stress intensified from 62.70 % (control) to 23.78% (20–25 % FC) implying a possible damage to cell membranes due to increasing drought severity. On the contrary, free proline content, which is an indicator of plant stress response, increase by 235.2% at the drought stress level of 20–25% FC compared to the control. Both polyphenol content (5.81 ± 0.07 GAE mg/g dry weight basis) and flavonoid content (2.91 ± 0.04 CEQ mg/ g dry weight basis) in the Ashwagandha root peaked as plants were subjected to 35–40% FC drought stress conditions (Figure 1). At this level, the polyphenol and flavonoid contents increased by 161.7% and 54.8%, respectively.

Similarly, the highest DPPH scavenging activity (81.03 ± 1.88 %), a measure of antioxidant capacity, was observed at 35–40% FC, with the lowest activity (30.56 ± 1.15 %) observed at 20–25% FC (Figure 1). These results demonstrate that moderate moisture stress can induce the synthesis of beneficial phytochemicals, whereas severe stress conditions significantly impair the growth, yield and physio-biochemical parameters of Ashwagandha plants, as further discussed below.

Table 3: Effect of different drought stress levels on relative water content, membrane stability, free proline content, polyphenol content, flavonoid content and DPPH scavenging activity of Ashwagandha root

Drought stress level	Leaf relative water content (%)	Membrane stability index (%)	Free proline content (µg/g)	DPPH scavenging activity (%)
50–100 % FC (control)	90.91 ± 0.82 a	62.70 ± 1.62 a	89.68 ± 0.39 g	57.79 ±1.63 c
45–50 % FC	82.74 ± 1.90 bc	59.67 ± 0.77 ab	123.56 ± 0.61 f	69.80 ± 1.27 b
40–45 % FC	86.61 ± 1.15 ab	54.19 ±1.52 b	150.52 ± 0.38 e	77.84 ± 0.66 a
35–40 % FC	77.65 ± 1.14 cd	56.67 ± 0.69 b	180.85 ± 0.57 d	81.03 ± 1.88 a
30–35 % FC	77.03 ± 1.03 cd	43.80 ± 1.28 c	200.56 ± 0.48 c	67.87 ± 0.61 b
25–30 % FC	72.21 ± 2.73 d	30.27 ± 1.36 d	250.63 ± 0.67 b	50.51 ± 2.82 c
20–25 % FC	73.06 ± 1.15 d	23.78 ± 0.93 e	300.59 ± 0.38 a	30.56 ± 1.15 d

Means followed by the same letters within a column are statistically similar based on Tukey's Honest significant difference test at $P \leq 0.05$; data are means of four replications ± standard errors. FC = Field capacity

The root is the main economically valuable part harvested from the Ashwagandha plant, used for treating various physiological disorders (Mikulska et al., 2023). In the present study, the highest root dry biomass was recorded at 35–40% FC, which is in accordance with findings of Absar et al., (2021), Shah et al., (2011) and Tapadia & Gajbhiye (2010). As reported by Absar et al., (2021), the maximum root yield of 1030 kg ha^{-1} was obtained under 20 ± 5% of total available water (total available water = field capacity – permanent wilting point), which is almost similar to the present study. As a drought tolerance mechanism, plants enhance their water absorption capacity by increasing root growth and biomass, enabling them to access water from deeper soil layers (Bhattacharya, 2021). This adaptation increases biomass partitioning to roots, leading to an increase in root/shoot ratio helping to prevent excess evapotranspiration (Comas et al., 2013). Similarly, in *Cichorium intybus*, the vegetative growth slowed under moderate drought stress, while the roots continued to grow into deeper soil layers (Vandoorne et al., 2012). In accordance with the results of our study, the RWC of *W. somnifera* variety 'Poshita' was decreased by 51% after applying drought stress suggesting a loss of leaf turgidity that would lead to a decrease in internal CO_2 concentration and a decline in photosynthesis rate (Sanchita et al., 2015). This finding was supported by reduced plant growth observed at severe drought stress levels in the present study. Similarly, the membrane stability index (MSI) declined as stress intensified, dropping from 62.70% in the control group to 23.78% under the most severe stress (20–25% FC), indicating considerable membrane damage.

In our study, the free proline content in leaves increased by 235.2% at 20–25% FC relative to the control, indicating an adaptive response to osmotic stress. In accordance with the results of this study, free proline content of Mullein (*Verbascum songaricum* Schrenk.) showed a significant increase with increasing of soil moisture deficit compared to the control (85–90% FC), reaching a maximum value at 30% FC (Ghahremani et al., 2020). A similar trend of increasing proline content under water stress conditions was also reported in sweet basil plants (Pirbalouti et al., 2017). The enhanced synthesis of free proline is associated with a decrease in photosynthetic pigments under moisture-deficient conditions as evident from SPAD values (Table 1) reported in the present study (Pirbalouti et al., 2017). Proline is a compatible osmolyte, enabling plants to maintain osmotic balance by regulating water potential besides acting as an antioxidant by scavenging ROS generated during stress (Alavi-Samani et al., 2015).

The drought stress conditions induced in plants due to high transpiration rates and less substrate moisture availability, result in reduced leaf water potential and turgor pressure. This alters the various physiological pathways, leading to the production of SMs that improves drought resistance in plants. The accumulation of these SMs protect the membranes from lipid peroxidation caused by oxidative stress (Yadav et al., 2021). Plants produce non-enzymatic antioxidants, flavonoids and polyphenols as an adaptive mechanism to scavenge reactive oxygen species (ROS), which are produced due to oxidative stress caused by drought (Treml & Smejkal, 2016). Under drought conditions, polyphenols act as antioxidants by donating electrons to guaiacol-type peroxidases. These enzymes detoxify hydrogen peroxide (H_2O_2), which is produced from stress, thereby protecting the plant from oxidative damage (Gill & Tuteja, 2010). In the present study, the highest polyphenol content, flavonoid content, and DPPH radical scavenging activity were recorded in plants grown under 35–40% FC. This is consistent with results in mullein plants, where increased irrigation intervals significantly increased polyphenol content in leaf and flower extracts (Ghahremani et al., 2020). Under drought stress, *W. somnifera* increases activity in the phenylpropanoid pathway, leading to increased synthesis of polyphenols and flavonoids. This pathway is initiated through increased activity of phenylalanine ammonia-lyase (PAL), the gateway enzyme to polyphenol biosynthesis. This pathway is directly involved in the plant's antioxidative defense, aiding in scavenging ROS and improving membrane integrity during stress (Tripathi et al., 2020). Even though this study did not directly quantify withanolide content, previous transcriptomic and molecular studies have shown that drought stress significantly upregulates key genes involved in withanolide biosynthesis, such as *WsHMGR*, *WsDXS*, and *WsCAS*, which are part of the mevalonate and MEP pathways (Mishra et al., 2020). Additionally, transcription factors such as *WsMYC2* and members of the WRKY family have been shown to enhance the expression of secondary metabolite pathway genes under abiotic stress, particularly drought (Sharma et al., 2019). The observed increase in polyphenol and flavonoid content in this study at 35–40% FC may therefore reflect activation of these secondary metabolite pathways, including those associated with withanolide production, which requires further investigation. In accordance with the results of our study, the flavonoid (baicalein) content of *Scutellaria baicalensis* Georgi (Chinese herb) increased with moderate drought stress but decreased under severe stress conditions (Cheng et al., 2018). In *Amaranthus tricolor*, upon application of four irrigation regimes (25, 50, 80 and 100% FC), the highest TPC was observed at 50% FC. In the same study, TFC and DPPH activity (antioxidant activity) was significantly elevated with increasing drought severity (Sarker & Oba, 2018), which contrasts with our results where TFC and DPPH activity peaked at 35–40% FC and decreased thereafter. Finally, drought stress induced by limited water supply in the growth substrate can significantly influence the content of active principles in Ashwagandha roots, with content decreasing proportionally as stress intensity increases (Shah et al., 2011).

These findings provide a practical strategy for Sri Lankan growers and policymakers seeking to increase the competitiveness of local Ashwagandha production. By optimizing irrigation to maintain moderate drought stress, it is possible to boost both yield and medicinal quality while conserving water in regions facing increasing water scarcity.

However, this study has several limitations. The experiments were conducted under controlled polyhouse conditions, which do not fully replicate the complexity of open-field environments, where variables such as temperature, humidity, soil type, and pest pressure may differ. Furthermore, while our analyses focused on polyphenols, flavonoids, and antioxidant activity, future research should include the direct quantification of withanolides, the main pharmacologically active compounds in Ashwagandha roots. Economic analyses and field-based trials will also be essential to validate these findings and assess their practical feasibility on a commercial scale. Since the Ashwagandha plant performs well under drought stress conditions, further research could investigate the suitability of the plant to grow in semi-arid and arid regions of Sri Lanka, as it is a good source of income. Further studies should explore the impact of other biotic and abiotic stress factors, including light intensity, pests, and salinity, on root yield of Ashwagandha. Future research can also investigate the integration of biostimulants such as seaweed extracts, beneficial microbial inoculants (e.g., *Azospirillum*, *Bacillus*, *Rhizophagus* spp.), and humic substances to enhance plant responses under moisture stress conditions.

CONCLUSION

This study highlights the significant impact of varying drought stress levels on the growth, yield, and secondary metabolite production in *W. somnifera*. The highest shoot growth (plant height, number of leaves, SPAD value)

was recorded at 50–100% FC. The significantly highest root dry biomass, polyphenol content, flavonoid content, and antioxidant activity (DPPH radical scavenging) were recorded in plants grown under 35–40% FC. Based on our findings, a drought stress level of 35–40% FC is recommended as the most suitable stress level for significantly enhancing root yield and secondary metabolite production in Ashwagandha roots. Our results suggest that an optimal balance of drought stress can enhance the production of economically and medicinally important secondary metabolites while conserving water.

REFERENCE

Absar, N., Singh, A. K., & Kumar, D. (2021). Evaluation of productivity and quality of *Withania somnifera* (L.) Dunal under different plant populations, irrigation levels and moisture conservation practices in sub-tropical plains of North India. *Journal of Medicinal and Aromatic Plant Sciences*, *43*(1–2), 37–48. https://www.researchgate.net/publication/359401096

Alam, A. U., Ullah, H., Himanshu, S. K., Praseartkul, P., Tisarum, R., Cha-um, S., & Datta, A. (2023). Seed Priming and Foliar Application of Salicylic Acid is Equally Beneficial in Mitigating Drought Stress in Cucumber. *Journal of Soil Science and Plant Nutrition*. https://doi.org/10.1007/s42729-023-01485-z

Alavi-Samani, S. M., Kachouei, M. A., & Pirbalouti, A. G. (2015). Growth, yield, chemical composition, and antioxidant activity of essential oils from two thyme species under foliar application of jasmonic acid and water deficit conditions. *Horticulture Environment and Biotechnology*, *56*(4), 411–420. https://doi.org/10.1007/s13580-015-0117-y

Azhar, N., Hussain, B., Yasin Ashraf, M., & Yar Abbasi, K. (2011). Water stress mediated changes in growth, physiology and secondary metabolites of desi ajwain (*Trachyspermum ammi* L.). *Pakistan Journal of Botany*, *43*, 15–19.

Babaei, K., Moghaddam, M., Farhadi, N., & Ghasemi Pirbalouti, A. (2021). Morphological, physiological and phytochemical responses of Mexican marigold (*Tagetes minuta* L.) to drought stress. *Scientia Horticulturae*, *284*. https://doi.org/10.1016/j.scienta.2021.110116

Bates, L. S., Waldren, R. P., & Teare, I. D. (1973). Rapid determination of free proline for water-stress studies. *Plant and Soil*, *39*, 205–207.

Bistgani, Z. E., Barker, A. V., & Hashemi, M. (2024). Physiology of medicinal and aromatic plants under drought stress. *The Crop Journal*, *12*(2), 330–339. https://doi.org/10.1016/j.cj.2023.12.003

Cheng, L., Han, M., Yang, L. min, Li, Y., Sun, Z., & Zhang, T. (2018). Changes in the physiological characteristics and baicalin biosynthesis metabolism of *Scutellaria baicalensis* Georgi under drought stress. *Industrial Crops and Products*, *122*, 473–482. https://doi.org/10.1016/j.indcrop.2018.06.030

Comas, L. H., Becker, S. R., Cruz, V. M. V., Byrne, P. F., & Dierig, D. A. (2013). Root traits contributing to plant productivity under drought. In *Frontiers in Plant Science* (Vol. 4, Number NOV). Frontiers Research Foundation. https://doi.org/10.3389/fpls.2013.00442

Dmapr, B., Jat, R. S., Reddy, R. N., Bansal, R., & Manivel, P. (2015). *Good Agricultural Practices for Ashwagandha Good Agricultural Practices for Ashwagandha Compiled by*. www.dmapr.org.in

Farooq, M., Wahid, A., Kobayashi, N., Fujita, D., & Basra, S. M. A. (2009). Plant drought stress: Effects, mechanisms and management. *Agronomy for Sustainable Development*, *29*(1), 185–212. https://doi.org/10.1051/agro:2008021

Ferreira, I. C. F. R., Aires, E., Barreira, J. C. M., & Estevinho, L. M. (2009). Antioxidant activity of Portuguese honey samples: Different contributions of the entire honey and phenolic extract. *Food Chemistry*, *114*(4), 1438–1443. https://doi.org/10.1016/j.foodchem.2008.11.028

Flexas, J., Barón, M., Bota, J., Ducruet, J. M., Gallé, A., Galmés, J., Jiménez, M., Pou, A., Ribas-Carbó, M., Sajnani, C., Tomàs, M., & Medrano, H. (2009). Photosynthesis limitations during water stress acclimation and recovery in the drought-adapted Vitis hybrid Richter-110 (V. berlandieri×V. rupestris). *Journal of Experimental Botany*, *60*(8), 2361–2377. https://doi.org/10.1093/jxb/erp069

Ghahremani, A., Ghasemi Pirbalouti, A., Mozafari, H., Habibi, D., & Sani, B. (2020). Phytochemical and morpho-physiological traits of mullein as a new medicinal crop under different planting pattern and soil moisture conditions. *Industrial Crops and Products*, *145*. https://doi.org/10.1016/j.indcrop.2019.111976

Ghasemi Pirbalouti, A., Malekpoor, F., Salimi, A., & Golparvar, A. (2017). Exogenous application of chitosan on biochemical and physiological characteristics, phenolic content and antioxidant activity of two species of basil (*Ocimum ciliatum* and *Ocimum basilicum*) under reduced irrigation. *Scientia Horticulturae*, *217*, 114–122. https://doi.org/10.1016/j.scienta.2017.01.031

Gill, S. S., & Tuteja, N. (2010). Reactive oxygen species and antioxidant machinery in abiotic stress tolerance in crop plants. *Plant Physiology and Biochemistry*, *48*(12), 909–930. https://doi.org/10.1016/j.plaphy.2010.08.016

Isah, T. (2019). Stress and defense responses in plant secondary metabolites production. *Biological Research*, *52*(1), 39. https://doi.org/10.1186/s40659-019-0246-3

Jayathilaka, M. S., Subasinghe, S., Rajawatta, K. M. W., & Karunarathna, K. H. T. (2025). Growth and polyphenol content of Ashwagandha (*Withania somnifera* L. Dunal) under combined drought stress and salicylic acid treatment. *Discover Plants*, *2*(1). https://doi.org/10.1007/s44372-025-00135-1

Kähkönen, M. P., Hopia, A. I., Vuorela, H. J., Rauha, J. P., Pihlaja, K., Kujala, T. S., & Heinonen, M. (1999). Antioxidant activity of plant extracts containing phenolic compounds. *Journal of Agricultural and Food Chemistry*, *47*(10), 3954–3962. https://doi.org/10.1021/jf990146l

Kaliyadasa, E., Jayasinghe, L., & Peiris, S. (2019). Tuber quality of Ashwagandha (*Withania somnifera* Duanal) affected by different growth conditions. *Korean Journal of Agricultural Science*, *46*(1), 151–161. https://doi.org/10.7744/kjoas.20190005

Khabiya, R., Choudhary, G. P., Jnanesha, A. C., Kumar, A., & Lal, R. K. (2024). An insight into the potential varieties of Ashwagandha (Indian ginseng) for better therapeutic efficacy. *Ecological Frontiers*, *44*(3), 444–450. https://doi.org/10.1016/J.CHNAES.2023.06.009

Kulkarni, S. K., & Dhir, A. (2008). Withania somnifera: An Indian ginseng. *Progress in Neuro-Psychopharmacology and Biological Psychiatry*, *32*(5), 1093–1105. https://doi.org/10.1016/j.pnpbp.2007.09.011

Kumar, R., Berwal, M. K., & Saroj, P. L. (2019). Morphological, Physiological, Biochemical and Molecular Facet of Drought Stress in Horticultural Crops. *International Journal of Bio-Resource and Stress Management*, *10*(5), 545–560. https://doi.org/10.23910/IJBSM/2019.10.5.2031

Mikulska, P., Malinowska, M., Ignacyk, M., Szustowski, P., Nowak, J., Pesta, K., Szeląg, M., Szklanny, D., Judasz, E., Kaczmarek, G., Ejiohuo, O. P., Paczkowska-Walendowska, M., Gościniak, A., & Cielecka-Piontek, J. (2023). Ashwagandha (*Withania somnifera*)—Current Research on the Health-Promoting Activities: A Narrative Review. *Pharmaceutics*, *15*(4). https://doi.org/10.3390/pharmaceutics15041057

Mishra, B., Bose, S. K., & Sangwan, N. S. (2020). Comparative investigation of therapeutic plant *Withania somnifera* for yield, productivity, withanolide contents, and expression of pathway genes during contrasting seasons. *Industrial Crops and Products*, *154*. https://doi.org/10.1016/j.indcrop.2020.112508

Naghizadeh, M., Kabiri, R., Hatami, A., Oloumi, H., Nasibi, F., & Tahmasei, Z. (2019). Exogenous application of melatonin mitigates the adverse effects of drought stress on morpho-physiological traits and secondary metabolites in Moldavian balm (*Dracocephalum moldavica*). *Physiology and Molecular Biology of Plants*, *25*(4), 881–894. https://doi.org/10.1007/s12298-019-00674-4

Nazeri, P., Rad, A. H. S., ValadAbadi, S. A., Mirakhori, M., & Masoule, E. H. (2018). Effect of sowing dates and late season water deficit stress on quantitative and qualitative traits of canola cultivars. *Outlook on Agriculture*, *47*(4), 291–297. https://doi.org/10.1177/0030727018793658

Ozyigit, I. I., Dogan, I., Hocaoglu-Ozyigit, A., Yalcin, B., Erdogan, A., Yalcin, I. E., Cabi, E., & Kaya, Y. (2023). Production of secondary metabolites using tissue culture-based biotechnological applications. *Frontiers in Plant Science*, *14*. https://doi.org/10.3389/fpls.2023.1132555

Pant, P., Pandey, S., & Dall'Acqua, S. (2021). The Influence of Environmental Conditions on Secondary Metabolites in Medicinal Plants: A Literature Review. In *Chemistry and Biodiversity* (Vol. 18, Number 11). John Wiley and Sons Inc. https://doi.org/10.1002/cbdv.202100345

Ramakrishna, A., & Ravishankar, G. A. (2011). Influence of abiotic stress signals on secondary metabolites in plants. In *Plant Signaling and Behavior* (Vol. 6, Number 11, pp. 1720–1731). https://doi.org/10.4161/psb.6.11.17613

Sanchita, Singh, R., Mishra, A., Dhawan, S. S., Shirke, P. A., Gupta, M. M., & Sharma, A. (2015). Physiological performance, secondary metabolite and expression profiling of genes associated with drought tolerance in *Withania somnifera*. *Protoplasma*, *252*(6), 1439–1450. https://doi.org/10.1007/s00709-015-0771-z

Sanchita, Singh, S., & Sharma, A. (2014). Bioinformatics approaches for structural and functional analysis of proteins in secondary metabolism in *Withania somnifera*. *Molecular Biology Reports*, *41*(11), 7323–7330. https://doi.org/10.1007/s11033-014-3618-3

Sarker, U., & Oba, S. (2018). Drought Stress Effects on Growth, ROS Markers, Compatible Solutes, Phenolics, Flavonoids, and Antioxidant Activity in *Amaranthus tricolor*. *Applied Biochemistry and Biotechnology*, *186*(4), 999–1016. https://doi.org/10.1007/s12010-018-2784-5

Selmar, D., & Kleinwachter, M. (2013). Influencing the product quality by deliberately applying drought stress during the cultivation of medicinal plants. *Industrial Crops and Products*, *42*(1), 558–566. https://doi.org/10.1016/j.indcrop.2012.06.020

Shah, S., Gajbhiye, N. A., & Saravanan, R. (2011). Phytochemical and physiological changes in Ashwagandha (*Withania somnifera* Dunal) under soil moisture stress. *Brazilian Journal of Plant Physiology*, *22*, 255–261.

Shao, H. B., Chu, L. Y., Jaleel, C. A., Manivannan, P., Panneerselvam, R., & Shao, M. A. (2009). Understanding water deficit stress-induced changes in the basic metabolism of higher plants-biotechnologically and sustainably improving agriculture and the ecoenvironment in arid regions of the globe. In *Critical Reviews in Biotechnology* (Vol. 29, Number 2, pp. 131–151). https://doi.org/10.1080/07388550902869792

Sharma, A., Rather, G. A., Misra, P., Dhar, M. K., & Lattoo, S. K. (2019). Jasmonate responsive transcription factor WsMYC2 regulates the biosynthesis of triterpenoid withanolides and phytosterol via key pathway genes in *Withania somnifera* (L.) Dunal. *Plant Molecular Biology*, *100*(4–5), 543–560. https://doi.org/10.1007/s11103-019-00880-4

Singh, R., Gupta, P., Khan, F., Singh, S. K., Sanchita, Mishra, T., Kumar, A., Dhawan, S. S., & Shirke, P. A. (2018). Modulations in primary and secondary metabolic pathways and adjustment in physiological behaviour of Withania somnifera under drought stress. *Plant Science*, *272*, 42–54. https://doi.org/10.1016/j.plantsci.2018.03.029

Tapadia, S., & Gajbhiye, N. A. (2010). Leaf gas exchange, chlorophyll fluorescence, growth and root yield of Ashwagandha (*Withania somnifera* Dunal) under soil moisture stress. *Indian Journal of Plant Physiology*, (No. 2), 117–124. https://www.researchgate.net/publication/266950731

Thakur, N., Sharma, V., & Kishore, K. (2016). Leaf senescence: an overview. In *Indian Journal of Plant Physiology* (Vol. 21, Number 3, pp. 225–238). Springer Verlag. https://doi.org/10.1007/s40502-016-0234-3

Treml, J., & Šmejkal, K. (2016). Flavonoids as Potent Scavengers

of Hydroxyl Radicals. In *Comprehensive Reviews in Food Science and Food Safety* (Vol. 15, Number 4, pp. 720–738). Blackwell Publishing Inc. https://doi.org/10.1111/1541-4337.12204

Tripathi, S., Sangwan, R. S., Mishra, B., Jadaun, J. S., & Sangwan, N. S. (2020). Berry transcriptome: insights into a novel resource to understand development dependent secondary metabolism in *Withania somnifera* (Ashwagandha). *Physiologia Plantarum*, *168*(1), 148–173. https://doi.org/10.1111/ppl.12943

Udpuay, S., Ullah, H., Himanshu, S. K., Tisarum, R., Cha–um, S., & Datta, A. (2023). Drought tolerance screening of okra genotypes in relation to growth and physio–biochemical traits at the vegetative stage. *Genetic Resources and Crop Evolution*. https://doi.org/10.1007/s10722-023-01689-3

Vandoorne, B., Mathieu, A.-S., Van den Ende, W., Vergauwen, R., Perilleux, C., Javaux, M., & Lutts, S. (2012). Water stress drastically reduces root growth and inulin yield in Cichorium intybus (var. sativum) independently of photosynthesis. *Journal of Experimental Botany*, *63*(2), 695–709. https://doi.org/10.1093/jxb/err313

VOLZA Grow Global. (2025). *Ashwagandha Buyers & Importers in Sri Lanka - Volza*. https://www.volza.com/p/ashwagandha/buyers/buyers-in-sri-lanka/

Yadav, B., Jogawat, A., Rahman, M. S., & Narayan, O. P. (2021). Secondary metabolites in the drought stress tolerance of crop plants: A review. *Gene Reports*, *23*. https://doi.org/10.1016/j.genrep.2021.101040

Yadav, R., & Pandey, P. (2020). Assessment of Air Pollution Tolerance Index (APTI) and Anticipated Performance Index (API) of Roadside Plants for the Development of Greenbelt in Urban Area of Bathinda City, Punjab, India. *Bulletin of Environmental Contamination and Toxicology*, *105*(6), 906–914. https://doi.org/10.1007/s00128-020-03027-0

Zhishen, J., Mengcheng, T., & Jianming, W. (1999). The determination of flavonoid contents in mulberry and their scavenging effects on superoxide radicals. *Food Chemistry*, *64*(4), 555–559.

J.Natn.Sci.Foundation Sri Lanka 2026 54 (3): 317 - 324
DOI: http://dx.doi.org/10.4038/jnsfsr.v54i3.12768

RESEARCH ARTICLE

Immunogenetics

First insights into HLA-Cw6 in Sri Lankan paediatric psoriasis: A pilot study on genetic susceptibility and oxidative stress

ND Wanniarachchi[1], S Samaraweera[2], J Seneviratne[2], HASG Dharmaratne[3] and ADDS Amarasekara[1*]

[1] *Department of Zoology and Environment Sciences, Faculty of Science, University of Colombo, Colombo, Sri Lanka.*
[2] *Pediatric Dermatology Unit , Lady Ridgeway Hospital for Children, Colombo, Sri Lanka.*
[3] *Department of Statistics, Faculty of Science, University of Colombo, Colombo, Sri Lanka.*

Submitted: 10 August 2025; Revised: 13 April 2026; Accepted: 29 April 2026

Abstract: Psoriasis is a chronic, inflammatory skin disease with one-third of the cases showing a childhood-onset. Genetic-based management of psoriasis in children enables early diagnosis, closer monitoring, and personalized treatment to prevent long-term impacts. Human leukocyte antigen (HLA)-Cw6 is the major risk allele associated with early-onset, severity, and disease susceptibility. Besides genetic predisposition, oxidative stress (OS) has been increasingly implicated in the pathogenesis of psoriasis. However, data on the prevalence of the HLA-Cw6 allele in paediatric psoriasis or the role of OS remain unexplored, leaving a gap in knowledge about its prevalence and clinical significance in the local paediatric population. Therefore, DNA extracted from patient samples (n=59) was subjected to the polymerase chain reaction (PCR) – sequence specific primer (SSP) method followed by restriction fragment length polymorphism to identify the HLA-Cw6 allele positivity. Total antioxidant capacity and lipid peroxide activity in patient serum (n=45) were assessed using ferric reducing antioxidant power assay and thiobarbituric acid reactive substances assays, respectively. Clinical data including BMI, disease severity, and age of onset were obtained from the clinical records. 23.7% of HLA-Cw6 allele positivity (heterozygotes -16. 9% and homozygotes -6.8%) was reported in this study. Moderate or severe disease was exhibited by the HLA-Cw6 homozygous genotype (p = 0.035: Fisher's exact test). No significant association was observed between oxidative stress, genotype, or disease severity, possibly reflecting limited sample size (p > 0.05, Kruskal-Wallis test). A significant correlation was observed between BMI and disease severity (p = 0.0028, Fisher's Exact Test). Female predominance was noted among total cases. This is the first study to report the prevalence of the HLA-Cw6 allele in Sri Lankan paediatric psoriasis patients and its potential link to disease severity. Larger studies are needed to confirm these findings.

Keywords: HLA-Cw6, oxidative stress, paediatric psoriasis, skin disease.

INTRODUCTION

Psoriasis in children, or paediatric psoriasis, affects approximately 0.1–1% of the global paediatric population (International Psoriasis Council, n.d.). Up to one-third of cases begin in childhood or adolescence, most commonly presenting as plaque psoriasis on the scalp, face, or flexural areas. It is characterized by epidermal hyperplasia, vasodilation, and leukocyte infiltration in the epidermis and is associated with numerous co-morbidities, including psoriatic arthritis, where the inflammation affects joints, significantly reducing quality of life (Busse & Liao 2010; Mak et al. 2009).

Driven by genetic and environmental factors, psoriasis is a multifactorial disease that leads to immune system dysregulation. Triggers of paediatric psoriasis are particularly associated with emotional stress, the

* Corresponding author (sachini@zoology.cmb.ac.lk; https://orcid.org/0000-0001-7085-0682)

This article is published under the Creative Commons CC-BY-ND License (http://creativecommons.org/licenses/by-nd/4.0/). This license permits use, distribution and reproduction, commercial and non-commercial, provided that the original work is properly cited and is not changed in anyway.

Koebner phenomenon, increased body mass index (BMI), secondary smoking, streptococcal infections, and withdrawal of corticoid medications (Burden-Teh et al., 2016; Menter et al., 2020). Human leukocyte antigen (HLA)-Cw6, the primary genetic susceptibility allele associated with Type I psoriasis (onset before 40 years), plays a crucial role in paediatric psoriasis, which typically manifests at a younger age and shows a higher genetic contribution compared with adult-onset disease. Moreover, there is significant evidence of gender bias in HLA-Cw6 in psoriasis patients, primarily highlighting earlier disease onset and greater disease severity in women compared to men. It also acts as a biomarker indicating distinct clinical, often more aggressive, phenotypes in females (Guðjónsson et al., 2002). HLA-Cw6 is a surface antigen molecule found on MHC class I cells, and it functions as an antigen-presenting molecule, activating CD8+ T cells. It has been identified as the primary risk allele within psoriatic susceptibility regions (PSORS)-1 locus and is reported to be widely associated with the early onset of psoriasis and guttate psoriasis (Kim et al. 2022). It is also linked with frequent relapses, higher severity, and higher susceptibility to metabolic co-morbidities like cardiovascular diseases and dyslipidemia (Griffiths et al. 2021).

Previous studies have shown that oxidative stress (OS) plays a significant role, supported by symptoms like keratinocyte hyperproliferation and inflammation (Pleńkowska et al. 2020). Mild OS promotes cell survival, making alterations in gene expressions and in post-translational modifications in proteins. Since psoriasis is characterized by keratinocyte activation, hyperproliferation, and survival, mild OS is assumed to play a role in psoriasis pathogenesis (Lin & Huang, 2016).

Despite its low prevalence in Sri Lanka (0.32% overall; 0.4% in adults; 0.05% in children), psoriasis significantly impacts mental health and social life (Burden-Teh et al. 2016; Global Psoriasis Atlas 2023). However, molecular data focused on the prevalence of HLA-Cw6 in paediatric psoriasis or its associations with clinical data or OS is scarce, limiting insights into disease mechanisms and personalized care. Thus, this study, for the first time in Sri Lanka, examined the prevalence of the HLA-Cw6 genotype in paediatric patients and its association with OS markers, aiming to support precision medicine and early intervention strategies.

MATERIALS AND METHODS

Ethical approval

Ethical approval was granted from the Institute of Biology, Sri Lanka (ERC IOBSL 307 07 2023) for the involvement of humans in this study. Data and sample collection were carried out under the permission and supervision of the Consultant Dermatologist of the Dermatology Clinic, Lady Ridgeway Hospital for Children.

Study population

Psoriasis patients under the age of 20 (n = 59), attending the dermatology clinic of the Lady Ridgeway Hospital for children from September 2023 to August 2024, were recruited, and written informed consent was taken from their parents for sample collection and participation in the study. Buccal cavity epithelial cells were collected for DNA extraction by gently rubbing a sterile buccal swab on both sides of the buccal mucosa and on the upper and lower gutter regions for 1 minute. The swab was then dipped in a tube containing lysis buffer. A volume of 2.5ml of blood was drawn by a trained professional into a clot-activating vacutainer tube. Clinical data were collected from patient records.

HLA-Cw6 genotyping

Genomic DNA was extracted from buccal cavity swabs using the modified phenol-chloroform method (Aidar & Line 2007). Detection of the HLA-Cw6 polymorphism was carried out using the polymerase chain reaction-Sequence Specific Primers (PCR-SSP) method followed by a restriction fragment length polymorphism (RFLP) as described previously (Rębała et al. 2010) (Table 1). Briefly, the first PCR step was carried out to detect the presence of the HLA-Cw6 allele under the cycling conditions: 2 minutes at 96 ℃, 30 cycles of amplification (25 s at 96 ℃, 1 minute at 60℃, 2 minutes at 72℃), and a final step of 5 minutes at 72℃. In the second step, homo/heterozygosity of HLA-Cw6 positive individuals was verified by amplifying the internal control at 95℃ for 2 minutes, 30 cycles of (95℃ for 1 minute, 62 ℃ for 1 minute, and 72℃ for 30 s), and a final cycle of 72 ℃ for 5 minutes. The amplicons were digested by the *Sma1* restriction enzyme. All reactions were carried out in 50 µL volumes, and 10 µL of each product was visualized on 2% agarose gels.

Table 1: The list of primers used in the study.

PCR step	Primer name	Primer sequence	Product size
Step 1 Detecting the presence of HLA-Cw6 allele	Allele specific	Forward 5'-TACTACAACCAGAGCGAGGA-3' Reverse 5'- GGTCGCAGCCATACATCCA-3'	297 bp
	Internal control	Forward 5'-TTGAGGATTCTCCACTCCCCTGAG-3' Reverse 5'- CTGTGCCTGGCGCTTGTACTT – 3'	618 bp
Step 2 Detecting the homo/ heterozygosity		Forward 5'-TTGAGGATTCTCCACTCCCCTGAG-3' Reverse 5'- CTGTGCCTGGCGCTTGTACTT – 3'	618 bp

Total antioxidant capacity

Ferric reducing antioxidant power assay (FRAP) for the determination of the total antioxidant capacity (TAC) in serum was performed as described previously (Cecchini & Fazio 2020). Briefly, 5 µL of serum was diluted in 20 µL of distilled water in a 96-well plate, and 150 µL of warmed (37°C) FRAP Working solution, made by mixing 300 mM sodium acetate buffer at pH 3.6, 10 mM tris (2-pyridyl)-s-triazine (TPTZ) in 40 mM HCl, and 20 mM iron(III) chloride hexahydrate, in a volume ratio of 10:1:1 were added and incubated for 9 minutes before taking readings at 595 nm (Cecchini & Fazio 2020). To plot the standard curve, a 2000 µM $FeSO_4$ stock solution was prepared by dissolving 0.0556 g of iron(II) sulphate heptahydrate in 10 mL of distilled water. This stock was subsequently diluted to obtain standard solutions of 0, 50, 100, 150, 200, 300, 400, 600, 1000, and 1500 µM. Aliquots of each standard were treated identically to the samples to construct the calibration curve, and sample concentrations were determined by interpolating their absorbance values from the linear regression equation of the standard curve. Each sample was analyzed in triplicate.

Lipid peroxidation assay

Measuring the amount of lipid peroxides in serum was carried out as previously described using the thiobarbituric acid reactive substances (TBARS) assay (Aguilar Diaz De Leon & Borges, 2020). Briefly, 200 µL of 8.1% SDS, 1.5 mL of sodium acetate buffer, 1.5 mL of TBA solution, and 600 µL of distilled water were added to a 100 µL of sample in a 15 mL tube and vortexed. The mixtures were incubated in a water bath (95°C) for one hour, followed by a 30-minute incubation on ice. Then, 5 ml of 15:1 (v/v) butanol : pyridine solution was added, vortexed, and centrifuged at 1700g for 10 minutes at 4°C. The solutions were allowed to settle for 10 minutes, 150 µL was loaded into a 96-well plate, and the readings were taken at 540 nm. Using the absorbance of the samples, the corresponding concentrations were obtained by interpolation from the standard curve. For the standard curve, a 550 µM MDA bis stock solution was diluted to obtain a 200 µM working solution. From this, standard solutions of 0, 2.5, 5, 10, 20, 40, 80, and 160 µM were prepared. Aliquots (100 µL) of each standard were then processed identically to the serum samples. Each sample was analyzed in triplicate.

Statistical analysis

Statistical analysis was carried out using Statistical Package for the Social Sciences version 26 for Microsoft Windows. Data were statistically described in terms of mean ± standard deviation (SD), median ± inter quartile range (IQR), and percentages where appropriate. All data were considered non-parametric, and the Kruskal-Wallis test was used to compare the means of more than two groups. Correlation analysis was carried out using the Spearman rank correlation test.

RESULTS AND DISCUSSION

Clinical data analysis

The study population consisted of 45 females (76.3%) and 14 males (23.7%) with a mean age of 11.03 (± 4.23) years (Figure 1A). The median age of onset was 7.5 (IQR: 6.0), and there was no sex bias in the age of onset. Out of 59 patients, 21 (35.6%) patients were underweight (BMI < 18.5), 5 (8.5%) patients were overweight (BMI 25 - 30), and 3 (5.1%) patients were obese (BMI>30) (Figure 1C). Plaque psoriasis (*psoriasis vulgaris*) was the most prevalent form among the study population (n = 46, 78.0%) (Figure 1B). Coexistence of different

clinical types of psoriasis in the same patient was not observed in this study population, although they differed based on the locations of lesions. With regard to the specific locations of lesions, scalp psoriasis was commonly seen (n = 26, 44.06%), while nail lesions (n = 3, 5.08%) were less common.

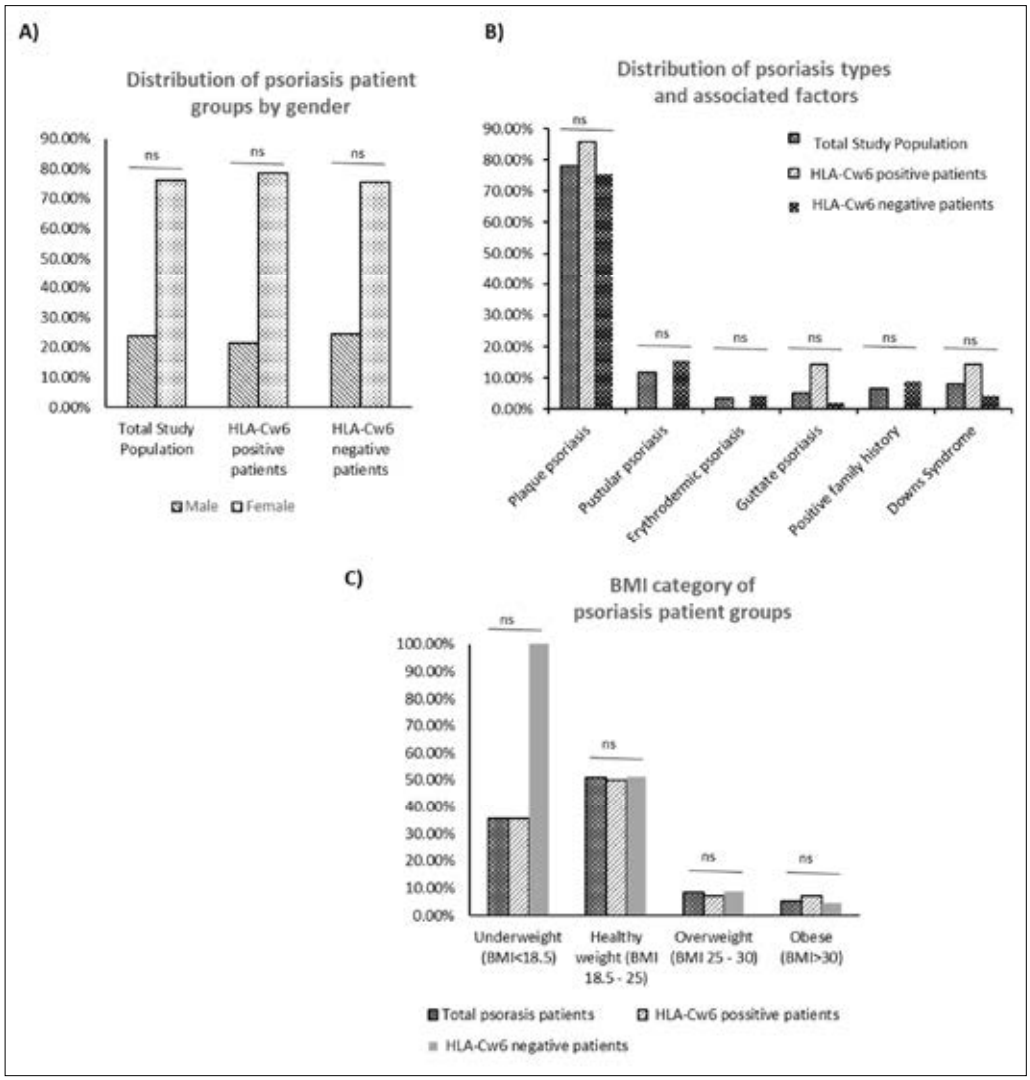

Figure 1: A) Percentage distribution of male and female psoriasis patients in total, HLA-Cw6 positive, and HLA-Cw6 negative groups. B) Percentage distribution of psoriasis types and associated factors C) BMI distribution among total psoriasis, HLA-Cw6 positive, and HLA-Cw6 negative groups. (χ^2 test, $p > 0.05$)

The patient's current disease severity status was obtained by assessing the active lesions on the skin during the time of sample collection. Patients were divided into three groups, namely mild, moderate, and severe disease, based on the body surface area (BSA) affected. The condition was recorded as mild when less than 3% of the BSA was affected, moderate when 3-10% of the BSA was affected, and severe when more than 10% of the BSA was affected (Menter et al*.,* 2020). The patient condition at the start of treatments was also obtained from their clinical records. According to the gathered data, 39 (66.1%) patients had a mild disease condition,

16 (27.1%) had a moderate and, 4 (6.8%) had a severe disease condition during the study period. A significant association was established between disease severity and the BMI (Fisher's exact test, $p = 0.0028$). Interestingly, only 4 (6.77%) patients had a family history of psoriasis in a first or second-degree relative. To our interest, out of 50 patients, 4 (8.0%) patients had Down's syndrome, and 3 of them (75%) had severe psoriasis disease (Fisher's exact test, p = 0.0019). However, this observation should be further confirmed by a large sample size.

HLA-Cw6 polymorphism

The presence of the HLA-Cw6 allele was identified by having 2 bands sized 618 bp and 297 bp in a 2% agarose gel (Figure 2A). Homozygosity was identified by the presence of 348 bp and 197 bp bands, while heterozygosity was identified by the presence of 348 bp, 270 bp, and 197 bp bands (Figure 2B). Despite HLA-Cw6 being the most common allele associated with psoriasis in many countries, in this study, only 14 (23.7%) out of 59 patients, showed positivity for the HLA-Cw6 allele. Among them, 4 (6.8%) patients were found to be homozygous for the allele, and 10 (16.9%) were found to be heterozygous. The remaining 45 patients (76.3%) were negative for the HLA-Cw6 allele.

Fisher's exact test indicated a statistically significant association between genotype and psoriasis severity ($p = 0.035$). Patients who were homozygous for the risk allele were more likely to present with moderate or severe psoriasis, whereas patients negative for the allele were more likely to present with mild psoriasis. No significant association was found between HLA-Cw6 positivity and a specific type of psoriasis, the BMI of patients or the age of onset (Figure 1).

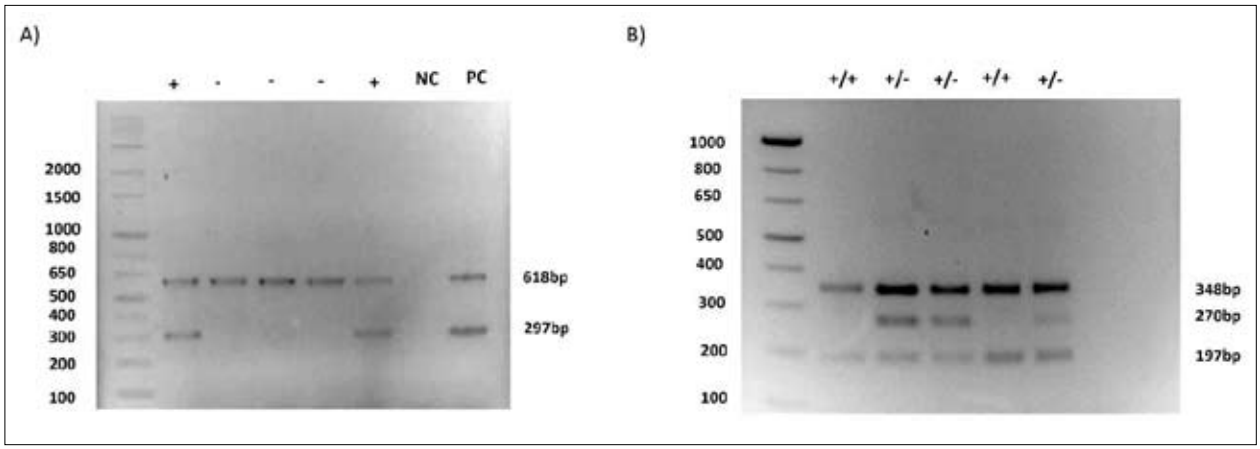

Figure 2: HLA-Cw06 polymorphism in psoriasis patients. A) Visualization of HLA-Cw6 allele genotyping. Lane 1-Enzynomics 1kb + Ladder Marker (Cat#DM003), (+): HLA-Cw6 positive, (-): HLA-Cw6 negative, NC: Negative control, PC: Positive control B) Zygosity status verification of HLA-Cw6. Lane 1-Enzynomics 1 kb (+) Ladder marker, (+/-): HLA-Cw6 heterozygous patient, (+/+): HLA-Cw6 homozygous patient.

Table 2: Oxidative stress parameters in patients with psoriasis according to HLA-Cw6 types. Values are presented as medians

Oxidative stress parameters	Negative (n = 34)	Heterozygous (n = 3)	Homozygous (n = 8)	P value
Total Antioxidant Potential (TAOP)	0.158	0.175	0.190	0.191
Lipid peroxidation levels	4.385	6.692	2.080	0.410

Oxidative stress (OS)

OS levels of patients were determined using FRAP and TBARS assays. According to results, there was no significant difference in OS levels between the three genotype groups: HLA-Cw6 negative, HLA-Cw6 homozygotes, and heterozygotes (Kruskal-Wallis test; $p > 0.05$) (Table 2). OS showed no statistically significant differences at the 95% confidence level across gender (Mann–Whitney U test; $p>0.05$), disease severity, or BMI (Kruskal–Wallis test; $p > 0.05$).

Despite its relatively low prevalence compared to other chronic diseases, psoriasis can have significant physical and psychosocial implications for affected individuals. The visible patches often appearing on exposed areas like the scalp, elbows, hands, and legs can lead to social stigma, embarrassment, and reduced self-esteem. Paediatric patients in particular carry a greater psychosocial burden as they have a heightened sensitivity to appearance-related stigma and peer judgment. Therefore, effective disease management is essential not only to relieve the physical, psychological, and social burden on patients but also to reduce the emotional strain on parents. Immunogenetic approaches allow researchers to identify genetic variants such as HLA-Cw6, improving the understanding of underlying mechanisms and better patient management strategies. Thus, this study for the first time investigated the prevalence of HLA-Cw6 polymorphism in paediatric psoriasis in Sri Lanka and is the first ever study conducted to analyze the correlations between HLA-Cw6 and OS in paediatric psoriatic patients globally.

Psoriasis affects both sexes equally, but early onset is more common in females (Huang & Tsai 2021), leading to a female predominance among paediatric cases. Similarly, this study reported a higher number of female paediatric patients than males. Obesity has been linked to a higher risk of psoriasis, more severe symptoms, and decreased effectiveness of treatment (Barros et al. 2022; Griffiths et al. 2021). Similarly, in this study, a significant association was established between higher BMI and increased disease severity. Obesity causes the deposition of extra adipose tissue layers, which produce adipokines, leading to enhanced inflammation and immune dysregulation. It is also accompanied by dyslipidaemia, characterized by high triglycerides and low-density lipoprotein (LDL) cholesterol levels and low high-density lipoprotein (HDL) cholesterol levels. Dyslipidaemia may exacerbate inflammation and contribute to endothelial dysfunction, which is implicated in the pathogenesis of psoriasis (Barros et al. 2022). Therefore, weight gain and obesity are considered triggers and a risk factor, and could also be a possible consequence of psoriasis (Barros et al. 2022).

Similar to earlier studies, plaque psoriasis was the most prevalent form observed (78%) (Indhumathi et al., 2016; Lubwama et al., 2025; Udayanga et al., 2024). Pustular psoriasis, though rare in children, affected 11.9%, while the relatively more common guttate type was seen in only 5.1% of patients. 36.7% of scalp psoriasis and 3.3% of nail involvement was reported in a similar study done by our group previously (Udayanga et al. 2024). This aligns with our observations of 44.06% of scalp and 5.08% of nail involvement.

The role of family history in psoriasis varies around the world, with values as high as 36% in the USA (Farber & Nall 1974), and as low as 5.8% in Japan (Mabuchi et al. 2014). In Sri Lanka, this value is about 6-7% as reported by this study (6.77%), and our previous report (Udayanga et al. 2024) (6.67%) suggesting that the Sri Lankan population may have a relatively lower tendency of familial inheritance or a probable unawareness of it.

As an antigen-presenting molecule, HLA-Cw6 molecules on keratinocytes and dendritic cells present antigens to CD8+ antigen-specific cytotoxic T cells and activate them to release inflammatory mediators, which results in increased OS (Alesci et al., 2022; Elmarakby & Sullivan, 2012). The close association between psoriasis and smoking and overweight people who carry HLA-Cw6 than non-carriers also indicates possible associations between HLA-Cw6 and OS.

The frequency of the HLA-Cw6 allele among psoriasis patients varies from 10.5% to 77.2% around the world (Chen & Tsai, 2018). Our study reported 23.7% HLA-Cw6 positive patients (6.8% homozygotes, 16.9% heterozygotes), and 76.3% negative patients. The carriers of the allele tend to show more severe disease, as presented in many studies. But it did not have significant associations with higher BMI, any particular type of psoriasis, or the age of onset. This contrasts with studies from Europe, where HLA-Cw6 positivity is not only more prevalent but also more strongly associated with guttate and early-onset disease. Even though HLA-Cw6 is also known to be strongly correlated with familial psoriasis, several studies have observed a lack of correlation between the two categories (Chen & Tsai, 2018).

In contrast to many studies, we could not find a significant association between OS and disease severity, age of onset, type of disease, BMI, or HLA-Cw6 positivity. This may be due to the small sample size and ongoing treatments such as creams, corticosteroids, vitamin D, and methotrexate. OS is often measured as a cumulative effect of higher levels of reactive oxygen species (ros) and reactive nitrogen species (RNS) and lowered levels of antioxidants. Hence, this study employed the TBARS assay as an indirect measure of ROS and the FRAP assay to assess antioxidant levels. To obtain a better understanding of OS, RNS also has to be measured, but due to the limited resources, this study was limited to the previous two assays. Moreover, in this study, the study population was limited to patients from nine districts in Sri Lanka, with the highest representation from Colombo. This geographic imbalance may limit the generalizability of the findings, and future studies should aim to include samples from other regions. Furthermore, a control group was not included to evaluate and compare the prevalence of HLA-Cw6 in healthy individuals, mainly due to ethical concerns related to obtaining samples from healthy infants.

The methodology of this study deviated from the original paper (Rębała et al. 2010) by using a 2% agarose gel to visualize PCR products instead of a 13% polyacrylamide gel. Polyacrylamide gels offer higher resolution compared to agarose gels, especially for separating small DNA fragments (less than 500 base pairs). The higher sensitivity of polyacrylamide detects low-abundance DNA fragments or DNA fragments present in small quantities. However, a 2% agarose gel gave an adequate resolution for the bands and was consistent across repeated trials.

Psoriasis can lead to secondary manifestations such as psoriatic arthritis (PsA), type 2 diabetes, hyperlipidaemia, dyslipidaemia, cardiovascular disease, and increased BMI (de Oliveira et al. 2015). Patients may also have an increased risk for chronic kidney disease, gastrointestinal diseases like Crohn's disease, and mild liver disease (Rendon & Schäkel 2019). Therefore, studying paediatric psoriasis patients and their genotypes would help them to adapt to an optimum lifestyle, predict their future, and receive the most effective personalized medicine when available.

CONCLUSION

This study, for the first time, revealed the prevalence of HLA-Cw6 polymorphism in Sri Lanka, and the HLA-Cw6 allele prevalence among paediatric psoriasis patients was lower than in most countries. No association between HLA-Cw6 and OS, type of psoriasis, BMI, or age of onset could be established, possibly due to the low sample size and the ongoing medication. HLA-Cw6 homozygotes and patients with higher BMI were more likely to have more severe disease. For a better understanding, a larger sample size and nitric oxide level determination can be accommodated.

Acknowledgements

Financial assistance given by the University of Colombo is acknowledged.

Availability of data and material

The data and material supporting the findings of this study are available from the corresponding author upon request.

REFERENCES

Aguilar Diaz De Leon, J., & Borges, C. R. (2020). Evaluation of Oxidative Stress in Biological Samples Using the Thiobarbituric Acid Reactive Substances Assay. *Journal of Visualized Experiments : JoVE*, (159), 10.3791/61122. https://doi.org/10.3791/61122

Aidar, M., & Line, S. R. P. (2007). A simple and cost-effective protocol for DNA isolation from buccal epithelial cells. *Brazilian Dental Journal*, *18*(2), 148–152. https://doi.org/10.1590/s0103-64402007000200012

Alesci, A., Lauriano, E. R., Fumia, A., Irrera, N., Mastrantonio, E., Vaccaro, M., Gangemi, S., Santini, A., Cicero, N., & Pergolizzi, S. (2022). Relationship between Immune Cells, Depression, Stress, and Psoriasis: Could the Use of Natural Products Be Helpful? *Molecules*, *27*(6), 1953. https://doi.org/10.3390/molecules27061953

Barros, G., Duran, P., Vera, I., & Bermúdez, V. (2022). Exploring the Links between Obesity and Psoriasis: A Comprehensive Review. International Journal of Molecular Sciences, 23(14), 7499. https://doi.org/10.3390/ijms23147499

Burden-Teh, E., Thomas, K. S., Ratib, S., Grindlay, D., Adaji, E., & Murphy, R. (2016). The epidemiology of childhood psoriasis: A scoping review. *British Journal of Dermatology*, *174*(6), 1242–1257. https://doi.org/10.1111/bjd.14507

Busse, K., & Liao, W. (2010). Which Psoriasis Patients Develop Psoriatic Arthritis? *Psoriasis Forum / National Psoriasis Foundation*, *16*(4), 17.

Cecchini, S., & Fazio, F. (2020). Assessment of Total Antioxidant Capacity in Serum of Heathy and Stressed Hens. *Animals*, *10*(11), 2019. https://doi.org/10.3390/ani10112019

Chen, L., & Tsai, T.-F. (2018). *HLA-Cw6* and psoriasis. *British Journal of Dermatology*, *178*(4), 854–862. https://doi.org/10.1111/bjd.16083

Elmarakby, A. A., & Sullivan, J. C. (2012). Relationship

between Oxidative Stress and Inflammatory Cytokines in Diabetic Nephropathy. *Cardiovascular Therapeutics*, *30*(1), 49–59. https://doi.org/10.1111/j.1755-5922.2010.00218.x

Farber, E. M., & Nall, M. L. (1974). The natural history of psoriasis in 5,600 patients. *Dermatologica*, 148(1), 1–18. https://doi.org/10.1159/000251595

Global Psoriasis Atlas. (2024). Global Psoriasis Atlas annual report 2023–2024. https://knowledge-action-portal.com/sites/default/files/gpa-annual-report-2023-2024.pdf

Griffiths, C. E. M., Armstrong, A. W., Gudjonsson, J. E., & Barker, J. N. W. N. (2021). Psoriasis. *The Lancet*, *397*(10281), 1301–1315. https://doi.org/10.1016/S0140-6736(20)32549-6

Guðjónsson, J. E., Valdimarsson, H., Kárason, A., Antonsdóttir, A. A., Hjaltey Rúnarsdóttir, E., Gulcher, J. R., & Stefánsson, K. (2002). HLA-Cw6-Positive and HLA-Cw6-Negative Patients with Psoriasis Vulgaris have Distinct Clinical Features. *Journal of Investigative Dermatology*, *118*(2), 362–365. https://doi.org/10.1046/j.0022-202x.2001.01656.x

Huang, YW., Tsai, TF. HLA-Cw1 and Psoriasis. *Am J Clin Dermatol* 22, 339–347 (2021). https://doi.org/10.1007/s40257-020-00585-1

Indhumathi, S., Rajappa, M., Chandrashekar, L., Ananthanarayanan, P. H., Thappa, D. M., & Negi, V. S. (2016). The HLA-C*06 allele as a possible genetic predisposing factor to psoriasis in South Indian Tamils. *Archives of Dermatological Research*, *308*(3), 193–199. https://doi.org/10.1007/s00403-016-1618-y

International Psoriasis Council. (n.d.). Pediatric psoriasis. https://psoriasiscouncil.org/ipc-resources/pediatric-psoriasis/ Retrieved April 11, 2026

Kim, S. M., Lee, H., & Lee, E.-S. (2022). Correlation of HLA-Cw6 Positivity with Clinical Characteristics and Treatment Efficacy in Korean Patients with Psoriasis. *Annals of Dermatology*, *34*(4), 253. https://doi.org/10.5021/ad.21.100

Lin, X., & Huang, T. (2016). Oxidative stress in psoriasis and potential therapeutic use of antioxidants. *Free Radical Research*, *50*(6), 585–595. https://doi.org/10.3109/10715762.2016.1162301

Lubwama, H., Mulyowa, G. K., Mirembe, S. K., Katungi, T. J., & Male, M. (2025). Psoriasis: Prevalence, Clinical Variants and Quality of Life, Among Patients Attending the Skin Clinic at Mbarara Regional Referral Hospital, Uganda. *Psoriasis: Targets and Therapy*, *15*, 117–126. https://doi.org/10.2147/PTT.S497092

Mabuchi, T., Ota, T., Manabe, Y., Ikoma, N., Ozawa, A., Terui, T., Ikeda, S., Inoko, H. and Oka, A. (2014), HLA-C*12:02 is a susceptibility factor in late-onset type of psoriasis in Japanese. *J Dermatol,* 41: 697-704. https://doi.org/10.1111/1346-8138.12569

Mak, R. K. H., Hundhausen, C., & Nestle, F. O. (2009). Progress in Understanding the Immunopathogenesis of Psoriasis. *Actas Dermo-Sifiliográficas*, *100*, 2–13. https://doi.org/10.1016/S0001-7310(09)73372-1

Menter, A., Cordoro, K. M., Davis, D. M. R., Kroshinsky, D., Paller, A. S., Armstrong, A. W., Connor, C., Elewski, B. E., Gelfand, J. M., Gordon, K. B., Gottlieb, A. B., Kaplan, D. H., Kavanaugh, A., Kiselica, M., Kivelevitch, D., Korman, N. J., Lebwohl, M., Leonardi, C. L., Lichten, J., … Elmets, C. A. (2020). Joint American Academy of Dermatology–National Psoriasis Foundation guidelines of care for the management and treatment of psoriasis in pediatric patients. *Journal of the American Academy of Dermatology*, *82*(1), 161–201. https://doi.org/10.1016/j.jaad.2019.08.049

Parisi, R., Symmons, D. P. M., Griffiths, C. E. M., & Ashcroft, D. M. (2013). Global Epidemiology of Psoriasis: A Systematic Review of Incidence and Prevalence. *Journal of Investigative Dermatology*, *133*(2), 377–385. https://doi.org/10.1038/jid.2012.339

Pleńkowska, J., Gabig-Cimińska, M., & Mozolewski, P. (2020). Oxidative Stress as an Important Contributor to the Pathogenesis of Psoriasis. *International journal of molecular sciences*, 21(17), 6206. https://doi.org/10.3390/ijms21176206

Rębała, K., Szczerkowska-Dobosz, A., Niespodziana, K., & Wysocka, J. (2010). Simple and rapid screening for HLA-Cw*06 in Polish patients with psoriasis. *Clinical and Experimental Dermatology*, *35*(4), 431–436. https://doi.org/10.1111/j.1365-2230.2009.03627.x

Rendon, A., & Schäkel, K. (2019). Psoriasis Pathogenesis and Treatment. *International journal of molecular sciences*, 20(6), 1475. https://doi.org/10.3390/ijms20061475

Udayanga, S. A. K., Seneviratne, J., Saumyamala, M. G. A., & Amarasekara, A. D. D. S. (2024). Association between Angiotensin-converting enzyme (ACE) insertion/deletion (I/D) polymorphism on the susceptibility to psoriasis and oxidative stress (OS) in a cohort of pediatric psoriatic patients in Sri Lanka: A cross sectional study. *Health Science Reports*, *7*(9), e2309. https://doi.org/10.1002/hsr2.2309

J.Natn.Sci.Foundation Sri Lanka 2026 54 (3): 325 - 337
DOI: http://dx.doi.org/10.4038/jnsfsr.v54i3.12704

RESEARCH ARTICLE

Agronomy

Adsorption characteristics and adsorption behavior of ammonium ions onto rice husk biochar pyrolyzed at different temperatures

N Jayarathna[1], S Dharmakeerthi[2*] and A Igalavithana[3]
[1] *Department of Soil Science, Faculty of Agricultural and Food Sciences, University of Manitoba, Canada.*
[2] *Department of Soil Science, Faculty of Agriculture, University of Peradeniya, Peradeniya, Sri Lanka.*
[3] *Adelaide Exposure Science and Health, School of Public Health, Adelaide University, Australia.*

Submitted: 14 June 2025; Revised: 29 May 2026; Accepted: 25 August 2026

Abstract: The low nitrogen use efficiency of applied fertilizers, often below 50% in most agroecosystems, is a significant concern. Biochar (BC) has large micropore structures, high surface area, and surface charges, which improve soil nutrient retention; these properties depend on pyrolysis conditions and the type of feedstock. This study investigated the adsorption of ammonium ion (NH_4^+) by rice husk BC (RHB) produced at three pyrolysis temperatures: 300 °C (RHB_300), 500 °C (RHB_500), and 600 °C (RHB_600) using a down draft double chamber (DDDC) pyrolyser (i.e., 500 °C) and a laboratory-scale muffle furnace (i.e., 300 °C and 600 °C). A batch sorption experiment was conducted to evaluate NH_4^+ sorption onto BC and Langmuir and Freundlich sorption isotherms were fitted to the data. Additionally, adsorption kinetics were studied by fitting three models – pseudo first order, pseudo second order and intra particle diffusion model – to the experimental data to understand the adsorption behaviour of NH_4^+. A significantly higher ash content of 45% was observed in RHB_500, which could be due to the DDDC pyrolysis method increasing BC surface heterogeneity. The low-temperature BC (RHB_300) showed the highest capacity for NH_4^+ sorption at pH 7 (4.53 mg/g) and rapid adsorption kinetics. Among the tested BCs, RHB_300 exhibited the highest NH_4^+ sorption capacity suggesting that low-temperature rice husk-derived BC may be particularly suitable for enhancing ammonium retention in soil systems.

Keywords: Adsorption isotherms, adsorption kinetics, ammonium adsorption, nitrogen use efficiency, rice husk biochar, pyrolysis temperature.

INTRODUCTION

Ammonium is a vital nutrient for the growth of plant and soil microorganisms and is primarily sourced from fertilizers, manure, and agricultural waste. However, excessive presence of NH_4^+ can result in environmental hazards such as eutrophication, greenhouse gas emissions, and nitrate pollution in water bodies, threatening ecosystems and human health after nitrification (Huang et al., 2017; Singh & Craswell, 2021; Townsend et al., 2003).

Although several techniques have been developed for ammonium removal, each approach presents notable limitations. Nano-remediation technologies can achieve high removal efficiencies;,however, their high cost, potential ecological toxicity, and challenges in large-scale application restrict their practical use (Hussain et al., 2022). Bioremediation approaches are environmentally friendly but are often slow, highly site-specific, and sensitive to environmental fluctuations such as pH and temperature (Morrissy et al., 2021). Chemical treatment methods can effectively reduce ammonium concentrations but may generate secondary pollutants and are generally unsustainable for long-term application (Cruz et al., 2019). Activated carbon-based adsorption is efficient but remains economically limited due to

* Corresponding author (dharmakeerthirs@agri.pdn.ac.lk; https://orcid.org/0000-0002-2538-4237)

This article is published under the Creative Commons CC-BY-ND License (http://creativecommons.org/licenses/by-nd/4.0/). This license permits use, distribution and reproduction, commercial and non-commercial, provided that the original work is properly cited and is not changed in anyway.

high production costs and reliance on non-renewable precursors (Neme et al., 2022). In contrast, biochar (BC) has emerged as a promising alternative due to its low cost, carbon sequestration potential, and ability to improve soil physicochemical properties (Laird et al., 2010; Lehmann, 2007). However, its ammonium adsorption capacity is highly variable and strongly dependent on feedstock type, pyrolysis temperature, and production system (Gai et al., 2014; Lehmann, 2007). Furthermore, reported adsorption capacities are often inconsistent across studies, and the underlying mechanisms governing ammonium retention under different BC production conditions remain insufficiently understood. This variability limits the predictive understanding of BC performance in nutrient management applications (Bolan et al., 2022; Joseph et al., 2021; Sumaraj & Padhye, 2017).

However, the NH_4^+ adsorption capacity of BC is generally low, typically less than 20 mg/g, due to adsorption mechanisms that rely on ion exchange and interactions with oxygen-containing functional groups on BC surfaces (Zhang et al., 2020). Studies have shown that BC derived from various feedstocks and pyrolysis conditions can significantly influence its NH_4^+ adsorption capacity. For instance, rice straw BC has been reported to achieve a 69.5% NH_4^+ removal efficiency with a maximum adsorption value of 4.5 mg/g in fish farm wastewater (Khalil et al., 2018). Factors such as pyrolysis temperature, feedstock type, and solution characteristics (e.g., pH, initial ion concentration) play key roles in determining BC adsorption efficiency (Begum et al., 2021; Gai et al., 2014). For a selected feedstock type, it is important to identify a suitable pyrolysis temperature that results in maximum adsorption capacity. Generally, adsorption capacity decreases at higher pyrolysis temperatures; for example, the NH_4^+ adsorption capacity of rice straw BC's dropped by 10% when produced at 700 °C compared to 300 °C (Xu et al., 2019). Similarly, BC from digested sludge showed the highest adsorption capacity at 450 °C among temperatures tested from 350 °C to 550 °C due to greater surface area and functional group density (Tang et al., 2019).

Rice husk, a widely available agricultural byproduct in Sri Lanka, has been used to produce BC; however, its NH_4^+ adsorption characteristics remain largely unstudied. This study aims to characterize locally produced rice husk biochar (RHB) to evaluate its potential as an affordable and effective NH_4^+ adsorbent. We hypothesized that, rice husk-derived BC can effectively adsorb NH_4^+ and the pyrolysis temperature influences the maximum adsorption capacity. To test this hypothesis, laboratory experiments were conducted to (1) characterize and investigate the NH_4^+ adsorption capacity, and (2) assess the adsorption kinetics of RHB produced at three pyrolysis temperatures (300 °C, 500 °C, and 600 °C) in an aqueous medium.

MATERIALS AND METHODS

Biochar production and characterization

Biochars were prepared from rice husk at three pyrolysis temperatures using a down draft double Chamber (DDDC) pyrolyzer (Alahakoon et al., 2018) and a laboratory- scale muffle furnace at 300 °C and 600 °C. The three types of BC were designated as RHB_DDDC, RHB_300, and RHB_600, respectively. The BC's were air-dried and crushed using a mortar and pestle, and passed through a 0.5 mm sieve. They were initially characterized for pH (1:20) using a pH electrode (Hanna Instruments, USA). Moisture content was calculated by mass loss of the BC after heating the BC at 105 °C for 24 hours to a constant weight (ASTM D1762-84). Volatile matter content was calculated by mass loss of the BC after heating at 450 °C for 2 hours (McLaughlin et al., 2009), and ash content was calculated from mass loss of the BC after heating at 750 °C for 2 hours (Ronsse et al., 2013). Elemental analysis was performed by a CHN analyzer for C, H and N (PerkinElmer® 2400 Series II, USA). BET surface area was analysed using a surface area analyzer (Quantachrome Autosorb-iQ, USA) and surface functional groups of the BC were determined by FT-IR analysis (Thermo Nicolet iS50, USA). The carbon structure of the RHB was characterized by Raman spectroscopy (Renishaw Invia Reflex Raman microscopy system, UK), with particular emphasis on assessing the degree of structural disorder and aromatic carbon ordering. Due to the heterogeneous nature of BC, overlapping signals from functional groups, amorphous carbon, and mineral residues may complicate the interpretation of both FT-IR and Raman spectra, limiting the sensitivity for detecting subtle NH_4^+ interactions (Ilić et al., 2022; Yuan et al., 2025). Consequently, these techniques were employed as complementary qualitative tools to assess relative variations in functional group composition and structural characteristics across BCs generated at different pyrolysis temperatures.

Batch experiment for ammonium adsorption

To evaluate NH_4^+ adsorption, adsorption experiments were conducted as described by Fidel et al. (2018) with slight modifications. Briefly, 0.05 g of BC was weighed into 50 mL Falcon tubes. Then, 10 mL of distilled water was added, and the mixture was shaken for 24 hours

at 100 rpm on an orbital shaker (Gemmy VRN-480, Taiwan) at room temperature (i.e., 30 ± 2 °C). The pH of the samples was adjusted to 7 using 2-3 drops of HCl (0.01 M) or $Ca(OH)_2$ (0.01 M). To this, 5 mL of NH_4NO_3 solution was added from a series of concentrations to achieve final NH_4^+ concentrations ranging from 0 to 10 µg L^{-1}. The lids of the Falcon tubes were closed and again shaken for 24 hours at 100 rpm. After adsorption, the residual NH_4^+ solution was filtered through Whatman No. 42 filter paper, and the NH_4^+ concentration in the solution was determined by a colorimetric method using a UV–Vis spectrophotometer at 660 nm (Markus et al., 1985). The BC residue was air-dried and stored for functional group analysis using FT-IR spectroscopy. All the adsorption tests were performed in triplicate.

The experimental data were fitted to Langmuir and Freundlich adsorption isotherm models as follows (Goldberg, 2005):

Langmuir equation:

$$Q_e = \frac{C_e\, Q_m}{(K_L + C_e}$$

where, Q_e (mg/g) and C_e (mg/L) are the amounts of adsorbed NH_4^+ and the NH_4^+ concentrations in the solution at equilibrium, respectively, Q_m (mg/g) is the maximum absorption capacity and K_L represents the Langmuir constant.

Separation factor (R_L) was calculated using the formula;

$$R_L = \frac{1}{(1 + C_o\, K_L)}$$

where, K_L is the Langmuir constant and C_0 is the initial concentration of solution (mg/L). R_L represents the effect of initial concentration of solution on the adsorption.

Freundlich equation:

$$Q_e = K_F\, Ce^{1/n}$$

where, K_F represents the Freundlich constant, C_e (mg/L) is the NH_4^+ concentrations in the solution at equilibrium and 1/n is the intensity of adsorption or affinity.

Adsorption kinetics study

Adsorption kinetics were employed to estimate the adsorption rate, which is critically important for characterizing the adsorption performance of adsorbents (Khalil et al., 2018). A 4 L plastic bottle with 8 g of BC (2 g/L) was filled with 3.5 L of distilled water and stirred for 24 hours at 950 rpm using a magnetic stirrer (Biologix MS-H280-Pro, China). The solution pH was adjusted to 7, and NH_4NO_3 was added to give a final concentration of 4 ppm in 4 L. Immediately after NH_4NO_3 addition, samples (1 mL/L) were collected at 1, 2, 3, 4, 5, 15, 30, 60, 120, 180, and 300-minute intervals. The samples were immediately filtered using 0.45 µm syringe filters and analyzed for NH_4^+ by the colorimetric method.

The adsorption kinetics were analyzed using pseudo-first order, pseudo-second order, and intra-particle diffusion models to elucidate the underlying adsorption mechanisms. The pseudo-first-order model assumes that adsorption occurs primarily through physical processes governed by diffusion and boundary layer effects, whereas the pseudo-second-order model describes chemisorption involving valence forces through the sharing or exchange of electrons between the adsorbent and adsorbate (Ho & McKay, 1999). The intra-particle diffusion model was applied to evaluate the contributions of pore diffusion and mass transfer resistance in controlling the adsorption rate (Allen et al., 1989).

Pseudo-first-order;

$$q_t = q_e(1 - e^{-k_1 t})$$

Pseudo-second –order;

$$q_t = \frac{K_2 q_e^2 t}{1 + (k_2 q_e t)}$$

Intra particle diffusion model;

$$q_t = K_{ip}\sqrt{t} + Ci$$

where, q_e and q_t (mg/g) are the amounts of NH_4^+-N adsorbed by the BC at equilibrium and at time t, respectively, C_i is the boundary layer thickness and k_1, k_2 and k_{ip} are the rate constants of the pseudo-first order, pseudo-second order and intra-particle diffusion scenarios.

Statistical analysis

One-time measurement data of the Raman spectra in the range of 1000-1750 cm^{-1} were curve-fitted using OriginPro 9 software, with 8 Gaussian bands. FT-IR data in the wave length range of 500-4000 cm^{-1} were also analyzed. Statistical analysis, kinetics and sorption isotherms were fitted using SigmaPlot 10.0 software and OriginPro 9.0 software, respectively.

RESULTS AND DISCUSSION

Assessment of proximate analysis, elemental composition and surface area analysis of biochar

The pH of the BCs were increased with increasing pyrolysis temperature (Table 1) ranging from 7.03 to 9.24. The fixed carbon (FC) content was significantly higher ($p < 0.05$) in RHB_500 and RHB_600 compared to RHB_300 by 32% and 44%, respectively. The volatile matter percentage (VM) decreased with increasing temperature by 16% and 22% in RHB_500 and RHB_600, respectively, relative to RHB_300. Ash content was significantly different ($p < 0.05$) among treatments (Table 1). The significantly higher ash content (45%) in RHB_500 can be attributed to the industrial-type DDDC continuous pyrolysis method, which may have increased ash production. The two-stage, slow downdraft path of the DDDC reactor exposes the feedstock to hot, mildly oxidising gases, long enough to drive off extra carbon while preventing fine-ash carry-over or alkali volatilisation. This concentrates the inorganic fraction, giving RHB_500 a high ash content (Alahakoon et al. 2018). Biochar prepared at high temperatures had higher pH values, which could be due to the degradation of acidic functional groups with removal of volatile matter such as carboxylic acids and phenols in biomass (Rafiq et al., 2016), and accumulation of alkaline elements such as sodium (Na), potassium (K), magnesium (Mg), and calcium (Ca), and some carbonates (such as $CaCO_3$ and $MgCO_3$) (Tu et al., 2022).

Table 1: pH and proximate analysis parameters of the rice husk biochar pyrolyzed at 300 °C, 500 °C and 600 °C ±SD (n=3).

	pH	Fixed carbon%	Ash%	Volatile matter%	Moisture%
RHB_300	7.03	9.53 ± 1.35 b	29.85 ± 0.18 c	45.24 ± 0.67 a	4.69 ± 0.06 a
RHB_500	8.16	41.01 ± 9.78 a	45.31 ± 0.62 a	29.49 ± 4.89 b	5.36 ± 0.24 a
RHB_600	9.24	53.43 ± 2.79 a	42.78 ± 0.16 b	23.29 ± 1.39 b	4.63 ± 0.07 a

Higher pyrolysis temperatures tend to increase the fixed-carbon (FC) content in low-ash BCs. Biochars containing ash contents with greater than approximately 20% are commonly classified as high-ash biochars (Enders et al., 2012). Once the ash fraction is higher than 20%, further temperature increases remove proportionally more carbon than mineral matter, causing the FC content to decline (Enders et al., 2012). Ash content represents the species and abundance of inorganic content and it is determined by pyrolysis temperature as well as feedstock properties (Li et al., 2017). The volatile matter or mobile matter, which represents the labile fraction of BC, can be utilized by soil microorganisms and plants (McLauglin, 2010). It decreases with increasing pyrolysis temperatures as the thermal degradation of uncharred hemicellulose residues followed by uncharred cellulose and lignin or other volatile pyro-compounds (Rafiq et al., 2016). The volatile matter percentage can be used to understand the stability of the material to some extent (Zimmerman, 2010). However, Crombie et al. (2013) has observed that the yield of stable C, fixed C and total C are independent of pyrolysis temperature from low ash feedstock (pine and wheat straw), but for high ash biomass (rice husk) they showed two levels for stable C yield between 350–450 °C and 550–650 °C. When the fixed C percentage is high in BC, it is more stable in soil (Zimmerman, 2010). Therefore, it persists for a long time in soil as an NH_4^+ adsorbent.

Table 2: Elemental composition and surface area of the rice husk biochar pyrolyzed at 300 °C, 500 °C and 600 °C

	C%	H%	N%	H/C	C/N	Specific surface area (m^2g^{-1})
RHB_300	56.34	4.29	0.49	0.08	114.98	5.3484
RHB_500	33.51	2.13	0.49	0.07	68.39	50.6783
RHB_600	38.42	1.43	0.05	0.04	768.40	81.7087

The increase in pyrolysis temperature increases the loss of biomass content, mainly C, H, N (Table 2). The atomic H/C ratio reflects the aromaticity of BC; a lower value indicates stronger aromaticity and a more stable BC structure (Pusceddu et al, 2019). RHB_600 showed the lowest H/C ratio (0.04) and had the highest aromaticity. Conversely a higher H/C indicates more organic carbon in BC, which provides more adsorption sites for inorganic ions (Wijitkosum & Jiwnok, 2019; Jiang et al., 2019). The highest H/C ratio was observed in RHB_300 (0.08), suggesting more potential adsorption sites. However, the specific surface area increased dramatically with increasing pyrolysis temperature, probably due to the removal of carbon mass and volatile substances in the material (Elnour et al., 2019).

Changes in surface functional groups by FTIR spectroscopy

In this study, FTIR analysis was performed to identify the major surface functional groups involved in NH_4^+ adsorption of RHB. The spectra of the initial BC and the residual BC after NH_4^+ adsorption (Figure 1) showed that RHB pyrolysed at all three temperatures had few similar characteristic peaks within the observed 4000 – 500 cm^{-1} region (Figure 2). The spectra showed bands characteristic of the functional groups present in the components of lignocellulosic fibers, including cellulose, hemicelluloses, and lignin. Rice husk raw material contains a high percentage of silica shown by the intense band at 1053 cm^{-1} corresponding to the stretching vibrations of silicon-oxygen tetrahedra (SiO_4). According to Morcali et al. (2013), the region 1000-1200 cm^{-1} are considered to result from superposition of vibrations from the C-OH bond and Si-O bond in the siloxane (Si-O-Si) groups.

There is a broad band between 3417 and 3431 cm^{-1}, despite the pyrolysis temperature, with a peak at 3420 cm^{-1} that may be related to the O-H stretching in the BC structure or other minerals derived from hydroxyl groups (Armynah et al., 2018). The decrease in the hydroxyl peak intensity with the increase in pyrolysis temperature from 300 °C to 600 °C indicates that the loss of hydrogen and oxygen atoms due to higher temperatures (Keiluweit et al., 2010). The small band at 2920-2922 cm^{-1} represents the aliphatic C-H bonds, which can be present due to the incomplete carbonization of cellulose during pyrolysis (Chia et al., 2012). Another peak observed at approximately 1437 cm^{-1} may represent the occurrence of aromatic compounds with C-C stretching (ester and phenol) in hemicellulose (Armynah et al. 2018), and COO- asymmetric stretching (Jindo et al. 2014).

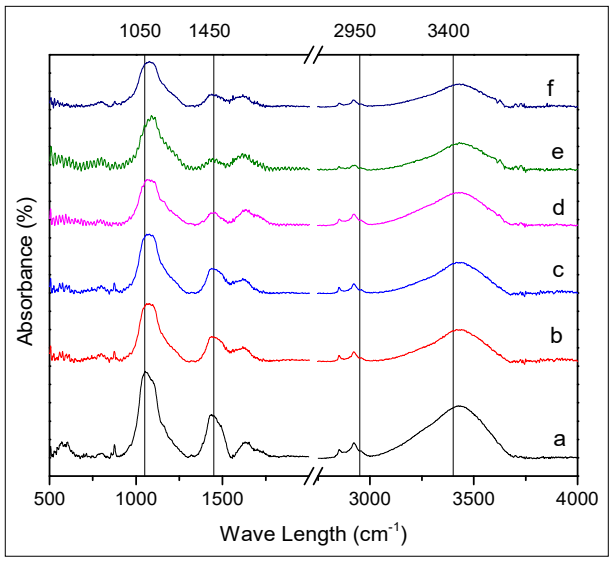

Figure 1: FTIR spectra of rice husk biochar. Before NH_4^+ adsorption: a. RHB_300, b. RHB_DDDC, c. RHB_600, and after NH_4^+ adsorption: d. RHB_300, e. RHB_DDDC, f. RHB_600)

The presence of alcoholic, phenolic, and carboxylic groups enable adsorption of cations on BC surfaces (Bustin & Guo, 1999). According to Zhang et al. (2020), NH_4^+-N adsorption onto BC is mainly driven by ion exchange and interactions with oxygen- containing functional groups on BC surfaces. Therefore, the presence of many oxygen- containing functional groups ensures a higher NH_4^+ adsorption capacity. The absence of amine and organic sulfate groups suggests weak binding and interaction of the NH_4^+ with the BC surface groups (Lee et al., 2021).

Changes in the carbon structure of biochar: Raman Spectroscopy

The averaged Raman spectrum of the three BC types from 1000 to 1750 cm^{-1} is shown in Figure 2. Raman spectroscopy of BC is effective for analysing the D and G bands, typically found at 1350 cm^{-1} and 1580 cm^{-1}, respectively, and are evidence of polyaromatic hydrocarbons and graphitic material. Several bands were identified through curve fitting of the Raman spectra of the three BC's between 1000-1750 cm^{-1}. Two main peaks were observed at the D band (1360 cm^{-1}) and the G band (1600 cm^{-1}). These two fundamental peaks are usually observed in Raman spectra, where the G band is attributed to graphitic carbon, and the D band corresponds to defects within the graphitic structure (Le et al., 2021). This peak in RHB typically arises from the

carbonaceous components formed during the pyrolysis or carbonization of the rice husks and does not correspond to specific compounds but rather reflects the overall structural characteristics related the aromaticity of BC (Ayiania et al., 2020).

The decrease in intensity between the D and G bands is represented by V (the valley region). The bands in this region, V_L (1440 cm^{-1}) and V_r (1460 cm^{-1}) represent amorphous carbon and small fragments that link the aromatic ring systems while the V_L represents the bending vibrations of aliphatic C-H bonds (CH_2 and CH_3 groups) and V_r represents methylene or methyl groups and the semi-circle breathing modes of aromatic rings (Feng et al., 2016). The intensity of V_r (1460 cm^{-1}) decreases with increasing temperature and disappears in RHB_600. The absence of the V_r band in RHB_600 may be due to the removal of amorphous carbon structures or volatile matter at high pyrolysis temperatures (Igalavithana et al., 2020). The G_L band (1560 cm^{-1}) was present between D and G is commonly associated with the skeletal vibrations of aromatic compounds, which is the carbon-carbon (C-C) stretching in aromatic rings. Phenolic compounds containing hydroxyl groups attached to aromatic ring with a hydroxyl group attached and polycyclic aromatic hydrocarbons (PAHs), which can form during the pyrolysis or incomplete combustion of organic materials, can exhibit Raman peaks around 1560 cm^{-1} (Ayiania et al., 2020).

D_L and S bands were observed at 1250 cm^{-1} and 1125-1180 cm^{-1}, respectively. The D_L band can be attributed to the para-aromatics such as aryl-alkyl ethers, while the S band represents substituent groups, and cross-linked groups, including aromatic and alkyl carbons, aromatic (aliphatic) ethers, C-C on hydroaromatic rings, hexagonal diamond carbon (sp^3) and C-H bonds on aromatic rings (Feng et al., 2016). In RHB, stretching vibrations of glucose units (C-O-C glycosidic bonds) in cellulose and aromatic structures, and C-O stretching vibrations in various functional groups, such as esters, ethers, or carboxylic acid derivatives can give rise to these Raman shifts (Makarem et al., 2019).

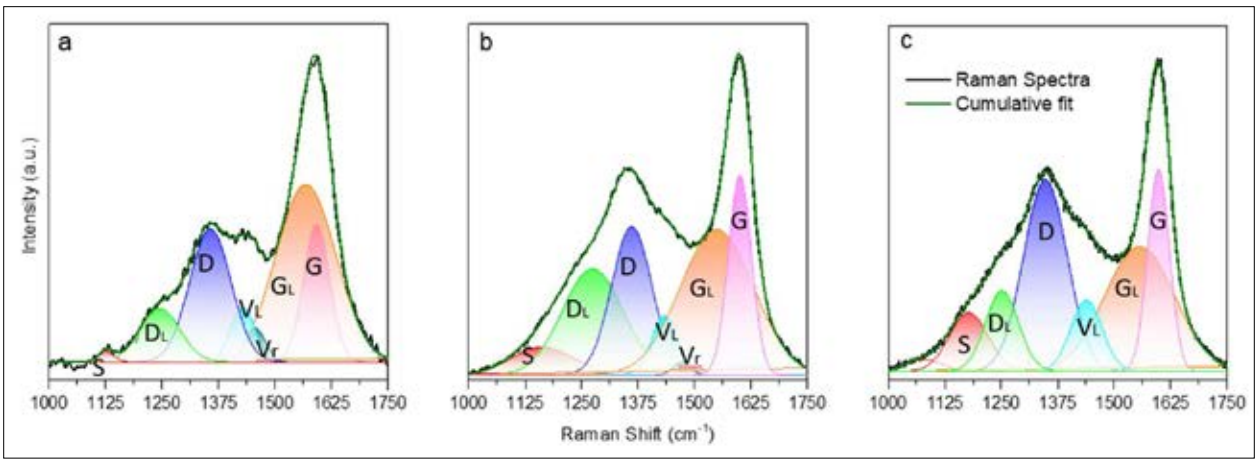

Figure 2: Curve fitting of Raman spectra. a) RHB_300, b) RHB_DDDC, and c) RHB_600

The ratios of integrated intensity (peak area A) of major Raman bands explain the alteration in BC structures at different temperatures. The ratio of AD/AG denote the defective structures to ordered structures in BC. The ratios for RHB_300, RHB_500, and RHB_600 are 1.51, 1.27, and 1.90, respectively. Biochar with lower ratios indicates a presence of higher amount of ordered carbon structures (Cançado et al., 2017). These values result from the higher area of the G band in RHB_500 compared to RHB_300 and the increased area of the D band in RHB_600 than in the other two samples. However, the AD/AG ratio of RHB_300 is lower than that of the RHB_600, implying that RHB_300 contained more amount of ordered carbon structures. It is apparent that the high pyrolysis temperature of RHB_600 increased the aromatic carbon structures compared to the other two samples. Higher pyrolysis temperatures can induce carbon dislocations, generating defects more easily (Xiao et al., 2017). Hence, the amount of highly ordered defective large aromatic ring structures is high in

RHB_600 compared to the other two (Igalavithana et al., 2020). Finally, after pyrolysis, BC has an amorphous form with several layers of graphene contributing to create the porous structure of the material (Le et al., 2021).

Evaluation of adsorption isotherms

Langmuir isotherm model was best described with the NH_4^+ adsorption data fitted with RHB_300 and RHB_600 (R^2=0.99), while RHB_500 was better described by the Freundlich isotherm model (R^2=0.97) (Figure 3). A good fit with the Langmuir isotherm implies that NH_4^+ adsorption occurs primarily through monolayer adsorption and a homogenous surface. In contrast, the Freundlich isotherm reflects a heterogenous surface and multi-layer adsorption can occur (Goldberg, 2005). The significantly higher ash content (45%) in RHB_500 likely contributes to this deviation as the DDDC method of pyrolysis can encourage ash production. Konstantinou and Albanis (2000) have observed that the sorption was increased with increasing ash content in soil-fly ash mixtures due to increasing surface heterogeneity of the adsorbate. The presence of ash introduces surface heterogeneity through non-uniform distribution and chemical heterogeneity (Amonette & Joseph, 2012).

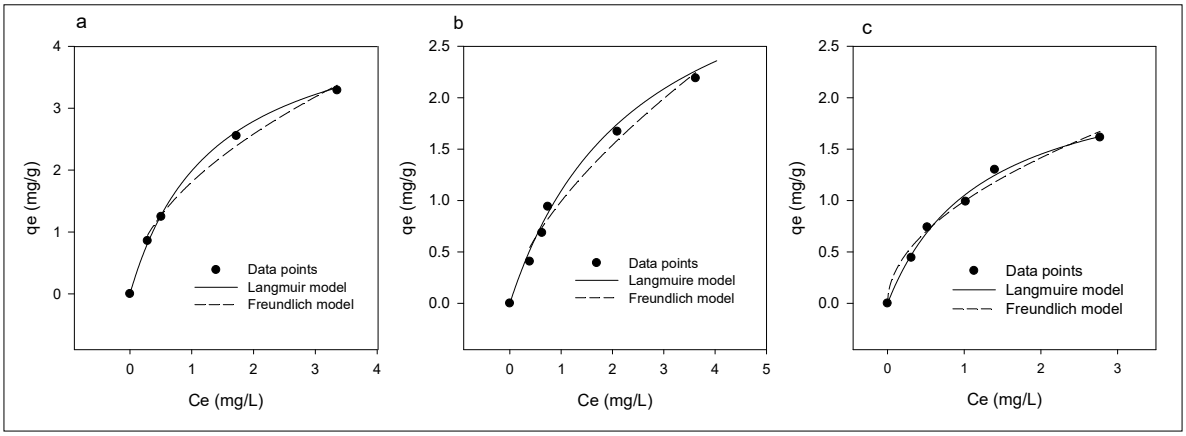

Figure 3: Adsorption isotherms of ammonium on biochars (a) RHB_300, (b) RHB_500, (c) RHB_600

The maximum NH_4^+ adsorption capacity (Q_{max}) decreased with increasing pyrolysis temperature (Table 3). Structural analysis (FT-IR), revealed that the functional groups of RHB were abundant at lower temperatures (RHB_300). With the increase in temperature, these functional groups gradually weakened and partly disappeared due to the volatalization associated with thermal degradation of cellulose and lignin structures in the feedstock (Zhang et al., 2015). This higher abundance of functional groups at low temperatures increases the density of surface charges, thereby facilitating better adsorption of NH_4^+ (Gai et al., 2014). The fixed carbon percentage (FC%) is increased with increasing pyrolysis temperature (Table 2). When the FC percentage is high in BC, it is more stable in soil (Zimmerman, 2010) allowing it to persist over a long period as an effective NH_4^+ adsorbent.

Table 3: Isothermal parameters for the Langmuir and Freundlich models of NH_4^+ adsorption on three types of rice husk biochar

	Langmuir model				Freundlich model		
	R^2	Q_{max}	K_L	R_L	K_F	1/n	R^2
RHB_300	0.9979	4.5269	1.2829	0.0723	1.8068	1.9394	0.9894
RHB_DDDC	0.8348	3.3145	1.7656	0.0661	0.9913	1.5741	0.9787
RHB_600	0.9936	2.3618	1.2614	0.1167	0.9934	1.9573	0.9826

R^2 is the regression coefficient, Q_{max} (mg/g) is the maximum absorption capacity, K_L represents the Langmuir constant, R_L represents the effect of initial concentration of solution on the adsorption, 1/n is the intensity of adsorption or affinity, K_F is the Freundlich constant.

The separation factor (R_L), a dimensionless constant,, represents the effectiveness of adsorption. R_L=1 indicates linear adsorption, and R_L=0 refers to irreversible adsorption and $0 < R_L < 1$ is the standard condition where there is a favorable adsorption. When $R_L > 1$ desorption occurs instead of adsorption, indicating an unfavorable adsorption or desorption (Dada et al, 2012; Jiang et al., 2019). Therefore, according to the Langmuir model, RHB has a favorable adsorption (Table 3). Based on the Freundlich constant 1/n , the use of RHB for the adsorption of NH_4^+ was unfavorable (1/n>1). The parameter 1/n represents surface heterogeneity; smaller values of 1/n, indicate greater heterogeneity (Kinniburgh, 1986).

Evaluations of adsorption kinetics

The adsorption kinetics of NH_4^+ on BC were investigated to determine the time required to reach adsorption equilibrium and to further examine the mechanisms of NH_4^+ adsorption. The relationship between the rate of adsorption and the contact time shows the kinetics of adsorption (Figure 4). The data were fitted using three kinetic models. Ammonium showed relatively rapid adsorption kinetics for RHB in an aqueous medium (Figure 4). The adsorption increased dramatically within the first 30 mins and then reached equilibrium after approximately 60 mins for RHB_500 and RHB_600, while RHB_300 showed an increasing trend in adsorption.

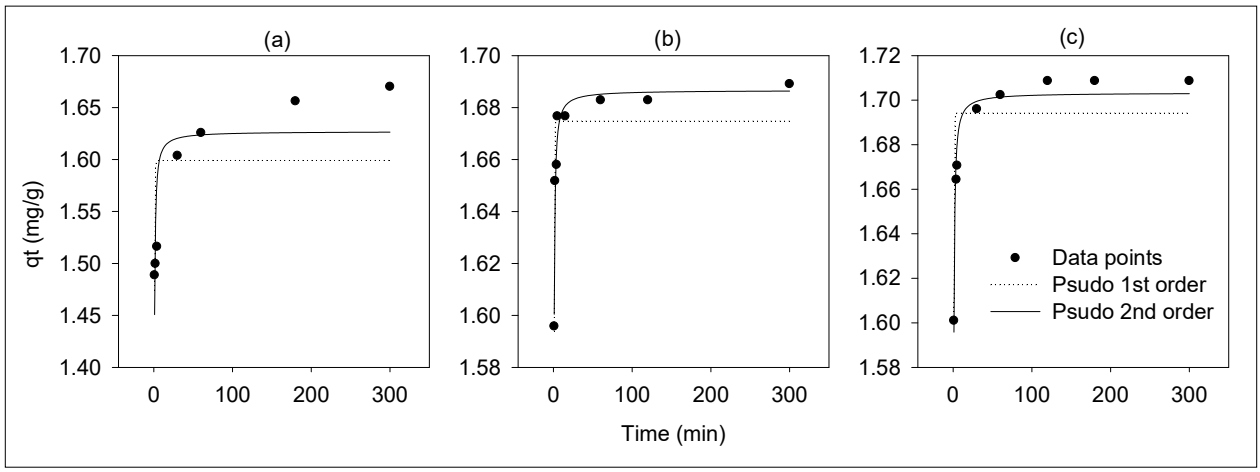

Figure 4: Adsorption kinetics of ammonium on biochar (a) RHB_300, (b) RHB_500, (c) RHB_600

The initial rapid adsorption rates may be due to the availability of a higher number of unoccupied adsorption sites and a steep solute concentration gradient at the beginning (Yang et al., 2018). Moreover, negatively charged surface functional groups, such as carboxylate and hydroxyl groups, may also contribute to the rapid adsorption process (Yu et al., 2016). The best-fitting model was determined based on the regression coefficient (R^2). The pseudo-second-order model is suitable for describing the adsorption kinetics of RHB_500 and RHB_600, as indicated by their higher R^2 values (Table 4), while RHB_300 is best described by the intra-particle diffusion model, with a higher regression coefficient (R^2 -0.9566) (Table 5). Furthermore, the experimental q_e values ($q_{e\ Exp}$) agree with the q_e values predicted by the pseudo-second-order model.

Pseudo-second-order kinetics assumes that the rate-limiting step is chemical sorption and that the adsorption rate is proportional to the adsorption capacity (Ho & McKay, 1999). Therefore, RHB_500 and RHB_600 predominantly undergo chemisorption.

The intraparticle diffusion model can be adopted to identify the diffusion rate of the NH_4^+ adsorption process (Nguyen et al., 2022). To identify the effects of intraparticle diffusion and boundary diffusion during the adsorption process, the fitting results of the intraparticle diffusion model are shown in Figure 5.

Table 4: Kinetics parameters for the pseudo first order and pseudo second order models of NH_4^+ adsorption on three types of rice husk biochar

	$q_{e\,Exp}$ (mg/g)	Pseudo first order model			Pseudo second order model		
		R^2	q_e (mg/g)	K_1	R^2	q_e (mg/g)	K_2
RHB_300	1.6257	0.3186	1.5992	2.5509	0.7270	1.6270	5.0598
RHB_500	1.6829	0.8472	1.6748	3.0310	0.9552	1.6867	11.0088
RHB_600	1.7023	0.7801	1.6942	2.9000	0.9626	1.7033	8.7187

$q_{e\,Exp}$ is the experimental value of NH_4^+-N adsorbed, q_e amount of NH_4^+-N adsorbed at equilibrium, R^2 is the regression coefficient, k_1 pseudo-first-order rate constants and k_2 pseudo-second –order rate constants.

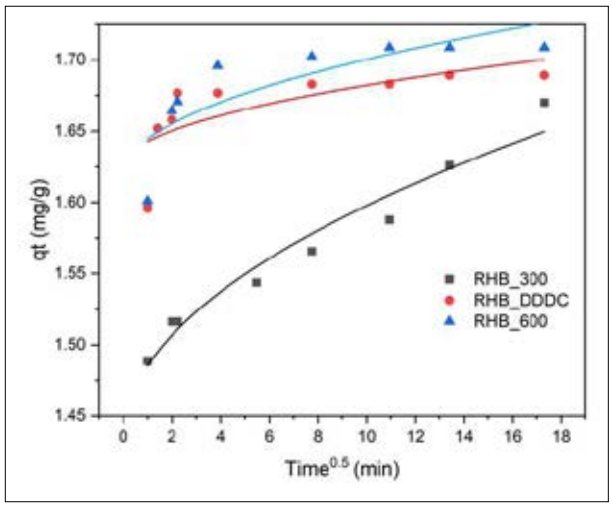

Figure 5: Adsorption kinetics of ammonium on biochar (RHB_300, RHB_DDDC, RHB_600) fitted with intraparticle diffusion model

The intraparticle diffusion model was used to assess the contribution of the diffusion of NH_4^+ in the entire adsorption process. This diffusion can be divided into three stages: rapid external diffusion from the bulk solution through the liquid film to the adsorbent's exterior surface; a slower adsorption phase with solute diffusion into the pores of adsorbent; and an equilibrium phase with sorption of solute on the interior surfaces of the pores and capillary spaces within the adsorbent (Nguyen et al., 2022, Allen et al., 1989). The overall rate of sorption is controlled by the slowest step, which would be either film diffusion or pore diffusion (Vadivelan & Kumar, 2005). From the perspective of the particle diffusion model, the adsorption process of RHB_300 on NH_4^+ in water could be roughly divided into two stages. During the first 9 minutes rapid adsorption of NH_4^+ occurs on the surface of the adsorbent. After 9 minutes, NH_4^+ diffuses more slowly into the BC. Due to the influence of molecular diffusion resistance, the rate of diffusion decreases until adsorption reaches an equilibrium (Xu et al., 2022).

Table 5: Kinetics parameters for the intraparticle diffusion models of NH_4^+ adsorption on three types of rice husk biochar.

	Intraparticle diffusion model		
	R^2	C_i (mg/g)	K_{ip} (mg/g)
RHB_300	0.9566	1.4332	0.0520
RHB_500	0.5216	1.6244	0.0183
RHB_600	0.6568	1.6185	0.0258

R^2 is the regression coefficient, C_i is the boundary layer thickness and K_{ip} is the intraparticle diffusion rate constant.

The $C_i > 0$, indicates that there is a boundary layer effect (Wang & Guo, 2020). The high positive value of the boundary layer diffusion (Table 6) suggests that, apart from intraparticle diffusion, the adsorption rate of NH_4^+-N may also be affected by boundary layer diffusion (Xu et al., 2022).

Mechanisms of the ammonium adsorption process

The adsorption behavior of NH_4^+ was strongly influenced by the structural and chemical characteristics of the produced BCs, including surface area, porosity, surface functional groups, and ion exchange properties (Zhang et al., 2020; Fidel et al., 2018). Although higher pyrolysis temperatures increased aromaticity and specific surface area, the NH_4^+ adsorption capacity decreased, indicating that surface chemistry played a more dominant role than physical surface area in governing adsorption performance. The abundance of oxygen-containing functional groups in RHB_300, as observed from FTIR analysis, likely enhanced NH_4^+ retention through electrostatic interactions and ion exchange mechanisms. In contrast, higher pyrolysis temperatures increased carbon structural ordering while reducing surface functional groups, thereby decreasing the availability of active adsorption sites despite improved porosity. Similar observations were reported by Kizito et al. (2016) for NH_4^+ adsorption onto woodchips and rice husk BCs. Furthermore, the high ash content observed in RHB_500 may have contributed to surface heterogeneity and multilayer adsorption behavior, consistent with the Freundlich isotherm fitting. Based on the kinetic analysis, the intraparticle diffusion model best described NH_4^+ adsorption in RHB_300, suggesting that diffusion was the dominant adsorption mechanism in the low-temperature BC.

CONCLUSION

Rice-husk BCs produced at 300 °C, 500 °C, and 600 °C displayed a clear temperature-driven trade-off. Proximate and elemental trends showed that from 300 °C to 600 °C, pH, fixed carbon (FC), aromaticity, and specific surface area increased, whereas volatile matter and surface functional groups declined. A marked ash-peak (45 %) occurred at 500 °C, linked to the DDDC's two-stage, slow-downdraft path that retains minerals while releasing extra carbon. FT-IR analysis confirmed the progressive loss of O- and H-containing functional groups with temperature, while Raman spectroscopy showed growing aromatic order but also defective generation at the highest temperature.

Adsorption isotherms fitted with the Langmuir model for RHB 300 and RHB 600 (monolayer, homogeneous sites), and the Freundlich model for ash-rich RHB 500 (heterogeneous, multilayer sites). Maximum NH_4^+ adsorption capacity (Q_{max}) ranged from 4.53 mg g^{-1} (at 300 °C) to 2.36 mg g^{-1} (at 600 °C). Adsorption is rapid (equilibrium $\leq$ 60 minutes), governed by intraparticle diffusion at 300 °C, and by pseudo-second-order chemisorption at higher temperatures.

Low-temperature BC (RHB_300) retained abundant oxygen-containing functional groups and showed the highest NH_4^+ adsorption capacity among the tested BCs, indicating its strong affinity for ammonium adsorption under aqueous conditions. In contrast, higher pyrolysis temperatures increased aromaticity, fixed carbon content, and structural stability while reducing adsorption capacity. The adsorption behavior observed in this study suggests that pyrolysis temperature strongly influences the balance between surface functionality and structural stability of rice husk BC.

Adsorption kinetics indicated rapid NH_4^+ uptake, with intraparticle diffusion contributing to adsorption in RHB_300, while chemisorption mechanisms were more prominent in RHB_500 and RHB_600. The heterogeneous surface characteristics of RHB_500, likely associated with its high ash content, influenced adsorption behavior and isotherm fitting.

Although the results demonstrate the potential of rice husk BC for NH_4^+ adsorption in aqueous systems, further studies are required to evaluate the release dynamics of adsorbed ammonium under different conditions and types of soils. In addition, interactions between NH_4^+ and competing ions within the BC matrix should be investigated, as these processes may influence nutrient retention and availability in practical applications.

Acknowledgements

This research was funded by the National Research Council of Sri Lanka [NRC/TO/16-07].

REFERENCES

Alahakoon, A. M. Y. W., Karunarathna, A. K., & Dharmakeerthi, R. S. (2018). Performance evaluation of a down draft double chamber pyrolysis reactor under field conditions. *Tropical Agricultural Research, 30,* 84-94. https://doi.org/10.4038/tar.v30i1.8280

Allen, S. J., McKay, G., & Khader, K. Y. H. (1989). Intraparticle diffusion of a basic dye during adsorption onto sphagnum peat. *Environmental Pollution, 56*(1), 39–50. https://doi.org/10.1016/0269-7491(88)90106-6

Amonette, J. E., & Joseph, S. (2012). Characteristics of biochar: Microchemical properties. In *Biochar for environmental management* (eds. J. Lehmann and S. Joseph), pp. 65–84. Earthscan, UK.

Armynah, B., Djafar, Z., Piarah, W. H., & Tahir, D. (2018). Analysis of chemical and physical properties of biochar from rice husk biomass. *Journal of Physics: Conference Series, 979*(1), 012038. https://doi.org/10.1088/1742-6596/979/1/012038

Ayiania, M., Weiss-Hortala, E., Smith, M., McEwen, J. S., & Garcia-Perez, M. (2020). Microstructural analysis of nitrogen-doped char by Raman spectroscopy: Raman shift analysis from first principles. *Carbon, 167*, 559–574. https://doi.org/10.1016/j.carbon.2020.05.055

Begum, S. A., Hyder, A. H. M. G., Hicklen, Q., Crocker, T., & Oni, B. (2021). Adsorption characteristics of ammonium onto biochar from an aqueous solution. *AQUA – Water Infrastructure, Ecosystems and Society, 70*(1), 113–122. https://doi.org/10.2166/aqua.2020.062

Bolan, N., Hoang, S. A., Beiyuan, J., Gupta, S., Hou, D., Karakoti, A., Joseph, S., Jung, S., Kim, K. H., Kirkham, M. B., & Kua, H. W. (2022). Multifunctional applications of biochar beyond carbon storage. *International Materials Reviews, 67*(2), 150–200. https://doi.org/10.1080/09506608.2021.1922047

Bustin, R. M., & Guo, Y. (1999). Abrupt changes (jumps) in reflectance values and chemical compositions of artificial charcoals and inertinite in coals. *International Journal of Coal Geology, 38*(3–4), 237–260. https://doi.org/10.1016/S0166-5162(98)00025-1

Cançado, L. G., Da Silva, M. G., Ferreira, E. H. M., Hof, F., Kampioti, K., Huang, K., Pénicaud, A., Achete, C. A., Capaz, R. B., & Jorio, A. (2017). Disentangling contributions of point and line defects in the Raman spectra of graphene-related materials. *2D Materials, 4*(2), 025039. https://doi.org/10.1088/2053-1583/aa5e77

Chia, C. H., Gong, B., Joseph, S. D., Marjo, C. E., Munroe, P., & Rich, A. M. (2012). Imaging of mineral-enriched biochar by FTIR, Raman and SEM–EDX. *Vibrational Spectroscopy, 62*, 248–257. https://doi.org/10.1016/j.vibspec.2012.06.006

Crombie, K., Mašek, O., Sohi, S. P., Brownsort, P., & Cross, A. (2013). The effect of pyrolysis conditions on biochar stability as determined by three methods. *GCB Bioenergy, 5*(2), 122–131. https://doi.org/10.1111/gcbb.12030

Cruz, H., Law, Y. Y., Guest, J. S., Rabaey, K., Batstone, D., Laycock, B., & Pikaar, I. (2019). Mainstream ammonium recovery to advance sustainable urban wastewater management. *Environmental Science & Technology, 53*(19), 11066–11079. https://doi.org/10.1021/acs.est.9b00603

Dada, A. O., Olalekan, A. P., Olatunya, A. M., & Dada, O. J. (2012). Langmuir, Freundlich, Temkin and Dubinin–Radushkevich isotherms studies of equilibrium sorption of Zn2+ onto phosphoric acid modified rice husk. *IOSR Journal of Applied Chemistry, 3*(1), 38–45. https://doi.org/10.9790/5736-0313845

Elnour, A. Y., Alghyamah, A. A., Shaikh, H. M., Poulose, A. M., Al-Zahrani, S. M., Anis, A., & Al-Wabel, M. I. (2019). Effect of pyrolysis temperature on biochar microstructural evolution, physicochemical characteristics, and its influence on biochar/polypropylene composites. *Applied Sciences, 9*(6), 1149. https://doi.org/10.3390/app9061149

Enders, A., Hanley, K., Whitman, T., Joseph, S., & Lehmann, J. (2012). Characterization of biochars to evaluate recalcitrance and agronomic performance. *Bioresource Technology, 114*, 644–653. https://doi.org/10.1016/j.biortech.2012.03.022

Feng, D., Zhao, Y., Zhang, Y., Sun, S., Meng, S., Guo, Y., & Huang, Y. (2016). Effects of K and Ca on reforming of model tar compounds with pyrolysis biochars under H_2O or CO_2. *Chemical Engineering Journal, 306*, 422–432. https://doi.org/10.1016/j.cej.2016.07.065

Fidel, R. B., Laird, D. A., & Spokas, K. A. (2018). Sorption of ammonium and nitrate to biochars is electrostatic and pH-dependent. *Scientific Reports, 8*, 17627. https://doi.org/10.1038/s41598-018-35534-w

Gai, X., Wang, H., Liu, J., Zhai, L., Liu, S., Ren, T., & Liu, H. (2014). Effects of feedstock and pyrolysis temperature on biochar adsorption of ammonium and nitrate. *PLOS ONE, 9*(12), e113888. https://doi.org/10.1371/journal.pone.0113888

Goldberg, S. (2005). Equations and models describing adsorption processes in soils. In *Chemical processes in soils* (eds. M.A. Tabatabai and D.L. Sparks), 8, pp. 489–517. https://doi.org/10.2136/sssabookser8.c10

Ho, Y. S., & McKay, G. (1999). Pseudo-second order model for sorption processes. *Process Biochemistry, 34*(5), 451–465. https://doi.org/10.1016/S0032-9592(98)00112-5

Huang, J., Xu, C. C., Ridoutt, B. G., Wang, X. C., & Ren, P. A. (2017). Nitrogen and phosphorus losses and eutrophication potential associated with fertilizer application to cropland in China. *Journal of Cleaner Production, 159*, 171–179. https://doi.org/10.1016/j.jclepro.2017.05.008

Hussain, A., Rehman, F., Rafeeq, H., Waqas, M., Asghar, A., Afsheen, N., Rahdar, A., Bilal, M., & Iqbal, H. M. (2022). In-situ, ex-situ, and nano-remediation strategies to treat polluted soil, water, and air–A review. *Chemosphere, 289*, 133252. https://doi.org/10.1016/j.chemosphere.2021.133252

Igalavithana, A. D., Choi, S. W., Shang, J., Hanif, A., Dissanayake, P. D., Tsang, D. C. W., Kwon, J. H., Lee, K. B., & Ok, Y. S. (2020). Carbon dioxide capture in biochar produced from pine sawdust and paper mill sludge: Effect of porous structure and surface chemistry. *Science of the Total Environment, 739*, 139845. https://doi.org/10.1016/j.scitotenv.2020.139845

Ilić, M., Haegel, F. H., Lolić, A., Nedić, Z., Tosti, T., Ignjatović, I. S., & Hartmann, H. (2022). Surface functional groups and degree of carbonization of selected chars from different processes and feedstock. *PLOS ONE, 17*(11), e0277365. https://doi.org/10.1371/journal.pone.0277365

Jiang, C., Wang, X., Qin, D., Da, W., Hou, B., Hao, C., & Wu, J. (2019). Construction of magnetic lignin-based

adsorbent and its adsorption properties for dyes. *Journal of Hazardous Materials, 369*, 50–61. https://doi.org/10.1016/j.jhazmat.2019.04.025

Jindo, K., Mizumoto, H., Sawada, Y., Sanchez-Monedero, M. A., & Sonoki, T. (2014). Physical and chemical characterization of biochars derived from different agricultural residues. *Biogeosciences, 11*(23), 6613–6621. https://doi.org/10.5194/bg-11-6613-2014

Joseph, S., Cowie, A. L., Van Zwieten, L., Bolan, N., Budai, A., Buss, W., Cayuela, M. L., Graber, E. R., Ippolito, J. A., Kuzyakov, Y., & Luo, Y. (2021). How biochar works, and when it doesn't: A review of mechanisms controlling soil and plant responses to biochar. *GCB Bioenergy, 13*(11), 1731–1764. https://doi.org/10.1111/gcbb.12885

Keiluweit, M., Nico, P. S., Johnson, M. G., & Kleber, M. (2010). Dynamic molecular structure of plant biomass-derived black carbon (biochar). *Environmental Science & Technology, 44*(4), 1247–1253. https://doi.org/10.1021/es9031419

Khalil, A., Sergeevich, N., & Borisova, V. (2018). Removal of ammonium from fish farms by biochar obtained from rice straw: Isotherm and kinetic studies for ammonium adsorption. *Adsorption Science & Technology, 36*(5–6), 1294–1309. https://doi.org/10.1177/0263617418768944

Kinniburgh, D. G. (1986). General purpose adsorption isotherms. *Environmental Science & Technology, 20*(9), 895–902. https://doi.org/10.1021/es00151a008

Kizito, S., Wu, S., Wandera, S. M., Guo, L., & Dong, R. (2016). Evaluation of ammonium adsorption in biochar-fixed beds for treatment of anaerobically digested swine slurry: Experimental optimization and modeling. *Science of the Total Environment, 563*, 1095–1104. https://doi.org/10.1016/j.scitotenv.2016.05.149

Konstantinou, I. K., & Albanis, T. A. (2000). Adsorption–desorption studies of selected herbicides in soil–fly ash mixtures. *Journal of Agricultural and Food Chemistry, 48*(10), 4780–4790. https://doi.org/10.1021/jf0003606

Laird, D. A., Fleming, P., Davis, D. D., Horton, R., Wang, B., & Karlen, D. L. (2010). Impact of biochar amendments on the quality of a typical Midwestern agricultural soil. *Geoderma, 158*(3–4), 443–449. https://doi.org/10.1016/j.geoderma.2010.05.013

Le, P. T., Bui, H. T., Le, D. N., Nguyen, T. H., Pham, L. A., Nguyen, H. N., Nguyen, Q. S., Nguyen, T. P., Bich, N. T., Duong, T. T., & Herrmann, M. (2021). Preparation and characterization of biochar derived from agricultural by-products for dye removal. *Adsorption Science & Technology, 2021*, 1–14. https://doi.org/10.1155/2021/9161904

Lee, Y. L., Ahmed, O. H., Wahid, S. A., Jalloh, M. B., & Muzah, A. A. (2021). Nutrient release and ammonia volatilization from biochar-blended fertilizer with and without densification. *Agronomy, 11*(10), 2082. https://doi.org/10.3390/agronomy11102082

Lehmann, J. (2007). Bio-energy in the black. *Frontiers in Ecology and the Environment, 5*(7), 381–387. https://doi.org/10.1890/1540-9295(2007)5[381:BITB]2.0.CO;2

Li, J., Liang, N., Jin, X., Zhou, D., Li, H., Wu, M., & Pan, B. (2017). The role of ash content on bisphenol A sorption to biochars derived from different agricultural wastes. *Chemosphere, 171*, 66–73. https://doi.org/10.1016/j.chemosphere.2016.12.041

Makarem, M., Lee, C. M., Kafle, K., Huang, S., Chae, I., Yang, H., Kubicki, J. D., & Kim, S. H. (2019). Probing cellulose structures with vibrational spectroscopy. *Cellulose, 26*, 35–79. https://doi.org/10.1007/s10570-018-2199-z

Markus, D. K., McKinnon, J. P., & Buccafuri, A. F. (1985). Automated analysis of nitrite, nitrate, and ammonium nitrogen in soils. *Soil Science Society of America Journal, 49*, 1208–1215. https://doi.org/10.2136/sssaj1985.03615995004900050028x

McLaughlin, H., Anderson, P. S., Shields, F. E., & Reed, T. B. (2009). All biochars are not created equal and how to tell them apart. *North American Biochar Conference 2*, 1–36.

McLaughlin, H. (2010). Characterizing biochars: Attributes, indicators, and at-home tests. In *The biochar revolution: Transforming agriculture & environment* (pp. 89–111). Taylor & Francis.

Morcali, M. H., Zeytuncu, B., & Yucel, O. (2013). Platinum uptake from chloride solutions using biosorbents. *Materials Research, 16*, 528–538. https://doi.org/10.1590/S1516-14392013005000006

Morrissy, J. G., Currell, M. J., Reichman, S. M., Surapaneni, A., Megharaj, M., Crosbie, N. D., Hirth, D., Aquilina, S., Rajendram, W., & Ball, A. S. (2021). Nitrogen contamination and bioremediation in groundwater and the environment: A review. *Earth-Science Reviews, 222*, 103816. https://doi.org/10.1016/j.earscirev.2021.103816

Neme, I., Gonfa, G., & Masi, C. (2022). Activated carbon from biomass precursors using phosphoric acid: A review. *Heliyon, 8*(12). https://doi.org/10.1016/j.heliyon.2022.e11940

Nguyen, C. T., Tungtakanpoung, D., & Kajitvichyanukul, P. (2022). Kinetic, isotherm and mechanism in paraquat removal by adsorption process using corn cob biochar produced from different pyrolysis conditions. *Case Studies in Chemical and Environmental Engineering, 6*, 100248. https://doi.org/10.1016/j.cscee.2022.100248

Pusceddu, E., Santilli, S. F., Fioravanti, G., Montanaro, A., Miglietta, F., & Foscolo, P. U. (2019). Chemical-physical analysis and exfoliation of biochar-carbon matter: From agriculture soil improver to starting material for advanced nanotechnologies. *Materials Research Express, 6*(11), 115612. https://doi.org/10.1088/2053-1591/ab4ba8

Rafiq, M. K., Bachmann, R. T., Rafiq, M. T., Shang, Z., Joseph, S., & Long, R. (2016). Influence of pyrolysis temperature on physico-chemical properties of corn stover biochar and feasibility for carbon capture and energy balance. *PLOS ONE, 11*(6), e0156894. https://doi.org/10.1371/journal.pone.0156894

Ronsse, F., Van Hecke, S., Dickinson, D., & Prins, W. (2013). Production and characterization of slow pyrolysis biochar: Influence of feedstock type and pyrolysis conditions. *GCB Bioenergy, 5*(2), 104–115. https://doi.org/10.1111/gcbb.12018

Singh, B., & Craswell, E. (2021). Fertilizers and nitrate pollution of surface and ground water: An increasingly

pervasive global problem. *SN Applied Sciences, 3*(4), 518. https://doi.org/10.1007/s42452-021-04521-8

Sumaraj, & Padhye, L. P. (2017). Influence of surface chemistry of carbon materials on their interactions with inorganic nitrogen contaminants in soil and water. *Chemosphere, 184*, 532–547. https://doi.org/10.1016/j.chemosphere.2017.06.021

Tang, Y., Alam, M. S., Konhauser, K. O., Alessi, D. S., Xu, S., Tian, W., & Liu, Y. (2019). Influence of pyrolysis temperature on production of digested sludge biochar and its application for ammonium removal from municipal wastewater. *Journal of Cleaner Production, 209*, 927–936. https://doi.org/10.1016/j.jclepro.2018.10.268

Townsend, A. R., Howarth, R. W., Bazzaz, F. A., Booth, M. S., Cleveland, C. C., Collinge, S. K., Dobson, A. P., Epstein, P. R., Holland, E. A., Keeney, D. R., & Mallin, M. A. (2003). Human health effects of a changing global nitrogen cycle. *Frontiers in Ecology and the Environment, 1*(5), 240–246. https://doi.org/10.1890/1540-9295(2003)001[0240:HHEOAC]2.0.CO;2

Tu, P., Zhang, G., Wei, G., Li, J., Li, Y., Deng, L., & Yuan, H. (2022). Influence of pyrolysis temperature on the physicochemical properties of biochars obtained from herbaceous and woody plants. *Bioresources and Bioprocessing, 9*(1), 131. https://doi.org/10.1186/s40643-022-00618-z

Vadivelan, V., & Kumar, K. V. (2005). Equilibrium, kinetics, mechanism, and process design for sorption of methylene blue onto rice husk. *Journal of Colloid and Interface Science, 286*(1), 90–100. https://doi.org/10.1016/j.jcis.2005.01.007

Wang, J., & Guo, X. (2020). Adsorption kinetic models: Physical meanings, applications, and solving methods. *Journal of Hazardous Materials, 390*, 122156. https://doi.org/10.1016/j.jhazmat.2020.122156

Wijitkosum, S., & Jiwnok, P. (2019). Elemental composition of biochar obtained from agricultural waste for soil amendment and carbon sequestration. *Applied Sciences, 9*(19), 3980. https://doi.org/10.3390/app9193980

Xiao, X., & Chen, B. (2017). A direct observation of the fine aromatic clusters and molecular structures of biochars. *Environmental Science & Technology, 51*(10), 5473–5482. https://doi.org/10.1021/acs.est.6b06300

Xu, D., Cao, J., Li, Y., Howard, A., & Yu, K. (2019). Effect of pyrolysis temperature on characteristics of biochars derived from different feedstocks: A case study on ammonium adsorption capacity. *Waste Management, 87*, 652–660. https://doi.org/10.1016/j.wasman.2019.02.049

Xu, H., Wang, B., Zhao, R., Wang, X., Pan, C., Jiang, Y., Zhang, X., & Ge, B. (2022). Adsorption behavior and performance of ammonium onto sorghum straw biochar from water. *Scientific Reports, 12*, 5358. https://doi.org/10.1038/s41598-022-08591-5

Yang, H. I., Lou, K., Rajapaksha, A. U., Ok, Y. S., Anyia, A. O., & Chang, S. X. (2018). Adsorption of ammonium in aqueous solutions by pine sawdust and wheat straw biochars. *Environmental Science and Pollution Research, 25*, 25638–25647. https://doi.org/10.1007/s11356-017-8551-2

Yu, Q., Xia, D., Li, H., Ke, L., Wang, Y., Wang, H., Zheng, Y., & Li, Q. (2016). Effectiveness and mechanisms of ammonium adsorption on biochars derived from biogas residues. *RSC Advances, 6*, 88373–88381. https://doi.org/10.1039/C6RA16913A

Yuan, R., Guo, Y., Gurgan, I., Siddique, N., Li, Y. S., Jang, S., & Kim, S. H. (2025). Raman spectroscopy analysis of disordered and amorphous carbon materials: A review of empirical correlations. *Carbon, 238*, 120214. https://doi.org/10.1016/j.carbon.2025.120214

Zhang, J., Liu, J., & Liu, R. (2015). Effects of pyrolysis temperature and heating time on biochar obtained from straw and lignosulfonate. *Bioresource Technology, 176*, 288–291. https://doi.org/10.1016/j.biortech.2014.11.011

Zhang, M., Song, G., Gelardi, D. L., Huang, L., Khan, E., Mašek, O., Parikh, S. J., & Ok, Y. S. (2020). Evaluating biochar and its modifications for removal of ammonium, nitrate, and phosphate in water. *Water Research, 186*, 116303. https://doi.org/10.1016/j.watres.2020.116303

Zimmerman, A. R. (2010). Abiotic and microbial oxidation of laboratory-produced black carbon (biochar). *Environmental Science & Technology, 44*(4), 1295–1301. https://doi.org/10.1021/es903140c

J.Natn.Sci.Foundation Sri Lanka 2026 54 (3): 339 - 346
DOI: http://dx.doi.org/10.4038/jnsfsr.v54i3.12777

RESEARCH ARTICLE

Applied Physics

Eco-friendly electrodeposited SnO_2/Cu_2O thin-film heterojunction solar cells for low-cost photovoltaic applications

BMUH Balasuriya[1], FSB Kafi[1*], WTRS Fernando[1], KMDC Jayathilaka[1], LSR Kumara[2], T Nakatani[2] RP Wijesundera[1] and W Siripala[1]

[1] *Department of Physics and Electronics, University of Kelaniya, Kelaniya.*
[2] *Japan Synchrotron Radiation Research Institute (JASRI) 1-1-1, Kouto, Sayo 679-5198, Hyogo Japan.*

Submitted: 21 August 2025; Revised: 26 June 2026; Accepted: 24 July 2026

Abstract: The rapid global population growth and technological transition have enhanced daily energy demands. This poses significant challenges to energy production from fossil fuels, whose reserves are finite. Solar energy offers a sustainable, renewable solution to the prevailing energy production issues. Photovoltaic energy, in particular, is favorable due to its widespread availability, free accessibility, eco-friendly nature, and low operational and maintenance costs. However, the available photovoltaics are expensive and unaffordable to the general public. This study focuses on the development of a low-cost eco-friendly SnO_2/Cu_2O heterojunction solar cell by the method of electrodeposition. The fabrication process involved the electrodeposition of an n-type SnO_2 thin film onto copper substrates, followed by the subsequent electrodeposition of p-type Cu_2O thin film. The photoresponse of the solar cell structured $Cu/SnO_2/Cu_2O/Au$ was optimized by tuning the bath temperature during SnO_2 thin film deposition. Structural, morphological, and optoelectronic properties were systematically investigated using X-ray diffraction (XRD), scanning electron microscopy (SEM), and current–voltage (I–V) measurements. Under AM 1.5G illumination at 100 mW/cm², the optimized device exhibited an open-circuit voltage (Voc) of 156.26 mV, a short-circuit current density (Jsc) of 1.09 mA/cm², a fill factor (FF) of 27.80%, and a power conversion efficiency (η) of 0.047%. Although the efficiency is relatively low, the results are promising due to the use of earth-abundant, non-toxic materials, low-temperature electrodeposition, and the clear potential for further performance enhancement through interface engineering.

Keywords: Cu_2O, electrodeposition, heterojunction, photovoltaic, SnO_2, thin film.

INTRODUCTION

The growth of the global population over the last decade of 900 million with a population growth rate of 1.2% per annum indicates that our energy daily requirements should increase at least by this rate (Ghosh et al., 2024). Our energy demand does not increase at this rate since we acquire energy demand through technological transitions too. Studies show that global energy demand rose by 9% over the last decades (Abu Al-Haija et al., 2023). If this remains we have a challenging energy production to face in the future. The Earth receives approximately 173,000 terawatts of solar energy continuously, while the global energy demand is 18 terawatts (Aboulouard et al., 2021). Thus, solar energy stands as a pivotal solution to the global energy crisis, offering a sustainable and renewable source to meet the escalating demand for electricity. Photovoltaic (PV) energy has emerged as a favorable substitute due to its widespread availability, free accessibility, eco-friendly nature, and lower operational and maintenance expenses.

In this context, heterojunction solar cells based on earth-abundant and non-toxic metal oxides have attracted

* Corresponding author (kafi@kln.ac.lk; https://orcid.org/0000-0002-8961-8637)

This article is published under the Creative Commons CC-BY-ND License (http://creativecommons.org/licenses/by-nd/4.0/). This license permits use, distribution and reproduction, commercial and non-commercial, provided that the original work is properly cited and is not changed in anyway.

growing research interest. Stannic oxide or tin (IV) oxide (SnO_2) has emerged as a pivotal non-toxic low-cost n-type material in the hetero-structured solar cells. It is a wide band gap material with a band gap of 3.6 eV (Akgul et al., 2013),owing to a high transparency for visible light and strong absorption of UV light (Chetri & Choudhury, 2013). It has excellent thermal stability (Korösi et al., 2005) and chemical inertness (Popescu et al., 2002). Further, the refractive index and the work function of SnO_2 are around 2.0 at a wavelength of 550 nm (Jarzebski & Morton, 1976) and range from 4.4 – 5.0 eV (Zlamalova et al., 2023), respectively. These exceptional properties render SnO_2 suitable for various applications such as gas sensors (Yu & Dutta, 2011), electrodes in Lithium-ion batteries (Chen & Lou, 2013), antistatic coatings (Gotlib-Vainstein et al., 2015, thin-film transistors (Priyadarshini et al., 2017), photoelectronic devices (Hassun et al., 2020). Various deposition techniques have been deployed to grow SnO_2. Chemical vapor deposition (CVD) (Liu et al., 2005), atomic layer deposition (ALD) (Sundqvist et al., 2006), spray pyrolysis(Gordillo et al., 1994), sol-gel methods (Aziz et al., 2012), liquid flow deposition (Supothina, 2003), and electrodeposition (Chen et al., 2010) are commonly used methods to grow high-quality SnO_2 layers. Among the various techniques available for depositing SnO_2, electrodeposition is less explored. However, growth of SnO_2 via electrodeposition offers several advantages, including cost-effectiveness, simplicity, and uniformity in the growth of thin film layers.

Copper (I) oxide (Cu_2O) is a non-toxic low-cost p-type semiconducting material with a band gap of 2.1 eV (Tahir & Tougard, 2012), making it suitable for absorbing visible light. Among various Cu_2O growth techniques, electrodeposition is a widely studied method for growing high-quality Cu_2O films due to its simplicity, cost-effectiveness, and ability to produce uniform thin films. Reported studies show that the Cu_2O thin films could grow in both acidic (Kafi et al., 2019) and basic baths (Kafi et al., 2021; Thejasiri et al., 2022). However, p-type conductivity results in basic baths, and qualitative p-type Cu_2O may be obtained at high pH values (Thejasiri et al., 2024). Growth of SnO_2/Cu_2O thin film layers by means of electrodeposition is a twofold advantage since both materials and deposition techniques are low-cost and eco-friendly.

Studies on SnO_2/Cu_2O heterojunction solar cells are limited in literature; one study reported the fabrication of Cu_2O/SnO_2 heterostructure solar cells using sol-gel deposition methods (Fukuda & Ichimura, 2013). The resulting devices exhibited a conversion efficiency of 0.066% with an open-circuit voltage of 0.29 V, a short-circuit current density of 0.58 mA/cm², and a fill factor of 39%. Research has been conducted on $Cu_2O/CuO/SnO_2$ transparent p-n junction film devices (Yu et al., 2021). However, these studies relied on multi-step or high-temperature fabrication routes and did not employ electrodeposition for both semiconductor layers. To the best of our knowledge, no previous reports exist on the fabrication of a $Cu/SnO_2/Cu_2O/Au$ heterojunction solar cell in which both the n-type $SnO_2$and p-type Cu_2O layers are grown exclusively by electrodeposition.

Accordingly, the primary objective of this study is to fabricate and systematically investigate a fully electrodeposited $Cu/SnO_2/Cu_2O/Au$ heterojunction solar cell, with particular emphasis on optimizing the SnO_2 deposition conditions and evaluating their impact on device performance. The findings of this work would provide valuable insights into the feasibility of low-cost, eco-friendly oxide-based heterojunction solar cells and offer a promising pathway for further optimization and performance enhancement.

MATERIALS AND METHODS

Materials

All chemicals used were of reagent grade and purchased from Sigma-Aldrich. Stannous chloride ($SnCl_2$, 98%), nitric acid (HNO_3, 69%), cupric sulfate pentahydrate ($CuSO_4 \cdot 5H_2O$, 85%), lactic acid ($C_3H_6O_3$, 85%), and sodium hydroxide (NaOH, 99%) were used without further purification. Distilled water was used throughout all experiments. A copper plate ($2 \times 1 \times 0.1$ cm³) was used as the substrate for device fabrication.

Device fabrication

Substrate preparation

Copper substrates were cleaned sequentially using detergent solution, diluted HCl, and distilled water, followed by ultrasonication in distilled water to remove surface contaminants.

Electrodeposition of SnO_2 thin films

An n-type SnO_2 thin film was electrodeposited on the cleaned copper substrate using a potentiostat (Hokuto Denko Potentiostat/Galvanostat HAB-151) in a three-electrode configuration. The electrolyte consisted of an aqueous solution of 30 mM $SnCl_2$ and 150 mM

HNO_3 aqueous solution. A platinum plate and Ag/AgCl electrode were used as the counter and reference electrodes, respectively.

As a pretreatment step, oxygen gas was bubbled into the electrolyte for 1 hour at a flow rate of 100 sccm at the deposition temperature to oxidize Sn^{2+} to Sn^{4+}. SnO_2 deposition was carried out potentiostatically at −0.85 V vs. Ag/AgCl for 2 minutes at bath temperatures of 70–90 °C (70, 75, 80, 85, and 90 °C) to optimize deposition conditions.

Electrodeposition of Cu_2O thin films

A p-type Cu_2O layer was electrodeposited onto the Cu/SnO_2 structure at −0.45 V vs. Ag/AgCl for 40 minutes in a three-electrode cell. The electrolyte consisted of 0.4 M $CuSO_4 \cdot 5H_2O$, 3 M lactic acid, and NaOH solution and was maintained at 60 °C and pH 13. A platinum counter electrode and Ag/AgCl reference electrode were used.

Device completion

Front contacts were fabricated by sputtering a thin Au layer (a few nm thick) onto a masked Cu_2O surface over an active area of approximately 2 × 2 mm^2 using a Cressington 108auto sputter coater. Sputtering was performed at 30 mA for 120 s. The copper substrate served as the back contact. Electrical contacts were made to the Cu substrate and Au pads.

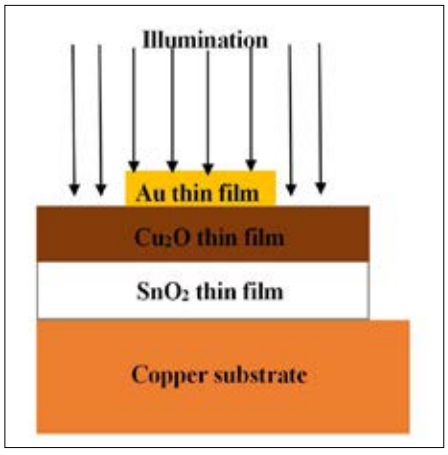

Figure 1: Structure of the Cu/SnO_2/Cu_2O/Au heterojunction solar cell

Characterization techniques

Electrical and photoresponse measurements

Photoresponse parameters including short-circuit current density (J_{sc}) and open-circuit voltage (V_{oc}) were measured using a Keithley 2100 digital multimeter. Current–voltage (I–V) characteristics were recorded using a Gamry G series potentiostat/galvanostat/ZRA under AM 1.5G illumination (100 mW/cm^2) provided by a Sci Sun-300 solar simulator. Illumination was modulated using a mechanical chopper and applied to the solar cell as shown in Figure 1.

Capacitance–voltage (C–V) measurements

C–V measurements for SnO_2 and Cu_2O thin films were performed using a Gamry instrument in a three-electrode electrochemical setup. A platinum counter electrode and Ag/AgCl reference electrode were used. Measurements were carried out in 0.1 M $NaNO_3$ electrolyte with a contact area of 4 mm^2, at a frequency of 3 kHz.

Morphological characterization

Surface morphology of SnO_2 and Cu_2O films was analyzed using a ZEISS EVO LS15 scanning electron microscope (SEM). Images were recorded at a magnification of ×50,000 on samples approximately 8 mm in width.

Structural characterization

Crystal structure was investigated using grazing incidence X-ray diffraction (GIXRD) at the BL19B2 beamline, SPring-8, Hyogo, Japan. The incident X-ray energy was 20 keV (λ = 0.0619917 nm), and diffracted beams were detected using a FMB $LaBr_3$ scintillation detector.

RESULTS AND DISCUSSION

Many reports suggest that the performance of a solar cell strongly depends on the growth parameters (Hreid et al., 2015; Singh & Ravindra, 2012; Thejasiri et al., 2022). It is crucial to tune these growth parameters to optimize a solar cell, particularly the bath temperature, which critically influences electrodeposition by affecting reaction kinetics, film morphology, crystallinity, and adhesion. These factors, in turn, determine the structural and electrical quality of the deposited layer and ultimately the overall device performance. We noted that

the bath temperature during SnO_2 thin-film deposition affects the overall performance of the Cu/SnO_2/Cu_2O/Au heterojunction of the solar cell. Thus, we fabricated these cells by varying the bath temperature of the SnO_2 film deposition while keeping all other film deposition parameters constant, as described in the methodology section.

In this study, SnO_2 thin films were successfully electrodeposited under potentiostatic conditions on Cu substrates using a three-electrode electrochemical cell containing an aqueous solution of 30 mM $SnCl_2$ and 150 mM HNO_3. Electrodeposition was performed at -0.85 V vs. Ag/AgCl for 2 minutes at different bath temperatures. It was observed that SnO_2 thin films grown at low temperatures (particularly below 75 °C) and at high temperatures, (above 90 °C) were of poor quality. In contrast, films deposited between 75 °C and 90 °C exhibited high quality with good adhesion to the Cu substrates. Subsequently, Cu_2O thin films were potentiostatically electrodeposited onto the SnO_2 layers. For this purpose, a lactate bath containing 0.4 M $CuSO_4 \cdot 5HO$, 3M $C_3H_6O_3$, and NaOH in aqueous solution was employed. The deposition potential, bath temperature, and duration for Cu_2O film growth were -0.45 V vs. Ag/AgCl for 40 minutes, at a bath temperature of 60 °C, respectively. At pH values below 13, Cu_2O thin film growth on the SnO_2layers was incomplete, whereas at pH 13, uniform and well-adhered Cu_2O thin films were obtained. The growth of high-quality SnO_2thin films on Cu substrates and the formation of a uniform SnO_2/Cu_2O bilayer, both achieved solely through the electrodeposition technique, are key highlights of this study.

Photoresponse measurements of the Cu/SnO_2/Cu_2O/Au heterojunction solar cells revealed that increasing the SnO_2film deposition bath temperature from 75 °C to 90 °C induced notable changes in the solar cell parameters such as Jsc, Voc, and FF. Specifically, at a bath temperature of 85 °C, Jsc, Voc, and FF values increased considerably leading to a more efficient solar cell. This improvement in performance, at 85 °C, can be attributed to the optimal crystal growth and surface morphology of the SnO_2thin film, which enhance charge carrier separation and reduce recombination losses. Furthermore, lower temperatures tended to produce films with incomplete coverage and poor crystallinity, resulting in higher recombination rates and lower Voc. Conversely, excessively high temperatures caused increased surface roughness and film stress, which degraded junction quality and device stability. An intermediate temperature thus yielded the best balance between structural integrity and carrier transport, resulting in improved Jsc and FF. Table 1 shows the short-circuit current density (Jsc), open-circuit voltage (Voc), fill factor (FF), and conversion efficiency (η) for solar cells fabricated with SnO_2 films deposited at different temperatures.

The measured I–V curve (Figure 2) for the SnO_2/Cu_2O heterojunction solar cell illustrates clear photovoltaic behavior under illumination. It also shows a well-defined Voc and short-circuit current (Isc), confirming the generation and separation of photo-induced charge carriers at the heterojunction interface. The shift from the dark to the illuminated curve highlights the rectifying nature of the junction and its ability to convert light into electrical power. The diode-like response observed under dark conditions suggests the proper formation of the p–n junction between n-type $SnO_2$and p-type Cu_2O. However, Figure 2 also shows that the high series resistance and low shunt resistance of the cell produce a linear I-V behavior, resulting in a low fill factor (FF) because the voltage drop across the series resistance dominates that across the space charge region. Additionally, the figure indicates that the fabricated solar cell is free of photo-corrosion and remains stable under illumination. The interplay between series and shunt resistances critically influences the fill factor and overall power conversion efficiency, highlighting the importance of controlling film uniformity and interface quality. These observations underscore the necessity of precise temperature control during electrodeposition to maximize solar cell performance while maintaining device durability under prolonged operation.

Table 1: Dependence of parameters of the Cu/SnO_2/Cu_2O/Au heterojunction solar cell on bath temperature of SnO_2 film deposition

Temperature (°C)	J_{sc} (mAcm^{-2})	V_{oc} (mV)	FF (%)	η(%)
75	0.69	125.49	27.20	0.024
80	0.90	137.53	25.70	0.032
85	1.09	156.26	27.80	0.047
90	0.52	111.04	26.70	0.015

The best fabricated cell achieved a low power conversion efficiency of approximately 0.05%, which is significantly below the theoretical Shockley–Queisser limit of around 24% for an SnO_2/Cu_2O heterojunction solar cell. Several factors may contribute to this discrepancy between the experimental efficiency and the theoretical limit. These include non-idealities such as interface defects, trap states, and recombination centers at the SnO_2/Cu_2O junction, which impede charge separation and carrier transport. Additionally, this solar cell was measured under rear-side illumination, which can introduce additional optical losses due to absorption and reflection before light reaches the active junction, thereby reducing the effective photon flux. Fabrication limitations related to thin film uniformity and crystallinity can also impair device performance. Nevertheless, this study provides useful insights into carrier collection efficiency and performance limitations in SnO_2/Cu_2O heterojunction solar cells.

The maximum power output of the best cell was about 2.47 W/m². While this output is modest compared to commercial solar cells, it provides a promising foundation for further development. The simplicity of the fabrication process, combined with low material costs, positions this cell as a strong candidate for scalable, eco-friendly photovoltaic technologies. The current performance highlights the potential of this heterojunction architecture, particularly for low-power or off-grid applications.

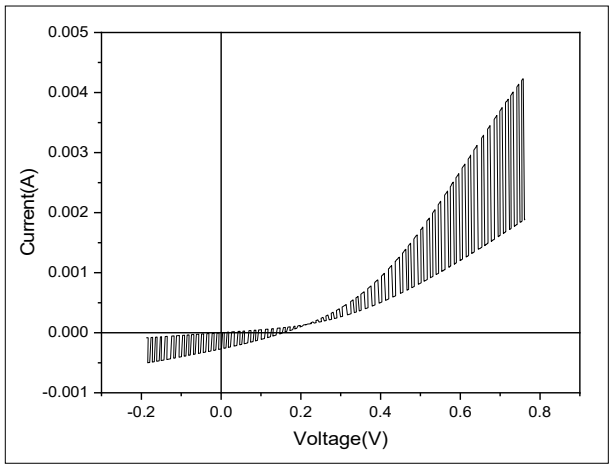

Figure 2: Modulated I-V characteristics for the Cu/SnO_2/Cu_2O/Au heterojunction solar cell.

C-V measurements were implemented to identify the conductivity of the SnO_2 and Cu_2O thin films in a three-electrode electrochemical cell using the Gamry instrument. Figure 3 shows the Mott-Schottky plot of the SnO_2thin film electrodeposited on a Cu substrate revealing n-type conductivity at a bath temperature of 85 °C. Similarly, Figure 4 displays the corresponding plot for Cu_2O thin film showing p-type conductivity.

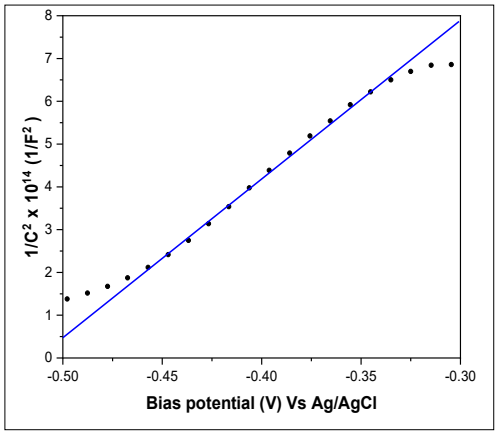

Figure 3: Mott-Schottky plot for SnO_2 thin film electrodeposited at a bath temperature of 85 ℃. All other growth parameters are the same as mentioned in the methodology section.

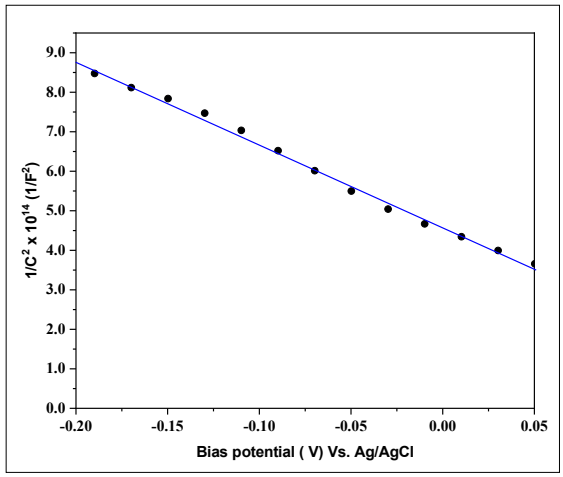

Figure 4: Mott-Schottky plot for Cu_2O thin film electrodeposited at a bath pH of 13.0. All other growth parameters are the same as mentioned in the methodology section.

These difference in conductivity types aligns well with the intrinsic defect chemistry of the materials: oxygen vacancies and interstitial tin atoms typically act as donor in SnO_2 while copper vacancies serve as acceptors in Cu_2O. These observations are consistent with previous literature, confirming the reliability of the electrodeposition process used in this study. Furthermore, the contrasting conductivity types of SnO2and Cu_2O suggests that the fabricated SnO_2/Cu_2O heterojunction solar cell consists of an n–p junction.

Figure 5 (i) shows the SEM image of the SnO_2 thin film electrodeposited at a bath temperature of 85 ℃. It reveals a cloud like nanostructured surface composed of agglomerated spherical nanoparticles (~100-200 nm) that are distributed uniformly with good substrate coverage and consistent nucleation. This uniform distribution of SnO2nanoparticles with nanoscale dimensions enhances surface area, which is beneficial for increased light absorption and improved charge-carrier collection in solar cells. Nanostructured morphology can also reduce reflection losses, thereby enhancing photon harvesting efficiency. Additionally, Figure 5 (ii) presents the SEM image of the Cu_2O thin film electrodeposited at a bath pH value of 13.0. The Cu_2O thin films are pyramid-shaped crystals and uniformly cover the substrates indicating a well-defined crystallographic growth. Such morphology typically improves charge transport properties and reduces recombination at grain boundaries. The well-covered Cu_2O layer ensures effective junction formation with the underlying SnO_2, promoting efficient charge separation. These morphological features directly influence the photovoltaic performance by influencing carrier mobility, recombination dynamics, and overall device stability.

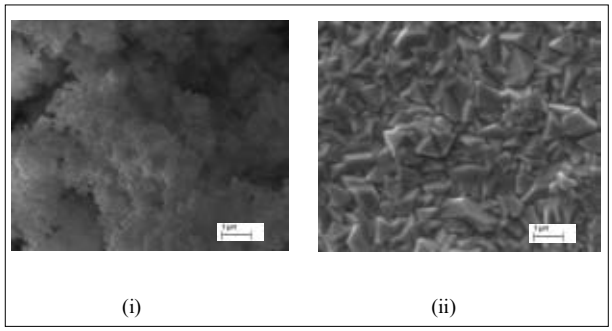

Figure 5: SEM images of (i) SnO_2 thin film electrodeposited at bath temperature of 85 ℃ and (ii) Cu_2O thin film electrodeposited at bath pH of 13.0. All other growth parameters are same as described in the methodology section.

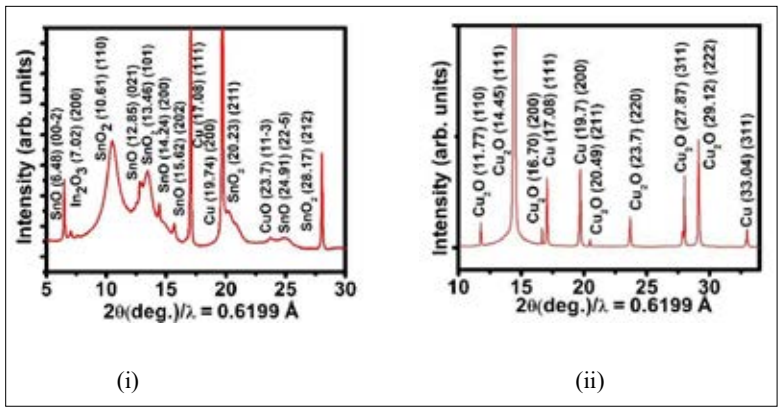

Figure 6: GIXRD profiles of electrodeposited (i) SnO_2 thin films at the bath temperature of 85 ℃ and (ii) Cu_2O thin films at bath pH of 13 on Cu substrates

Structural information of SnO_2 and Cu_2O layers were studied using GIXRD at an X-ray wavelength of 0.62 Å. Figure 6 (i) represents the XRD data of electrodeposited SnO_2 thin films at a bath temperature of 85 ℃ (other parameters of SnO_2 thin film deposition follow those described in the methodology). Four dominant peaks correspond to the reflection from (110), (101), (211) and (212) atomic planes of SnO_2. This indicates that the primary phase is SnO_2. Additionally, a few faint peaks of SnO and CuO are are also present likely arising

from incomplete oxidation of Sn^{2+} to Sn^{4+} and oxidation of Cu to Cu^{2+}. These minor SnO and CuO impurities suggests areas for improvement in oxidation control during electrodeposition, to enhance film quality and reproducibility. Figure 6 (ii) represents the GIXRD profiles of electrodeposited Cu_2O thin films corresponding to the reflection from (110), (111), (200), (211), (220), (311) and (222) atomic planes. Additionally, few Cu peaks were observed due to the substrate. The GIXRD data reveals that the electrodeposited SnO_2 and Cu_2O thin films are rutile and cubic structures, respectively. These data are analogous to previous reports (Jabeen et al., 2023;. Thejasiri et al., 2024).

CONCLUSION

In conclusion, we have demonstrated the possibility of the fabrication of a $Cu/SnO_2/Cu_2O/Au$ heterojunction solar cell by electrodepositing both $SnO_2$and Cu_2O thin films. Surface- morphology studies have shown that the electrodeposited $SnO_2$and Cu_2O thin films are of high quality and GIXRD measurements verify their crystal structure of these films. The best cell was obtained with a bath temperature of 85 °C for SnO_2film deposition. .The best $Cu/SnO_2/Cu_2O$ /Au heterojunction solar cell obtained in this study exhibited a V_{oc} of 156 mV, J_{sc} of 1.09 mA/cm², FF of 27.80%, and η of 0.047%. This study has shown a two-fold improvement in the J_{sc} value compared to previous reports. Even though the efficiency obtained in this study is poor for a SnO_2/Cu_2O heterojunction solar cell, the reported values are remarkable for rear illumination. The relatively low efficiency is primarily attributed to interfacial defects and incomplete charge collection at the rear-illuminated junction, which are typical limitations in such device configurations. Further optimization of deposition parameters, such as precursor concentration, pH level, and annealing conditions, could lead to enhanced film quality and device performance. This study provides valuable insights into the electrodeposition of SnO_2thin films and the formation of a well-adhered, high-quality Cu_2O thin film on SnO_2, which will be useful in the development of SnO_2/Cu_2O junction devices.

Acknowledgment

Financial assistance by Internal Research Grant, University of Kelaniya under research grant RP/03/02/05/01/2022and National Science Foundationof Sri Lanka under grant RG/2025/BS/06 are acknowledged. The GIXRD measurements were performed at SPring-8 with the approval of JASRI under proposals 2024A1761 and 2025A1568.

REFERENCES

Aboulouard, A., Mtougui, S., Demir, N., Moubarik, A., idrissi, M. El, & Can, M. (2021). New non-fullerene electron acceptors-based on quinoxaline derivatives for organic photovoltaic cells: DFT computational study. *Synthetic Metals*, *279*, 116846. https://doi.org/10.1016/J.SYNTHMET.2021.116846

Abu Al-Haija, Qasem, Mohamed, Omar, & Abu Elhaija, Wejdan. (2023). Predicting global energy demand for the next decade: A time-series model using nonlinear autoregressive neural networks. *Energy Exploration & Exploitation*, *41*(6), 1884–1898. https://doi.org/10.1177/01445987231181919

Akgul, F. A., Gumus, C., Er, A. O., Farha, A. H., Akgul, G., Ufuktepe, Y., & Liu, Z. (2013). Structural and electronic properties of SnO_2. *Journal of Alloys and Compounds*, *579*, 50–56. https://doi.org/10.1016/J.JALLCOM.2013.05.057

Aziz, M., Abbas, S. S., Baharom, W. R. W., & Mahmud, W. Z. W. (2012). Structure of SnO_2 nanoparticles by sol–gel method. *Materials Letters*, *74*, 62–64. https://doi.org/10.1016/J.MATLET.2012.01.073

Chen, J. S., & Lou, X. W. (David). (2013). SnO_2-Based Nanomaterials: Synthesis and Application in Lithium-Ion Batteries. *Small*, *9*(11), 1877–1893. https://doi.org/10.1002/smll.201202601

Chen, X., Liang, J., Zhou, Z., Duan, H., Li, B., & Yang, Q. (2010). The preparation of SnO_2 film by electrodeposition. *Materials Research Bulletin*, *45*(12), 2006–2011. https://doi.org/10.1016/J.MATERRESBULL.2010.07.029

Chetri, P., & Choudhury, A. (2013). Investigation of optical properties of SnO_2 nanoparticles. *Physica E: Low-Dimensional Systems and Nanostructures*, *47*, 257–263. https://doi.org/10.1016/J.PHYSE.2012.11.011

Priyadarshini D.M., Mannam, R., Rao, M. S. R., & DasGupta, N. (2017). Effect of annealing ambient on SnO_2 thin film transistors. *Applied Surface Science*, *418*, 414–417. https://doi.org/10.1016/J.APSUSC.2016.11.233

Fukuda, A., & Ichimura, M. (2013). Heterostructure Solar Cells Based on Sol-Gel Deposited SnO_2 and Electrochemically DepositedCu_2O *Materials Sciences and Applications*, *04*(06), 1–4. https://doi.org/10.4236/msa.2013.46A001

Ghosh, A., Kumar, A., & Biswas, G. (2024). Exponential population growth and global food security: challenges and alternatives. *Bioremediation of Emerging Contaminants from Soils: Soil Health Conservation for Improved Ecology and Food Security*, 1–20. https://doi.org/10.1016/B978-0-443-13993-2.00001-3

Gordillo, G., Moreno, L. C., de la Cruz, W., & Teheran, P. (1994). Preparation and characterization of SnO_2 thin films deposited by spray pyrolysis from SnC_{l2} and SnC_{l4} precursors. *Thin Solid Films*, *252*(1), 61–66. https://doi.org/10.1016/0040-6090(94)90826-5

Gotlib-Vainstein, K., Gouzman, I., Girshevitz, O., Bolker, A., Atar, N., Grossman, E., & Sukenik, C. N. (2015). Liquid Phase Deposition of a Space-Durable, Antistatic SnO_2 Coating on Kapton. *ACS Applied Materials & Interfaces*,

7(6), 3539–3546. https://doi.org/10.1021/am5072817

Hassun, H. K., Hussein, B. H., Salman, E. M. T., & Shaban, A. H. (2020). Photoelectric properties of SnO_2: Ag/P–Si heterojunction photodetector. *Energy Reports*, *6*, 46–54. https://doi.org/10.1016/J.EGYR.2019.10.017

Hreid, T., Li, J., Zhang, Y., Spratt, H. J., Wang, H., & Will, G. (2015). Effects of metal ion concentration on electrodeposited CuZnSn film and its application in kesterite Cu_2ZnSnS_4 solar cells. *RSC Adv.*, *5*(80), 65114–65122. https://doi.org/10.1039/C5RA09966H

Jabeen, N., Hussain, A., Elsaeedy, H. I., Rahman, A. U., & Tarique, M. (2023). Unique hierarchical architecture of SnO_2 hexagonal interconnected nanolayered arrays as negative electrode for high performance asymmetric supercapacitors. *Materials Chemistry and Physics*, *303*, 127796. https://doi.org/10.1016/J.MATCHEMPHYS.2023.127796

Jarzebski, Z. M., & Morton, J. P. (1976). Physical Properties of SnO_2 Materials: III . Optical Properties. *Journal of The Electrochemical Society*, *123*(10), 333C-346C. https://doi.org/10.1149/1.2132647

Kafi, F. S. B., Jayathilaka, K. M. D. C., Wijesundera, R. P., & Siripala, W. (2021). Effect of pre-surface treatments on p-Cu_2O/Au Schottky junctions. *Journal of the National Science Foundation of Sri Lanka*. https://doi.org/10.4038/jnsfsr.v49i1.8942

Kafi, F. S. B., Jayathileka, K. M. D. C., Wijesundera, R. P., & Siripala, W. (2019). Improvement of photovoltaic properties of n-Cu_2O/Au Schottky junctions. *Materials Research Express*, *6*(8), 085520. https://doi.org/10.1088/2053-1591/ab20b6

Korösi, L., Papp, S., Meynen, V., Cool, P., Vansant, E. F., & Dékány, I. (2005). Preparation and characterization of SnO_2 nanoparticles of enhanced thermal stability: The effect of phosphoric acid treatment on $SnO_2 \cdot nH_2O$. *Colloids and Surfaces A: Physicochemical and Engineering Aspects*, *268*(1–3), 147–154. https://doi.org/10.1016/J.COLSURFA.2005.05.074

Liu, Y., Koep, E., & Liu, M. (2005). A Highly Sensitive and Fast-Responding SnO_2 Sensor Fabricated by Combustion Chemical Vapor Deposition. *Chemistry of Materials*, *17*(15), 3997–4000. https://doi.org/10.1021/cm050451o

Popescu, A.-M., Mihaiu, S., & Zuca, S. (2002). *Microstructure and Electrochemical Behaviour of some SnO_2-based Inert Electrodes in Aluminium Electrolysis*. *Zeitschrift Für Naturforschung A*, *57*(1–2), 71–75. https://doi.org/doi:10.1515/zna-2002-1-210

Singh, P., & Ravindra, N. M. (2012). Temperature dependence of solar cell performance—an analysis. *Solar Energy Materials and Solar Cells*, *101*, 36–45. https://doi.org/10.1016/J.SOLMAT.2012.02.019

Sundqvist, J., Lu, J., Ottosson, M., & Hårsta, A. (2006). Growth of SnO_2 thin films by atomic layer deposition and chemical vapour deposition: A comparative study. *Thin Solid Films*, *514*(1–2), 63–68. https://doi.org/10.1016/J.TSF.2006.02.031

Supothina, S. (2003). Gas sensing properties of nanocrystalline SnO_2 thin films prepared by liquid flow deposition. *Sensors and Actuators B: Chemical*, *93*(1–3), 526–530. https://doi.org/10.1016/S0925-4005(03)00178-3

Tahir, D., & Tougaard, S. (2012). Electronic and optical properties of Cu, CuO and Cu_2O studied by electron spectroscopy. *Journal of Physics: Condensed Matter*, *24*(17), 175002. https://doi.org/10.1088/0953-8984/24/17/175002

Thejasiri, A., Kafi, F. S. B., Wijesundera, R., & Siripala, W. (2022). Fabrication Of Cuprous Oxide Homojunction Solar Cell By Varying The Lactic Acid Ion Concentration Of Thin Film p-Cu_2O Deposition Bath. *ECS Transactions*, *107*(1), 19543–19550. https://doi.org/10.1149/10701.19543ecst

Thejasiri, S. A. A. B., Jayathilaka, K. M. D. C., Kafi, F. S. B., Kumara, L. S. R., Seo, O., Yasuno, S., Sakata, O., Siripala, W., & Wijesundera, R. P. (2024). Cu_2O Homojunction Solar Cells: Efficiency Enhancement with a High Short Circuit Current. *Coatings*, *14*(8). https://doi.org/10.3390/coatings14080932

Yu, Q., Pan, J., Mei, J., Chen, Z., Wang, P., Wang, P., Wang, J., Song, C., Zheng, Y., & Li, C. (2021). The Cu_2O/CuO/SnO_2 transparent pn junction film device towards photovoltaic enhancement with Cu_2+ self-oxidation transition layer. *Journal of Materials Science*, *56*(9), 5736–5747. https://doi.org/10.1007/s10853-020-05704-1

Yu, Y. T., & Dutta, P. (2011). Examination of Au/SnO_2 core-shell architecture nanoparticle for low temperature gas sensing applications. *Sensors and Actuators B: Chemical*, *157*(2), 444–449. https://doi.org/10.1016/J.SNB.2011.04.088

Zlamalova, M., Mansfeldova, V., Tarabkova, H., Krysova, H., & Kavan, L. (2023). Variable work function of semiconducting thin-film oxide electrodes: a case study of SnO_2 and TiO_2. *Journal of Solid State Electrochemistry*, *27*(7), 1935–1943. https://doi.org/10.1007/s10008-022-05353-1

J.Natn.Sci.Foundation Sri Lanka 2026 54 (3): 347 - 367
DOI: http://dx.doi.org/10.4038/jnsfsr.v54i3.12633

RESEARCH ARTICLE

Environmental Science

Identification of rainfall and water level fluctuations and their relationships in the Kelani River Basin

S Wijesekera[1*], A Dewan[2] and M Khun[2]
[1] *Department of Geography, Faculty of Social Sciences, University of Kelaniya, Kelaniya, Sri Lanka.*
[2] *School of Earth and Planetary Sciences, Curtin University, Bentley, Perth, Australia.*

Submitted: 07 April 2025; Revised: 22 July 2026; Accepted: 21 August 2026

Abstract: The Kelani River Basin (KRB), located in Sri Lanka's wet zone, frequently experiences flooding and is more urbanized and densely populated than other basins. It flows through Colombo, the country's commercial capital, making changes in the KRB highly impactful. To assess recent rainfall and water level fluctuations, daily rainfall data from 10 meteorological stations (1991–2020) were obtained from the Department of Meteorology, while water level data for Hanwella and Nagalagam Street were sourced from the Irrigation Department. Data were homogenized using a mean-based adjustment technique. The modified Mann-Kendall test, Sen's slope, Pearson's correlation, and lag correlation were applied. Extreme rainfall indices PRCPTOT, SDII, R99p, R95p, CWD, RX5day, RX1day were calculated. Results showed a significant increase in annual rainfall over the KRB but a contrasting trend in water levels: decreasing at Hanwella, increasing at Nagalagam Street. Around 40% of stations, especially in the upper KRB, showed decreasing rainfall trends most notably during the Southwest Monsoon. In contrast, the Northeast Monsoon showed increased rainfall in 70% of stations. While rainfall intensity has decreased, frequency and duration have risen. A moderate positive correlation between rainfall and water level suggests additional influencing factors. These findings are vital for sustainable water management in the KRB.

Keywords: Extreme rainfall indices, Kelani River Basin, lag correlation, rainfall, water level,

INTRODUCTION

The global climate is changing and the impact of this on river flow changes is unavoidable (Palmer et al., 2008). At present, most of the major rivers in the world do not show the same magnitudes of fluctuation in their water flows as they did in the past (Palmer et al., 2008). Climate change connects extreme rainfall events and sea level rise, and influences the flow variability of rivers, while some river basins are also under water stress due to increasing population. Due to many parameters, including precipitation, temperature, and solar radiation, the relationship between climate and water is complicated and varies greatly from region to region (Oti et al., 2020). Changing any of these variables can increase or decrease runoff, precipitation, and evaporation rates, thus altering the water cycle.

Studying river flow variability provides valuable background in understanding the interaction between a region's hydrological processes, climate patterns, and environmental systems (Döll & Schmied, 2012; Jain & Singh, 2018). There is significant spatial variation in the discharges of local and regional rivers, due to their complex interaction with climate and other geographical variables (Arnell & Gosling, 2013; Frans et al., 2013).

* Corresponding author (saseeka@kln.ac.lk; https://orcid.org/0000-0002-6409-7601)

This article is published under the Creative Commons CC-BY-ND License (http://creativecommons.org/licenses/by-nd/4.0/). This license permits use, distribution and reproduction, commercial and non-commercial, provided that the original work is properly cited and is not changed in anyway.

However, the results of modelling indicate that changes in discharges into the world's rivers will continue to be driven by climate change and land use and land cover (LULC) (Tao et al., 2014). The average annual flows in nearly half of the world's major river basins are projected to decline, while flows are expected to increase in over 35% of these basins by the mid-21st century (Arnell & Gosling, 2013). Furthermore, Santini and di Paola (2015) have explained that extreme water discharge will decrease in 60% of the major river basins in the northern hemisphere by the end of the 21st century. Accordingly, Jain and Singh (2018) argue that studying river flow variability is paramount for assessing freshwater climate change risks (Jain & Singh, 2018). Hence, many studies have been conducted to assess how climate change impacts river flow variability across the globe. For instance, the study by Hariadi et al. (2023) analysed extreme rainfall and river flow variability in Myanmar, revealing that northern Myanmar will experience longer dry spells in future. In contrast, its east coast will experience more extreme rainfall conditions, which will lead to lower river flows across Myanmar. The study by Rameshwaran et al. (2021) demonstrated that river flow variability across West Africa, particularly in the Sahelian region, will increase due to climate change. Martins et al. (2016) studied the impact of rainfall and land cover on river flow changes in the Ivai River Basin of Brazil. They found that river flows change mainly due to land cover changes. Furthermore, a study by Manawadu and Wijeratne (2021) showed that human activities are major contributors to the complex patterns of river flow variability.

In the Sri Lankan context, the scholarly work of Imbulana et al. (2018), Ampitiyawatta and Guo (2009), Khaniya et al. (2019), Panditharathne et al. (2022), and Alahacoon and Edirisinghe (2021) assessed the complex interactions between rainfall and river flow variability in the nation's different watersheds. As the fourth largest watershed on the island, the Kelani River Basin (KRB) covers a significant portion of the country's western and central hill regions (Jayasekara et al., 2020). Socioeconomically, the basin is much more important than other basins in the island, as it surrounds critical urban and industrial centres like Colombo, Sri Lanka's commercial centre and capital city (Manawadu & Wijeratne, 2021). The KRB is home to more than 20% of the Sri Lankan population (Mahagamage & Manage, 2018). High population density exerts enormous pressure on the basin's water resources, sanitation processes, and infrastructure development (Manawadu & Wijeratne, 2021; Samarasinghe et al., 2022). Randil et al. (2022) stressed that the basin is vulnerable to annual flooding. Therefore, plenty of studies have been carried out in the KRB to analyse floods (De Silva et al., 2012; Samarasinghe et al., 2022; Wijetunge & Neluwala, 2023), human activities (Manawadu & Wijeratne, 2021; Wijeratne & Li, 2022), rainfall (Dissanayaka & Rajapakse, 2019; Perera et al., 2022), and so on. However, given the changing climatic conditions, it is clear that there is a compelling need to examine the link between rainfall and water level dynamics in the KRB. Jayasekara et al. (2020) discussed in depth the relationship between rainfall and stream flow variability in the KRB between 1983 and 2013. They found that rainfall variation is significantly attributable to catchment streamflow. Further, most studies (Dissanayaka & Rajapakse, 2018; Jayasekara et al., 2020; Samarasinghe et al., 2022) revealed that the average rainfall over the basin is decreasing in past decades. However, the climate and the environment are changing day by day. The study by Samarasinghe et al. (2022) explained that increased flood intensities and land use changes in the KRB had significantly contributed to the severity of flooding. Hence, it should be confirmed that the rainfall over the KRB has changed over the past decades. Also, there should be more studies to investigate whether current fluctuations in rainfall in the KRB are continuing to affect streamflow patterns, or whether there are significant changes in this relationship.

MATERIALS AND METHODS

Study area

The Kelani River Basin (KRB) is a region of great ecological and socioeconomic significance. The basin covers a vast area of about 2230 km^2 and stretches from the central highland to the coastal plains (Figure 1). The KRB lies between northern latitudes 6^0 47' and 7^0 05' and between eastern longitudes of 79^0 52' and 80^0 13', with a mean altitude of between 1.8 m and 2300 m above sea level (Samarasinghe et al., 2022). The Kelani River originates in the peak wilderness sanctuary of the central hills. It provides vital freshwater to a large population through its tributaries, which make it the primary local source of drinking water, irrigation, and hydropower. It meanders through lush forests, picturesque landscapes, and urban areas, before finally discharging into the Indian Ocean close to the commercial city of Colombo. The whole KRB is situated in the wet zone of the country. Centred on the Hanwella hydrology station, the KRB is divided into two main parts, the lower KRB (LKRB) and upper KRB (UKRB) (Samarasinghe et al., 2022). The lower KRB is highly urbanised, while the upper areas have dense vegetation. The rainfall distribution across the catchment

varies, with the upper catchment receiving an average annual rainfall of around 5700 mm, while the lower basin receives approximately 2300 mm (Hettiarachchi, 2016). This rainfall corresponds to an approximately 7860 X 10^6 water volume, of which 43% is discharged into the Indian Ocean. The basin receives its highest rainfall during the SWM. During the monsoon season, streamflow varies between 600 and 1800 m^3/s along the river's length (Dissanayaka & Rajapakse, 2019).

Data

Rainfall data

The study used rainfall data from 1991 to 2020 from the Department of Meteorology of Sri Lanka for ten stations spread over the KRB (Table 1). These stations had less than 2% missing data, which was essential for this study. Azman et al. (2021) have suggested that inverse distance

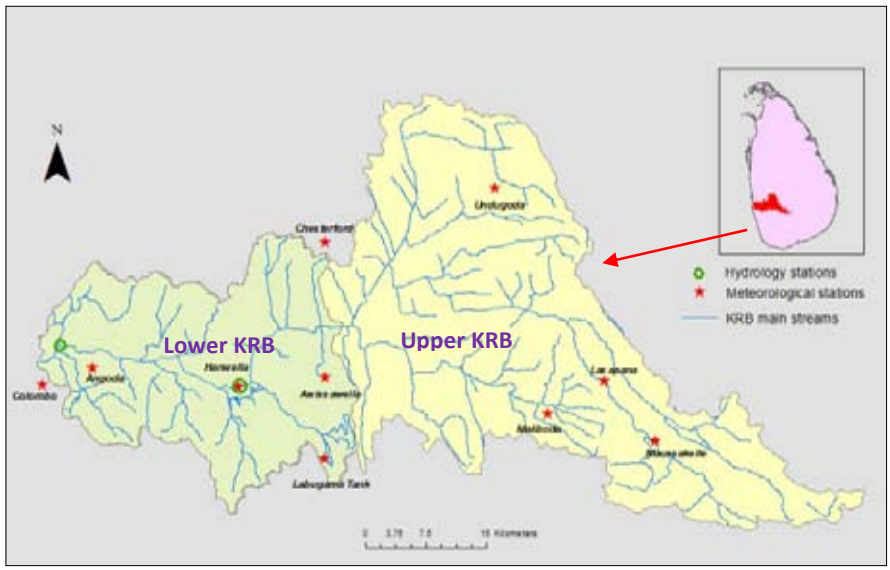

Figure 1: The KRB with meteorology and hydrological stations

Table 1: Rainfall stations and hydrology stations in the KRB

No	Station name	Latitude (⁰)	Longitude (⁰)	Elevation (m)
Meteorology stations				
1	Awissawella Estate	6.92	80.18	229
2	Chesterford	7.07	80.18	198
3	Hanwella Group	6.88	80.12	82
4	Labugama Tank	6.83	80.18	172
5	Laxapana	6.90	80.52	1105
6	Maliboda	6.88	80.43	274
7	Maussakelle	6.85	80.55	1195
8	Undugoda	7.13	80.37	332
9	Angoda Hospital	6.93	79.92	15
10	Colombo	6.90	79.87	7
Hydrology stations				
1	Hanwella Station	6.91	80.08	17
2	Nagalagam Street	6.98	79.88	7

weighted (IDW) is the best method to estimate missing rainfall values because it has minimum root mean square error (RMSE) and mean absolute error (MAE) values. Hence, this study used the IDW method to estimate the missing rainfall values.

Discharge and water level data

The study used water level data from 1991 to 2020 from Hanwella and Nagalagam Street (N'Street) hydrological stations (Table 1), provided by the Irrigation Department of Sri Lanka. The reason for choosing these two stations was that they are located in the lower river basin area, which has a high population density and is most vulnerable to flood hazards. Dushyantha and Ptuhina (2020) found that these two stations are at high risk of being inundated due to heavy rainfall. The Hanwella hydrology station is located approximately 25 km from the sea, whereas the N'Street station is situated nearly 2 km from the coast.

Methods

Processing rainfall and water level data

Non-climatic factors such as changes in station location or data processing methods can introduce artificial shifts in climatic time-series (Costa & Soares, 2009). To address this, the RHtestsV4 and RHtests_dlyPrcp packages in R were used for homogeneity testing and adjustment of daily water level and rainfall data (R-Core-Team, 2013). These tools apply a Box-Cox transformation and penalised maximal F test to account for non-normal distributions (Wang et al., 2010), followed by mean-based adjustments for homogenisation.

Extreme precipitation indices

This study examined extreme rainfall over Sri Lanka. For this purpose, this research used nine extreme precipitation indices (Table 2) to identify extreme precipitation over the island, defined by the expert team on climate change detection indices (ETCCDI) of the WMO (2020).

Table 2: List of indices used in this study (after ETCCDI, 2012)

Index	Name	Description	Unit
RX5day	Wettest 5-day period	Monthly maximum consecutive 5-day precipitation.	mm/year
RX1day	Wettest day	Monthly maximum 1-day precipitation.	mm/year
R99p	Rainfall on Extremely wet days	Annual total precipitation when daily rainfall amount on a wet day > 99 percentile.	mm/year
R95p	Rainfall on very wet days	Annual total precipitation when daily rainfall amount on a wet day > 95 percentile.	mm/year
SDII	Average daily Rainfall Intensity	Annual total precipitation divided by the number of wet days (mm/day) in the year. Wet days are defined as precipitation ≥ 1.0 mm.	mm/days/year
PRCPTOT	Total precipitation	Annual total precipitation in wet days (precipitation ≥ 1 mm).	mm/year
CWD	Consecutive wet days	Annual count of maximum number of consecutive days when daily precipitation exceeds at least 1 mm (R ≥ 1 mm).	days/year

SDII and PRCPTOT indices provide average and total values, respectively, while the other five indices identify extreme events.

Statistical techniques

Mann-Kendall (MK) test and modified Mann-Kendall (MMK) test

This study used MK and MMK tests to identify the trends in rainfall and water level data. The non-parametric MK test is widely applied in the analysis of trends in precipitation indices (Alahacoon & Edirisinghe, 2021; Jiang et al., 2019). The MK test (Kendall, 1962; Mann, 1945) is based on a nonparametric approach that searches for monotonic changes over time without necessarily assuming their statistical distribution.

However, serial correlation, very often found in hydro-climatic time-series, is not considered by the MK test (Hamed & Rao, 1998). When there is a serial correlation in a dataset, it increases the probability of

finding significant trends even if they don't exist, which may lead to a misleading interpretation of results. Hamed and Rao (1998) propose the MMK method to avoid serial correlation in hydro-climatic datasets. In the presence of autocorrelation, this methodology is strong and relies on modified variations of the MK test (Hamed & Rao, 1998). To compensate for the effects of serial correlation on variance, the modified variance should be calculated using an effective sample size (Hamed & Rao, 1998).

Sen's slope estimator

The MK test shows only the direction of a trend but does not quantify its magnitude. Therefore, the nonparametric Sen's slope (Sen, 1968) is used to determine the magnitude of an underlying trend. This test is recommended by WMO (2018) for detecting trends in hydro-meteorological data. In this study, Sen's slope value was calculated to detecting the magnitude of the rainfall and water level trend.

Pearson's correlation coefficient

The Pearson's correlation coefficient is used to determine the relationship that exists between two variables and it is used when both variables being studied are normally distributed (Mukaka, 2012).

Lag correlation

Lag correlation (also known as cross-correlation with lag) is a statistical method used to determine the relationship between two time series where one series is shifted forward or backward in time. It's especially useful in hydrology, climatology, and economics to detect delayed responses between variables. If we use X-values from earlier periods to explain present Y-values, then a lag correlation should be used for the two different time-series (Good data, 2023).

RESULTS AND DISCUSSION

Detecting long-term trends in rainfall and water level in the KRB during the period 1991 to 2020

The current study carried out an important analysis of overall trends for rainfall distribution and water level fluctuations in the KRB as a preliminary phase. In this first effort, a calculation of the total annual and seasonal rainfall was carried out for the ten meteorological stations. Subsequently, as illustrated in Figure 2 and Figure 3, the resulting total values have been used to calculate the annual average and seasonal average rainfall in the KRB.

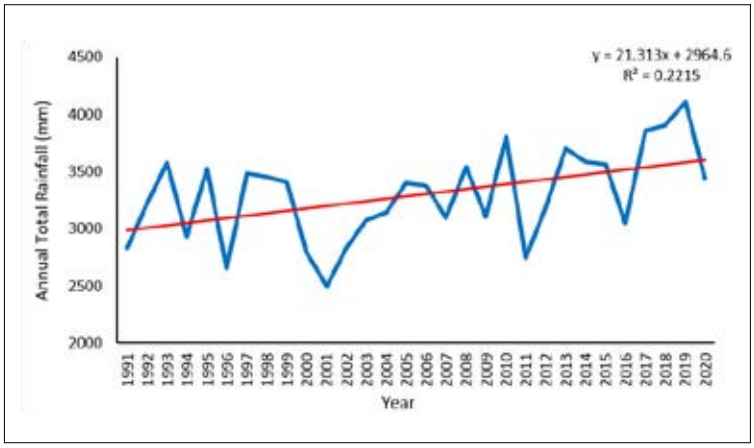

Figure 2: Annual total rainfall of the KRB (at 95% confidence level)

Figure 2 clearly displays that annual total rainfall had a gradual increase from 1991 to 2020. Upon initial examination, it was apparent that annual precipitation patterns vary from year to year. The lowest annual total rainfall occurred in the year 2001 with a value of 2494.2 mm, while the highest value was reported in 2019, reaching 4108.9 mm. The inherent dynamism of the rainfall levels is underlined by this very wide range in annual variability. The variability indicates that the region has experienced both dry and wet years, which

is typical of many climate systems. As for the overall temporal trend, it appears that, from the early 1990s to the early 2000s, there was a period of decreasing precipitation, followed by increases in the period from the late 2000s to the early 2020s. There was a very high annual total precipitation of 4108.9 mm in 2019, which is considered to be an extreme year. It's possible this was due to a particularly wet year. On the other hand, 2001 is a year with significantly lower precipitation, 2494.2 mm, suggesting a dry year. The last few years, such as 2017 to 2020, appear to have had more precipitation than is typical.

The seasonal behaviour of rainfall also showed interesting patterns between 1991 and 2020 (Figure 3).

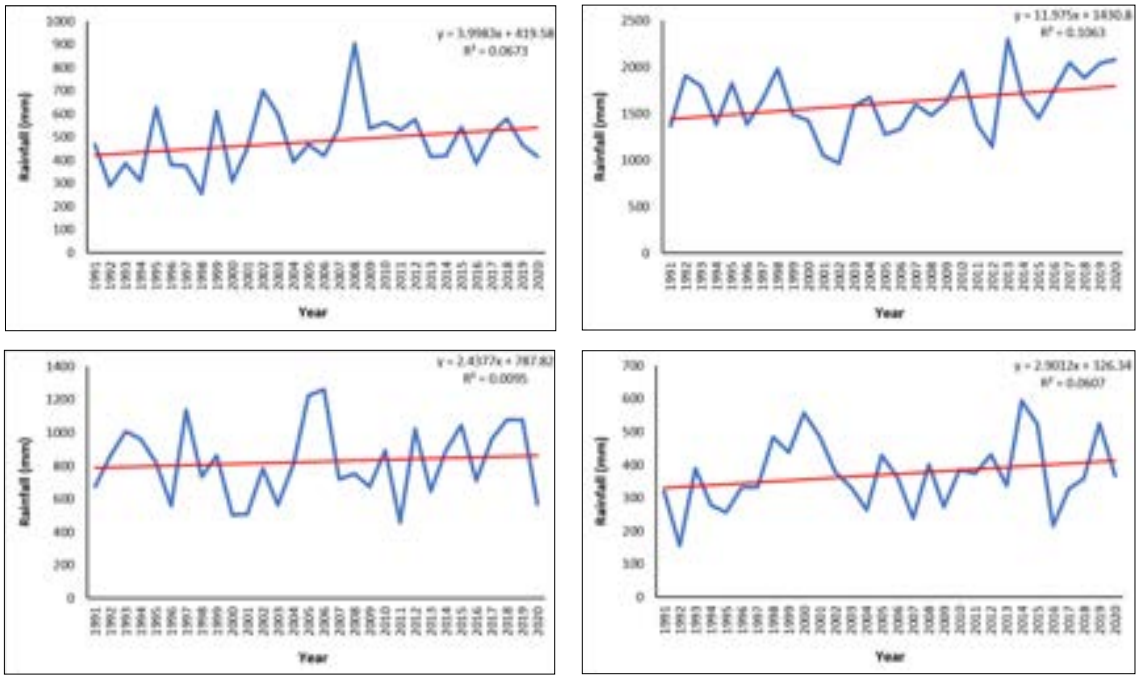

Figure 3: Seasonal rainfall in the KRB. Note:(a) IM1; (b) SWM; (c) IM2; (d) NEM (at 95% confidence level).

Upon initial examination, a clear upward trend can be observed in the amount of precipitation across all seasons. Focusing on Figure 3 (a) as characteristic of the IM1 season, year-to-year variability is noted in common rainfall amounts. Examining temporal trends, the study observed several fluctuations over time. For instance, in the years 1991 to 2002, there was a significant increase in IM1 rainfall, with notable fluctuations between 1995 and 2002. Overall, rainfall during IM1 has been decreasing steadily since 2002, with occasional peaks and troughs. This shows that rainfall patterns in the IM1 have changed during this period. The year 2008 is an outlier, with exceptionally high IM1 precipitation of 903.66 mm, whilst the lowest rainfall was 254.23 mm, in 1998. Figure 3 (b) illustrates the SWM rainfall pattern during the study period. Looking at temporal trends, SWM rainfall has been fluctuating over time. A strong linear trend is not apparent, but there are periods in which more or less rainfall can be observed. For instance, the incidence of high rainfalls in 1992, 1998, and 2010 is noted, while 2001 and 2012 were characterised by low precipitation. Exceptionally high SWM rainfalls of 2298.41 mm in 2013 and 2082.49 mm in 2020 are noted as extremes. Conversely, 2002 recorded the lowest SWM rainfall (967.01 mm). Figure 3 (c) depicts the total rainfall amount in the IM2. The fluctuations in IM2 rainfall can be observed by examining time patterns. The exceptional rainfall of 1225.30 mm in 2005 and 1260.25 mm in 2006 represent some remarkable extremes. On the other hand, the lowest IM2 rainfalls of 455.59 mm were observed in 2011. Figure 3 (d) shows the total rainfall pattern for the NEM season for the 1991 to 2020 period

considered. Due to the transitional and variable nature of NEM seasons, there is a significant difference in annual rainfall totals between years. In the catchment area of the KRB, this season is linked to the lowest rainfall amounts. However, high total rainfalls in 2014 (593.14 mm) and 2015 (523.04 mm) were among the most significant extremes. By contrast, NEM rainfall was at an all-time low of 214.55 mm in 2016. As this study is about the relationship between rainfall and water level in the KRB, the general pattern of water levels at the Hanwella and N'Street hydrology stations was also studied.

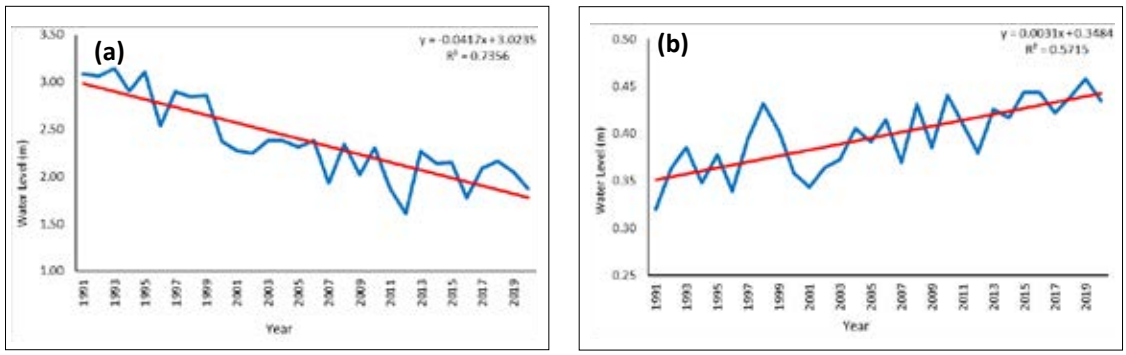

Figure 4: Water level at hydrology station. Note: (a) Hanwella and (b) N'Street stations.

An interesting observation can be made about the levels of water recorded at Hanwella and N'Street hydrology stations. During the period between 1991 and 2020, there has been a decline in water levels at the Hanwella hydrographic station (Figure 4 (a)), whereas N'Street hydrographic station shows an increasing trend Figure 4 (b). The seasonal pattern also provides a clear picture of water level changes in the KRB (Figure 5).

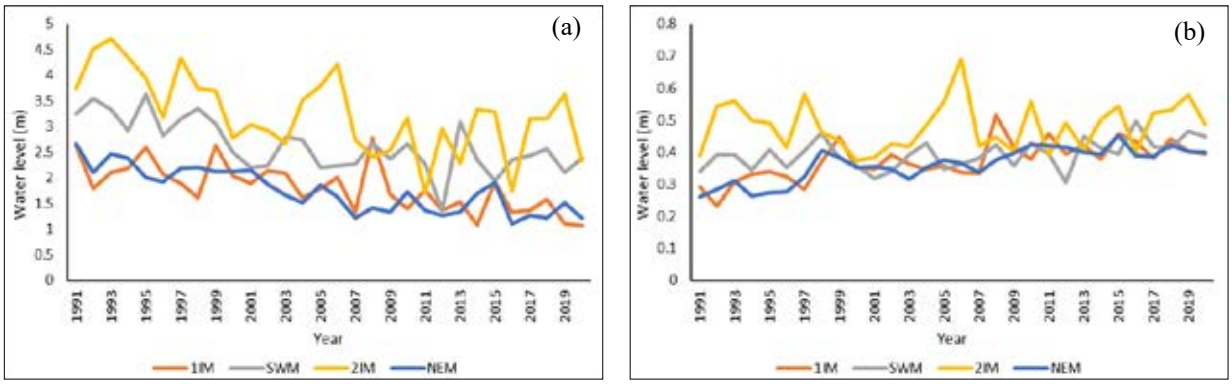

Figure 5: Seasonal water level. Note: (a) Hanwell (b) N'Street stations

In all seasons, Hanwella station shows a decreasing trend while N'Street has an increasing trend. For Hanwella station, the highest water levels are observed in the IM2 season, from October to November, which is associated with heavy rainfall convection currents. The second highest water levels are observed in the SWM season, from May to September. This corresponds to a period of heavy rainfall in Sri Lanka associated with the SWM. Even though during the SWM season the general pattern of water levels shows a decreasing trend, after 2015 there is an increasing trend towards 2020. Conversely, the lowest water levels have been recorded during the NEM season, which is consistent with the drier weather conditions which are characteristic of NEM due to

the orography of the island. The IM1 season displays intermediate water levels, which are characterised by the development of transitional weather patterns between major monsoon seasons. The water level variation is comparatively high among the seasons. The N'Street station also has its highest water levels in the IM2 and second-highest during the SWM season. The lowest levels were recorded in the NEM and IM1 periods. However, variations between the water levels in climate seasons were minimal during the study period.

After identifying the general pattern of rainfall and water level in the KRB, the MMK test and Sen's slope were used to identify trends in these two variables. The MMK results indicate that the basin had a significant increasing (Z-value 5.36, P-value of 0.05) trend over the study period. Figure 6 depicts the MMK Z-values for rainfall at meteorological stations.

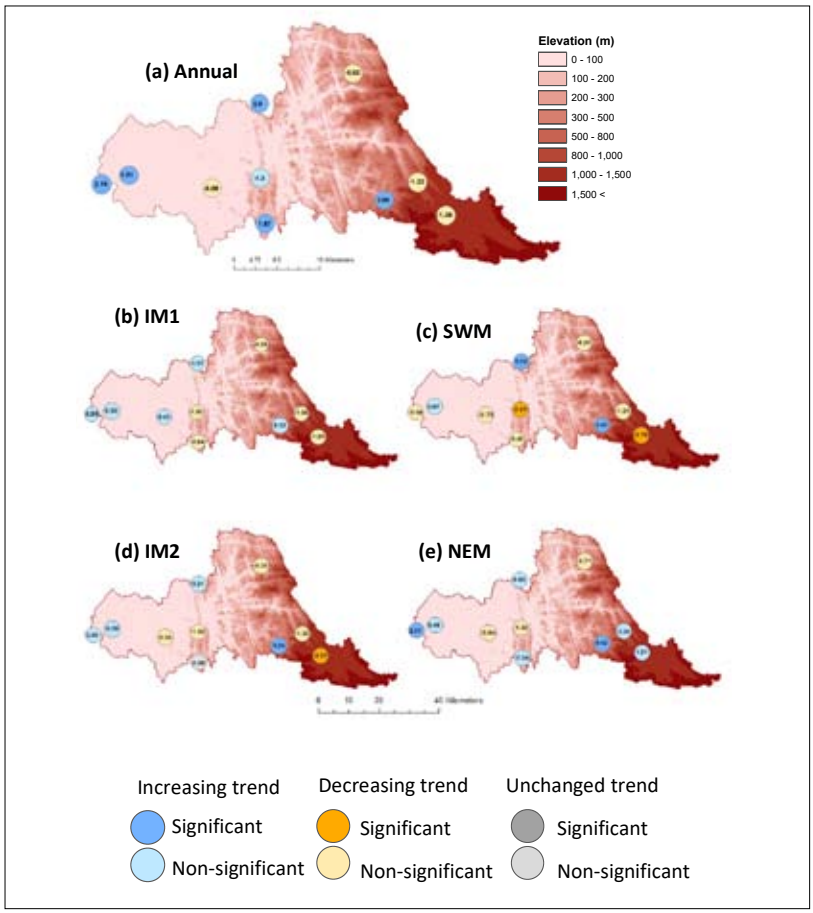

Figure 6: Rainfall trends in the KRB. Note: The values generated at 95% confidence level.

According to the MMK results, 60% of the meteorological stations show an increasing trend in the 1991 to 2020 period (Figure 6 (a)). Colombo, Angoda, Chesterford, Labugama Tank, and Maliboda stations show a significant increasing trend. Out of the other four stations, three stations (Undugoda, Laxapana, and Maussakelle) in the more elevated areas show a decreasing trend.

During the IM1 period (Figure 6 (b)), Colombo, Angoda, Maliboda, Chesterford, and Hanwella meteorological stations show an increasing but not significant trend. Further, stations in more elevated areas (except Maliboda) show a decreasing trend. During the SWM season (Figure 6 (c)), 70% of the meteorological stations showed a decreasing trend. Among the stations with

decreasing trends, Awissawella, and Maussakelle show a significant decrease trend (P-values of 0.0269 and 0.0295 respectively). The highest increasing trend belongs to the Maliboda meteorological station, with a P-value of 0.00. Chesterford Meteorological Station also has a significant increasing trend in rainfall (P-value of 0.0034). During the IM2 season (Figure 6 (d)), 50% of the meteorological stations showed a decreasing trend, with Maussakelle having a significant P-value (0.04). During this season, the Maliboda meteorological station showed the highest significant increasing trend (P-value of 0). It is notable that the Labugama Tank station had an unchanged trend during this season, from 1991 to 2020. During the NEM season (Figure 6 (e)), 70% of the meteorological stations had an increasing trend. Colombo and Maliboda meteorological stations had a prominent increasing trend, with P-values of 0.0385 and 0, respectively. Hanwella, Awissawella, and Udugoda stations showed a decreasing trend. Even though Colombo, Labugama Tank, Maussakelle, and Laxapana meteorological stations showed an increasing trend during NEM, the picture was different during the SWM season. Accordingly, trends in water levels at Hanwella and N'Street stations are shown in Table 3.

Table 3: Trends in water level in the KRB. Note: Values generated at 95% confidence level.

1991-2020 period	Annual		1IM		SWM		2IM		NEM	
	Z-value	Sen's Slope	Z-value	Sen's Slope	Z-value	Sen's Slope	Z-value	Sen's Slope	Z-value	Sen's Slope
Hanwella Station	-7.52*	-0.04	-15.65	-0.04	-5.67*	-0.04	-6.5*	-0.05	-9.03*	-0.04
N'Street Station	13.27*	0.00	9*	0.00	5.26*	0.00	1.58	0.00	8.21*	0.00

*Denotes significant trends.

The annual trend in both these hydrological stations shows a completely different direction during the study period. The water level at Hanwella station shows a significant decrease, while N'Street station shows a significant increase. During all four seasons, Hanwella hydrology station has a decreasing trend. Among all four seasons, only the IM1 shows a non-significant decreasing trend, at Hanwella. For N'Street hydrology station, all four seasons show an increasing trend. Remarkably, during the IM2 season, the station had a non-significant increasing trend while other three seasons had significant increasing trend.

Extreme rainfall in the KRB

In order to identify the extreme rainfall over the basin, extremes precipitation indices, including R99p, R95p, RX5day, PRCPTOT, CWD and SDII were calculated based on daily rainfall data of the ten meteorological stations. To evaluate the intensity and variability of extreme rainfall events within an area, the calculation of these extreme rainfall indices has served as a comprehensive measure. The general pattern of extreme rainfall events in the KRB is illustrated in Figure 7.

The general pattern of extreme rainfall over the basin shows that, contrasting with other indices, there is a reduction in the intensity of extreme rainfall. Also, from 1993 to 2001 a general decline in extreme rainfall is observed in all the indices. Except for the SDII, all indices have shown an increasing trend since 2001. It revealed that, although with lower intensity, increased incidents of extreme rainfall events are expected in the basin.

After calculating extreme rainfall indices, the MK and Sen's Slope tests were employed to identify the trends in extreme rainfall indices (Table 4).

In the analysis of extreme rainfall patterns in the KRB, a discernible trend of overall increase is evident across all averages of indices except SDII. Notably, the Maliboda station shows a significant increase in extreme rainfall. Contrariwise, the Avissawella station portrays a significant decreasing trend.

When focusing on the monthly maximum 5-day precipitation (RX5day) index, 70% of stations exhibit a decreasing trend. The Avissawella and Maussakelle stations have a significant decreasing trend with Sen's slope values of -2.05 and -1.24, respectively. Chesterford, Colombo, and Maliboda stations show an increasing trend. Among these three stations, Maliboda exhibits a significant trend (Sen's slope value is 8.13). The average values of RX5day indicate an increasing trend.

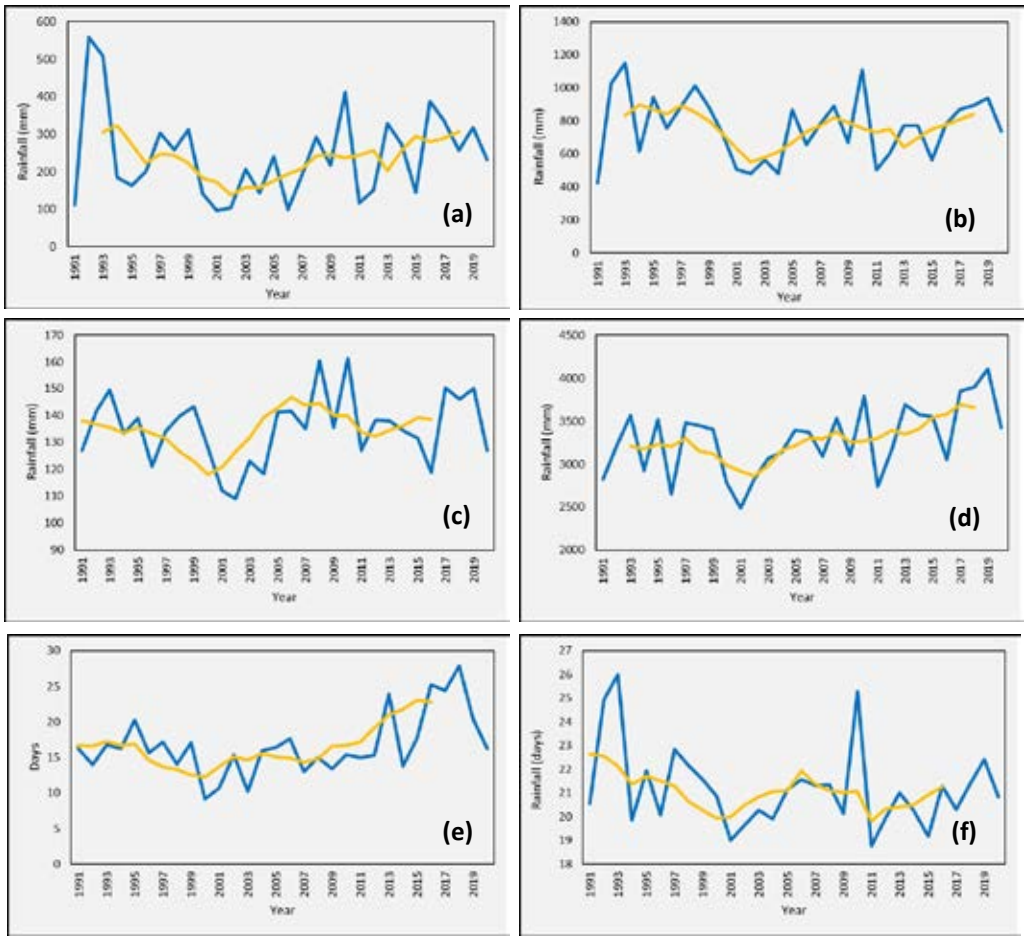

Figure 7: General pattern of extreme rainfall in the KRB (95% confidence level). Note: (a) R99p, (b) R95p, (c) RX5day, (d) PRCPTOT, (e) CWD, and (f) SDII. Blue line indicates average extreme values and yellow line indicates five year moving average values

Table 4: Trends in extreme rainfall over the KRB. Note: These MK Z values generated at 95% confidence level and * presents significant trends.

Met stations	RX5day	R95p	R99p	PRCPTOT	CWD	SDII
Angoda	-0.57	-0.75	1.69	0.71	0.90	-3.57*
Avissawella	-3.89*	-2.82*	-3.14*	-2.85*	-0.32	-3.32*
Chesterford	1.21	0.78	0.34	2.66*	3.13*	-0.09
Colombo	0.14	-0.07	0.62	0.14	0.47	0.14
Hanwella	-1.39	-1.50	-0.84	-0.43	0.43	0.54
Labugama	-0.71	-0.64	-0.47	-0.43	-0.23	-1.37
Laxapana	-1.71	-0.64	-0.36	-1.82	-1.50	-1.04
Maliboda	5.82*	4.69*	3.42*	6.60*	6.00*	3.53*
Maussakelle	-2.36*	-1.64	-0.81	-2.78*	-1.15	-2.79*
Undugoda	-1.00	0.57	1.23	-0.54	-0.45	-1.64
Average of indices	0.68	0.01	0.89	2.39*	1.52	-0.75

The heavy rainfall (R95p) in the basin also shows an increasing trend (with the lowest increasing trend found in the average value) during the study period. However, only three stations (Undugoda, Maliboda, and Chesterford) have an increasing trend. The Maliboda station has a significant trend with Sen's slope value of 0.15. Further, all 70% of other stations show a decreasing trend in R95p. The extreme rainfall in the basin (R99p) is also on the rise. Fifty percent of stations (Angoda, Chesterford, Colombo, Maliboda, and Undugoda) indicate an increasing trend. Regarding the decreasing trend, the Avissawella station stands out with a significant trend having Sen's slope value of -11.4. It is ascertained that the increasing trend of R99p leads to more extreme rainfall-related hazards in the basin.

The annual total precipitation on wet days (PRCPTOT) presents a significantly increasing trend in the basin for the average value (Z-value of 2.39, Sen's slope value of 21.02). This marks the highest increasing value among any average index value in the basin. However, 60% of stations indicate an increasing trend, with the Avissawella and Maussakelle trends being significant (Sen's slope value of -44.76 and -29.69, respectively). On the other hand, Chesterford and Maliboda stations exhibit a significant increasing trend (Sen's slope value of 35.22 and 286.71). The average CWD index value also increases in the KRB. Fifty percent of stations show an increasing trend from the CWD index. Among them, Chesterford and Maliboda stations display a significant increasing trend (Sen's slope value of 0.71 and 1, respectively). The other five stations with decreasing trends do not have any significant value. Nevertheless, an increasing trend in the CWD index signals flood hazards in the KRB. When focusing on the SDII index, the basin exhibits a decreasing trend, though it is not significant (Sen's slope value of -0.26). The Maliboda station is the only station having a significant increasing trend (Sen's slope value of 0.53). Angoda, Avissawella, and Maussakelle stations have a significant decreasing trend (Sen's slope value of -0.25, -0.21, and -0.14, respectively). In general, 70% of the stations show a decreasing pattern.

Relationship between rainfall and water levels in the KRB

When considering the relationship between rainfall and water levels in the basin, as its first step this study calculated correlation coefficients for these two variables on a daily basis. The correlation coefficient value for daily rainfall and water level at Hanwella station is 0.42, a moderately positive relationship. On the other hand, the coefficient value for N'Street is 0.36, a weakly positive correlation (with a 95% confidence interval). Subsequently, the monthly relations between rainfall and water level in the KRB were considered. According to Figure 8, it is apparent that the increase in rainfall has led to increased water levels, a positive correlation between water levels in the KRB and precipitation.

During the Southwest Monsoon (IM2) season, where strong winds with widespread rain affect the whole island, the peak of water level and precipitation is discernible in the months of October and November. The correlation between seasonal average water level and rainfall during the IM2 is 0.63 (Hanwella station) and 0.88 (N'Street station), the highest among all four seasons, with a 95% confidence level.

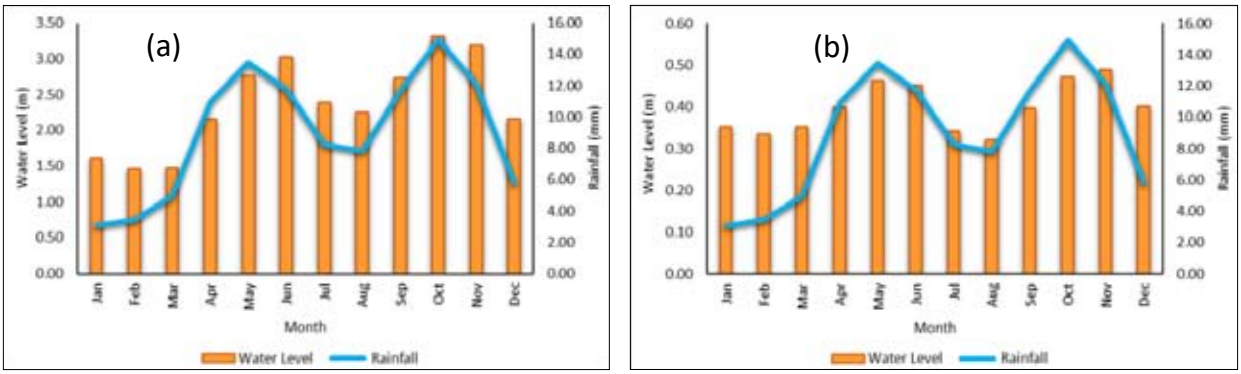

Figure 8: Monthly water levels and rainfall in the KRB from 1991 to 2020.

After the IM2, the first phase of SWM (May and June) shows the second-highest peaks in rainfall and water discharge/water level. In the SWM period, there is a 0.41 and 0.81 correlation between rainfall and water discharge in Hanwella and N'Street stations respectively. This correlation value is 0.16 (Hanwella) and 0.48 (N'Street) during NEM, the lowest of the four seasons. During the IM1, 0.34 and 0.6 correlation is seen at Hanwella and N'Street stations respectively, with a 5% significance level. Even though the correlation shows a moderate to high positive correlation between water levels and rainfall, season-wise, it shows a strong positive correlation. Further, the study examined the relationship between monthly rainfall and water levels.

As mentioned above, an analysis of daily rainfall and water levels in the KRB shows a moderately positive correlation. Nevertheless, the monthly relationship between these two variables shown in Figure 9 and 10 demonstrate a fascinating pattern. It is generally a positive relationship throughout the year, except for January. During the month of January, the N'Street station showed a negative correlation of 0.03 (Figure 9 (b)), with a 95% confidence level, while the Hanwella station showed a moderately positive correlation (0.49). Nevertheless, the monthly correlation coefficient varies between moderately positive (0.4) and highly positive (0.9) for the remaining months at N'Street station. On the other hand, correlation coefficients ranged from 0.3 to 0.83 at Hanwella station, indicating a variation between low and high positive correlations throughout the year. The month of May has a nearly perfect relationship at both stations (Figure 9 (i) and (j)). Also, the highest positive coefficient values belong to the month of May, 0.83 and 0.9 for Hanwella and N'Street stations, respectively. In particular, the strong relationship observed in Figure 4.14 for the relevant months is apparent between the SWM and IM2 seasons. Both stations indicate that the relationship of water level to rainfall approaches a near-perfect relationship (Figure 9 (k), (l), and Figure 10 (a), (b), (f), (h), (i), (j)) in the months of June, July, September, and November. During these months, the correlation coefficients for Hanwella station were 0.63, 0.76, 0.75, and 0.64, respectively. Correlation coefficients of 0.71, 0.76, 0.87, and 0.81 were observed at N'Street station in the same months. This detailed analysis shows the complex monthly and seasonal dynamic of the correlation between rainfall and water levels in the KRB, which is essential for information management and planning regarding water resources.

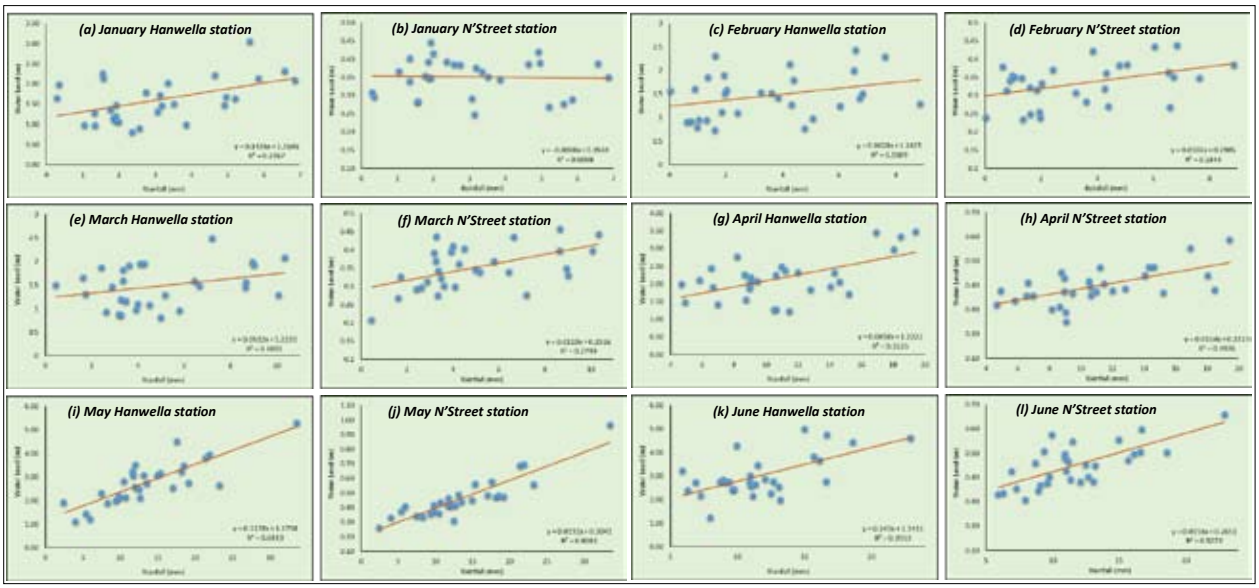

Figure 9: Relationship between rainfall and water level in the KRB on a monthly scale.

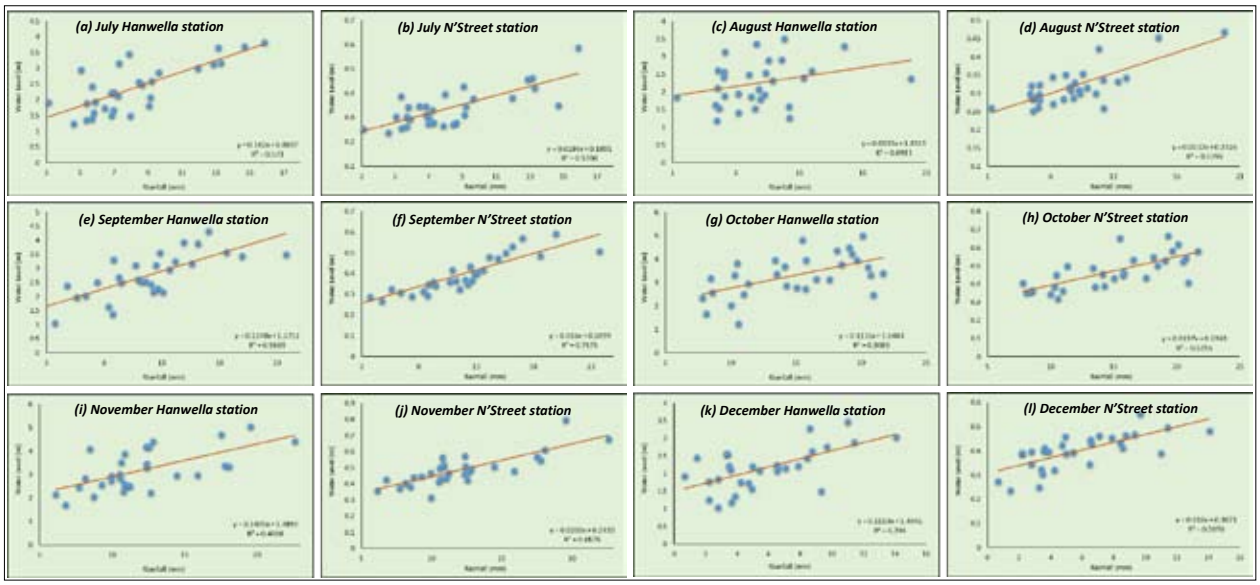

Figure 10: Relationship between rainfall and water level in the KRB on a monthly scale.

As its next step, this study tried to identify when rainfall increases will be in sync with water levels at different time lags. The study used lag correlation for this task. Figures 11 and 12 illustrate a scatter plot for the lag correlation over 10 days. The study used a 10-day period for lag correlation because when floods occur in the basin their effects remain for at least 7-10 days.

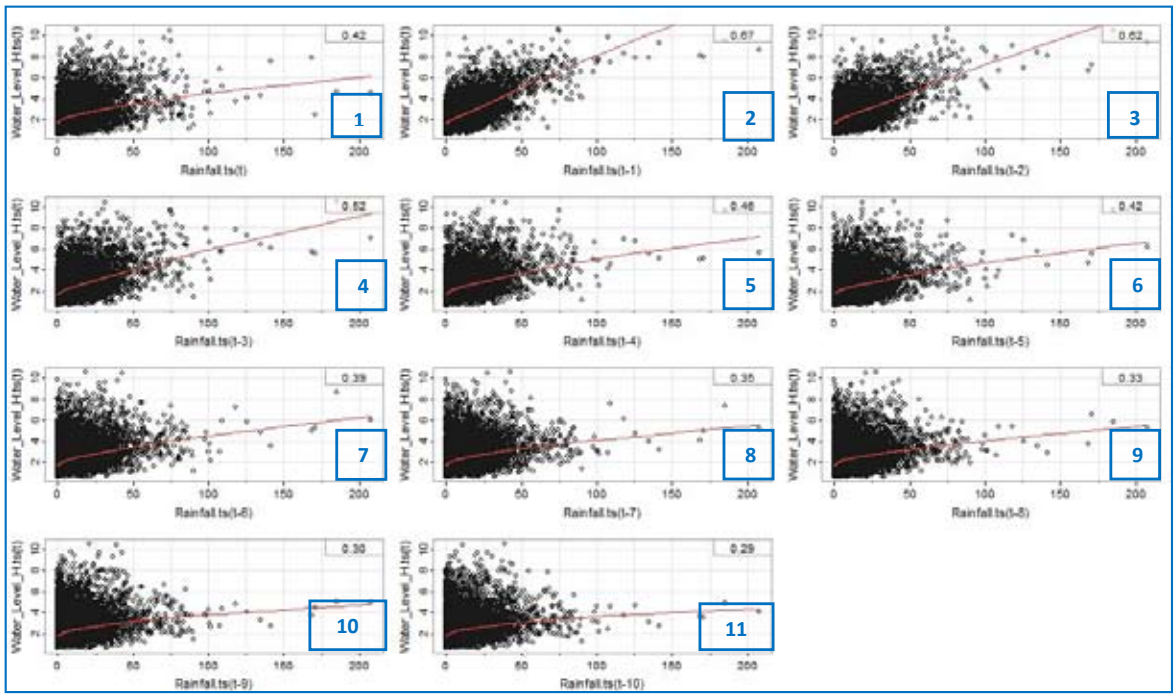

Figure 11: Lag effect between rainfall and water levels at Hanwella hydrology station (at 95% confidence level)

The lag correlation analysis shows that the station at Hanwella (Figure 11) exhibits a moderate positive correlation of 0.42 during the initial interval. Subsequently, the correlation increases in the second lag interval and gradually decreases from the second to the eleventh lag. In particular, there were notably high positive correlation coefficients of 0.65, 0.62, and 0.52 for the second, third, and fourth lags. This positive correlation indicates that, after a certain period of time, an increase in rainfall in the Kelani River Basin is accompanied by an increase in water levels. Such correlation patterns can be observed in the lag analysis for N'Street station shown in Figure 12. A moderately positive correlation is shown for the first lag of the N'Street station, though with a slightly lower coefficient of 0.36 than for the first lag correlation of the Hanwella station. N'Street, on the other hand, shows a strong positive correlation, with coefficients of 0.61, 0.62, and 0.51 in the second, third, and fourth lags, similarly to Hanwella. It should be noted that there are certain differences between these two stations' lag correlation patterns, mainly regarding the lags where a higher correlation coefficient was recorded. In particular, the Hanwella station has the highest lag correlation in the second lag, while the N'Street station has the highest lag correlation in the third lag. These findings provide insight into the temporal dynamics of rainfall and water levels at these two hydrological stations in the KRB. The lag correlation clearly illustrated that, when rainfall is high, it is linked with water level increases in the basin which is useful for understanding extreme rainfall related flooding.

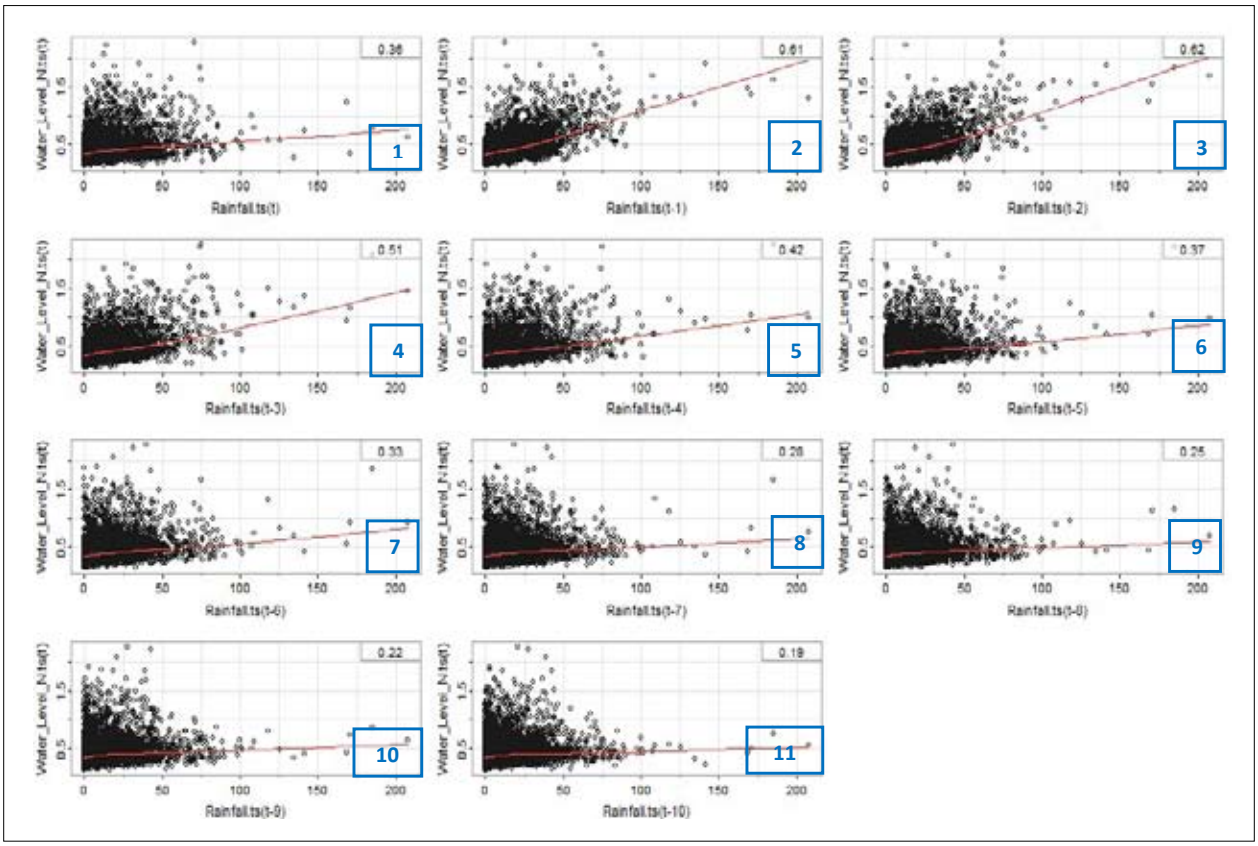

Figure 12: Lag effect between rainfall and water level at N'Street hydrology station (at 95% confidence level)

According to the results, it is clearly visible that there is a positive relationship between rainfall and water levels in the KRB. There is thus a high tendency toward flood hazards with extreme rainfall over the basin.

However, evidence suggests that climate change has altered the spatiotemporal characteristics of rainfall, including total magnitude and seasonal dispersal (Feng et al., 2013). Also, the United Nations Office for Disaster Risk Reduction and World Meteorological Organization (2023) projects that extreme rainfall events will escalate threefold with a temperature increase of 2°C. In this scenario, Sri Lankan river basins would be highly vulnerable to floods, especially in the wet zone. Nevertheless, there should be a detailed examination of the relationship between rainfall and water levels in river basins in Sri Lanka.

Rainfall acts as one of the critical factors influencing the increase of river water levels. The amount of rainfall directly influences the volume of water that flows across a river basin and causes flooding when extreme rainfall occurs. Accordingly, this study chose KRB to examine rainfall and water levels and the relationship between them. The findings indicate noteworthy outcomes, which are discussed in the following discussion.

Overall, the KRB has a significantly increasing trend in annual total rainfall, which is not in line with the study by Jayasekara et al. (2020) that shows a decreasing rainfall trend in the KRB from 1983 to 2013. Similarly, the study of Ampitiyawatta and Guo (2009) found that the Kalu River basin in the wet zone showed a decreasing rainfall trend. These two studies discussed the rainfall pattern in river basins in the wet zone over a decade ago. However, as documented by Alahacoon and Edirisinghe (2021), the rainfall pattern over Sri Lanka shows a significant increase in annual rainfall during the 1989-2019 period, due to climate change. This could be the reason for the significant increasing trend in rainfall over the KRB in this study. Further, this increasing trend may be influenced by using mean based adjusted homogeneity daily rainfall data that this study used. At the same time, all four seasons demonstrate an increasing trend in rainfall patterns, but the increasing trend in SWM and 2IM is incompatible with the results of the study of the KRB by Jayasekara et al. (2020).

Furthermore, the study of Chandimala and Zubair (2007) showed how the El Niño – Southern Oscillation (ENSO) and Indian Ocean Dipole (IOD) affect rainfall and streamflow in the KRB, especially during April – September. Therefore, rainfall over the basin significantly varies depending on these teleconnections (De Silva & Hornberger, 2019). During La Niña events, SWM rainfall increases, whereas during El Niño events it decreases. Zubair et al. (2015) explained that the flooding of May 2016 in the KRB was caused by the El Niño event. However, examining the influence of these dipolar ocean-atmosphere phenomena on rainfall distribution is beyond the scope of this study. In additional, this study found that, during 2017-2020 period, the KRB appeared to have more rainfall than typical and this may suggest that there has recently been a shift in climatic conditions. However, a more thorough analysis would need to be undertaken before that can be confirmed.

The changes in the water levels of the KRB can be summarised as follows. Just like the overall water levels during the period, Hanwella station showed a decreasing trend. However, several factors have caused the reduction of water discharging into the river basin. Land use changes and river water management projects are prominent among them. In the KRB, reduced water volume is strongly connected to hydropower plants. The KRB has five major hydropower stations (JICA, 2004). To meet demand for electricity, the Ceylon Electricity Board has expanded hydropower projects in the major river basins of Sri Lanka in recent years. With decreasing rainfall and increasing electricity consumption, these hydropower stations must hold more dammed water to produce electricity, which may be a reason for decreasing water levels in this lower basin station.

Dissanayaka and Rajapakse (2019) also showed that the annual and SWM precipitation, and the IM2 streamflow at Hanwella hydrology stations will show negative trends in the 2020s. These results are in line with this study. Further, the reduction in streamflow largely affects urban water consumption of tap water by the metropolitan cities of the Colombo and Gampaha regions, mainly from the Kelani River Basin (Jayasekara et al., 2020). There are two major industrial areas in the river basin, at Seethawaka and Biyagama, as well as a significant number of industries that are not in the industrial zone along the river (Abeykoon & Nawarathna, 2011), but which also use water from the Kelani River.

Malede et al. (2022) found that rainfall alone does not affect water flows, but also changes in land cover and uses, as well as human interventions like extractions from groundwater. Decreasing water discharges at the Hanwella Hydrology Station may influence future land use changes and human intervention. In addition, the decline in streamflow may have a negative impact on the aquatic biodiversity of the river and its ecosystem, the recharging capacity of the groundwater, and the natural degradability of KRB water (Jayasekara et al., 2020).

Water levels in the N'Steet showed an increasing trend during the study period. As this station is close to the Indian Ocean (only about 2 km away), increased water levels there may affect tidal and climate change. The study by Palamakumbure et al. (2020) shows that, in the next 50 years, seasonally adjusted tidal gauge data in Colombo, Sri Lanka (rate of sea-level rising = 0.288 ± 0.118 mm/month) suggest an inundation height of approximately 0.1 to 0.2 m. It revealed that increasing water levels will lead to inundations at heights up to about 3.5 – 15.0 m above today's sea level. Furthermore, the study by Samarasinghe et al. (2022) clearly explained how the effect of the tidal wave backwashes the Kelani River water closer to the N'Street station area. This tidal effect may result in an increasing trend at this hydrology station. Figure 13 depicts the increase in Indian ocean tidal wave heights over recent years.

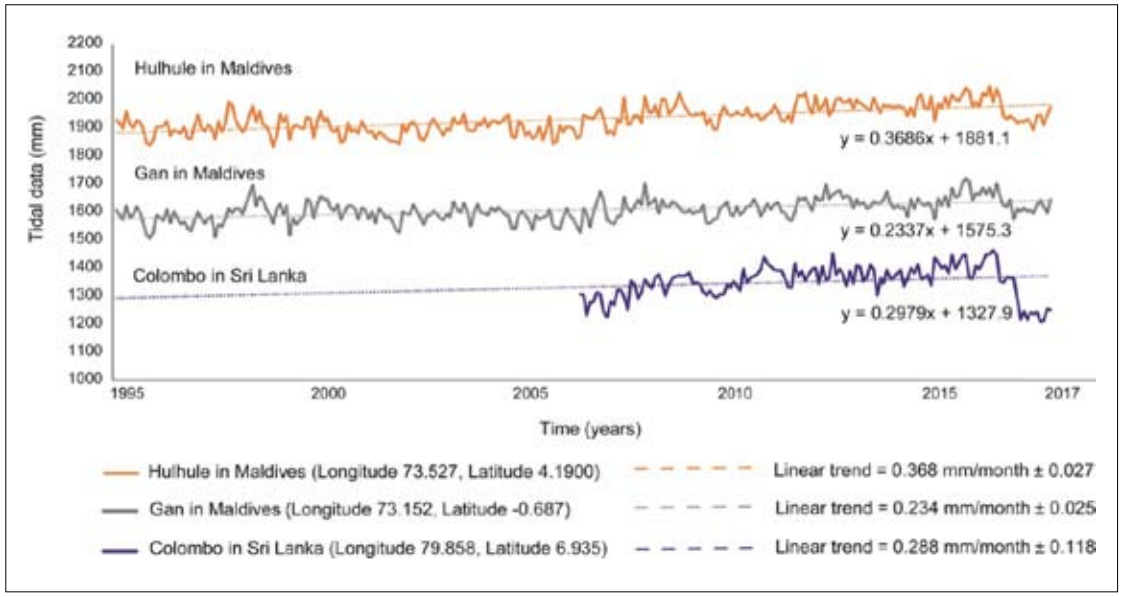

Figure 13: easonal pattern of tidal waves. Note: Seasonal component (solid lines) and linear trend line (dotted lines) for the Hulhule and Gan tidal stations in the Maldives and the Colombo tidal station in Sri Lanka (Source: Palamkumbure et al., 2020)

In this scenario, as this station is close to the sea, continual increases in water levels may be linked with increasing sea levels. The salt intrusion into the lower basin, which comes with rising sea levels, could pose another problem for users of KRB water. This phenomenon can be seen when salty water flows into Ambathale's treatment plant in the lower flow periods (Abeykoon & Nawarathna, 2011), but it needs more detailed research.

Jayasekara et al. (2020) specified that variations in streamflow are mainly attributed to the rainfall generated over the KRB catchment. However, this study found that the relation between rainfall and water level in the KRB shows a moderately positive correlation which is evidence of the implementation of water resources and flood management plans (Samarasinghe et al., 2022). Also, human interventions in land use/land cover are rapidly increasing in the KRB (Samarasinghe et al., 2022). Land use changes and human interventions may be the reasons for the moderately positive correlation between rainfall and water level observed during the study period. Nevertheless, monthly correlation shows positive correlations between rainfall and water level at the two stations. However, in the month of January the N'Street Hydrology station had a slightly negative correlation. January is in the NEM period, where the KRB receives less rainfall.

The lower KRB is experiencing increased flood events with increased rainfall intensity (Wijeratne & Li, 2022). The lag correlation results for the basin clearly show how the rainfall synchronises with water level on a daily basis. This has provided a background to understand extreme rainfall and its relation to flood

hazard. Especially when upper KRB meteorological stations recorded a total rainfall of more than 500 mm for more than two days, there is a chance that water levels in the basin will rise and cause a flood. The two recent major flood incidents in the KRB are shown below to visualise the relationship between extreme rainfall and the water level at two hydrology stations, which were not considered in this study.

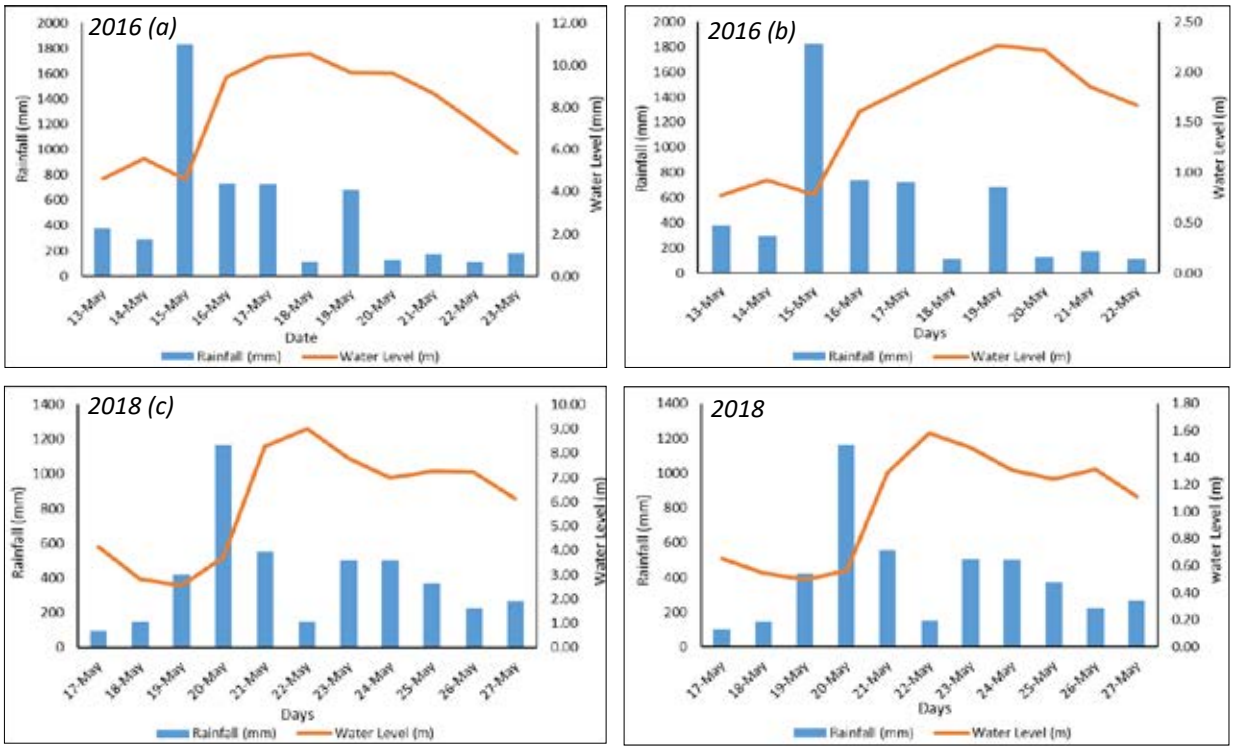

Figure 14: Rainfall and water levels during flood events in the lower KRB. Note: (a) & (c) Hanwella Station; (b) & (d) N'Street Station.

Table 5: Average rainfall received in 10-day periods in the month of May for 2016 and 2018 (Source: Department of Meteorology of Sri Lanka)

2016 Day	Average Rainfall (mm)	2018 Day	Average Rainfall (mm)
13-May	37.45	17-May	9.83
14-May	29.15	18-May	14.58
15-May	182.90	19-May	42.24
16-May	73.42	20-May	116.54
17-May	72.69	21-May	55.59
18-May	10.69	22-May	14.78
19-May	68.47	23-May	50.57
20-May	12.52	24-May	50.29
21-May	17.30	25-May	37.05
22-May	11.12	26-May	22.57
23-May	18.09	27-May	26.75

In the month of May in both 2016 and 2018, during the SWM, the KRB faced flood hazards after extreme rainfall. Table 5 indicates the average rainfall received in the KRB over 10 days during these flood events.

It is visible on the graphs that, when average rainfall across the basin is over 100 mm, it tends to cause water level increases at the two stations on the following day (Figure 14).

At the Hanwella station the water level reached nearly 10 m, indicating a high flood event. During the 2016 flood event, from 15 – 17 May, the upper KRB meteorological stations received total rainfalls of 1083.5 mm, 695.4 mm, and 662.0 mm, respectively. In 2018, the same stations received total rainfall of 901.0 mm and 533.3 mm on May 20th and 21st.

It is apparent that, after the heavy rainfall over the basin, these two hydrology stations in the lower KRB recorded increases in water levels. Most probably, the water level reached its maximum the day after the extreme rainfall event, signalling a flood hazard in the LKRB. The maximum water level remained for a few days, severely damaging the people and environment of the river area. Samarasinghe et al. (2022) revealed that rapid land use changes and urbanisation in the KRB have significantly contributed to flooding and its severity in recent years.

Reports suggest that the KRB is flooding frequently. Approximately two-third of the KRB is hilly uplands, while the rest is in the lowlands and flat coastal areas (Abeykoon & Nawarathna, 2011). Due to heavy rainfall and rapid water discharge from upstream, the river may overflow its banks on the lower flats.

Samarasinghe et al. (2022) also explained that land use changes in the KRB have greatly impacted the severity of flooding in the basin. Wijeratne and Li (2022) also explained that flood events have increased due to the stress of urban sprawl in the LKRB. Further, during the last few years, some flooding events caused by extreme rainfall events have occurred where there was no time to evacuate (Wijeratne & Li, 2022), a tragic scenario for people and property. For example, in the 2016 flood event, 228,871 and 74,003 people were affected by floods in the Colombo and Gampaha districts along the Kelani River (CRIP, 2018). Paying attention to all these matters, Dissanayake et al. (2018) suggest several reasons for this unprecedented flooding in the KRB.

- The hydropower reservoirs located upstream at Laksapana, Castlereigh, and other points were full and were generating maximum power and discharging water into the Kelani River.
- The mouth of the Kelani River, where water discharges into the sea, was partially blocked during the dry months due to poor water outflow and the sea sand brought into the river mouth by littoral drift.
- The large amount of unauthorised housing in the vicinity of the riverbank.
- Unauthorised filling of marshes, canals, and drainage paths which drain or discharge rainwater remaining blocked and unable to discharge to their total capacity.

When considering these facts, it is evident that changes caused by human behaviour have increased flood severity and resulted in more significant damage to society and the environment. The government of Sri Lanka has implemented several actions in the past to mitigate flood hazards. Accordingly, the Irrigation Department introduced the Flood Protection Act No. 22 of 1955. As this Act is outdated, a review with input from the Ministry of Disaster Management has been initiated (Dissanayake et al., 2018). Furthermore, the government collaborates with international institutions to implement flood management projects in the study area. The World Bank funded "Strategic Environmental Assessment (SEA) for the Kelani River" is the most recent ongoing project aiming to propose flood and drought mitigation measures for the study area (CRIP, 2018).

CONCLUSION

The study's conclusions are summarised as follows:

- Annual total rainfall over the Kelani River Basin (KRB) showed a significant increase from 1991 to 2020.
- Annually, 50% of meteorological stations around KRB (Colombo, Angoda, Chesterford, Labugama Tank, and Maliboda) showed a significant increasing trend, while 40% showed a decreasing trend.
- Water levels declined significantly at Hanwella, but increased at N'Street during the study period.
- Seasonally, rainfall decreased at 70% of stations during the Southwest Monsoon (SWM), 50% in Second Inter-Monsoon (IM2), 30% in the Northeast Monsoon (NEM), and 50% in First Inter-Monsoon (IM1).
- In the Lower KRB (LKRB), all stations showed increasing trends except the Hanwella Group. In

the Upper KRB (UKRB), most stations showed decreasing trends, except Maliboda, which had a significant increase.
- While the intensity of extreme rainfall events is decreasing, the duration and frequency of such events are increasing.
- A moderate positive correlation exists between daily rainfall and water levels (1991–2020), suggesting rainfall is a key factor, though not the only one.
- Lag correlation analysis indicated that daily rainfall impacts water levels, increasing flood vulnerability.
- The strongest correlations between rainfall and water levels occurred in May, June, July, September, and November.

Although rainfall is a major driver of hydrological change in the KRB, human activities further complicate the basin's response to climatic variability. Given the basin's high population and flood risk, the Sri Lankan government is prioritizing sustainable water management. These findings support future planning and mitigation strategies.

REFERENCES

Abeykoon, A. M. H. K., & Nawarathna, N. M. A. L. B. (2011, 25–29 September). *Enhancing water quality by salinity barriers and its impact on environment* XIVth IWRA World Water Congress, Pernambuco, Brazil.

Alahacoon, N., & Edirisinghe, M. (2021). Spatial Variability of Rainfall Trends in Sri Lanka from 1989 to 2019 as an Indication of Climate Change. *ISPRS International Journal of Geo-Information, 10*(2). https://doi.org/10.3390/ijgi10020084

Ampitiyawatta, A. D., & Guo, S. (2009). PRECIPITATION TRENDS IN THE KALU GANGA BASIN IN SRI LANKA. *The Journal of Agricultural Science, vol.4, no.1*.

Arnell, N. W., & Gosling, S. N. (2013). The impacts of climate change on river flow regimes at the global scale. *Journal of Hydrology, 486*, 351-364. https://doi.org/https://doi.org/10.1016/j.jhydrol.2013.02.010

Azman, A. H., Nurul Nadrah Aqilah, T., & Malek, M. A. (2021). Comparison of Missing Rainfall Data Treatment Analysis at Kenyir Lake. *IOP Conference Series. Materials Science and Engineering, 1144*(1). https://doi.org/https://doi.org/10.1088/1757-899X/1144/1/012046

Chandimala, J., & Zubair, L. (2007). Predictability of stream flow and rainfall based on ENSO for water resources management in Sri Lanka. *Journal of Hydrology, 335*(3), 303-312. https://doi.org/https://doi.org/10.1016/j.jhydrol.2006.11.024

Costa, A. C., & Soares, A. (2009). Homogenization of Climate Data: Review and New Perspectives Using Geostatistics. *Mathematical Geosciences, 41*(3), 291-305. https://doi.org/10.1007/s11004-008-9203-3

CRIP. (2018). *Strategic Environmental Assessment of Development of River Basin Level Flood 399 and Drought Mitigation Investment Plans (DBIP)*. http://crip.lk/wp-content/uploads/2019/01/Kelani-River-SEA-Study-Final-Report.pdf.

De Silva, M. T., & Hornberger, G. M. (2019). Identifying El Niño–Southern Oscillation influences on rainfall with classification models: implications for water resource management of Sri Lanka. *Hydrology and Earth System Sciences, 23*(4), 1905-1929. https://doi.org/10.5194/hess-23-1905-2019

De Silva, M., Ratnyake, U., Mahanama, S., Herath, S., & Weerakoon, S. (2012). Flood inundation mapping along the lower reach of Kelani river basin under the impact of climatic change.

Dissanayaka, K., & Rajapakse, R. (2018). Climate extremes and precipitation trends in Kelani river basin, Sri Lanka and impacts on streamflow variability under climate change. The Proceedings of The International Conference on Climate Change,

Dissanayaka, K., & Rajapakse, R. (2019). Long-term precipitation trends and climate extremes in the Kelani River basin, Sri Lanka, and their impact on streamflow variability under climate change. *Paddy and Water Environment, 17*, 281-289.

Dissanayake, P., Hettiarachchi, S., & Siriwardana, C. (2018). Increase in Disaster Risk due to inefficient Environmental Management, Land use policies and Relocation Policies. Case studies from Sri Lanka. *Procedia Engineering, 212*, 1326-1333. https://doi.org/https://doi.org/10.1016/j.proeng.2018.01.171

Döll, P., & Schmied, H. M. (2012). How is the impact of climate change on river flow regimes related to the impact on mean annual runoff? A global-scale analysis. *Environmental Research Letters, 7*(1). https://doi.org/10.1088/1748-9326/7/1/014037

Dushyantha, C., & Ptuhina, I. (2020). Flood risk assessment of river "Kelani Ganga" exceeding its threshold water level. *E3S Web Conf., 157*, 02006. https://doi.org/10.1051/e3sconf/202015702006

Feng, X., Porporato, A., & Rodriguez-Iturbe, I. (2013). Changes in rainfall seasonality in the tropics. *Nature Climate Change, 3*(9), 811-815.

Frans, C., Istanbulluoglu, E., Mishra, V., Munoz-Arriola, F., & Lettenmaier, D. P. (2013). Are climatic or land cover changes the dominant cause of runoff trends in the Upper Mississippi River Basin? *Geophysical Research Letters, 40*(6), 1104-1110. https://doi.org/https://doi.org/10.1002/grl.50262

Good data. (2023). *Time Series Analysis - Lagged Correlation and R-Squared*. Retrieved 30/10/2023, from https://community.gooddata.com/metrics-and-maql-kb-articles-43/time-series-analysis-lagged-correlation-and-r-squared-233

Hamed, K. H., & Rao, A. R. (1998). A modified Mann-Kendall trend test for autocorrelated data. *Journal of Hydrology, 204*(1), 182-196. https://doi.org/https://doi.org/10.1016/

S0022-1694(97)00125-X

Hariadi, M. H., van der Schrier, G., Steeneveld, G. J., Sutanto, S., Sutanudjaja, E., Ratri, D. N., Sopaheluwakan, A., & Klein Tank, A. (2023). A high-resolution perspective of extreme rainfall and river flow under extreme climate change in Southeast Asia. *Hydrol. Earth Syst. Sci. Discuss., 2023*, 1-29. https://doi.org/10.5194/hess-2023-14

Hettiarachchi, P. (2016). Hydrological report on the Kelani River flood in May 2016. *Hydrological annual, irrigation department*.

Imbulana, N., Gunawardana, S., Shrestha, S., & Datta, A. (2018). Projections of extreme precipitation events under climate change scenarios in Mahaweli River Basin of Sri Lanka. *Current Science, 114*(7), 1495-1509. http://www.jstor.org/stable/26495505

Jain, C. K., & Singh, S. (2018). Impact of climate change on the hydrological dynamics of River Ganga, India. *Journal of Water and Climate Change, 11*(1), 274-290. https://doi.org/10.2166/wcc.2018.029

Jayasekara, S. M., Abeysingha, N. S., & Meegastenna, T. J. (2020). Streamflow trends of Kelani river basin in Sri Lanka (1983-2013). *Journal of the National Science Foundation of Sri Lanka, 48*(4). https://doi.org/10.4038/jnsfsr.v48i4.9440

Jiang, R., Wang, Y., Xie, J., Zhao, Y., Li, F., & Wang, X. (2019). Assessment of extreme precipitation events and their teleconnections to El Niño Southern Oscillation, a case study in the Wei River Basin of China. *Atmospheric Research, 218*, 372-384. https://doi.org/10.1016/j.atmosres.2018.12.015

JICA (2004). *Study of hydropower optimization in Sri Lanka* (Final Report, Issue. Kendall, M. G. (1962). Rank correlation methods. *J. Am. Stat. Assoc., , 63(324)*, 1379 – 1389. https://doi.org/doi:10.1080/01621459.1968.10480934.

Kendall, M. G. (1962). Rank correlation methods. J. Am. Stat. Assoc., , 63(324), 1379 – 1389. https://doi.org/doi:10.1080/01621459.1968.10480934.

Khaniya, B., Jayanayaka, I., Jayasanka, P., & Rathnayake, U. (2019). Rainfall Trend Analysis in Uma Oya Basin, Sri Lanka, and Future Water Scarcity Problems in Perspective of Climate Variability. *Advances in Meteorology, 2019*, 3636158. https://doi.org/10.1155/2019/3636158

Mahagamage, M. G. Y. L., & Manage, P. M. (2018). Socio-economic background of the head and transitional regions of the Kelani River Basin, Sri Lanka. *Asian Jr. of Microbiol. Biotech. Env. Sc. , ol. 20, No. (3) : 2018 : 744-756*.

Malede, D. A., Agumassie, T. A., Kosgei, J. R., Linh, N. T. T., & Andualem, T. G. (2022). Analysis of rainfall and streamflow trend and variability over Birr River watershed, Abbay basin, Ethiopia. *Environmental Challenges, 7*, 100528. https://doi.org/https://doi.org/10.1016/j.envc.2022.100528

Manawadu, L., & Wijeratne, V. (2021). Anthropogenic drivers and impacts of urban flooding-A case study in Lower Kelani River Basin, Colombo Sri Lanka. *International Journal of Disaster Risk Reduction, 57*, 102076.

Mann, H. B. (1945). Nonparametric Tests Against Trend. *Econometrica, , 13(3)*, 245–259.

Martins, J. A., Brand, V. S., Capucim, M. N., Machado, C. B., Piccilli, D. G. A., & Martins, L. D. (2016). The Impact of Rainfall and Land Cover Changes on the Flow of a Medium-sized River in the South of Brazil. *Energy Procedia, 95*, 272-278. https://doi.org/10.1016/j.egypro.2016.09.068

Mukaka, M. M. (2012). Statistics corner: A guide to appropriate use of correlation coefficient in medical research. *Malawi Med J, 24*(3), 69-71.

Oti, J. O., Kabo-Bah, A. T., & Ofosu, E. (2020). Hydrologic response to climate change in the Densu River Basin in Ghana. *Heliyon, 6*(8), e04722. https://doi.org/10.1016/j.heliyon.2020.e04722

Palamakumbure, L., Ratnayake, A. S., Premasiri, H. M. R., Ratnayake, N. P., Katupotha, J., Dushyantha, N., Weththasinghe, S., & Weerakoon, W. A. P. (2020). Sea-level inundation and risk assessment along the south and southwest coasts of Sri Lanka. *Geoenvironmental Disasters, 7*(1), 17. https://doi.org/10.1186/s40677-020-00154-y

Palmer, M. A., Reidy Liermann, C. A., Nilsson, C., Flörke, M., Alcamo, J., Lake, P. S., & Bond, N. (2008). Climate change and the world's river basins: anticipating management options. *Frontiers in Ecology and the Environment, 6*(2), 81-89. https://doi.org/10.1890/060148

Panditharathne, R., Gunathilake, M. B., Chathuranika, I. M., Rathnayake, U., Babel, M. S., & Jha, M. K. (2022). Trends and Variabilities in Rainfall and Streamflow: A Case Study of the Nilwala River Basin in Sri Lanka. *Hydrology, 10*(1). https://doi.org/10.3390/hydrology10010008

Perera, H., Gunathilake, M. B., Panditharathne, R., Al-mahbashi, N., & Rathnayake, U. (2022). Statistical Evaluation and Trend Analysis of ANN Based Satellite Products (PERSIANN) for the Kelani River Basin, Sri Lanka. *Applied Computational Intelligence and Soft Computing, 2022*.

Rameshwaran, P., Bell, V. A., Davies, H. N., & Kay, A. L. (2021). How might climate change affect river flows across West Africa? *Climatic Change, 169*(3), 21. https://doi.org/10.1007/s10584-021-03256-0

Randil, C., Siriwardana, C., & Sandaruwan Rathnayaka, B. (2022). A statistical method for pre-estimating impacts from a disaster: A case study of floods in Kaduwela, Sri Lanka. *International Journal of Disaster Risk Reduction, 76*, 103010. https://doi.org/https://doi.org/10.1016/j.ijdrr.2022.103010

R-Core-Team. [V. Foundation for Statistical Computing, Austra]. (2013). *R: A language and environment for statistical computing.* . http://wwww.Rproject.org.

Samarasinghe, J. T., Makumbura, R. K., Wickramarachchi, C., Sirisena, J., Gunathilake, M. B., Muttil, N., Teo, F. Y., & Rathnayake, U. (2022). The Assessment of Climate Change Impacts and Land-use Changes on Flood Characteristics: The Case Study of the Kelani River Basin, Sri Lanka. *Hydrology, 9*(10), 177.

Santini, M., & di Paola, A. (2015). Changes in the world rivers' discharge projected from an updated high resolution dataset of current and future climate zones. *Journal of Hydrology, 531*, 768-780. https://doi.org/https://doi.org/10.1016/j.jhydrol.2015.10.050

Sen, P. K. (1968). Estimates of the Regression Coefficient Based on Kendall's Tau. *Journal of the American Statistical Association, 63(324)*. https://doi.org/https://doi.org/10.2307/2285891

Tao, B., Tian, H., Ren, W., Yang, J., Yang, Q., He, R., Cai, W., & Lohrenz, S. (2014). Increasing Mississippi river discharge throughout the 21st century influenced by changes in climate, land use, and atmospheric CO2. *Geophysical Research Letters, 41*(14), 4978-4986.

United Nations Office for Disaster Risk Reduction and World Meteorological Organization. (2023). *Global Status of Multi-Hazard Early Warning Systems*. https://www.undrr.org/media/91954/download?startDownload=true

Wang, X. L., Chen, H., Wu, Y., Feng, Y., & Pu, Q. (2010). New Techniques for the Detection and Adjustment of Shifts in Daily Precipitation Data Series. *Journal of Applied Meteorology and Climatology, 49*(12), 2416-2436. https://doi.org/https://doi.org/10.1175/2010JAMC2376.1

Wijeratne, V., & Li, G. (2022). Urban sprawl and its stress on the risk of extreme hydrological events (EHEs) in the Kelani River basin, Sri Lanka. *International Journal of Disaster Risk Reduction, 68*, 102715.

Wijetunge, J., & Neluwala, N. (2023). Compound flood hazard assessment and analysis due to tropical cyclone-induced storm surges, waves and precipitation: a case study for coastal lowlands of Kelani river basin in Sri Lanka. *Natural Hazards, 116*(3), 3979-4007.

WMO (2018). *Guide to climatological practices*.

WMO (2020). *Climate change detection and indices*. World Meteorological Organization (WMO). Retrieved 22 October 2022, from https://community.wmo.int/climate-change-detection-and-indices

Zubair, L., Nissanka, S. P., Weerakoon, W. M. W., Herath, D. I., Karunaratne, A. S., Prabodha, A. S. M., Agalawatte, M. B., Herath, R. M., Yahiya, S. Z., Punyawardhene, B. V. R., Vishwanathan, J., Delpitiya, P., Wijekoon, A. E. N., Gunaratna, J., Chandrasekara, S. S. K., Wickramagamage, P., Weerasinghe, K. D. N., Navaratne, C. M., Perera, R. S., . . . McDermid, S. (2015). Climate Change Impacts on Rice Farming Systems in Northwestern Sri Lanka. In *Handbook of Climate Change and Agroecosystems* (pp. 315-352). https://doi.org/10.1142/9781783265640_0022

J.Natn.Sci.Foundation Sri Lanka 2026 54 (3): 369 - 388
DOI: http://dx.doi.org/10.4038/jnsfsr.v54i3.12718

RESEARCH ARTICLE

Deep Learning

A hybrid adaptive artificial bee colony - liquid neural network scheduler for multi-objective task optimization in dynamic cloud environments

NR Sabat[1], RR Sahoo[2] and S Radhakrishnan[3*]
Faculty of Engineering, Biju Patnaik University of Technology (BPUT), Rourkela, Odisha, 769015, India.
Department of Computer Science and Engineering, Parala Maharaja Engineering College (PMEC), Berhampur, Odisha, 761003, India.
Department of Computer Engineering, Faculty of Engineering, University of Peradeniya, Peradeniya, 20400, Sri Lanka.

Submitted: 24 June 2025; Revised: 07 June 2026; Accepted: 07 July 2026

Abstract: The scheduling of tasks in cloud computing systems, which are characterised by fluctuating workloads and computing resources, requires efficiency to achieve optimal performance. Traditional metaheuristic scheduling algorithms sometimes converge prematurely, fail to adapt adequately to fluctuating system conditions, and waste resources under heavy task loads. Notwithstanding the widespread adoption of these methodologies, occurrences of this nature transpire regularly. This research utilizes liquid neural networks and the artificial bee colony (ABC) method to enhance cloud task load scheduling. The proposed hybrid adaptive artificial bee colony - liquid neural network scheduler (AALS) dynamically modifies scheduling decisions through ABC algorithm exploration and LNN adaptive learning, utilizing real-time system metrics. Task load traces from the Alibaba Cluster dataset have been used in simulation testing through CloudSim Plus. The proposed approach has been tested with 1,000-10,000 tasks on 200-1,000 VMs and compared to other metaheuristic scheduling techniques. The proposed AALS scheduler enhances several QoS parameters, including makespan, latency, throughput, resource utilization, and load balancing. The Friedman, Nemenyi, and Wilcoxon tests confirm that the proposed approach consistently surpasses compared algorithms through statistical validation. These findings demonstrate that the hybrid framework is capable of resolving adaptive task scheduling in large-scale cloud computing systems.

Keywords: Artificial bee colony (ABC), cloud computing, liquid neural networks (LNN), multi-objective optimization, resource allocation, task scheduling.

INTRODUCTION

Cloud computing has become a fundamental paradigm for delivering scalable, on-demand, and cost-effective computing resources to support diverse applications across scientific, industrial, healthcare, Internet of Things (IoT), and big data domains. The increasing complexity and heterogeneity of cloud environments have significantly intensified the challenge of efficiently scheduling large volumes of independent and dependent tasks while satisfying multiple Quality of Service (QoS) requirements, including makespan, latency, throughput, resource utilization, energy efficiency, load balancing, fairness, and fault tolerance. Since cloud task scheduling is an NP-hard optimization problem, numerous intelligent scheduling algorithms have been proposed to improve resource allocation and system performance (Abraham et al., 2025; Agrawal et al., 2025; Patni et al., 2025). Recent advances in artificial intelligence, swarm intelligence, and hybrid optimization techniques have further accelerated the development of adaptive scheduling strategies capable of addressing dynamic workload variations and heterogeneous computing resources. To better understand the current state of research and identify existing limitations, the literature is organized into three major themes: (i) metaheuristic scheduling approaches,

* Corresponding author (swarnar@eng.pdn.lk; https://orcid.org/0009-0005-4844-1635)

This article is published under the Creative Commons CC-BY-ND License (http://creativecommons.org/licenses/by-nd/4.0/). This license permits use, distribution and reproduction, commercial and non-commercial, provided that the original work is properly cited and is not changed in anyway.

(ii) deep learning-based scheduling approaches, and (iii) hybrid intelligent scheduling approaches. This thematic organization facilitates a critical analysis of existing scheduling techniques and provides a clear foundation for identifying the research gap addressed by the proposed adaptive artificial bee colony–liquid neural network scheduler (AALS).

Metaheuristic optimization algorithms have been extensively employed for cloud task scheduling because of their ability to solve NP-hard optimization problems while optimizing multiple QoS objectives, including makespan, latency, throughput, resource utilization, and load balancing (Abraham et al., 2025; Djebbar & Belalem, 2025).

Particle swarm optimization (PSO) has been widely used because of its fast convergence and simple implementation; however, it often suffers from premature convergence and local optima when solving large-scale scheduling problems (Johari & Pandey, 2025; Kumar & Vardhan, 2025).

Ant colony optimization (ACO) efficiently explores the search space through pheromone-guided path selection but incurs increased computational overhead as the scheduling space expands (Siruvoru & Aparna, 2025; Shah et al., 2025).

Grey wolf optimization (GWO) and Harris Hawks optimization (HHO) improve the balance between exploration and exploitation and enhance scheduling performance under heterogeneous cloud environments, although their effectiveness decreases under rapidly changing workloads (Jangu & Raza, 2025; Shen et al., 2025).

Artificial bee colony (ABC), whale optimization algorithm (WOA), cuckoo search (CS), and other swarm intelligence techniques have also demonstrated competitive scheduling performance by improving resource utilization, energy efficiency, and load balancing (Feng et al., 2025; Kushwaha et al., 2025; Sui et al., 2025; Zhao et al., 2024).

Several researchers have incorporated multi-objective optimization, dynamic load prediction, and energy-aware scheduling strategies to improve cloud resource allocation (Agrawal et al., 2025; Beena et al., 2025; Chen et al., 2025; Mahapatra et al., 2025; Salehnia et al., 2024).

Despite these advances, existing metaheuristic scheduling algorithms continue to experience premature convergence, static parameter adaptation, and limited adaptability to dynamic cloud environments, thereby motivating the integration of adaptive learning mechanisms.

Deep learning-based scheduling approaches have emerged as a promising solution for improving cloud task scheduling by enabling intelligent decision-making, workload prediction, and adaptive resource allocation. Unlike conventional optimization techniques, deep learning models continuously learn scheduling policies from historical execution data and dynamically changing cloud environments (Gu et al., 2025; Chen et al., 2025).

Artificial neural networks (ANNs) have been widely employed to predict task execution time, estimate resource demand, and optimize task-to-resource mapping, thereby improving scheduling efficiency and resource utilization (Wang et al., 2025; Zhao et al., 2025).

Reinforcement learning (RL) and deep reinforcement learning (DRL) have demonstrated significant potential for cloud scheduling by enabling agents to learn optimal scheduling policies through continuous interaction with cloud environments. These approaches have been successfully applied to dynamic task scheduling, workflow optimization, multicloud resource management, and latency-aware task offloading (Farooq et al., 2025; Gu et al., 2025; He et al., 2025; Sankaran et al., 2025; Smithamol & Sridhar, 2025; Tang et al., 2025; Zou et al., 2025).

Graph-based deep learning models and convolutional neural networks have also been proposed to capture complex task dependencies and improve scheduling decisions in distributed cloud infrastructures (Chen et al., 2025; Gu et al., 2025).

Recently, liquid neural networks (LNNs) have attracted considerable attention because of their continuously adaptive neuron dynamics, which enable real-time learning with lower computational complexity than conventional deep neural networks. Their capability to model time-varying systems makes them particularly suitable for dynamic cloud scheduling (Kumar et al., 2023).

Despite their superior adaptability and prediction accuracy, deep learning-based scheduling methods generally require extensive training datasets, high computational resources, and prolonged training time

before deployment. These limitations reduce their suitability for real-time cloud scheduling under rapidly changing workloads.

To overcome the limitations of standalone optimization techniques, recent studies have focused on hybrid scheduling frameworks that integrate metaheuristic optimization with machine learning, reinforcement learning, and digital twin technologies. These hybrid approaches combine the global search capability of swarm intelligence algorithms with the adaptive learning ability of artificial intelligence to improve scheduling accuracy, convergence speed, and resource utilization (Kaur et al., 2025; Khan et al., 2025; Luo et al., 2025; Mahmoudi et al., 2025).

Hybrid optimization algorithms that combine Artificial bee colony (ABC), Genetic Algorithms (GA), and other evolutionary techniques have demonstrated improved exploration–exploitation balance, enabling better scheduling performance than individual optimization methods (Kaur et al., 2025; Luo et al., 2025).

Several researchers have integrated reinforcement learning with metaheuristic optimization to dynamically adjust search parameters and improve adaptive scheduling decisions in cloud and edge computing environments (Khan et al., 2025; Mahmoudi et al., 2025).

Digital Twin (DT)-based scheduling has recently emerged as an effective paradigm for intelligent cloud resource management by creating virtual replicas of physical cloud infrastructures. These virtual models enable predictive workload analysis, intelligent monitoring, dynamic resource allocation, and real-time scheduling optimization in distributed cloud environments (Hayawi et al., 2025; Wajid et al., 2025).

Hybrid scheduling approaches have also been extended to workflow scheduling, security-aware resource allocation, and heterogeneous cloud environments to improve robustness, scalability, and service quality (Guan, 2025; Peng et al., 2025).

Although hybrid scheduling frameworks outperform conventional optimization algorithms, most existing approaches rely on static neural architectures or computationally expensive reinforcement learning models. The integration of artificial bee colony optimization with liquid neural networks for adaptive multi-objective cloud task scheduling remains largely unexplored. Consequently, there is a need for an intelligent scheduling framework capable of continuously adapting to workload variations while simultaneously optimizing multiple QoS objectives in dynamic cloud environments.

Research Gap

Despite significant advances in cloud task scheduling, several important research gaps remain:

- Conventional metaheuristic scheduling algorithms (e.g., PSO, ACO, GWO, HHO, WOA, and CS) often suffer from premature convergence, local optima, and limited adaptability when scheduling large-scale and highly dynamic cloud workloads.
- Deep learning and reinforcement learning (RL)-based scheduling approaches provide intelligent and adaptive decision-making; however, they generally require high computational resources, large training datasets, and long training times, limiting their applicability for real-time cloud scheduling.
- LNNs have demonstrated excellent capability for modelling dynamic systems with continuous adaptation, yet their application to cloud task scheduling remains largely unexplored, particularly in multi-objective optimization scenarios.
- Existing hybrid scheduling approaches primarily combine metaheuristic algorithms with conventional machine learning or deep learning techniques but lack adaptive neural architectures capable of continuously responding to workload variations and changing cloud conditions.
- Most existing schedulers optimize only a limited set of QoS objectives, such as makespan or energy consumption, while simultaneous optimization of multiple QoS metrics including Makespan, Latency, Throughput, Resource Utilization, Fairness, Scalability, and Fault Tolerance remains insufficiently investigated.
- There is a lack of an adaptive multi-objective scheduling framework that effectively integrates the global search capability of Artificial Bee Colony (ABC) optimization with the real-time adaptive learning capability of LNNs to improve scheduling efficiency in heterogeneous cloud environments.

These research gaps motivate the development of the proposed AALS, which combines swarm intelligence with adaptive neural computation to achieve intelligent, scalable, and multi-objective cloud task scheduling.

Research Objective

To develop an AALS that integrates ABC optimization and LNNs to achieve adaptive, efficient, and multi-objective task scheduling in dynamic cloud computing environments.

This research has made the following major contributions:

- Hybrid adaptive event scheduling framework: A novel hybrid AALS has been created to optimize task scheduling and resource allocation in cloud computing environments.
- Enhancements to the multi-objective optimization framework: bees for local refinement, onlooker bees for probabilistic selection, and scout bees for global exploration have all been used to improve multi-objective optimization. This approach improves search efficiency, prevents premature convergence, and optimizes multiple objectives across QoS parameters.
- Liquid neural networks facilitated real-time adaptive learning: In order to accommodate the numerous components of the system that are distinct from one another, the scheduling strategy simultaneously employs liquid neural networks. Variations include load, resource availability, and task execution unpredictability. Dynamic reservoirs reduce temporal processing training overhead.
- Robust & fault-tolerant scheduling: Fault-tolerant scheduling includes real-time failure detection and adaptive task rescheduling. It performs well in dynamic clouds.

METERIALS AND METHODS

The hybrid AALS approach is comprehensively outlined in this section. This approach aims to optimize twelve different quality of service metrics in order to achieve optimal performance by leveraging a single multi-objective fitness function. Global search capabilities of the ABC are coupled with real-time dynamic adaption capabilities of liquid neural networks to attain this goal. A complete system model, mathematical formulations of all quality-of-service metrics, the AALS pseudo code, time and space complexity analysis, and CloudSim Plus with Python 3.8 simulation environment are included for reliability and performance validation. These are all provided to ensure consistency.

Threats to Validity

Although the proposed AALS demonstrates promising performance, several threats to validity should be acknowledged.

Internal validity: The experiments were conducted in CloudSim Plus using predefined virtual machine configurations, workload characteristics, and scheduling parameters. While these assumptions ensure fair and reproducible comparisons, they may not fully capture runtime uncertainties such as network delays, resource contention, and hardware failures encountered in real cloud environments.

External validity: The proposed scheduler was evaluated using the CloudSim Plus simulator. Although CloudSim Plus is widely used for cloud scheduling research, simulation results may differ from those obtained on real cloud platforms due to differences in infrastructure, virtualization, and operational conditions.

Construct validity: The evaluation considered multiple QoS metrics, including makespan, latency, throughput, resource utilization, fairness, load imbalance, scalability, fault tolerance, and energy efficiency. However, additional factors such as SLA violations, execution cost, and security overhead were not considered and could be investigated in future work.

Conclusion validity: The conclusions are based on experiments using the Alibaba Cluster Trace dataset and validated through multiple simulation runs and statistical significance tests. Nevertheless, evaluating the proposed scheduler on additional benchmark datasets and real cloud environments would further strengthen the reliability and generalizability of the findings.

Proposed methodology

The Hybrid AALS was initially introduced as a solution to the complex nature of cloud task scheduling, which is becoming increasingly challenging to manage. Liquid neural networks combine the global optimization of artificial bee colony algorithms with the dynamic adaptability of ABN algorithms in this scheduler. The proposed framework facilitates the development of a scalable solution with integrated fault tolerance for a wide range of cloud environments by offering full system modelling, multi-objective quality of service optimization, and thorough complexity analysis.

Hyperparameter selection and sensitivity analysis

The performance of the proposed AALS depends on the appropriate selection of the LNN and ABC hyper parameters. The final configuration was determined through empirical tuning using the Alibaba Cluster Trace dataset by balancing scheduling accuracy, convergence stability, and computational efficiency.

The LNN reservoir size was evaluated using 64, 128, 256, and 512 neurons. A reservoir of 256 neurons achieved the best trade-off between modelling capability and computational overhead, whereas smaller reservoirs reduced scheduling accuracy and larger reservoirs provided only marginal performance improvements.

Similarly, the model was trained using 20, 30, 50, 75, and 100 epochs. Stable convergence was consistently achieved within 50 epochs, while additional epochs produced negligible performance gains at the cost of increased training time.

The remaining hyper parameters were selected through empirical evaluation by varying one parameter at a time while keeping the others fixed. The final hyper parameter settings are summarized in Table 1.
A sensitivity analysis was conducted by varying the learning rate, reservoir size, colony size, and training epochs under identical workload conditions. The proposed AALS framework maintained stable performance for moderate parameter variations, indicating that the scheduler is robust and does not rely on highly sensitive hyper parameter settings.

Table 1: Hyperparameter settings

Hyperparameter	Evaluated values	Selected value
Reservoir size	64, 128, 256, 512	256
Training epochs	20, 30, 50, 75, 100	50
Learning rate	0.0005-0.002	0.001
Batch size	16, 32, 64	32
ABC colony size	20, 30, 40, 50	40
Maximum iterations	50, 100, 150, 200	100

System representation

To represent a collection of potential solutions for the allocation of tasks to resources, consider the set $S = \{s_1, s_2, \dots, s_p\}$, where p denotes the population size. Each solution, s_i, is represented as a vector $T = \{T_1, T_2, \dots, T_n\}$, where T_i reflects task $i's$ resource assignment. The resource set, $VM = \{VM_1, VM_2, \dots, VM_m\}$ includes all available resources.

Artificial bee colony (ABC) algorithm

The artificial bee colony algorithm uses three different kinds of agents: scout bees, employed bees, and observer bees. Employed bees are in charge of implementing local solution refinement, observer bees are in charge of probabilistically picking high-fitness solutions, and scout bees are in charge of enabling global exploration by replacing stationary solutions. Biologically, this algorithm is intended to replicate the foraging behaviour of honeybees. It is feasible to avoid premature convergence to local optimality through the use of this tripartite approach, which balances exploitation and exploration.

Liquid neural networks (LNNs)

Utilising their continuous learning architecture, which facilitates real-time adaptability to fluctuating workloads and resource levels, LNNs provide exceptional capabilities for managing dynamic cloud environments. It is feasible due to the fact that LNNs demonstrate advanced capabilities. They are particularly effective for time-sensitive scheduling and load balancing operations in distributed computing systems due to their inherent adaptability.

Hybrid adaptive artificial bee colony - liquid neural network scheduler (AALS) algorithm

The proposed hybrid scheduler adeptly combines the dynamic adaptation features of liquid neural networks with the global optimisation abilities of artificial bee colony for cloud task scheduling. At the inception of the process of getting strong and efficient resource management in dynamic cloud environments, ABC is in charge of making the right initial task-resource mappings. However, LNN is responsible for the continuous modification of allocations in response to runtime variables, including task delays and node failures.

QoS parameters in the hybrid liquid neural network scheduler AALS algorithm

By considering each of the twelve quality of service (QoS) attributes, the hybrid model simplifies performance evaluation. The system's performance will be comprehensively assessed in subsequent sections. A mathematical formulation and conceptual explanation that are both exhaustive and comprehensive will be presented for each parameter in this assessment.

Makespan

Makespan is total time to complete all tasks as described in equation (1).

$$makespan(S) = \max_{j \in R}\left(\sum_{i \in T} T_{ij} \cdot x_{ij}\right) \quad ...(1)$$

Where t_{ij} represents the execution time of task i on resource task j, x_{ij} represents the binary (1 if task i is assigned to task j, else 0), S is the scheduling solution, T is the set of tasks, R is the set of resources, and the outer maximum $\max_{j \in R}$ selects the resource with the latest task completion.

Latency

Latency represents the delay between task submission and execution start according to equation (2).

$$Latency(S) = \frac{1}{|T|}\sum_{i \in T}\left(T_i^{start} - T_i^{submit}\right) \quad ...(2)$$

Where T_i^{start} denotes the start time of task i, T_i^{submit} denotes the submission time of task i, and $|T|$ is the total number of tasks.

Response time

Response time is the time taken from submission to completion in view of equation (3).

$$Response\ time(S) = \frac{1}{|T|}\sum_{i \in T}\left(t_i^{end} - t_i^{submit}\right) \quad ...(3)$$

Where T_i^{end} denotes the completion time of task i, T_i^{submit} denotes the submission time of task i, and $|T|$ is the total number of tasks.

Throughput

Throughput represents the number of tasks completed per unit time, as indicated by equation (4).

$$Throughput(S) = \frac{|T|}{Makespan(S)} \quad ...(4)$$

Where T is the total count of tasks, and $Makespan(S)$ is as defined above.

Resource utilization

Resource utilization denotes the efficiency of resources like CPU, memory, and network usage etc., as established by equation (5)

$$Resource\ utilization(S) = \frac{1}{VM}\sum_{j \in VM}\left(\frac{\sum_{i \in T} T_{ij} \cdot x_{ij}}{Makespan(S)}\right) \quad ...(5)$$

Where T_{ij} is the execution time of task i on resource j, x_{ij} shows if task i is assigned to VM_j (1 if yes, 0 if not), and makespan(S) is the total completion time for the schedule.

Load balancing

Load balancing process ensures even distribution of tasks across resources, as demonstrated in equation (6).

$$LoadImbalance(S) = \sqrt{\frac{1}{|VM|}\sum_{j \in VM}\left(\sum_{i \in T} x_{ij} - \mu\right)^2},\ \mu = \frac{|T|}{|VM|} \quad ...(6)$$

Where $\sum_{i \in T} x_{ij}$ is the number of tasks assigned to VM_j and μ is the average number of tasks per resource.

Convergence speed

Convergence speed is the number of iterations required for the ABC algorithm (S) to stabilize (reach a stopping condition) and it measures how quickly the algorithm finds a near-optimal solution, as reflected in equation (7).

$$Convergence\ time\ (S) = Iterations\ until |F(S_t) - F(S_{t-1})| < \epsilon \quad ...(7)$$

Where $F(S_t)$ is the objective function value (fitness, cost, or performance measure) of the solution S at iteration t, $F(S_{t-1})$ is the objective function value at the previous iteration $(t-1)$, and ϵ (epsilon) is a small positive threshold determining convergence.

Training time (LNN)

Training time is the time taken for the LNN to adjust its parameters (*e.g.*, synaptic weights, time constants

etc.) to a new workload or environment, and it measures adaptation speed, as elucidated in equation (8).

$$Training\ time(S) = Time\ to\ reach\ \|h(t) - h_{target}\|_2 < \delta \quad ...(8)$$

Where $Training\ time(S)$ is the time taken for the LNN to adjust its parameters (*e.g.*, synaptic weights, time constants) to a new workload or environment, $h(t)$ represents the hidden state of the LNN at time t, h_{target} represents the desired hidden state (or equilibrium state) for optimal performance on the new workload, and $\|h(t) - h_{target}\|_2$ is the Euclidean distance between the current state and the target state. It quantifies the "error" or "deviation" from the ideal adaptation. δ is a convergence threshold. Training stops when the distance between *h(t)* & h_{target} is smaller than δ, indicating sufficient adaptation, and Time to reach $\|h(t) - h_{target}\|_2 < \delta$ represents the clock time (seconds) or iterations needed to meet the convergence criterion.

Fault tolerance & recovery time

Recovery time represents the time to reschedule after VM failure, as outlined in equation (9).

$$Recovery\ time(S) = \frac{1}{|F|}\sum_{f \in F} T_f^{recover} - T_f^{fail} \quad ...(9)$$

Where *recovery time (S)* is the average time taken to reschedule tasks after a VM failure in schedule S. It measures the system's resilience, and lower values indicate faster recovery. F is the set of all failure events (*e.g.*, VM crashes, hardware faults), $|F|$ is the total number of failures observed, $f \in F$ represents a specific failure event from the set F, T_f^{fail} is the timestamp when failure f occurs, $T_f^{recover}$ is the timestamp when the system fully recovers from failure F (*e.g.*, tasks are rescheduled, VMs are restored), and $T_f^{recover} - T_f^{fail}$ is the downtime duration for failure *f, i.e.*, time between failure and recovery.

Fairness Index (Jain's Index)

The fairness index, based on Jain's fairness index, quantifies how equitably resources are allocated among users in a system (*e.g.*, network bandwidth, CPU time, cloud resources), as is clear from equation (10).

$$Fairness\ index(S) = \frac{(\sum_{j \epsilon U} VM_j)^2}{|U| \cdot \sum_{j \epsilon U} VM_j^2} \quad ...(10)$$

Where VM_i represents the resources allocated to user i, $Fairness\ index(S)$ is a score between *0* and *1* measuring the fairness of resource allocation in system S, U is the set of users (or tasks, flows, VMs) competing for resources, $|U|$ is the total number of users, $i \epsilon U$ is a specific user in the set U, and VM_j is the resources allocated to user i (*e.g.*, bandwidth, CPU cycles, memory).

Speedup ratio

Speedup ratio represents the improvement over baseline schedulers, as detailed in equation (11).

$$Speedup\ ratio(S) = \frac{Makespan_{Baseline}}{Makespan_{ABC-LNN}} \quad ...(11)$$

Where $Makespan_{Baseline}$ is the makespan under a reference scheduler, and $Makespan_{ABC-LNN}$ is the makespan with the proposed method.

Scalability

Scalability measures how well a system can handle increasing workloads (*e.g.*, users, tasks, data) while maintaining performance, a general scalability metric can be defined as equation (12).

$$Scalability(N) = \frac{Performance(N)}{Performance(1)} X \frac{1}{N} \quad ...(12)$$

Where *N* represents the scaling factor (*e.g.*, number of nodes, users, or parallel tasks), performance (*N*) is a performance metric (*e.g.*, throughput, speedup, latency) at scale *N* and performance (*1*) is baseline performance representing the initial condition.

All parameters are scaled to $[0,1]$ for the fitness function. dynamic weights (w_i) are adjusted via LNN based on real-time priorities. LNN continuously optimizes η_i and refines ABC solutions using equation (13).

$$\eta_i(t+1) = LNN(\eta_i(t), QoS\ Metrics(t)) \quad ...(13)$$

This framework ensures multi-objective optimization while adapting to cloud dynamics.

Objective function

The hybrid model optimizes twelve QoS parameters to minimize makespan, latency, and resource imbalance while maximizing throughput, fairness, and scalability. The multi-objective fitness function is formulated as equation (14).

$$F(S) = w_1 \cdot Makespan(S) + w_2 \cdot Latency(S) + w_3 . Response\ time(S) + w_4 . \left(\frac{1}{Throughput\ (S)}\right) + w_5 . \left(1 - Resource\ utilization(S)\right) + w_6 . Load\ imbalance(S) + w_7 . Convergence\ time\ (S) + w_8 . Training\ time(S) + w_9 . Recovery\ time(S) + w_{10} . \left(1 - Fairness\ index(S)\right) w_{11} . \frac{1}{Speed\ Up\ Ratio(S)} + w_{12} . Scalability\ penalty(S)$$ ...(14)

Where S represents the task-resource mapping solution, α_i represents the normalized weight coefficients, and goal of the objective function is to minimize (S).

ABC optimization for global task-resource mapping

The ABC optimization mechanism employs employed bees, onlooker bees, and scout bees for global task-resource mapping. Employed bees modify solutions using equation (15).

$$s_{ij}^{new} = s_{ij} + \phi_{ij}\left(s_{ij} - s_{kj}\right) \quad ...(15)$$

Where $\phi_{ij} \in [-1,1]$ is a random perturbation. Onlooker bees select solutions probabilistically using equation (16), scout bees replace stagnant solutions with random ones.

$$P_i = \frac{\frac{1}{F(S_i)}}{\sum_{j=1}^{P} \frac{1}{F(S_j)}} \quad ...(16)$$

Where P_i represents the probability of selecting the i_{th} solution by an onlooker bee, $F(S_i)$ is the objective function value (fitness) of the i_{th} solution S_i, P is the total number of solutions in the population, and S_i denotes the j_{th} solution in the population.

Liquid neural network (LNN) for dynamic adaptation

The LNN processes real-time cloud metrics (CPU, memory, task delays) and adjusts ABC-generated solutions. The LNN state transition is modelled as equation (17).

$$\frac{dh(t)}{dt} = -\frac{h(t)}{\tau} + W.\sigma\left(h(t)\right) + B.x(t) \quad ...(17)$$

Where $h(t)$ represents the hidden state at time t , τ represents the time constant that controls adaptability, recurrent weights are represented by W, σ symbolizes the leaky-ReLU activation, B represents the input weights, and real-time QoS metrics are represented by $x(t)$.

The LNN has 256 neurones, use a 12-dimensional vector representing CPU consumption and task delays, and features a linear output layer for adaptation signals. The output readout layer employs untrained, high-dimensional reservoir dynamics for cost-effective temporal processing. Optimizer, loss function, epochs, batch size, and update frequency are training hyper parameters. Online supervision is used for training. The Adam optimiser uses 0.001 learning rate, $\beta_1 = 0.9$, and $\beta_2 = 0.999$ for consistent gradient updates to meet the target. The mean squared error (MSE) between ground-truth targets produced from simulated optimal states and predicted adaption adjustments (such as QoS weight perturbations) is shown in equation (18).

$$L = \frac{1}{N}\sum_{i=1}^{N} \|\hat{y}_t - y_t\|^2 \quad ...(18)$$

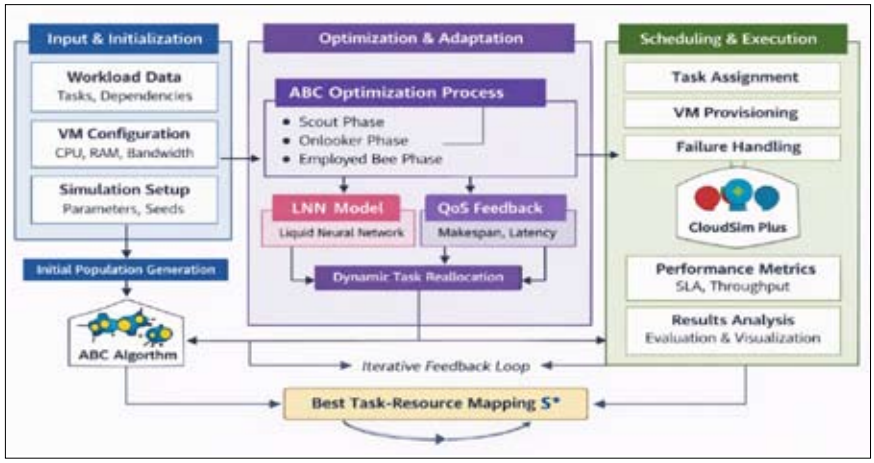

Figure 1: System architecture of proposed AALS algorithm.

Algorithm adaptive ABC - LNN scheduler (AALS) algorithm

Input:

Task set $T = \{T_1, T_2, \ldots, T_n\}$, Resource set $VM = \{VM_1, VM_2, \ldots, VM_m\}$

QoS weights w_i (initialized uniformly, later adapted by LNN)

ABC parameters: Colony size p, max iterations I_{max}, abandonment limit L

LNN parameters: Time constant τ, hidden state dimension d, learning rate η

Output: Optimized Task-Resource Mapping S^*

1. Artificial Bee Colony (ABC) Global Optimization
2. Employed Bee Phase (Exploitation)
3. Generate a new candidate s_i^{new}.
4. $s_{ij}^{new} = s_{ij} + \Phi_{ij}(s_{ij} - s_{kj})\ (\Phi_{ij} \in [-1,1], k \neq i)$
5. Evaluate $F(s_i^{new})$ and apply greedy selection between s_i and s_i^{new}.
6. Onlooker Bee Phase (Selection & Refinement)
7. Compute selection probabilities $P_i = \frac{\frac{1}{F(S_i)}}{\sum_{j=1}^{P} \frac{1}{F(S_j)}}$
8. Select solutions based on P_i and refine them using the same perturbation as employed bees.
9. Scout Bee Phase (Exploration)
10. If a solution s_i does not improve for L iterations, replace it with

    $s_i^{rand} = RandomSolution()$
11. Liquid Neural Network (LNN) Dynamic Adaptation
12. Input Real-time QoS metrics

    $x(t) = [CPU, Memory, Latency, Load, \ldots]$
13. LNN State Update $\frac{dh(t)}{dt} = -\frac{h(t)}{\tau} + W \cdot \sigma(h(t)) + B \cdot x(t)$

    where σ is Leaky-ReLU, W and B are learned weights.
14. Dynamic Weight Adjustment

    $\alpha_i(t+1) = Softmax\left(LNN(h(t), x(t))\right)$
15. If LoadImbalance(S) >*Threshold*, LNN modifies ABC solutions by

    $s_{ij}^{adopted} = s_{ij} + \Delta_{ij},\ \ \Delta_{ij} \sim N(0, \sigma^2)$

    where σ is adjusted based on LNN's hidden state.
16. Failure Detection
17. Remove all t_i assigned to r_j.
18. Reassign using LNN-guided rescheduling

    $$s_{ik}^{new} = arg\min_{k \in R}(F(s) + \lambda \cdot RecoveryTime)$$
19. Stop

    If $\text{ConvergenceTime}(S) < \epsilon$ or $I = I_{max}$
20. Output Best solution $S^* = arg\min_{s} F(S)$

Output of LNN is $\widehat{y_t}$, while goal deviation from equilibrium is y_t. A 50 epoch adaption cycle uses 32 sample streaming quality of service data mini-batches. Auto training commences when task load changes exceed 10%. At five ABC method iterations (0.1 seconds in simulation), incremental updates enable real-time refinement. In the LNN method, the QoS vector of the present solution is processed as input (x_t) after each ABC step has been completed. Adaptive perturbations Δw_i are generated for dynamic weights in the multi-objective fitness function, as shown in equation (19).

$$w_i^{(t+1)} = w_i^{(t)} + \eta \cdot \Delta w_i \quad ...(19)$$

For prioritizing poor performing metrics, such as high latency, Δw_i is used with $\eta = 0.05$ threshold. Figure 1 illustrates the system architecture of the proposed AALS. This scheduler combines ABC-based global optimisation with LNN-driven adaptive decision-making to facilitate efficient task-resource mapping in cloud environments. The architecture comprises input initialisation, optimisation and adaptation, and scheduling execution stages, which facilitate dynamic QoS-aware scheduling with real-time fault detection and rescheduling.

The proposed hybrid adaptive ABC - LNN scheduler (AALS) approach optimizes twelve QoS parameters (makespan, latency, throughput, fault tolerance) and outperforms eight benchmarks while maintaining polynomial time complexity $O(I.(P \cdot n \cdot m + d^2))$ and linear space complexity $O(P.n.m + d^2)$, where I denotes the number of iterations, P is the population (colony) size, n represents the number of tasks, m is the number of resources (VMs), and d is the dimensionality of the LNN hidden state.

Time and space complexity analysis

The overall computational complexity of the proposed AALS is obtained by summing the computational costs of the ABC optimization module and the Liquid Neural Network (LNN) adaptation module.

Derivation of time complexity

Let $P =$ colony size, $I =$ maximum number of iterations, $n =$ number of cloud tasks, $m =$ number of virtual machines, $P =$ hidden-state (reservoir) dimension of the LNN, $L =$ abandonment limit.

The initialization phase generates P candidate schedules for n tasks over m virtual machines. Therefore,

$$T_{init} = O(P \cdot n \cdot m) \quad ...(20)$$

The employed bee phase evaluates one neighbouring solution for every candidate solution. Hence,

$$T_{emp} = O(P \cdot n \cdot m) \quad ...(21)$$

The onlooker bee phase computes selection probabilities and refines candidate schedules. Thus,

$$T_{onl} = O(P^2 + P \cdot n \cdot m) \quad ...(22)$$

The scout bee phase replaces abandoned solutions, resulting in

$$T_{scout} = O(P \cdot L) \quad ...(23)$$

The Liquid Neural Network updates the hidden state using matrix-vector computations. Therefore,

$$T_{LNN} = O(d^2) \quad ...(24)$$

The total computational cost during one optimization iteration is obtained as

$$T_{iter} = T_{emp} + T_{onl} + T_{scout} + T_{LNN}$$

$$= O(P \cdot n \cdot m) + O(P^2 + P \cdot n \cdot m) + O(P \cdot L) + O(d^2) \quad ...(25)$$

Since $P^2 \ll P \cdot n \cdot m, P \cdot L \ll P \cdot n \cdot m,$ for practical cloud scheduling problems where $n \geq P$ and $m \geq 1$,

$$T_{iter} = O(P \cdot n \cdot m + d^2) \quad ...(26)$$

Considering I optimization iterations,

$$T_{AALS} = O(I(P \cdot n \cdot m + d^2)) \quad ...(27)$$

Derivation of space complexity

The memory requirement consists of the ABC population and the LNN parameters.The ABC population stores P candidate schedules.

Hence, $S_{ABC} = O(P \cdot n \cdot m) \quad ...(28)$

The LNN stores hidden-state vector, recurrent weight matrix, input weight matrix, bias vector.

Therefore, $S_{LNN} = O(d^2) \quad ...(29)$

The overall memory requirement becomes

$$S_{AALS} = S_{ABC} + S_{LNN} = O(P \cdot n \cdot m) + O(d^2) \quad ...(30)$$

$$S_{AALS} = O(P \cdot n \cdot m + d^2) \quad ...(31)$$

The proposed AALS approach exhibits a good computational complexity when compared with the base optimization algorithms, as summarized in Table 2.

Table 2: Complexity Comparison

Algorithm	Time Complexity	Space Complexity
ABC	$O(I \cdot P \cdot n \cdot m)$	$O(P \cdot n \cdot m)$
PSO	$O(I \cdot P \cdot n \cdot m)$	$O(P \cdot n \cdot m)$
ACO	$O(I \cdot n^2 \cdot m)$	$O(n^2)$
ABC-GA	$O\big(I(P \cdot n \cdot m + G)\big)$	$O(P \cdot n \cdot m)$
Proposed AALS	$O\big(I(P \cdot n \cdot m + d^2)\big)$	$O(P \cdot n \cdot m + d^2)$

Where G denotes the computational cost associated with genetic crossover and mutation operations.

Simulation set up

To assess the effectiveness for task scheduling and resource allocation in dynamic cloud systems, the simulation environment for the hybrid AALS scheduler has been developed. In order to satisfy the evaluation criteria, this was implemented. The framework is capable of accommodating scalable tasks, with tasks ranging from one thousand to ten thousand, and was executed on two hundred to one thousand virtual machines (VMs). Subsets of Alibaba cluster trace medium-duration task loads with computational sizes from 500 to 5,000 million Instructions (MI) are used to generate workloads. These workloads are derived from the total workloads. The simulation framework provided by CloudSim Plus is employed to conduct experimental procedures. Detailed information regarding the framework of the simulation environment is presented in Table 3, which illustrates the key components of the environment.

Table 3: Simulation environment for the AALS algorithm.

Category	Parameter	Value
Simulation environment	Simulation platform	CloudSim Plus
	Programming language	Java (JDK 17), Python 3.11
	Operating system	Ubuntu 22.04 LTS
Cloud infrastructure	Number of data centres	4
	Hosts per data centre	50
	Host CPU	64 cores
	Host RAM	64 GB
	Host storage	2 TB NVMe
	Network bandwidth	10 Gbps
Virtual machine configuration	Number of VMs	200-1,000
	Processing capacity	2,000 MIPS
	VM configuration	8 vCPUs, 4 GB RAM
	VM storage	20 GB
	VM bandwidth	500 Mbps
Taskload characteristics	Number of tasks	1,000-10,000
	Task length	500-5,000 MI
	Input data size	100-500 MB
	Inter-task data transfer	100-500 MB

The parameter values for the nine baseline metaheuristic algorithms listed in Table 4, as well as the proposed hybrid adaptive artificial bee colony liquid neural network scheduler, can be identified. The proposed

scheduler is included in this table. This was completed with the objective of guaranteeing that each algorithm comparison is both fair and reproducible, and it was successful in achieving this objective. Each technique had a population or colony size of fifty, and a maximum of three hundred iterations were used to ensure that the information processing work was done consistently.

Table 4: Parameters for baseline algorithms and the proposed AALS.

Algorithm	Key parameters with values
PSO	Swarm size = 50, Max iterations = 300, Inertia weight (w) = 0.9→0.4 (linear), c1 = 2.0, c2 = 2.0
ACO	Colony size = 50, α = 1, β = 5, Evaporation rate (ρ) = 0.1, Q = 100
GWO	Pack size = 50, Max iterations = 300, a (control parameter) = 2→0
HHO	Hawk population = 50, Max iterations = 300, Escape energy (E) = 2→0
CS	Nest size = 50, Discovery probability (Pa) = 0.25
WOA	Whale population = 50, Max iterations = 300, a = 2→0, b = 1
ABC	Colony size (employed + onlooker) = 50, employed = 25, Limit = 100
FPA	Population size = 50, Switch probability (p) = 0.8
ABC-GA	Population size = 50, ABC Limit = 100, GA crossover (pc) = 0.9, mutation (pm) = 0.05
AALS (Proposed)	ABC component: Colony size = 50 (employed + observer), Employed = 25, Limit = 100, Max iterations = 300 LNN component: Reservoir size = 256, Optimizer = Adam, Learning rate = 0.001, Loss = MSE on adaptation error, Update frequency = every 5 ABC iterations, Adaptation rate η = 0.05

The AALS paradigm is constructed by employing this methodology. This platform optimizes cloud task scheduling and resource allocation. This framework enables automation and simplification. Both techniques are essential for the functionality of cloud computing. cloud computing is inoperative without them. Therefore, extensive simulation studies are needed to evaluate this method and ensure it achieves the desired results.

RESULTS AND DISCUSSION

This section evaluates the adaptive artificial bee colony liquid neural network scheduler (AALS) approach discussed earlier in the study. Testing took place in CloudSim Plus. The most crucial QoS features for various scheduling systems were compared. The Friedman, Nemenyi, and Wilcoxon tests established statistical significance. The purpose of this was to determine the data for any unusual features.

Performance evaluation of the proposed AALS scheduler

This subsection compares the proposed AALS experimental results against baseline methods for various task loads and virtual machine setups. A multitude of tasks encompasses this difference. The findings are analyzed for similarities and differences. More specifically, the comparison and contrast pertain to the two sets of results. The analysis of comparison and contrast is conducted across a wide range of task sizes. The study considers a diverse array of significant aspects related to the excellence of service. This category encompasses a variety of ancillary characteristics, such as makespan, latency, reaction time, throughput, resource utilization, and load balancing.

The AALS is evaluated using a variety of task load scenarios. This makes it possible to conduct a thorough analysis of the AALS. Also, Figures 2-13 illustrate the results of the investigation conducted on this methodology. Twelve different quality of service measures were used in the analysis. Measures such as throughput, latency, makespan, and scalability are included in this category. Contrary to other well-known metaheuristic scheduling strategies, this specific metaheuristic scheduling approach has been explored and implemented in reality. article swarm optimization (PSO), Ant colony optimization (ACO), grey wolf optimization (GWO), Harris Hawks optimization (HHO), Cuckoo search (CS), whale optimization algorithm (WOA), artificial bee colony (ABC), flower pollination algorithm (FPA), and the enhanced hybrid artificial bee colony - genetic algorithm (ABC-GA) approach are among the techniques that have

been explored. The proposed scheduling paradigm was assessed under different task load scenarios. The AALS scheduler's efficacy across a variety of QoS metrics is summarized in Table 5. The Alibaba cluster trace task load subset has been utilized. The results exhibited consistent percentage enhancements over the efficient baseline algorithms in all configurations.

The hybrid adaptive artificial bee colony-liquid neural network scheduler (AALS) demonstrates exceptional scalability when executing tasks. These data are illustrated in Table 4 by a multiplicity of experiments. The makespan decreases from 68.94 seconds (1,000 tasks on 200 virtual machines) to 57 seconds as the capacity increases. Throughput increases almost linearly to 10.642 tasks per second, while latency and response time decrease. CPU utilisation increases to 86.42%, load imbalance is reduced, and the speedup ratio and scalability factor achieve values between 1.80 and 1.86 at 10,000 tasks over 1,000 virtual machines.

Table 5: Simulated compact performance comparison summary.

Tasks	VMs	Makespan (s)	Throughput (tasks/s)	Latency (ms)	Response time (ms)	CPU utilization (%)	Load imbalance (std)	Speedup ratio	Scalability factor
1000	200	68.94	1.443	31.44	35.44	64.55	2.42	1.25	1.22
2000	250	66.68	4.04	29.36	33.47	66.97	2.12	1.31	1.29
3000	300	64.53	6.655	27.84	31.91	69.92	1.93	1.38	1.36
4000	400	62.1	7.821	26.11	29.84	72.33	1.81	1.42	1.42
5000	500	60.57	8.704	24.68	28.11	74.81	1.68	1.48	1.48
6000	600	59.57	9.343	23.46	26.79	77.24	1.56	1.54	1.53
7000	700	58.88	9.833	22.34	25.68	79.68	1.49	1.61	1.6
8000	800	57.57	10.195	21.79	24.91	82.13	1.46	1.68	1.68
9000	900	56.94	10.447	21.23	24.34	84.57	1.42	1.74	1.76
10000	1000	57.05	10.642	20.99	24.25	86.42	1.41	1.8	1.86

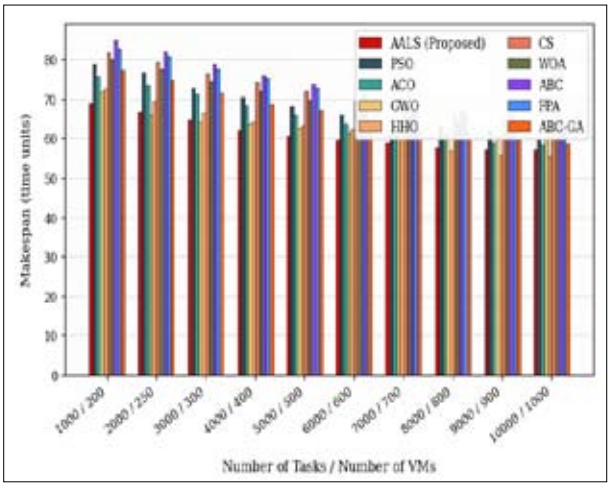

Figure 2: Makespan comparison.

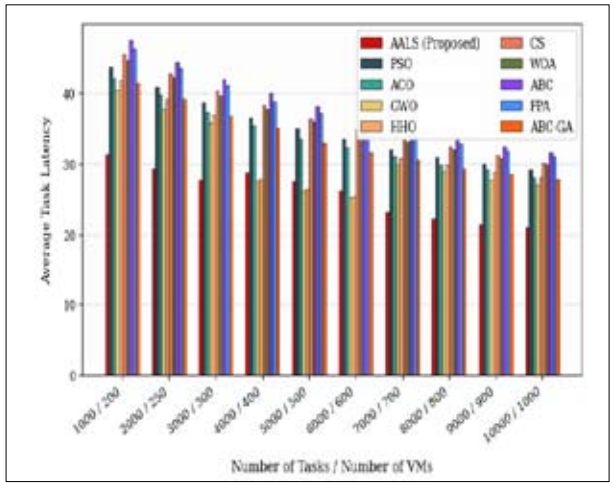

Figure 3: Latency comparison.

Figure 2 shows average makespan across workloads (1,000-10,000 tasks). AALS consistently achieves the lowest values, from 68.94 s (1,000 tasks) to 57.05 s (10,000 tasks). The hybrid ABC-LNN approach enables strong scaling, outperforming PSO (59.80 - 78.82 s), ACO (58.29 - 75.71 s), and others by 5 - 15% in most configurations. Figure 3 compares average latency (×10² ms). AALS records the lowest latency, decreasing from 31.44 to 20.99 across scales, thanks to LNN-driven real-time adaptation. It reduces latency by 20 - 35% compared to GWO (27.04 - 40.47) and HHO (28.03 - 41.96), minimizing queuing delays effectively.

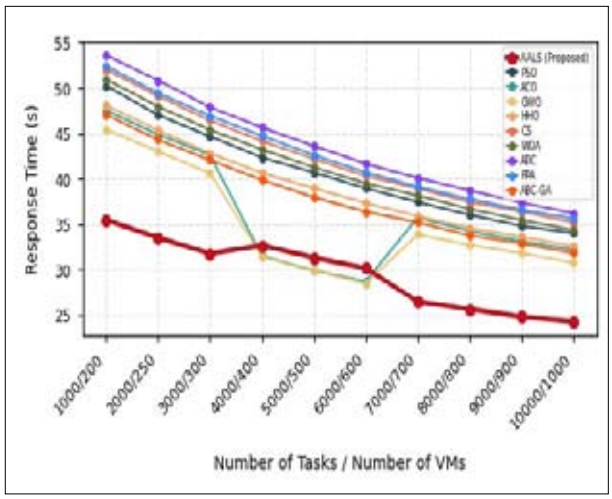

Figure 4: Response time comparison.

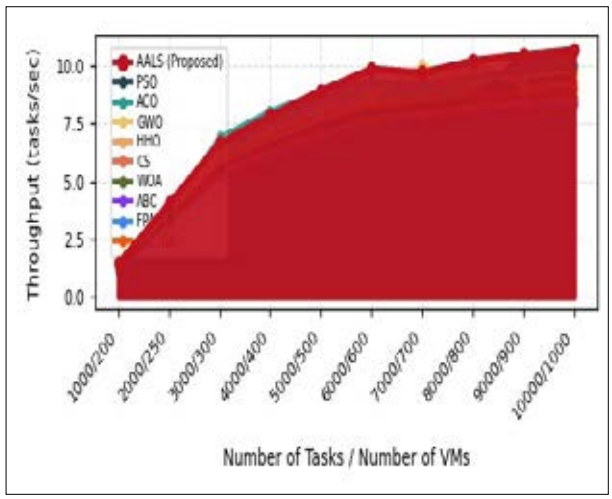

Figure 5: Throughput comparison.

The normal response time appears in Figure 4, where it is expressed in milliseconds in accordance with the metrics. AALS's most notable accomplishment is the decrease of the score from 35.44 to 24.25. This is the most remarkable success that it has achieved. Dynamic Quality of Service refinement reduces response times by 15 - 40% compared to PSO (33.98 - 50.20), ACO (32.16 - 47.49), and ABC. These guarantees tasks are completed on time throughout the process. Figure 5 depicts the standard throughput, quantified in tasks per second. The AALS algorithm typically achieves maximum or near-maximum performance, capable of scaling from 1.443 to 10.642 jobs per second. It achieves enhanced performance compared to ACO (9.979), GWO (9.698), and HHO (9.221) when substantially implemented, hence optimizing the capacity for parallel processing.

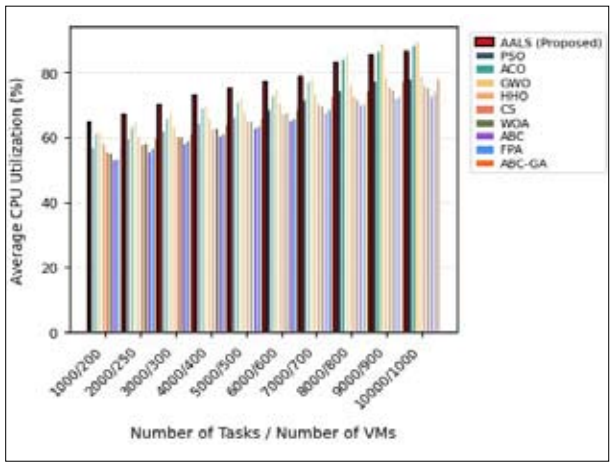

Figure 6: Resource utilization comparison.

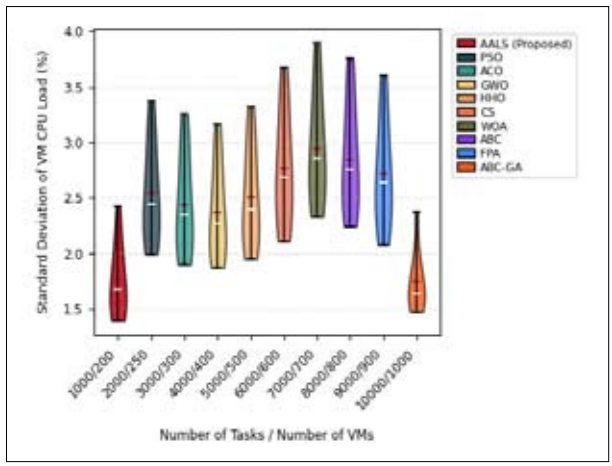

Figure 7: Load imbalance comparison.

Figure 6 illustrates the typical percentage of CPU utilization. As a result of the greater load balancing, AALS reaches the maximum levels, which range from 64.55 percent to 86.42 percent. It consistently exceeds the majority of baselines by 5 - 15%, with GWO occasionally being competitive at extremely large dimensions. Figure 7, which depicts the standard deviation of CPU load, shows that there is an imbalance in the load. By attaining the lowest values (2.422 → 1.412), the AALS algorithm effectively ensures that the distribution is uniform across the entire dataset. It minimizes imbalance by 20% to 50% more effectively than most baseline approaches and surpasses ABC-GA on a broader scale.

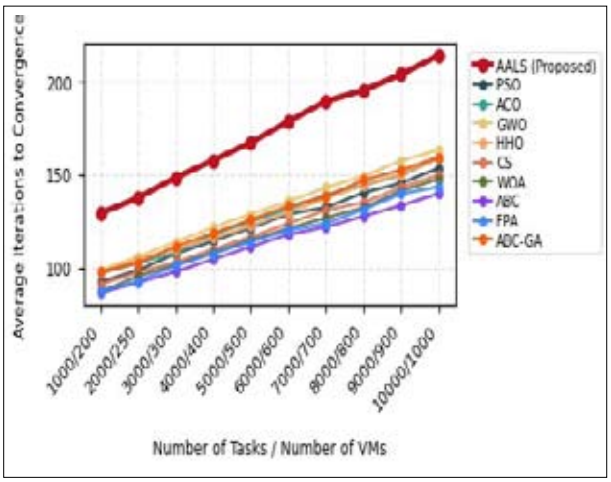

Figure 8: Convergence speed comparison.

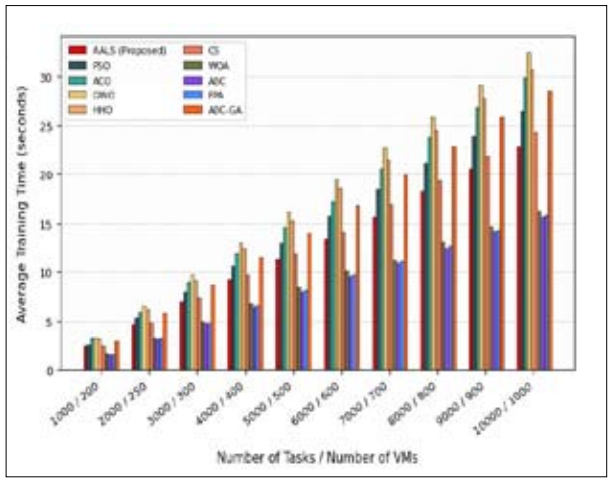

Figure 9: Training time comparison.

Figure 8 illustrates various average convergences. Comprehensive LNN research identified between 129 and 214 iterations for AALS. This is required by the algorithm. Although exceeding WOA/ABC (87-148), it enhances end-to-end quality of service trade-offs. This remains accurate regardless of its immutability. A comparison of the time spent on training is illustrated in Figure 9. Compensation for the adaptive advantages available can be achieved by offsetting the significant overhead encountered by AALS, which varies from 2.41 to 2.85 seconds. Notwithstanding the quick implementation of lightweight methodologies like WOA, ABC, and FPA, AALS demonstrates greater overall efficacy.

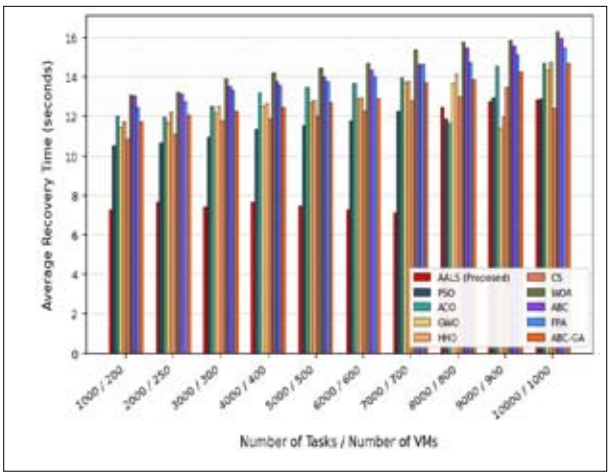

Figure 10: Recovery time comparison.

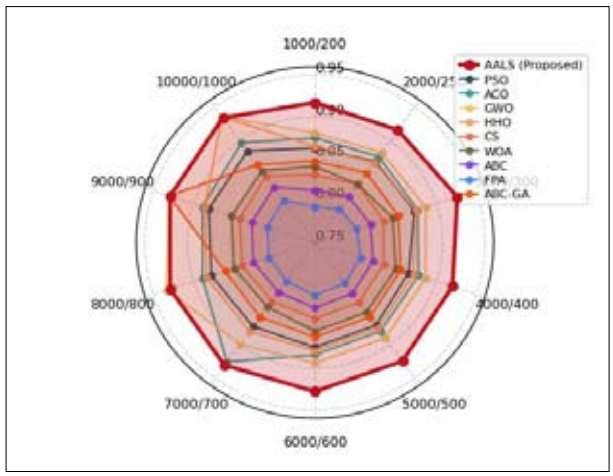

Figure 11: Fairness index comparison.

Figure 10 illustrates the duration of failure recovery. The AALS typically recovers most rapidly, within 7.29 to 12.86 seconds. Rescheduling with LNN can do this. PSO/CS can attain elevated velocities at substantial scales, whereas AALS can accommodate faults in certain instances. Figure 11 illustrates that Jain's fairness index indicates the AALS possesses the greatest significant values (0.917-0.934), reflecting resource equity. This is accurate as AALS metrics are at their peak. It surpasses the majority of baselines at extensive scales, with GWO closely behind.

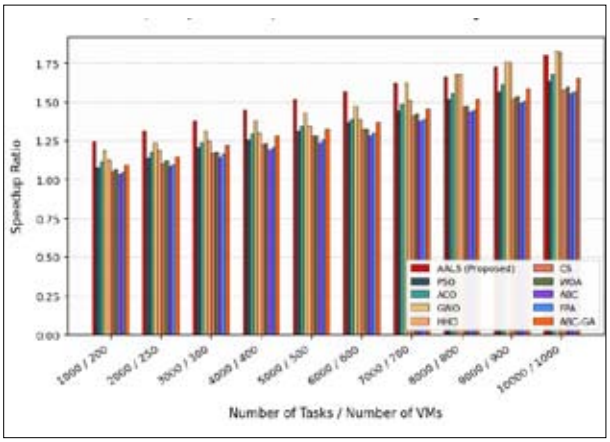

Figure 12: Speedup ratio comparison.

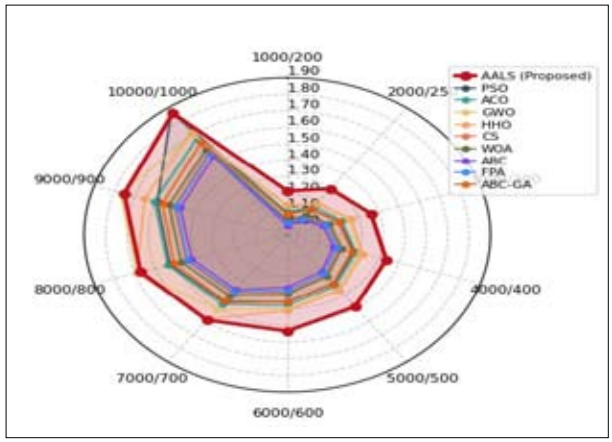

Figure 13: Scalability comparison.

Figure 12 illustrates the speedup ratio. If tasks exceed 10,000, the AALS will reach a maximum of 1.80. This figure shows performance in comparison to the baseline. That the AALS has these features means that it has a lot of promise for parallel scalability and optimization. Figure 13 represents the methodology for estimating the scalability ratio. The AALS scales approximately linearly at maximum load, with a value of 1.861. This may provide a competitive advantage over baselines, which reduce in performance after 7,000-8,000 tasks.

Comparative analysis and discussion of scheduling behaviour

This subsection intends to deliver thorough quantitative comparisons of the scheduling behaviour of all algorithms. This quantitative analysis is performed utilizing the precise data shown in Figures 2-13. AALS completes 1,000 tasks in an average of 68.94 seconds, while 10,000 tasks necessitate 57.05 seconds. This is illustrated in Figure 2. Consequently, it outperforms PSO, ACO, GWO, HHO, CS, WOA, FPA, and ABC-GA across all evaluated metrics. All auxiliary algorithms consistently exhibit prolonged overall execution times over the complete workload spectrum. AALS may decrease latency from 31.44 milliseconds to 20.99 milliseconds, consistently outperforming PSO, ACO, GWO, HHO, CS, WOA, FPA, and ABC-GA across all work sizes. This stays applicable irrespective of any other considerations. Figure 3 succinctly depicts this. The response time for the AALS diminishes from 35.44 to 24.25 milliseconds, sustaining low values in comparison to other methodologies. Figure 4 illustrates this. It outperforms PSO and ACO, which demonstrate enhanced efficacy during operation. PSO, ACO, GWO (9.70 tasks/s), HHO, CS, WOA, FPA, and ABC-GA demonstrate suboptimal throughput relative to AALS. It can maintain a throughput of 1.44 tasks per second and 10.64 tasks per second (Figure 5). Although ACO is inferior to AALS, it is capable of completing 9.98 tasks per second at its maximum capacity. The CPU utilization of AALS increases from 64.6% to 86.4% (Figure 6), while PSO, ACO, GWO, HHO, CS, WOA, FPA, and ABC-GA constantly remain below this threshold, regardless of task load. AALS demonstrates a consistent increase in CPU use. AALS achieves the lowest load imbalance among all methods, decreasing values from 2.422 to 1.412, as illustrated in Figure 7. Alternative algorithms demonstrate more load imbalance. The imbalance values of PSO, ACO, GWO, HHO, CS, WOA, FPA, and ABC-GA continually surpass each other. The scalability research (Fig. 8) demonstrates that the AALS has risen from 1.22 to 1.86, indicating improved scaling efficiency compared to baseline techniques, which show delayed

saturation at higher workloads. AALS demonstrates 129 to 214 convergence iterations (Figure 9), somewhat surpassing lightweight algorithms like WOA and ABC, but remaining comparable to hybrid and metaheuristic methods. This range is illustrated in the accompanying figure. The integration of LNN resulted in a significant increase in the training duration, from 2.41 to 22.85 seconds (Figure10). Performance is improved by this approach; however, it necessitates a longer timeframe than PSO, ACO, CS, WOA, and FPA. When AALS fails, it recovers more quickly than PSO, ACO, GWO, HHO, CS, WOA, FPA, and ABC-GA (Figure 11). Furthermore, AALS dominates all QoS metrics (Figure 12, 13). AALS utilises ABC-based global search and LNN-driven adaptive learning to enhance performance, in contrast to PSO and ACO, which exhibit premature convergence, CS, WOA, and FPA, which demonstrate stochastic instability, and GWO, HHO, and ABC-GA, which lack real-time adaptability. Every QoS evaluation corresponds with this arrangement and exhibits resilience and scalability. Comprehensive algorithmic assessments indicate that this framework exhibits reliable performance.

Descriptive performance and stability

To assess the hybrid adaptive artificial bee colony - liquid neural network scheduler (AALS), mean values and standard deviations were computed from thirty trials spanning ten workload configurations (ranging from 1,000 to 10,000 tasks) and nine metaheuristic methods. These measures were executed to evaluate the AALS. AALS has minimal values for makespan (62.53 ± 3.84 s), latency (25.18 ± 2.96 ms), response time (29.61 ± 3.12 ms), training time (12.63 ± 5.41 s), and recovery time (10.42 ± 2.11 s). It attains ideal CPU utilization (75.62 ± 6.48%), throughput (6.84 ± 3.21 tasks/s), fairness index (0.93 ± 0.04), speedup ratio (1.48 ± 0.16), and scalability factor (1.54 ± 0.22), demonstrating its efficacy across all QoS dimensions. Most indicators exhibit a low standard deviation, indicating that AALS is more stable than baseline techniques. Makespan, latency, and load balancing can be scheduled consistently with minimal trial and error. AALS improves cloud performance and dependability by regulating dispersion and providing beneficial mean values.

Statistical validation

AALS exhibited strong performance with minimal volatility across thirty service quality parameter assessments. The Friedman test indicates substantial differences ($p < 1 \times 10^{-13}$), with the AALS group exhibiting superior performance. The Wilcoxon and Nemenyi tests surpass the majority of baseline methods in determining statistical significance. This enables it to contest leading methodologies. Friedman ranking, Nemenyi post-hoc comparison, and Wilcoxon signed-rank testing analysed scheduling algorithm performance gaps for twelve quality of service parameters and ten workload configurations (1,000-10,000 tasks). It guaranteed an exhaustive evaluation.

Friedman test

The Friedman test was initially employed to compare algorithms. Results below 1×10^{-13} indicate that the null hypothesis of similar performance is rejected. AALS averages 1.08, HHO 2.11, ABC-GA 3.27, and GWO 3.94. The mean GWO is 3.94. The mean GWO score of 3.94 occupies the highest rank. PSO, ACO, CS, WOA, and FPA are prioritised higher due to substandard service quality. The statistics demonstrate that AALS excels in several tasks.

Nemenyi post-hoc test

The Nemenyi post-hoc test identified pairwise differences. The critical difference (CD) of 4.49 was statistically significant at $\alpha = 0.05$. The rank discrepancies between AALS and FPA, CS, WOA, PSO, and ACO above the CD threshold indicate substantial enhancements. AALS has rank discrepancies beneath the significant threshold, although surpassing GWO, ABC-GA, and HHO. This signifies that these differences lack statistical significance at the specified confidence level.

Wilcoxon signed-rank test

AALS was compared to each baseline algorithm for all quality of service and workload variables using the Wilcoxon signed-rank test. It was noteworthy that this research corroborated such findings. AALS outperformed PSO, ACO, CS, WOA, and FPA, disproving the null hypothesis. Significant increases ($p < 0.01$) were identified in the statistical analysis. HHO, GWO, and ABC-GA have all made significant improvements, as well as minor adjustments, resulting in significant improvements in all essential metrics. Large-scale, statistically valid real cloud scheduling updates have moderate to high practical effects, due to the fact that enhancements are much larger. The data indicate that AALS consistently enhances performance, rather than irregularly. Dynamic cloud task scheduling is feasible due to the fact that AALS is not arbitrary.

Experimental and statistical evidence demonstrates that the proposed AALS scheduler outperforms current metaheuristic algorithms in scheduling across several QoS measures. The conclusion section encapsulates these findings and discusses prospective research avenues.

CONCLUSION

Research introduces a hybrid scheduling approach designed to enhance task scheduling and resource allocation in cloud computing environments. Integrating artificial bee colony optimization with liquid neural networks accomplishes this goal. The usage of the hybrid scheduling strategy enables this to be accomplished. It overcomes the constraints associated with traditional metaheuristic scheduling systems by combining population-based search with adaptive learning. This is accomplished by integrating the two approaches. A dynamic scheduler considers the number of resources available and the pressure exerted on the system's responsibilities. The proposed AALS scheduler was demonstrated to increase makespan, latency, response time, throughput, and resource utilization using CloudSim Plus simulations. This allows for better task and resource mapping and load distribution among virtual machines. The Friedman, Nemenyi and Wilcoxon tests show that the suggested scheduling algorithm outperforms others. Adaptive neural network models and metaheuristic optimization have been shown to increase scheduling performance in large scale cloud computing, as demonstrated by research. The proposed AALS scheduler reduced makespan by up to 27%, reduced latency by 35%, improved throughput by approximately 20%, and achieved CPU utilization of 86.42%, outperforming nine state-of-the-art cloud scheduling algorithms.

The paradigm may be applied to more intricate distributed computing architectures, including cloud, edge, and fog infrastructures, in order to stimulate more research. It would be vital to implement this in the future. With these technologies, scheduling must consider global resources and latency sensitive applications. Furthermore, to improve the dependability of multi-tenant cloud infrastructures, it is feasible to implement security aware scheduling algorithms as a potential solution. Uncertainty quantification can also improve scheduling resilience to changing task arrivals and execution times. The reason for this is that these methodologies enable the management of uncertainty in tasks features. Besides, it is possible that the incorporation of energy aware and carbon aware scheduling algorithms, which take into account actual energy usage, carbon emission metrics, and environmental sustainability, will play a role in the development of environmentally friendly cloud data centres. In the subsequent phase, the solution must be tested on actual cloud platforms or container orchestration environments. As a result, the technology's applicability and scalability in cloud systems that are currently operational will be revealed.

Acknowledgement

The authors extend their sincere gratitude to the Principal of the College of IT & Management Education (CIME), Bhubaneswar, Odisha, India-751010, for his support, guidance, and encouragement during this endeavor. They extend sincere appreciation to the esteemed academics and dedicated staff of CIME for their unwavering support, collaboration, and shared quest for knowledge, which have significantly contributed to this venture and facilitated its successful completion.

REFERENCES

Abraham, O. L., Ngadi, M. A. B., Sharif, J. B. M., & Sidik, M. K. M. (2025). Multi-objective optimization techniques in cloud task scheduling: A systematic literature review. *IEEE Access, 13*, 12255–12291. https://doi.org/10.1109/access.2025.3529839

Agrawal, K. K., Kumar, S., Seth, J. K., Gupta, A. K., & Lamba, S. (2025). An effective algorithm for predicting load and dynamic task scheduling in cloud fog architecture for smart homes. *International Journal of Cloud Computing, 14*(1), 54–85. https://doi.org/10.1504/ijcc.2025.145657

Beena, B. M., Prashanth, C. S. R., Manideep, T. S. S., Saragadam, S., & Karthik, G. (2025). A green cloud-based framework for energy-efficient task scheduling using carbon intensity data for heterogeneous cloud servers. *IEEE Access, 13*, 73916–73938. https://doi.org/10.1109/access.2025.3562882

Chen, H., Liu, J., & Zhu, Z. (2025). A dynamic energy-efficient scheduling method for periodic workflows based on collaboration of edge-cloud computing resources. *Concurrency and Computation: Practice and Experience, 37*(3), Article e8362. https://doi.org/10.1002/cpe.8362

Chen, K., Yu, Q., Li, L., & Chen, J. (2025). Deep reinforcement learning for dynamic task scheduling in data relay satellite networks. *IEEE Transactions on Vehicular Technology*. Advance online publication. https://doi.org/10.1109/tvt.2025.3555594

Djebbar, E. I., & Belalem, G. (2025). Improvement of the ACO algorithm for intelligent task scheduling in cloud systems. *Scalable Computing: Practice and Experience, 26*(2), 531–539. https://doi.org/10.12694/scpe.v26i2.3946

Farooq, M., Zafar, A., & Samad, A. (2025). FR-EAHTS: Federated reinforcement learning for enhanced task scheduling with hierarchical load balancing and dynamic

power adjustment in multi-core systems. *Telecommunication Systems, 88*(2), 1–23. https://doi.org/10.1007/s11235-025-01276-0

Feng, H., Li, H., Liu, Y., Cao, K., & Zhou, X. (2025). A novel virtual machine placement algorithm based on grey wolf optimization. *Journal of Cloud Computing, 14*(1), Article 7. https://doi.org/10.1186/s13677-025-00730-3

Gu, Y., Liu, Z., Dai, S., Liu, C., Wang, Y., Wang, S., Theodoropoulos, G., & Cheng, L. (2025). *Deep reinforcement learning for job scheduling and resource management in cloud computing: An algorithm-level review* [Preprint]. arXiv. https://doi.org/10.48550/arXiv.2501.01007

Guan, J. (2025). Enhanced network security hybrid cloud workflow scheduling using Levy-optimized slime mould algorithm. *Informatica, 49*(1), Article 18. https://doi.org/10.31449/inf.v49i18.7327

Hayawi, K., Sajid, J., Malik, A. W., & Mathew, S. S. (2025). Digital twin assisted task offloading for workload management at fog nodes. *IEEE Internet of Things Journal*, *12*(13), 23061–23072. https://doi.org/10.1109/jiot.2025.3550832

He, H., Gu, Y., Hu, Y., Fang, F., Ning, X., Chen, X., & Cheng, L. (2025). Real-time workflow scheduling in hybrid clouds with privacy and security constraints: A deep reinforcement learning approach. *Expert Systems With Applications*, 278, *Article 127376*. https://doi.org/10.1016/j.eswa.2025.127376

Jangu, N., & Raza, Z. (2025). A modified jellyfish search algorithm for task scheduling in fog-cloud systems. *Concurrency and Computation: Practice and Experience, 37*(9–11), Article e70054. https://doi.org/10.1002/cpe.70054

Johari, V., & Pandey, R. (2025). Load balancing in cloud using improved GWO (iGWO). *International Journal on Science and Technology, 16*(2). https://doi.org/10.71097/IJSAT.v16.i2.3323

Kaur, S., Singh, J., & Bharti, V. (2025). An optimised AI-driven swarm-based enhanced task scheduling model for cloud computing environment. *International Journal of Cloud Computing, 14*(1), 25–53. https://doi.org/10.1504/ijcc.2025.145660

Khan, A., Ullah, F., Shah, D., Khan, M. H., Ali, S., & Tahir, M. (2025). EcoTaskSched: A hybrid machine learning approach for energy-efficient task scheduling in IoT-based fog-cloud environments. *Scientific Reports, 15*(1), Article 12296. https://doi.org/10.1038/s41598-025-96974-9

Kumar, K., Verma, A., Gupta, N., & Yadav, A. (2023). Liquid neural networks: A novel approach to dynamic information processing. In *2023 International Conference on Advances in Computation, Communication and Information Technology (ICAICCIT)* (pp. 725–730). IEEE. https://doi.org/10.1109/icaiccit60255.2023.10466162

Kumar, R., & Vardhan, M. (2025). IBWC: A user-centric approach to multi-objective cloud task scheduling using improved beluga whale optimization. *Knowledge and Information Systems*. Advance online publication. https://doi.org/10.1007/s10115-024-02325-x

Kushwaha, S., Shankar Singh, R., & Prajapati, K. (2025). Multi-objective workflow scheduling in cloud using Archimedes optimization algorithm. *Concurrency and Computation: Practice and Experience, 37*(4–5), Article e8393. https://doi.org/10.1002/cpe.8393

Luo, Q., Xie, B., Wang, J., Shuai, J., & Cui, H. (2025). A hybrid approach to task offloading optimization: Integrating hybrid whale genetic algorithm and reinforcement learning. *The Computer Journal, 68(9), 1225–1236*. Advance online publication. https://doi.org/10.1093/comjnl/bxaf033

Mahapatra, A., Pradhan, R., Majhi, S. K., & Mishra, K. (2025). DELTa: Dynamic energy-and-latency-aware task scheduling for fog-cloud paradigm. *IEEE Access, 13, 74613–74629*. Advance online publication. https://doi.org/10.1109/access.2025.3563103

Mahmoudi, A., Farzinvash, L., & Taheri, J. (2025). GPTOR: Gridded GA and PSO-based task offloading and ordering in IoT-edge-cloud computing. *Results in Engineering*, 25, *Article 104196*. https://doi.org/10.1016/j.rineng.2025.104196

Patni, S., Saxena, D., & Singh, A. K. (2025). Dynamic resource allocation models. In *Resource management in cloud computing: Concepts and implementation* (pp. 67–87). Springer. https://doi.org/10.1007/978-3-031-83053-2_4

Peng, K., Hu, Y., Ding, H., Chen, H., Wang, L., Cai, C., & Hu, M. (2025). Large-scale service mesh orchestration with probabilistic routing in cloud data centers. *IEEE Transactions on Services Computing*. Advance online publication. https://doi.org/10.1109/tsc.2025.3526373

Salehnia, T., Seyfollahi, A., Raziani, S., Noori, A., Ghaffari, A., Alsoud, A. R., & Abualigah, L. (2024). An optimal task scheduling method in IoT-fog-cloud network using multi-objective moth-flame algorithm. *Multimedia Tools and Applications, 83*(12), 34351–34372. https://doi.org/10.1007/s11042-023-16971-w

Sankaran, P., Lingishetty, S. K., & Kumar, M. (2025). Leveraging reinforcement learning for efficient task scheduling in multi-cloud environments. *International Journal of Innovative Research in Computer Science and Technology, 13*(2), 35–41. https://doi.org/10.55524/ijircst.2025.13.2.6

Shah, M., Rajwar, D., Dehury, J. P., & Kumar, D. (2025). VM placement in cloud computing using nature-inspired optimization algorithms. In *Nature-inspired optimization algorithms for cyber-physical systems* (pp. 251–282). IGI Global Scientific Publishing. https://doi.org/10.4018/979-8-3693-6834-3.ch008

Shen, Q., Hu, B.-J., & Xia, E. (2025). Cuckoo search-enabled task scheduling and cache updating in vehicular edge-fog computing. *IEEE Transactions on Vehicular Technology, 74*(6), 9656–9670. https://doi.org/10.1109/tvt.2025.3540639

Siruvoru, V., & Aparna, S. (2025). Harmonic migration algorithm for virtual machine migration and switching strategy in cloud computing. *Concurrency and Computation: Practice and Experience, 37*(1), Article e8320. https://doi.org/10.1002/cpe.8320

Smithamol, M. B., & Sridhar, R. (2025). REACT: Reinforcement learning and multi-objective optimization

for task scheduling in ultra-dense edge networks. *Ad Hoc Networks, 174*, Article 103834. https://doi.org/10.1016/j.adhoc.2025.103834

Suganthi, E., & Selvi, F. K. M. (2025). Virtual machine load balancing model framework for cloud computing. *Engineering, Technology & Applied Science Research, 15*(3), 22553–22558. https://doi.org/10.48084/etasr.10556

Sui, X. F., Zhang, S. W., Wang, J. S., Zhang, S. H., Zhang, Y. H., & Bai, X. L. (2025). Mayfly algorithm with elementary functions and mathematical spirals for task scheduling in cloud computing system. *The Journal of Supercomputing, 81*(6), Article 766. https://doi.org/10.1007/s11227-025-07231-9

Tang, X., Liu, F., Wang, B., Zhang, M., Jiang, J., Tang, Q., Wu, Q., & Chen, C. P. (2025). Cost and makespan-aware task scheduling with deep reinforcement learning in multicloud environments. *IEEE Transactions on Computational Social Systems, 12*(6), 4217–4230. https://doi.org/10.1109/tcss.2025.3553856

Wajid, M. A., Wajid, M. S., Zafar, A., & Terashima-Marin, H. (2025). Digital twin technology for multimodal-based smart mobility using hybrid Co-ABC optimization based deep CNN. *Cluster Computing, 28*(3), Article 194. https://doi.org/10.1007/s10586-024-04903-8

Wang, H., Gill, S. S., & Uhlig, S. (2025). *COUNTER: Cluster GCN based energy efficient resource management for sustainable cloud computing environments* [Preprint]. arXiv. https://doi.org/10.48550/arXiv.2504.09995

Zhao, F., Lin, W., Lin, S., Tang, S., & Li, K. (2025). MSCNet: Multi-scale network with convolutions for long-term cloud workload prediction. *IEEE Transactions on Services Computing, 18*(2), 969–982. https://doi.org/10.1109/tsc.2025.3536313

Zhao, S., Yan, H., Lin, Q., Lin, Y., & Zhang, D. (2024). Cloud computing resource scheduling based on modified bee colony algorithm. In 2024 36th Chinese Control and Decision Conference (CCDC) (pp. 1558–1561). IEEE. https://doi.org/10.1109/ccdc62350.2024.10587717

Zou, W., Zhang, Z., Wang, N., Tian, Y., & Tian, L. (2025). ReflexPilot: Startup-aware dependent task scheduling based on deep reinforcement learning for edge-cloud collaborative computing. IEEE Transactions on Cloud Computing, 13(2), 641–654. https://doi.org/10.1109/tcc.2025.3555231

J.Natn.Sci.Foundation Sri Lanka 2026 54 (3): 389 - 406
DOI: http://dx.doi.org/10.4038/jnsfsr.v54i3.12687

RESEARCH ARTICLE

Deep Learning

Nerenchi Bot: A robotic system for playing the board game 'Nerenchi' against a human opponent

MKMGPA Jayasinghe[1*] and B Hettige[2]
1 Department of Computer Engineering, Faculty of Computing General Sir John Kotelawala Defence University, Sri Lanka.
2 Department of Knowledge Engineering and Communication, Faculty of Computing, University of Sri Jayewardenepura, Sri Lanka.

Submitted: 11 July 2025; Revised: 15 May 2026; Accepted: 26 June 2026

Abstract: The Sri Lankan board game Nerenchi, known for its rules and strategic depth, is played by two players, which requires skill and strategy. Nerenchi has two stages: the placing stage to place tokens and the moving stage to move tokens along the lines. The objective is to arrange three tokens in a straight line. Due to technological evolution and the modern world, people cannot experience the actual experience in the physical environment. Although Nerenchi is on the verge of extinction, innovative approaches to updating and conserving these games are necessary to keep them culturally relevant and engaging for modern audiences. This Paper reports the design and development of an intelligent gaming-robot capable of competing against a human, named as 'Nerenchi Bot'. The proposed main system comprises three sub systems, mainly, the Monitoring system, the Decision-making system and the Robotic system. The Monitoring System automatically determines all the positions of the board and the tokens, using edge detection, grid detection and colour detection techniques through OpenCV at 95% of accuracy and generates 24 index position array. The Decision-making system used an algorithm that acts according to game rules, to decide the next movement. The monitoring system and the decision-making system communicate through the position array. According to the index values, the system is capable of deciding the next step according to the principles and game rules. The Robotic system, comprised of a robotic arm, using servo motors, performs actions such as placing, removing, and replacing tokens. These subsystems and the whole system were separately tested with experienced human opponents. More than 100 matches were played with human opponents, and the results were encouraging. This paper also demonstrates the system's viability by detailing its hardware, computer vision, and decision-making methods.

Keywords: Computer vision, gaming robots, human-computer gaming, Nerenchi, Sri Lankan traditional board games

INTRODUCTION

A game with rules and regulations governing the tokens and objects moved, taken out, put back, or replaced on a board or other previously marked surface is called a board game. These board games are played to demonstrate intellectual engagement without requiring many resources or logistics (Meththananda & Hettige, 2015; Pandithage & Hettige, n.d.). A large portion of well-known board games in history are adaptations of real military conflicts (Kruthika et al., 2016). Traditional board games are a type of tabletop gaming that involves social interaction among players gathered around a table to create a shared, engaging, and enjoyable experience. Players' actions are transferred through interactions with tangible objects (Bandaranaike & Hettige, n.d.).

Board games have been an important part of human culture and entertainment for centuries. Ancient people spent their leisure time developing strategic thinking, social interaction and problem solving skills through physical gameplay. With the rapid development of digital technology and lifestyle, people often have limited time to gather and play board games physically and many games are now played using mobile phones and computers, reducing the real interactive experience of

* Corresponding author (pamudithajayasinghe2000@gmail.com; https://orcid.org/0009-0003-0972-1007)

This article is published under the Creative Commons CC-BY-ND License (http://creativecommons.org/licenses/by-nd/4.0/). This license permits use, distribution and reproduction, commercial and non-commercial, provided that the original work is properly cited and is not changed in anyway.

physical gameplay. Recent advancements in robotics and modern technology have created new ways to modernise and preserve the physical nature of board games through human robot interaction.

There have been many kinds of folk games in Sri Lanka since ancient times, including board and field games. "Pancha Keliya", "Olinda Keliya", "An Keliya", “Peralikatuma”, “Batta”, “Gudu Keliya” and "Porapol gasima" are a few of the folk games that are still well-known in Sri Lanka today. Among them is "Nerenchi", which is on the verge of extinction and was once a favourite among Sri Lankan women (Gawesha et al., 2022).

The board game "Nerenchi," which was found in Sri Lanka (c. AD 10), is very similar to Nine Men's Morris, which is said to be among the oldest games ever found in an Egyptian temple in Kurna in Egypt, dating to approximately 1440 BC. In contrast to Nine Men's Morris and its regulations, the Nerenchi board features diagonal lines connecting the square corners. Evidence of these boards has been discovered in Sri Lanka on a rock near Lankarama Dageba (Stupa) and on the steps leading to the holy hill at Mihintale (Meththananda & Hettige, 2015). Although Nerenchi is a part of Sri Lankan culture and was popular in earlier generations, its popularity has declined due to technological advancements in the Sri Lankan lifestyle (Gawesha et al., 2022).

Nerenchi is designed on a straightforward board with two distinct sets of tokens, with diagonal lines connecting the corners and horizontal and vertical lines joining the middle of three concentric squares, as shown in Figure 1. This arrangement allows for two players to compete against one another. There are two main phases / levels in Nerenchi.

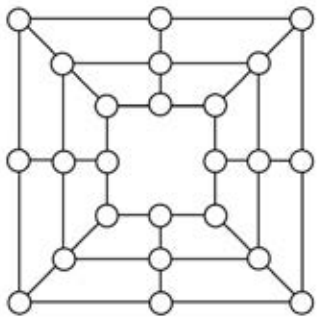

Figure 1: Nerenchi board with empty positions

Placing Stage: Nerenchi tokens should be laid on the board. Each player hosts 12 tokens. If a player's three tokens are arranged vertically, horizontally or diagonally, the player receives an additional placing chance known as a "nerenchi". With this additional opportunity, the layer can disrupt the turn-sharing process by playing again. This stage lasts until there are 22 Tokens on the board or until one player has placed all 12 of their Tokens on the board. After that, it is the opponent's turn to begin the next phase (even if the current player had three Tokens on the board at the end of his or her last move). The conclusion of the placing phase is the beginning of the Moving phase. Figure 2 depicts the three Tokens in a line that were rewarded as “Nerenchi”.

Moving Stage: On this stage, players can move tokens to an adjacent circle along the line vertically and horizontally, but players are not allowed to move tokens diagonally. The possible moves are shown in Figure 3.

With the most recent move, players can acquire three tokens of the opponent’s in a straight line, vertically,

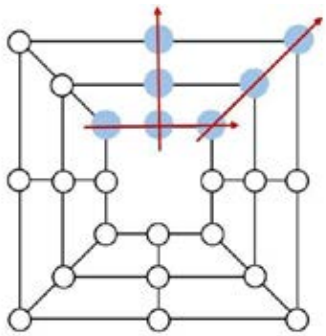

Figure 2: Three (3) tokens on Nerenchi state

horizontally, or diagonally, allowing them to capture the opponent’s counters. The opponent then takes turns moving after the player has had the opportunity to collect any tokens they may have.

Winning Conditions: The game’s winning criterion is determined after the end of the moving stage. The opponent can be eliminated from the game by capturing every token on the board except two that belong to them, or the current player can win if the opponent is unable to make any acceptable moves at all (Jayasinghe et al., 2024).

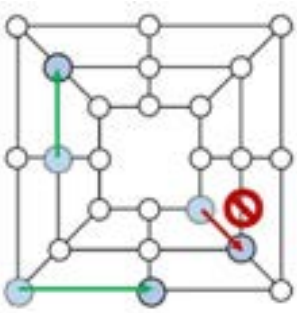

Figure 3: Possible moves

Developers attempted to use computers to play these card and board games as a result of technological advancements. They created those human-versus-computer games in place of human-versus-human ones. This marked a significant turning point in the history of both computing and gaming, following decades of overcoming numerous obstacles since the 1950s.

Board games like Chess, Checkers, Chinese Go, etc., have already been automated with modern technology, but the board game Nerenchi has not yet been automated. This study proposes an approach for implementing an intelligent gaming robot system that physically interacts with the Nerenchi board and tokens using a robotic arm. The system uses an algorithm to generate and execute game moves, relying on computer vision algorithms to identify board positions and tokens. With the help of a link, the robotic arm precisely executes the movements, ensuring an easy and engaging gaming experience for human gamers.

The objective of this project is to use computer vision and rule-based processing to create and deploy an intelligent robotic arm capable of playing Nerenchi against a human opponent. Games like Nerenchi are at risk of becoming obsolete in the digital age. Creative solutions are required to conserve and modernise ancient games and make them interesting to audiences in the modern era. It is often impossible for modern robotic gaming systems to engage with classic board games in an intelligent, smooth way through physical interaction.
The rest of this paper is organised as follows. Section 2 discusses the related work, Section 3 presents the methodology, Section 4 describes the implementation and Section 5 presents the Testing and evaluation. Section 6 concludes the paper, and the Further Work section follows.

Related work

Human-computer gaming has a long history, and the Turing (Saygin et al., 2000), proposed in 1950, was the first human–computer game. It judges whether a machine has the intelligence of a human, and it was a main tool for verifying the key Artificial Intelligence technologies (Cagiltay, 2007; Crouser & Chang, 2012). Researchers are inspired by this to develop Artificial Intelligence capable of challenging and beating professional-level human players. Due to advancements in the field and the evolution of computers, several projects by developers are being developed that can beat humans.

For example, in 1989, the draughts AI called 'Chinook' defeated the world champion. Then, in 1994, Marion Tinsley failed to achieve the target (Schaeffer et al., 1996). In 1995, IBM developed a prototype of a chess-playing expert system and released it in 1996, naming it 'Deep Blue'. In 1997, Deep Blue defeated Garry Kasparov, the chess grandmaster, by 2 wins for Deep Blue, 3 draws and 1 win for Kasparov. It was a great achievement in the history of computing (Deep Blue | Semantic Scholar, n.d.).

Later, the rapid development of computers and the human – computer gaming AIs such as DQN agent (Mnih et al., 2015), Libratus (*Superhuman AI for Heads-up No-Limit Poker: Libratus Beats Top Professionals*, n.d.), AlphaGo (Silver et al., 2016), OpenAI Five (*Dota 2 with Large Scale Deep Reinforcement Learning | BibSonomy*, n.d.), Alpha Star (Vinyals et al., 2019), etc. With a combination of modern techniques, these AIs can defeat professional human players in certain games easily, indicating a big step in the decision-making intelligence (Badia et al., 2020; Baker et al., 2020; *Superhuman AI for Multiplayer Poker*, n.d.; Zribi & Sung, 1998).

In 2018, Vito Janko presented a robotic system that can play the card game Briscola by combining artificial intelligence, computer vision, and a robotic arm. This system can recognise cards, decide optimal moves using algorithms and physically interact with the game, demonstrating a complete integration of perception, decision making and action (Janko, 2018). The paper by Lin Yong and team presents a blended board game system that integrates a physical game with a robotic arm to support the development of computational thinking skills. It emphasises human-machine competition, where students play against the robot (Yong et al., 2023). In 2011, Cynthia Matuszek and team presented their

study about a fully autonomous robot that can play chess against a human or another player. It integrates Computer vision to recognise the chessboard and tokens, an AI system to decide the moves and a robotic arm to physically move the tokens on the board (Matuszek et al., 2011).

Table 1: Comparison between existing systems

	Game	Technology used	Year	Success rate
Deep-Blue by IBM	Chess	chess-playing expert system	1995 (prototype) 1996 (release) 1997 (upgrade)	2 wins for Deep Blue, 1 win for Kasparov (Chess grandmaster), and 3 draws
AlphaGo by Deepmind Technologies	Go	computer programme (combination of machine learning and tree search techniques such as Monte Carlo tree search, guided by a "value network" and a "policy network," both implemented using deep neural network technology)	2012	Defeated the world Go champion, Lee Sedol, in a five-game match in 2016. AlphaGo won four of the five games, with Lee Sedol winning one.
AlphaZero by Deepmind Technologies, the AI research company	Go Chess Shogi	computer programme, as in AlphaGo (neural networks)	2017, December 05	three games by defeating world-champion programmes Stockfish, Elmo, and the three-day version of AlphaGo Zero
Stockfish by the Stockfish community	Chess	free and open-source chess engine	Initial release : 2008 Stable release : June 30, 2023	Elo rating was around 3600 or higher, which is significantly above the highest human rating ever achieved
Libratus by researchers at Carnegie Mellon University	Poker	AI computer programme (The technique involved is a new variant of counterfactual regret minimisation, namely the CFR+ method introduced in 2014 by Oskari Tammelin)	2015	emerged as the clear victor in the 20-day tournament called "Brains vs. AI" against four top human professional poker players
Leela Chess Zero (LCZero) by programmer Gary Linscott, developer for the Stockfish chess engine	Chess	free, open-source, and deep neural network–based chess engine (machine-learning algorithm, mirrored from AlphaZero)	Initial release : 9 January 2018 Stable release : 21 July 2023	Elo rating exceeding 3,500
Computer Go (Tsume-Go)	Go	AI dedicated, to creating a computer programme (some form of tree search, pattern matching and knowledge-based systems, The application of Monte Carlo methods, use of machine learning.)	1980 - 2015	-
DeepStack by an international team from Charles University, Czech Technical University and University of Alberta.	Poker	artificial intelligence computer programme (neural networks and continual resolving)	2015	Over all games played, DeepStack won 49 big blinds/100 (always folding would only lose 75 bb/100), over four standard deviations from zero
Dark Horse" (□□) by Beijing Shuanghuai Information Technology Development Co., Ltd	Xiangqi (Chinese chess)	chess-playing AI, such as minimax algorithms, alpha-beta pruning, and heuristic evaluations	-	-

When developing these games, several types of technologies were used. These approaches also positively affect the modern computer gaming industry. Comparisons between outstanding and famous existing systems are shown in Table 1.

Peitz, Eriksson, and Björk explained how traditional board games can be improved by adding Electronics and Computing. They proposed new game ideas and prototypes where physical board games are combined with digital features such as sensors and interactive systems to make board games more engaging, interactive and modern while preserving the physical playing experience (Peitz et al., 2005). In 2026, Zhiyi He and Lee conducted a study to build a system that connects virtual games with real physical robots, allowing actions in a computer game to be carried out by a robot in the real world, creating a more interactive and realistic experience (He & Lee, 2026).

In 2025, Alexander and Emil explored the potential of electronic board games by developing a prototype that integrates digital components such as OLED displays, RFID tags, and microcontrollers into a traditional board game setup to improve engagement and simplify gameplay tracking (Karlsson & Påsse, 2025). Thabet and Judhi present the design and implementation of a smart, automated chessboard that uses embedded systems and automation techniques, such as RFID, magnetic sensors, optical detection, and software and game logic algorithms, to physically move chess tokens and manage gameplay (Thabet & Prasetyo, 2025).

Related to Nerenchi

In 2015, Meththananda and Hettige developed and implemented the Nerenchi board game using a web-based architecture. The design and implementation of the web-based architecture for the Nerenchi game are presented in their paper. The computational model for the game Nerenchi uses two matrices to control user failures and a set of rules (Meththananda & Hettige, 2015).

To identify tokens on a Nerenchi Board, Pandithage and Hettige used an image processing technique in 2020. To identify the current locations of each party's tokens on the board and to produce the token positions as an array, they used an image-processing system (Pandithage & Hettige, 2020).

Hettige and Bandaranaike developed a communication platform for the Sri Lankan board game Nerenchi in 2021. They used a novel technique to develop a digital Nerenchi game that can recognise the board's current state (Bandaranaike & Hettige, 2021).

The article titled "Implementation of Autonomous Robotic Arm for Nerenchi" was written by Gawesha, Hettige, and Goonatilleke in 2022. They proposed a methodology for evaluating in a laboratory setting and for contrasting the detection accuracy of image processing methods (Gawesha et al., 2022).

Jayasinghe, Hettige, and Meththananda implemented a robotic solution for playing Nerenchi against a human opponent, physically using a robotic arm, computer vision, and a knowledge-based decision-making system (Jayasinghe et al., 2024).

MATERIALS AND METHODS

The diagram in Figure 4 illustrates the Engineering Design Process, a structured approach engineers follow to develop effective solutions. It begins by defining the problem, clearly identifying the core issue or need. Once the problem is understood, the next step is to conduct background research, gathering information and understanding existing solutions or constraints. This is followed by specifying the requirements, outlining what the solution must achieve and any limitations involved. With this foundation, engineers brainstorm, evaluate, and choose the best solution, exploring different ideas and selecting the most viable one. Next, they develop and prototype the solution, building a working model or system based on the chosen design. The prototype is then tested to determine whether it functions as expected. If the solution meets the requirements, the process moves on to communicating the results. However, if the solution partially meets or fails to meet the requirements, the team returns to earlier steps to revise the design, rework the prototype, and test again. This iterative loop—powered by testing, feedback, and improvements—is key to refining the solution until it effectively meets the defined objectives (*Engineering Design Process*, n.d.).

The reverse engineering method, with the engineering design process approach, is used to develop this solution.

Design

The webcam is mounted on top of the board to capture top-view real-time footage to detect the positions and the Nerenchi Tokens, and it sends the data to the monitoring system for identification. The monitoring system runs on

a computer, uses algorithms to generate and decide the next step based on the positions, and sends instructions to the PCB to execute the required movement of the robotic arm to place, replace, and remove tokens. Figure 5 depicts the fully designed system.

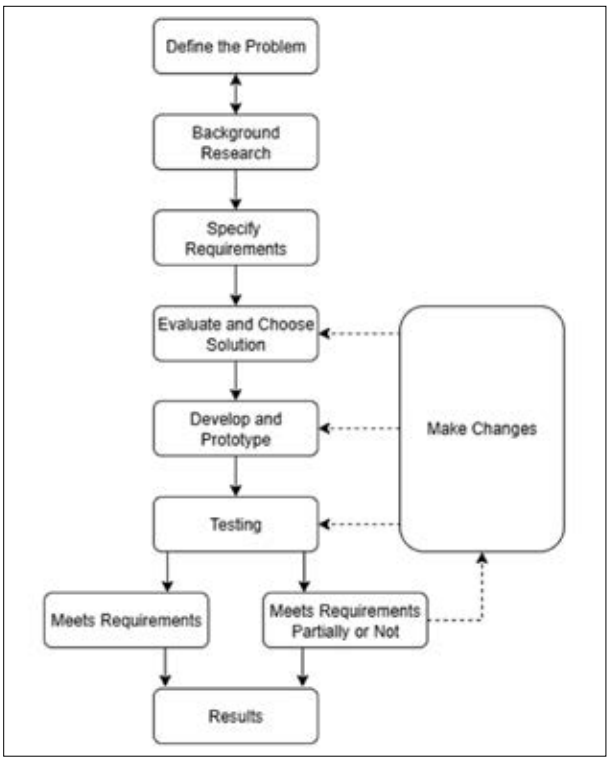

Figure 4: Engineering design process approach

A webcam connected to the computer captures the board's status and changes using computer vision algorithms running on the computer. This helps identify the board's current state and generate the position array for the next step.

Black and white are the only colours used in the Nerenchi Board design (Figure 6). Because the board is black and white, a webcam can simply capture it and distinguish the tokens from the board's hue. The board of Nerenchi was placed on an 18" x 18" piece of plastic board. Due to its matte surface, the sticker helps prevent light reflections that could cause the webcam to provide inaccurate data. Round pieces are laser-cut from 3 mm thick coloured acrylic board. These pieces are coloured

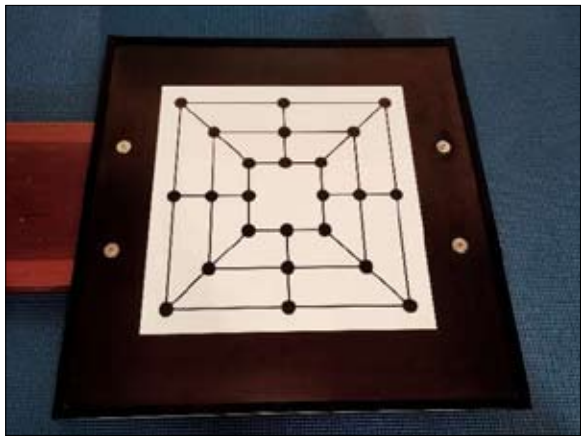

Figure 6: Designed Nerenchi board

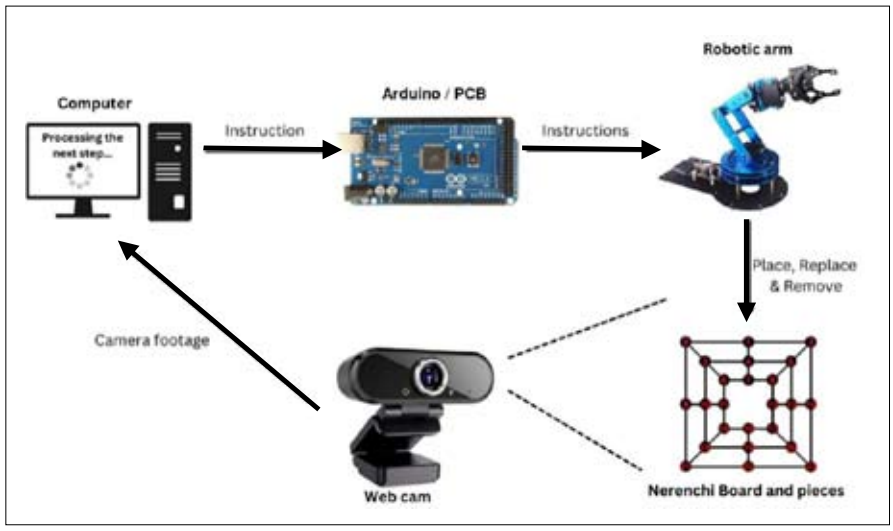

Figure 5: Basic design

red and blue, which makes it easier for the webcam to detect them. The Nerenchi tokens are shown in both hues in Figure 7.

The 4 DOF Robotic Arm is fully designed in accordance with the project's specifications, as shown in Figure 7. The movements are done by the servo motors that are connected with a specially designed PCB to operate the entire Robotic system.

Tokens made from steel washers covered with plastic boards. Red and Blue colours are used for these tokens, which help the webcam detect the tokens more easily. Figure 7 depicts the Nerenchi Tokens in both colours.

The entire system is shown in Figure 8.

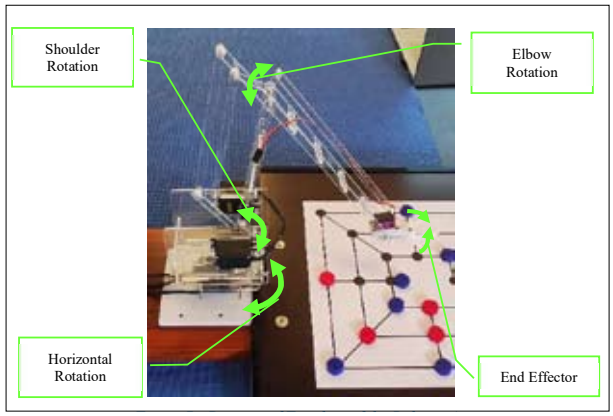

Figure 7: Degrees of freedom of the robotic arm



Figure 8: Fully designed system

Monitoring system

The monitoring system of the intelligent gaming robot, ensures seamless interaction between the game components and the decision-making system. It contains the webcam that is connected to the computer and the token and position detection algorithm running on the computer using OpenCV and creating a 24-index position array to represent the status of the positions (Noel et al., 2011; Zribi & Sung, 1998).

A webcam serves as the primary vision sensor, continuously capturing the game board and transmitting real-time images to the processing unit. Figure 9 depicts the algorithm used in the Monitoring system. Firstly, the programme starts, and it creates a text file naming it with the date and time that the match starts and accesses the webcam. If the webcam is accessed by the programme, then it divides the video footage into a 7x7 grid and starts the 10-second colour calibration process to increase the colour identification ability of red and blue colours. After the calibration, the system uses computer vision techniques to detect and track the positions of red and blue tokens after the opponent presses the button, updating a digital representation of the board as a 24-index position array. All the 24-index position arrays were recorded in the previously created text file for further use. This data is cross-referenced with the algorithms implemented in the decision making system to determine optimal moves.

The monitoring system also records human player moves to identify strategies and maintain game

accuracy. The integration of visual feedback ensures precise movement of the robotic arm, which physically manipulates game tokens on the board (Chen & Wang, 2019; Wölflein & Arandjelović, 2021). Figure 9 depicts the algorithm of the Monitoring system.

Token detection

Token detection is an important part and depends on the system's overall output. Figure 10 shows the flowchart of the token detection algorithm.

Before detecting the tokens, the programme must calibrate the colours and obtain the average red and blue values. Then the camera footage is divided into a 7 x 7 grid, as in Figure 11. Then, the colours are checked to identify the tokens on squares that have a position assigned to a 24-index array (Seewald, 2010).

If the position is empty, then the corresponding index will be 0. If a token is in the position, the array index that place will be 1 or 2 due to the colour of the token. Figure 12 depicts the numbered positions of the Nerenchi Board according to the array indexes.

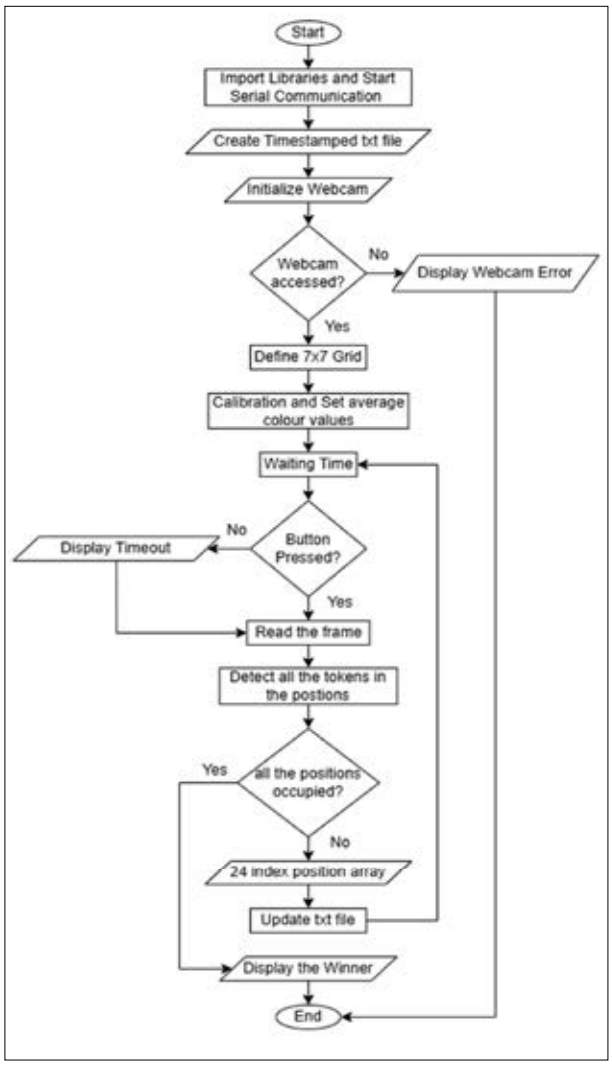

Figure 9: Algorithm of the Monitoring system

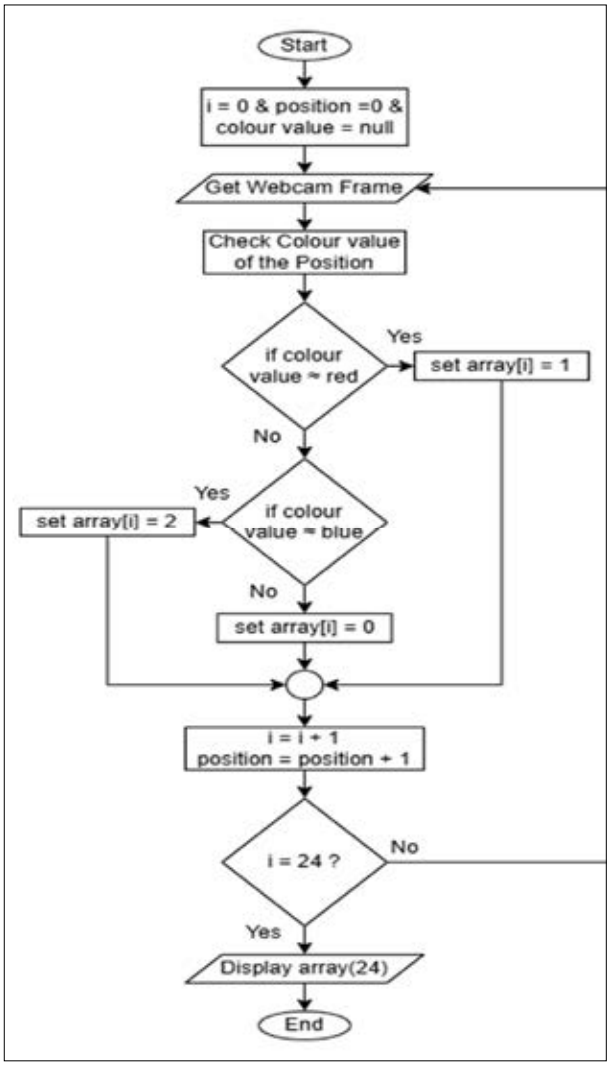

Figure 10: Token Detection algorithm

As an example, Position Array of an empty board:
[0 0 0 0 0 0 0 0 0 0 0 0 0 0 0 0 0 0 0 0 0 0 0 0]

Position Array of a board in the match:
[1 0 2 0 1 1 0 2 2 2 0 1 0 0 0 2 0 1 0 2 0 1 0 0]

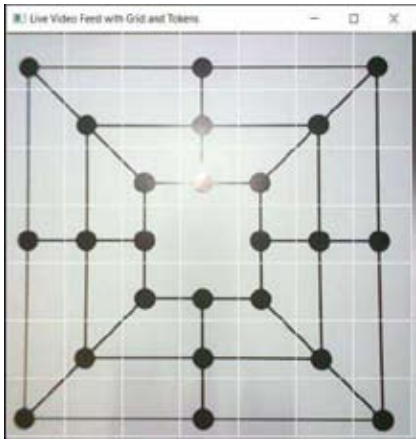

Figure 11: Divided 7x7 grid

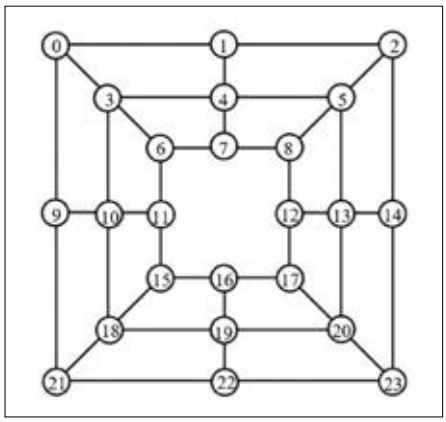

Figure 12: Numbered positions of the Nerenchi board

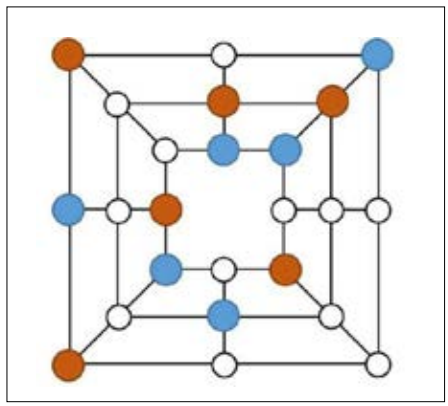

Figure 13: Board according to the above array

Figure 13 depicts how tokens are on the Board according to the above array.

Figure 14 depicts a screenshot of detected tokens that were captured while the game was going on. Figure 15 depicts the screenshot of the generated 24 index array.

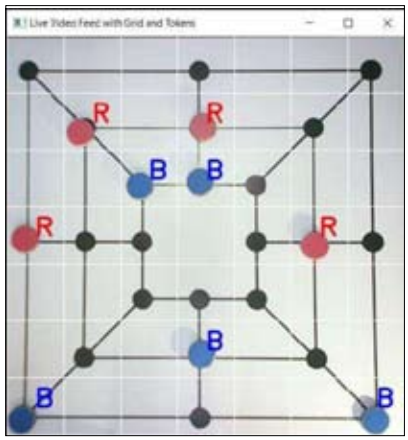

Figure 14: Random capture

```
C:\Users\ACER\Desktop>python cam.py
Calibration phase: Adjust the lighting and camera settings. Calibration will end in 10 seconds.
Calibration complete. Starting detection...
Average Red Color: [ 97.20454735  88.56530751 169.33212906]
Average Blue Color: [145.95587698  98.61860553  63.89467739]
Press the button to capture and process the frame. Press 'q' to quit.
Processing captured frame...
24-Index Token Array: [0, 0, 0, 1, 1, 0, 2, 2, 0, 1, 0, 0, 0, 1, 0, 0, 0, 0, 0, 2, 0, 2, 0, 2]
```

Figure 15: Generated 24 index array

Knowledge-based decision-making system

The decision-making system for the Nerenchi gaming robot is a crucial component that interprets game states and determines the robot's next move. There are 3 facts that have to be considered when playing using this system.

1. Make a Nerenchi state using 3 tokens.
2. Avoid the opponent making a Nerenchi state
3. If there is a token, place a token next to it to make a Nerenchi state in the next turn.

It begins by analysing a 24-index array that represents the current state of the Nerenchi board. Each index corresponds to a specific position on the board, with values indicating whether the position is empty (0), occupied by a red token (1), or occupied by a blue token (2). By reading this array, the system identifies the board's current status and any changes since the last analysis.

Once the changes are detected, the system processes the information to determine the next action, following a predefined rule-based algorithm. The algorithm is designed to evaluate the 20 possible Nerenchi states in the game and to consider 60 specific state combinations required to form a Nerenchi (a winning move or a significant progression). The system iterates through these combinations, methodically checking each one to determine if a valid Nerenchi can be formed.

If a match is found among the 60 combinations, the system identifies this as an opportunity to make a strategic Nerenchi move. It generates detailed instructions based on this move and transmits them to the robotic system, enabling precise execution on the physical board. In the absence of a match, when no Nerenchi is possible, the system selects a random move to maintain game progression while waiting for future opportunities to achieve a winning state.

The entire process operates in real time, ensuring that the robotic system remains responsive to the game's dynamic state. By combining structured, rule-based decision-making with random moves as a fallback, this system ensures intelligent gameplay while adhering to Nerenchi's traditional rules. This algorithm was developed for the placement stage of the game. Figure 16 shows the algorithm used in the decision making system.

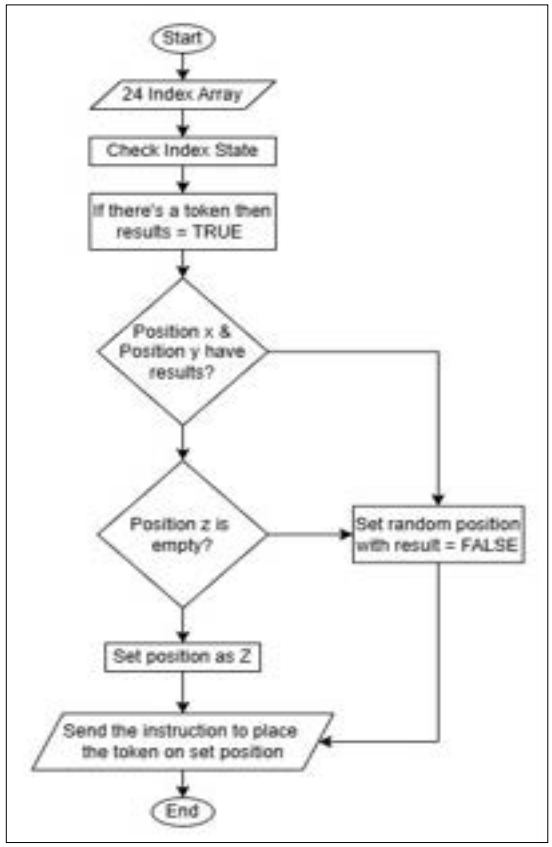

Figure 16: Algorithm of the Decision making system

To make these movements possible, the decision making system has to send an instruction array to the robotics system. An instruction array is generated by the decision making system according to the decision.

There are 3 key words.

- Place
- Replace
- Remove.

And each and every position is numbered as P1, P2, P3 …up to P24.

To generate the instruction array, the system has to identify the status and the position that requires changes to be made. Then the programme generates an instruction when the <keyword> <position> is given. As an example, to place a token on P1, then the instruction should be 'Place P1'; to replace P1 with P2, 'Replace P1 P2'.

There are 3 pre-defined instruction arrays for each keyword that place only the position given by the system.

Example for instruction array for
'Place P1': D,0,P1,1,D,R,0,D,S

In each Character of the instruction array, commands are given in order to execute. Table 2 shows the meanings of the values.

Table 2: Pre defined Instructions

Instruction	action
P1	Move to position 1
P2	Move to position 2
P24	Move to position 24
G	Get position
R	Remove position
D	Default position
S	Break
1	Turn on Electromagnet
0	Turn off Electromagnet

Robotic system

Design

The Robotic Arm is fully designed in accordance with the project's specifications. Adobe Illustrator was used to create each component, which was then laser-cut from a 3 mm-thick acrylic board and assembled with nuts and bolts. The arm has servo motors attached. The file intended for laser cutting is shown in Figure 17. Figure 18 depicts the arm assembled.

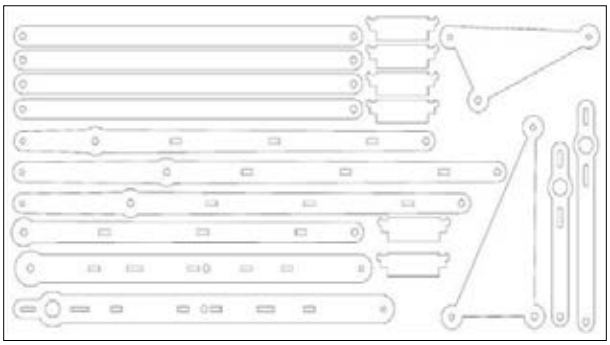

Figure 17: Design File of the Arm

This arm is designed to grab, place, replace and remove Nerenchi okens on its work envelope. The arm is 4 DOF (Degree of Freedom). The Robotic arm, PCB, and Nerenchi Board are attached to and fixed to the wooden base, which can hold all components of the system. In Figure 18, the Nerenchi board is fixed to the wooden base using screws.

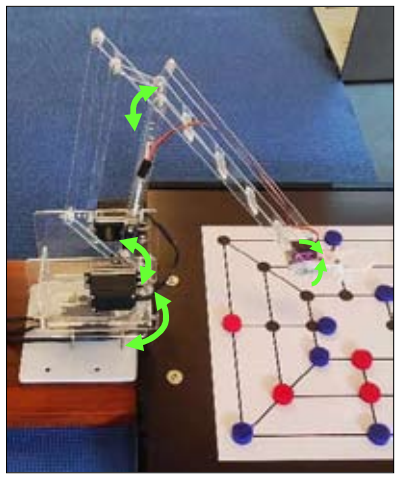

Figure 18: Robotic arm

Tokens are made from steel washers covered with plastic boards. Red and Blue colours are used for these tokens, which help the webcam detect the tokens more easily. Figure 18 depicts the Nerenchi tokens in both colours.

The MG995 and MG90S are popular servomotors widely used in robotics and electronics projects. The MG995 is a high-torque servo, known for its strong performance and reliability, making it suitable for applications requiring significant force, such as robotic arms and remote control vehicles. It operates at 4.8 V to 7.2 V and offers a stall torque of around 10 kg-cm. The MG90S, on the other hand, is a micro servo that provides a good balance of power and size, ideal for smaller projects and precise movements. It operates at 4.8 V to 6.0 V with a stall torque of about 2.2 kg-cm, making it perfect for lightweight and compact applications. Both servos are valued for their ease of use and versatility in various DIY and professional projects. 3 MG995 servo motors are used to operate the robotic arm, and 1 MG90S servo motor is used to operate the gripper.

The PCB shown in Figure 19, integrates the ESP32-S3 microcontroller, enabling multitasking and wireless communication for advanced IoT applications. It features a TPS6217-series power supply that efficiently delivers

5V and 3.3V outputs, ensuring stable operation for all components. The BTT6050 driver manages the digital output channels, supporting robust signal handling. The board includes 2 digital inputs, 4 digital outputs, and 2 analogue outputs, alongside dedicated I2C pins for interfacing with displays. Additionally, 4 PWM-enabled pins allow precise control of servo motors, making the PCB ideal for applications requiring motor actuation, display integration, and versatile input/output capabilities.

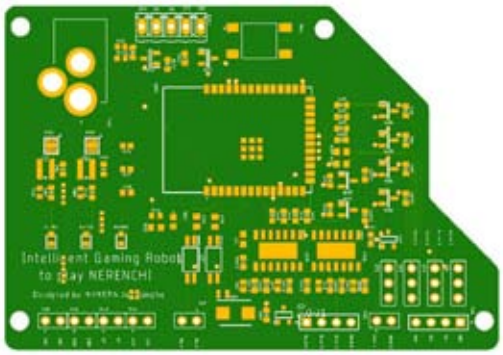

Figure 19: Designed PCB

Microcontroller: Espressif Systems' ESP32-S3 is a powerful and versatile microcontroller designed for edge computing, AI, and Internet of Things applications. It has a dual-core Xtensa LX7 CPU that can run at up to 240 MHz, Bluetooth 5.0 LE, integrated Wi-Fi (802.11 b/g/n), and extensive peripherals including SPI, I2C, UART, ADC, DAC, and more. It provides strong memory capabilities with 512 KB of SRAM, up to 16 MB of flash, and compatibility for external PSRAM. Notably, the ESP32-S3 combines vector instructions with AI acceleration, making it well-suited for signal processing and machine learning tasks. It is a great option for contemporary embedded systems, wearable technology, and networked applications due to its low power consumption, varied power modes, and sophisticated security features, including safe boot and encryption.

Implementation of the robotic system

The robotic system is a vital component of the Nerenchi gaming robot, designed to execute precise movements based on predefined instructions from the decision-making system. It features a 4-DOF robotic arm (Zribi & Sung, 1998) (*Superhuman AI for Multiplayer Poker*, n.d.), specially constructed using acrylic boards tailored to the project requirements.

The arm operates with three main functionalities:
Place, where it retrieves a token from a queue and positions it on the board;
Replace, where it relocates a token already on the board to a new position; and
Remove, where it takes a token from the board and returns it to the removed queue.

The end effector is a 12 V DC electromagnet, selected over a gripper for its efficiency and reliability in handling tokens. The electromagnet is controlled via a relay integrated into the robotic system.

The robotic arm's movements are calibrated to the board positions, with each position corresponding to a specific array of servo angles. For instance, Position 1 requires servo angles of [45°, 90°, 75°] for servos 1, 2, and 3, respectively. This calibration ensures that every movement is accurate and repeatable, enhancing the system's precision.

During gameplay, the robotic arm follows instructions transmitted by the computer, formatted as comma-separated sequences, as shown in Figure 20. These instructions direct the arm's movements for placing, replacing, or removing tokens. After executing its move, the system gives the human opponent time to make their move, displaying a countdown for the time left. Once the opponent completes their move, they press a switch to

```
Menu:
1. Place
2. Replace
3. Remove
4. Exit
Select an option (1-4): 2
Enter the position (P1 to P24 or G): P1
Enter the new position (P1 to P24): P6
Command sent: D,0,P1,1,D,P6,0,D,S
Arduino response: Relay set to: LOW

Menu:
1. Place
2. Replace
3. Remove
4. Exit
Select an option (1-4): 3
Enter the position to remove (P1 to P24): P6
Command sent: D,0,P6,1,D,R,0,D,S
Arduino response: BUTTON_PRESSED

Menu:
1. Place
2. Replace
3. Remove
4. Exit
Select an option (1-4): 1
Enter the position (P1 to P24): P1
Command sent: D,0,G,1,D,P1,0,D,S
```

Figure 20: Commands sends to Robotic system

confirm it. The PCB detects this confirmation, prompting the computer to capture an updated image of the board so gameplay can continue seamlessly.

By integrating the decision-making system with the robotic arm's precise mechanics, the robotic system ensures smooth, intelligent interaction between the game's physical and digital components, adhering to Nerenchi's rules and dynamics.

Implementation

When placing a token on a position, the robotic arm will grab a Token from a special place on the side of the board where Tokens are kept. Then it comes to a default position that is set, and then it places the token in the position that is instructed by the PCB. Then again, the arm is set to the default position and waits for a specific period before the opponent makes changes, which is then confirmedwith a push button switch. Until the switch is true, the time will count down on an OLED screen.



Figure 21: OLED Display

When replacing, the arm gets a token from the board, sets it to the default position, and then keeps the token in the instructed position. Then, waiting begins until the opponent moves.

When removing, the arm will reach the token and set it to the default location, keeping it out of the board that is specially designed according to the instructions.

The UART communication between the computer and the PCB is done through a USB cable. To detect Nerenchi tokens and positions of the board, the webcam is attached to a holder that can get the top view of the board. Edge and Grid detection were used. A method similar to that used in position and token detecting methods in chess was used for implementation.

An I2C OLED screen was used to interact with the opponent and to display and give instructions, stage, time, scores, and winning conditions.

A push switch is attached to the opponent's side of the board to press it after making a change in the board. It is used to keep track of time and wait until the opponent makes a move. While the game is in progress, the system and a basic visualisation of the board's current status will display on the computer screen, showing the next moves and changes made to the board.

To slow down and increase the smoothness of the Robotic arm, the delays are set to the servo motor operations. This may increase the accuracy of the arm. The Gripper is proposed to make rougher, reduce slipperiness, and increase the gripping area to easily and accurately grab Nerenchi tokens and drop them at the desired positions (Jayasinghe, n.d.). The Queue is where tokens wait to be picked up by the gripper. The gripper should get a token from the queue to place it on the board. When removing a token, again, the gripper has to drop it into the queue.

Testing and evaluation

System testing

System testing for the Nerenchi gaming robot focused on ensuring the seamless functionality and accuracy of its components, with extensive calibration and validation of the robotic arm and decision-making system. The robotic arm was rigorously tested by executing movements for each board position more than 10 times after calibration. These tests confirmed that the robotic system accurately performed its Place, Replace, and Remove functions in response to predefined instructions. Despite the overall success, slight variations in precision were observed based on the position of the arm and the weight of the token. Specifically, when the arm extended to far-reaching positions, even a 1-degree angle deviation resulted in reduced precision of the far positions from the centre point of the work envelope, highlighting the need for precise control at these limits.

The decision-making algorithm underwent comprehensive testing across all possible Nerenchi states. The system successfully identified and executed the correct moves with high accuracy, ensuring adherence to the game's rules and logic. Video feedback enabled the generation of the 24-index position array, accurately reflecting the board's state. Token detection during

gameplay was also evaluated, achieving a detection accuracy of approximately 95%, which ensures reliable interaction between the vision and decision-making systems.

Figure 22 shows the data of token colour detection accuracy, tested colour-wise. These tests were conducted on various levels of brightness and lighting. Each colour was tested 200 times. Out of 200 tests, 32 tests failed to detect Red colour, and out of 200 tests, 24 tests failed to detect blue tokens. Out of 400 tests, 56 tests failed to detect the token colour due to lighting and disruptions, as in Figure 23. In conclusion, under low levels of brightness, the low Kelvin colours (such as warm white) failed to be detected and identified accurately.

Overall, the system testing demonstrated the effectiveness of the robotic system and decision-making algorithm. All movements, reactions, and feedback processes were performed with a high degree of accuracy, ensuring the robot's capability to interact dynamically with the Nerenchi board and maintain the flow of the game.

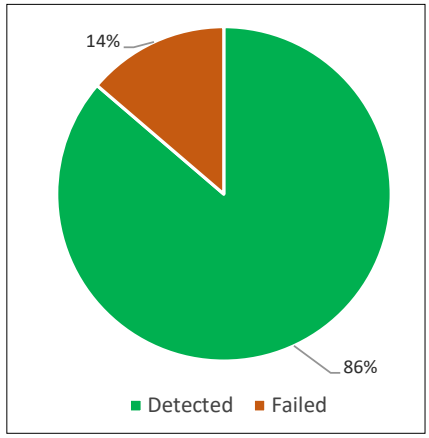

Figure 22: Results of token detection testing colour wisely

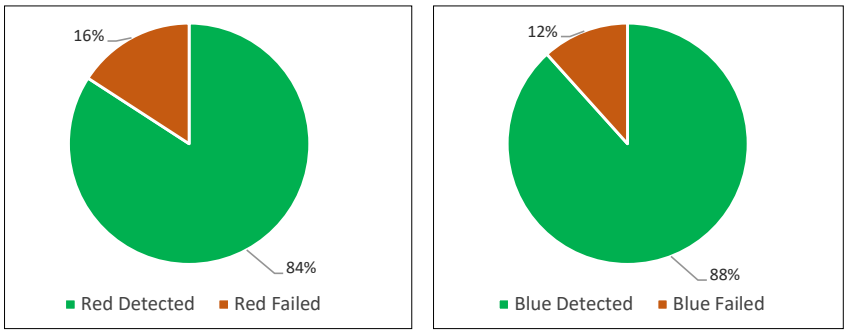

Figure 23: Overall Token Colour Recognition

Functional and non-functional testing

Functional testing was conducted to verify that each component of the gaming robot operates in accordance with predefined requirements. The system's ability to detect the Nerenchi board layout and correctly classify red and blue tokens was tested under different lighting conditions and angles. The algorithm-based decision-making system was assessed to ensure it adheres to legal moves and game logic, including normal gameplay, special moves, and handling of invalid moves. The robotic arm's movement was tested to check its precision in picking up, moving, and placing tokens correctly. Communication between the Robotic system, responsible for decision-making, and the Microcontroller, controlling the robotic arm, was analysed to ensure smooth data exchange and minimal delays.

Non-functional testing was performed to evaluate system quality beyond core functionality. Reliability and stability were tested by running 20 consecutive game sessions, where the system maintained around 88% operational stability, with only 12% of cases experiencing minor errors, such as delayed moves or incorrect token detection. The latency of image processing, decision-making, and robotic movements was measured, with the system achieving an average response time of 8.1 seconds per move. Error handling and recovery mechanisms

were tested by simulating unexpected disruptions, such as power failures and accidental board disturbances, in which the system successfully recovered in 95% of cases by recalibrating the board state and resuming play. The Computer vision programme is tested for every position with both token colours (red and blue) under different lighting conditions. Poor lighting conditions cause some detection errors up to 14%, and under rich lighting conditions, the accuracy rises to around 95%.

Performance evaluation

The gaming robot's effectiveness was assessed through various performance metrics. The accuracy of the token recognition system was tested in 240 trials (for each place, 5 trials each colour) of the board, ensuring consistent classification of red and blue tokens. The algorithm achieved an overall classification accuracy of 86.25%, with 13.75% of cases misclassifying tokens due to lighting variations or occlusions. Additional optimisations, such as adaptive thresholding, improved accuracy to around 95%.

The robotic arm's movement precision was evaluated by measuring the deviation between the intended and actual placement positions, with an average error margin of ±5 mm. The robotic arm's grip strength was also tested, achieving a 96% success rate in correctly lifting and placing tokens, while 4% of trials experienced slippage due to power and noise errors.

The overall game processing speed was analysed by measuring the time taken for each stage, with video feedback, board state analysis, rule-based decision-making, and robotic movement execution around 6 seconds to place and 10 seconds to end the full action of the arm, resulting in an average total move execution time of 9.2 seconds. Stress testing was performed by running the system continuously over 20 full game sessions, where it maintained consistent performance with no significant slowdowns or overheating issues.

User interaction feedback and testing

User experience was evaluated by inviting 10 participants to play against the robot and provide feedback. Players were asked to assess the system based on responsiveness, ease of understanding, and the level of challenge provided by the game. The feedback results showed that 10 of the participants found the system responsive and engaging, while 2 participants noted occasional delays in token recognition, and 4 experienced difficulty in understanding the robot's decision-making process.

Adaptive gameplay testing was conducted to refine the robot's strategy and improve the overall gaming experience. If users found the robot's moves too predictable, refinements were made to introduce slight randomness while maintaining adherence to game rules.

The system's error recovery and usability were tested by allowing players to make incorrect moves or intentionally disturb the board. Enhancements were made to provide better visual and auditory feedback, with the users finding the updated interface more intuitive after improvements.

Final refinements based on testing results

Based on the test results and user feedback, several improvements were made to optimise the robot's performance. The token detection algorithm was refined to enhance accuracy under different lighting conditions, improving classification accuracy. The robotic arm's movement speed and placement precision were fine-tuned, reducing the placement error margin from ±5 mm to ±2 mm. Communication delays between the robotic system and the decision-making system were minimised, reducing total move execution time from more than 11 seconds to 8.1 seconds on average. Additional user-friendly features, such as visual indicators and confirmation prompts, were incorporated to enhance interaction. The system's ability to recover from disruptions was strengthened, improving error recovery success rates.

These testing and evaluation processes helped in refining the intelligent gaming robot, ensuring its accuracy, efficiency, and overall usability. Continuous improvements based on real-world testing and user feedback contributed to making the system more reliable and engaging for players.

Match data creation and collection

Every time the webcam captures the Nerenchi board during a game, the array shows the exact state of the board at that moment and is saved into a text file. For each match played between the robot and a human, one separate text file is created, storing all the arrays recorded throughout that game. Over time, as more matches are played, the system builds up a collection of these files. This growing dataset is then used to train a machine learning model, helping the robot learn from past games, recognise patterns in play, and gradually improve its strategies. The aim is for the robot to get smarter and more competitive the more it plays.

In these arrays in the text document, there are 25 indexes. 24 indexes for positions and the last index (25th) for showing and identifying which player is to play next. If the value of the 25th index is 0, it is red, and if the value is 1, then it is blue. The figure below shows a screenshot of a created text document.

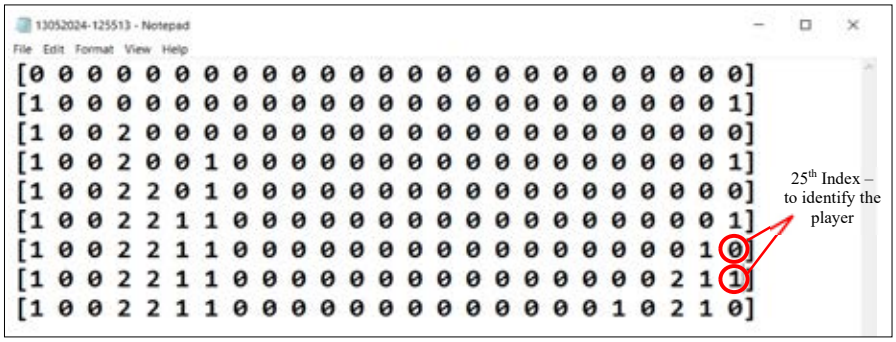

Figure 24: Array data text document

CONCLUSION

This study presented the design and implementation of an intelligent robotic system for playing the traditional Sri Lankan Board game Nerenchi against a human opponent, addressing the objective of preserving and modernising a culturally significant yet declining game through advanced technology. The system integrates three core subsystems – monitoring, decision making and robotic actuation, forming a complete closed loop human-robot gaming framework.

The monitoring system, implemented using computer vision techniques, successfully detects the geometry of the board and token positions, representing the game state as a 24 index position array. This structured representation enables efficient state evaluation and seamless communication with the decision making module. The knowledge and algorithm based system applies a rule driven algorithm to evaluate possible Nerenchi formations and enforce gameplay logic, ensuring adherence to traditional rules while maintaining computational efficiency. The robotic system, consisting of a calibrated 4 DOF arm with servo motors and an electromagnetic end effector, accurately executes Place, Replace, and Remove operations, enabling physical interactions with the board environment.

Experimental evaluation demonstrates that the system achieves high functional reliability, with token detection accuracy approaching 95% under controlled lighting conditions and consistent robotic manipulation with an acceptable positional error margin. The decision making algorithm successfully identifies valid game states and executes structured board games. However, the deterministic nature of the algorithm introduces limitations in strategic adaptability and predictability, particularly in complex gameplay scenarios.

Overall, the system validates the feasibility of integrating computer vision, embedded systems, and robotics to realise a physically interactive intelligent gaming platform. Furthermore, it establishes a scalable foundation for future enhancements, including data driven strategy optimisation through machine learning and improved perception using advanced vision models. By bridging traditional gameplay with modern intelligent systems, this work contributes both to the preservation of cultural heritage and to the advancement of human-robot interactive gaming systems.

Further work

As the main point, the recorded text files containing 24-index data sets from each Nerenchi match will be used to train a machine learning model. By analysing this real gameplay data, the model will be able to identify patterns in human strategies and determine the most effective moves for different board states. This approach aims to enhance the robot's decision-making capabilities beyond the current rule-based system, allowing it to play more intelligently and adaptively. As the dataset grows with more matches, the model's accuracy and performance are expected to improve, enabling the robot to become a more competitive and strategic Nerenchi player.

To increase the precision and speed of detecting the board and token positions, the computer vision system must be improved. This could involve integrating deep learning models for object tracking and recognition or employing more complex image processing algorithms. Using several cameras to monitor the game board from various viewpoints and angles, hence improving the vision system's robustness and reliability, could be explored.

To achieve smoother and more accurate movements, the robotic arm may be upgraded to a model with additional degrees of freedom, and other improved Robotic arms that use modern technology. This might enhance the robot's precision in moving the game components. To handle more complex computations and reduce command execution latency, utilising more potent microcontrollers or single-board computers, like a Raspberry Pi, that can operate the whole system in a single board computer without using a computer for processing, could be considered.

A more user-friendly interface could be provided, with gesture detection, so that human gamers may communicate with the robot. This might improve the game's accessibility and engagement. Features that allow the robot to give the human player immediate feedback or pointers could be included, making the game more engaging and instructive.

Acknowledgement

I would like to express my gratitude to the Department of Computer Engineering, Faculty of Computing, General Sir John Kotelawala Defence University, for allowing me to conduct this research and project under their guidance.

REFERENCES

Badia, A. P., Piot, B., Kapturowski, S., Sprechmann, P., Vitvitskyi, A., Guo, Z. D., & Blundell, C. (2020). Agent57: Outperforming the Atari human benchmark. *Proceedings of the 37th International Conference on Machine Learning*, 507–517. https://proceedings.mlr.press/v119/badia20a.html

Baker, B., Kanitscheider, I., Markov, T., Wu, Y., Powell, G., McGrew, B., & Mordatch, I. (2020). *Emergent tool use from multi-agent autocurricula* (arXiv:1909.07528). arXiv. https://doi.org/10.48550/arXiv.1909.07528

Bandaranaike, A., & Hettige, B. (2021). Communication platform for Sri Lankan board game Nerenchi. In *Proceedings of the 14th International Research Conference, General Sir John Kotelawala Defence University* (pp. 324–329).

Cagiltay, N. E. (2007). Teaching software engineering by means of computer-game development: Challenges and opportunities. *British Journal of Educational Technology*, *38(3)*, 405–415. https://doi.org/10.1111/j.1467-8535.2007.00705.x

Chen, A. T.-Y., & Wang, K. I.-K. (2019). Robust computer vision chess analysis and interaction with a humanoid robot. *Computers, 8*(1), Article 14. https://doi.org/10.3390/computers8010014

Crouser, R. J., & Chang, R. (2012). An affordance-based framework for human computation and human-computer collaboration. *IEEE Transactions on Visualization and Computer Graphics, 18*(12), 2859–2868. https://doi.org/10.1109/TVCG.2012.195

Dota 2 with Large Scale Deep Reinforcement Learning | BibSonomy. (n.d.). Retrieved November 12, 2023, from https://www.bibsonomy.org/bibtex/23e53e9a9c51add485735bfab05e384e

Engineering Design Process. (n.d.). Retrieved November 2, 2024, from https://www.sciencebuddies.org/science-fair-projects/engineering-design-process/engineering-design-process-steps

Gawesha, A. H. B. K. Y., Hettige, B., & Goonatilleke, M. A. S. T. (2022). Implementation of autonomous robotic arm for Nerenchi board game. In *Proceedings of the 15th International Research Conference, General Sir John Kotelawala Defence University*.

He, Z., & Lee, D. L. (2026). Design of an interactive system integrating virtual games and physical robots. *AIP Advances*, *16*(2). https://doi.org/10.1063/5.0317460

Janko, V., Mlakar, N., & Bizjak, J. (2018). Robot gaming based on computer vision. *Electronic Devices, 7*(2), 55–61.

Jayasinghe, M. (n.d.). *Intelligent Nerenchi Bot—LinkedIn Post*. Retrieved https://www.linkedin.com/posts/pamuditha-jayasinghe_research-engineering-robotics-activity-7274452353393508352-_8ir?utm_source=social_share_send&utm_medium=member_desktop_web&rcm=ACoAAEEbrYoBIA8dK7pmvLgeUiH-efR_OBVv-OU

Jayasinghe, M., Meththananda, R., Hettige, B., & Perera, D. B. Y. (2024). *Intelligent gaming robot: Robotic solution for the traditional Sri Lankan board game 'Nerenchi.'* http://ir.kdu.ac.lk/handle/345/8539

Karlsson, A., & Påsse, E. (2025). *The potential of electronic board games*.

Kruthika, K., Kiran Kumar, B. M., & Lakshminarayanan, S. (2016). Design and development of a robotic arm. In *2016 International Conference on Circuits, Controls, Communications and Computing (I4C)* (pp. 1–4). IEEE. https://doi.org/10.1109/CIMCA.2016.8053274

Matuszek, C., Mayton, B., Aimi, R., Deisenroth, M., Bo, L., Chu, R., Kung, M., LeGrand, L., Smith, J., & Fox, D. (2011). Gambit: An autonomous chess-playing robotic system. In *2011 IEEE International Conference on Robotics and Automation* (pp. 4291–4297). IEEE. https://doi.org/10.1109/ICRA.2011.5980528

Meththananda, R. G. U. I., & Hettige, B. (2015). Computational

model for Sri Lankan board game Nerenchi. In *Proceedings of the 8th International Research Conference, General Sir John Kotelawala Defence University* (p. 48).

Mnih, V., Kavukcuoglu, K., Silver, D., Rusu, A. A., Veness, J., Bellemare, M. G., Graves, A., Riedmiller, M., Fidjeland, A. K., Ostrovski, G., Petersen, S., Beattie, C., Sadik, A., Antonoglou, I., King, H., Kumaran, D., Wierstra, D., Legg, S., & Hassabis, D. (2015). Human-level control through deep reinforcement learning. *Nature*, *518*(7540), Article 7540. https://doi.org/10.1038/nature14236

Noel, G., Djouani, K., & Hamam, Y. (2011). Edge detection in grayscale images using grid smoothing. In T. Kim, H. Adeli, R. J. Robles, & M. Balitanas (Eds.), *Ubiquitous Computing and Multimedia Applications* (Vol. 150, pp. 110–119). Springer Berlin Heidelberg. https://doi.org/10.1007/978-3-642-20975-8_12

Pandithage, D., & Hettige, B. (2020). Image processing approach to detect tokens on a Nerenchi board. *FOC Student Symposium 2020, General Sir John Kotelawala Defence University*.

Deep Blue | Semantic Scholar. (n.d.). Retrieved July 6, 2024, from https://www.semanticscholar.org/paper/Deep-Blue-Campbell-Hoane/3e4bc1aa55c752918ae99b1a125f6adef61afad2

Peitz, J., Eriksson, D., & Björk, S. (2005). Augmented board games—Enhancing board games with electronics. In *Proceedings of DiGRA 2005 Conference: Changing Views: Worlds in Play*. DiGRA. https://doi.org/10.26503/dl.v2005i1.171

Saygin, A. P., Cicekli, I., & Akman, V. (2000). Turing test: 50 years later. *Minds and Machines*, *10*. https://doi.org/10.1023/A:1011288000451

Schaeffer, J., Lake, R., Lu, P., & Bryant, M. (1996). CHINOOK the world man-machine checkers champion. *AI Magazine*, *17*(1), Article 1. https://doi.org/10.1609/aimag.v17i1.1208

Seewald, A. (2010). Automatic extraction of Go game positions from Images: A multi-strategical approach to constrained multi-object recognition. *Applied Artificial Intelligence*, *24*, 233–252. https://doi.org/10.1080/08839510903572657

Silver, D., Huang, A., Maddison, C. J., Guez, A., Sifre, L., van den Driessche, G., Schrittwieser, J., Antonoglou, I., Panneershelvam, V., Lanctot, M., Dieleman, S., Grewe, D., Nham, J., Kalchbrenner, N., Sutskever, I., Lillicrap, T., Leach, M., Kavukcuoglu, K., Graepel, T., & Hassabis, D. (2016). Mastering the game of Go with deep neural networks and tree search. *Nature*, *529*(7587), Article 7587. https://doi.org/10.1038/nature16961

Superhuman AI for heads-up no-limit poker: Libratus beats top professionals. (n.d.). Retrieved November 12, 2023, from https://www.researchgate.net/publication/321878591_Superhuman_AI_for_heads-up_no-limit_poker_Libratus_beats_top_professionals

Superhuman AI for multiplayer poker. (n.d.). Retrieved November 12, 2023, from https://www.researchgate.net/publication/334407224_Superhuman_AI_for_multiplayer_poker

Thabet, A., & Prasetyo, J. (2025). Design and implementation of a smart automated chess board. *Journal of Applied Science and Advanced Engineering*, *3*, 64–72. https://doi.org/10.59097/jasae.v3i2.52

Vinyals, O., Babuschkin, I., Czarnecki, W. M., Mathieu, M., Dudzik, A., Chung, J., Choi, D. H., Powell, R., Ewalds, T., Georgiev, P., Oh, J., Horgan, D., Kroiss, M., Danihelka, I., Huang, A., Sifre, L., Cai, T., Agapiou, J. P., Jaderberg, M., … Silver, D. (2019). Grandmaster level in StarCraft II using multi-agent reinforcement learning. *Nature*, *575*(7782), Article 7782. https://doi.org/10.1038/s41586-019-1724-z

Wölflein, G., & Arandjelović, O. (2021). Determining chess game state from an image. *Journal of Imaging, 7*(6), Article 94. https://doi.org/10.3390/jimaging7060094

Yong, L., Zhan, Z., Zou, X., Chen, L., Lin, Z., & Zhan, W. (2023). Applying a blended board game system with robotic arm for training computational thinking: Learning through human-machine competition. In *Proceedings of the 7th International Conference on Education and Multimedia Technology, ICEMT '23*, 74–81. https://doi.org/10.1145/3625704.3625766

Zribi, M., & Sung, E. (1998). An autonomous robot playing the board game checkers. *International Journal of Electrical Engineering & Education*, *35*(1), 14–28. https://doi.org/10.1177/002072099803500102

J.Natn.Sci.Foundation Sri Lanka 2026 54 (3): 407 - 423
DOI: http://dx.doi.org/10.4038/jnsfsr.v54i3.12882

RESEARCH ARTICLE

Statistics

Robust quantile regression for improved population mean estimation under simple random sampling

A Subhani, M Irfan*, M Javed and T Nawaz
Department of Statistics, Government College University Faisalabad, Pakistan.

Submitted: 06 December 2025; Revised: 19 May 2026; Accepted: 26 June 2026

Abstract: To handle outliers in data, researchers increasingly use robust regression techniques since traditional methods like ordinary least squares are sensitive to outliers/extreme values. Quantile regression is being widely applied in survey sampling to obtain more reliable and efficient estimates. This study proposes a novel family of quantile regression-ratio-type estimators that incorporate auxiliary information to estimate the finite population mean under simple random sampling. We derived mathematical expressions for bias, mean squared error (MSE), and minimum MSE. Furthermore, we conducted numerical illustrations to confirm these theoretical findings using diverse real-life data sets from various fields such as agriculture loan, cereal nutrition, population, agriculture, and school education. Additionally, a Monte Carlo simulation study based on these real-life data sets is also added to check the performance of the proposed estimators. The numerical findings endorse the effectiveness of the proposed estimators compared to competing estimators. Ultimately this research provides the researcher with a tool to obtain a more precise population mean estimate, which is highly applicable across various scientific disciplines.

Keywords: Mean squared error (MSE), outliers, quantile regression, regression-ratio-type estimators, simple random sampling.

INTRODUCTION

The contemporary era is characterized by an unprecedented volume and velocity of information, underscoring the imperative of ensuring its accuracy and reliability. This highlights the critical importance of effective data collection methods. By acquiring precise data, we can develop a comprehensive understanding of our environment, enabling informed decision-making. Sampling theory and methods constitute a foundational component of multidisciplinary research, with applications in diverse fields. The utility of survey and sampling methods is exemplified in areas such as market research, where they facilitate market segmentation and profiling and in national surveys, such as the national co-morbidity survey, which assesses substance use disorders and anxiety levels. These examples demonstrate the significance of sampling methods in informing strategic decisions and policy initiatives.

The primary philosophical aim of sampling methods is to estimate the prevalence of patterns or attributes within a study population. In certain instances, survey research has access to complete information on every unit in the population, enabling comprehensive analysis. The incorporation of auxiliary information can significantly enhance estimation accuracy. For instance, auxiliary information has been effectively utilized in the field of biomedical engineering, including the distance from heart attack patients' homes to the nearest cardiovascular catheterization clinic and the distance to the nearest emergency room, to improve estimates of catheterization's impact on patient health outcomes (McClellan et al., 1994). To estimate cotton output in agricultural engineering, the planting area is an important auxiliary variable. Similarly, for the estimation

* Corresponding author (mirfan@gcuf.edu.pk; https://orcid.org/0000-0002-1739-1293)

This article is published under the Creative Commons CC-BY-ND License (http://creativecommons.org/licenses/by-nd/4.0/). This license permits use, distribution and reproduction, commercial and non-commercial, provided that the original work is properly cited and is not changed in anyway.

of average milk yield in the dairy industry, the breed of the cow is an important auxiliary attribute. The strategic use of auxiliary information is a hallmark of ratio, product, and regression-type estimation methods, which aim to optimize the efficiency of the estimators in survey sampling.

Outliers are data points that deviate significantly from the overall pattern, potentially skewing mean estimates. Traditional methods like ordinary least squares (OLS) are sensitive to outliers / extreme values. To control the effect of outliers, non-conventional measures, Poisson regression, M-estimators, quantile regression, and robust regression methods are used. Many researchers, for example Irfan et al. (2019), suggested an optimal class of regression-ratio-type estimators for the estimation of population mean under simple random sampling (SRS). They used both conventional and non-conventional measures including mean, standard deviation, coefficient of variation, Hodges-Lehmann estimator, mid-range and tri-mean. Koc (2021) suggested a novel ratio-type estimator for the estimation of the population mean based on Poisson regression under SRS. Zaman et al. (2021) suggested robust regression-type estimators for estimating the population mean of sensitive variables, a longstanding challenge in survey research. Zaman et al. (2019, 2022, 2024) proposed estimators for unknown population means when the data sets contain outliers, by using robust regression methods under SRS.

Quantile regression is one of the new techniques, which are used to control the effect of outliers. It is strong even in the cases where the data is not Gaussian. Shahzad et al. (2021) proposed a class of regression-ratio-type estimators by utilization of quantile regression with minimum covariance determinant-based measures. Anas et al. (2022) suggested an effective family of estimators for estimating a finite population mean by applying the quantile regression method in case of missing observations. Khalid et al. (2023) proposed some estimators for the estimation of the population mean under SRS by using the quantile regression approach. Koc and Koc (2023) suggested a new robust class for the estimation of the population mean based on quantile regression under stratified random sampling. Shahzad et al. (2023) suggested a robust estimation technique for the estimation of the population mean using quantile regression in systematic sampling. Alomair and Iftikhar (2024) proposed a novel dual-type estimator for the population mean based on quantile regression. Using asymmetric data, the performance of the proposed estimator was compared with existing estimators, both in the presence and absence of scrambled response. Zaman and Sozen (2026) proposed quantile-based neutrosophic combined and separate regression estimators for the finite mean under stratified random sampling, and they also provided efficiency conditions under which the estimators improve upon their classical counterparts. Afzal et al. (2026) suggested novel ratio-type estimators for the finite population mean under circular systematic sampling using the quantile regression approach.

The present study fills an important gap in sampling theory by developing new estimators for the population mean under simple random sampling using the quantile regression approach. A generalized estimator is proposed which can generate several robust estimators, contingent on the availability of auxiliary information, thereby enhancing estimation flexibility.

Quantile regression model

Quantile regression is a regression method that does not assume that the errors follow a normal distribution or that the variance is constant, unlike classical linear regression. Because of this, it is more flexible and requires fewer assumptions. Instead of estimating only the average (mean) of the dependent variable, quantile regression estimates different parts of its distribution. For example: 0.25 represents the lower 25% (first quartile), 0.50 represents the median (middle value) and 0.75 represents the upper 75%. In quantile regression, the model coefficients are calculated separately for these different quantiles. In contrast, classical regression only estimates the average response. The classical regression model for the average response is given below as follows:

$$y_i = \beta_o + \beta_1 x_{i1} + \cdots + \beta_k x_{ik}, \quad i = 1,2,\ldots,n$$

where y_i is the dependent random variable, x_{ij} is the j_{th} independent variable(s) for the i_{th} observation, $\beta_1, \beta_2, \ldots, \beta_k$ are the regression coefficients. These coefficients are obtained by minimizing the sum of squared residuals using the OLS method.

$$min(\beta_o, \beta_1, \ldots, \beta_k) \sum_{i=1}^{n} \left(y_i - \beta_o - \sum_{j=1}^{k} x_{ij}\beta_j \right)^2$$

The regression model for quantile level "τ" of the response is $Q_\tau(y_i) = \beta_o(\tau) + \beta_1(\tau)x_{i1} + \cdots + \beta_k(\tau)x_{ik}$ and the $\beta_j(\tau)s$ are estimated by solving the minimization problem

$$min\, \beta_o(\tau), \beta_1(\tau), \ldots, \beta_k(\tau) \sum_{i=1}^{n} \rho_\tau \left(y_i - \beta_o(\tau) - \sum_{j=1}^{k} x_{ij}\beta_j(\tau) \right)$$

The remaining section has been organized as follows: Section 2 presents important notations and reviewing estimators along with their expressions for bias and

MSE. In Section 3, we proposed a novel family of quantile regression-ratio-type estimators for the unknown population mean, incorporating robust auxiliary information measures. We derived mathematical expressions for bias and MSE of the suggested estimators. Numerical illustration is carried out through real-life data sets taken from agriculture loan, cereal nutrition, population, agriculture, and school education in Section 4. Monte Carlo simulation based on real-life applications is added in section 5. Numerical findings from both sections 4 & 5 confirm the practical applicability of the proposed estimators in case of outliers and non-normality. Finally, concluding remarks and future research directions are addressed in the last section.

MATERIALS AND METHODS

Let $U = \{U_1, U_2, U_3, \ldots, U_N\}$ be a population of size "N" and let a sample of size "n" be drawn under SRS without replacement subject to the constraint $n < N$. Consider the n pair of observations (y_i, x_i) where $i = 1,2,3, \ldots, n$ for the study and auxiliary variable, respectively. Let, $\bar{Y} = N^{-1}\sum_{i=1}^{N} y_i, \bar{X} = N^{-1}\sum_{i=1}^{N} x_i, \bar{y} = n^{-1}\sum_{i=1}^{n} y_i$ and $\bar{x} = n^{-1}\sum_{i=1}^{n} x_i$ be the population mean of the study variable, population mean of the auxiliary variable, sample mean of the study variable, and sample mean of the auxiliary variable respectively. To initiate the expressions for the bias, mean squared error (MSE) and minimum MSE of the existing and proposed estimators, we define the following relative error terms as:

$$\zeta_0 = \frac{\bar{y}-\bar{Y}}{\bar{Y}} \text{ and } \zeta_1 = \frac{\bar{x}-\bar{X}}{\bar{X}} \quad \ldots(01)$$

Such that

$$E(\zeta_0) = E(\zeta_1) = 0$$

$$E(\zeta_0^2) = \theta C_y^2, E(\zeta_1^2) = \theta C_x^2 \text{ and } E(\zeta_0\zeta_1) = \theta\rho_{yx}C_yC_x = \theta C_{yx}$$

where

$$\theta = \left(\frac{1}{n} - \frac{1}{N}\right), \quad C_y^2 = (\bar{Y}^2)^{-1}S_y^2, \quad C_x^2 = (\bar{X}^2)^{-1}S_x^2,$$

$$S_y^2 = (N-1)^{-1}\sum_{i=1}^{N}(y_i - \bar{Y})^2,$$

$$S_x^2 = (N-1)^{-1}\sum_{i=1}^{N}(x_i - \bar{X})^2, \quad S_{yx} = (N-1)^{-1}\sum_{i=1}^{N}(y_i - \bar{Y})(x_i - \bar{X}),$$

$$\rho_{yx} = (S_yS_x)^{-1}S_{yx}.$$

Traditional estimators and class of estimators under SRS without replacement for the estimation of the unknown population mean are:

1. Classical unbiased estimator:

$$\hat{\bar{Y}} = \bar{y} \quad \ldots(02)$$

2. Regression estimator:

$$\hat{\bar{Y}}_{Reg} = \bar{y} + \hat{\beta}_{(ols)}(\bar{X} - \bar{x}) \quad \ldots(03)$$

where $\hat{\beta}_{(ols)}$ refers to the regression coefficient (slope) computed using the OLS technique.

Expressions for the MSE of $\hat{\bar{Y}}$ and $\hat{\bar{Y}}_{Reg}$ up to first degree of approximation are respectively given by:

$$MSE\left(\hat{\bar{Y}}\right) = V\left(\hat{\bar{Y}}\right) \cong \theta\bar{Y}^2C_y^2 \quad \ldots(04)$$

$$MSE\left(\hat{\bar{Y}}_{Reg}\right) \cong \theta\bar{Y}^2C_y^2\left[1 - \rho_{yx}^2\right] \quad \ldots(05)$$

3. Shahzad et al. (2022) proposed a class of quantile regression-ratio-type estimators for the unknown population mean. They used conventional and non-conventional measures of the auxiliary variable. Table 1 presents some conventional and non-conventional measures related with the auxiliary variable. Their proposed estimator is given in Eq. (6) as:

$$\hat{\bar{Y}}_{USi} = \frac{\bar{y}+\hat{\beta}_{(q)}(\bar{X}-\bar{x})}{(a\bar{x}+b)}(a\bar{X} + b) \quad \ldots(06)$$

where $\hat{\beta}_{(q)}$ is the quantile regression coefficient, "a" & "b" are the unknown constants such as the coefficient of variation (C_x), coefficient of correlation (ρ_{yx}), quartile average (Q_A), tri-mean (T_M) and Hodges-Lehmann estimator (H_L). Table 2 presents some family members of their proposed class of estimators. Expression of bias and MSE of $\hat{\bar{Y}}_{USi}$ is given by:

$$\text{Bias}\left(\hat{\bar{Y}}_{USi}\right) \cong \frac{\theta}{\bar{Y}}S_x^2v_i^2 \quad \ldots(07)$$

$$MSE(\hat{\bar{Y}}_{USi}) \cong \theta\left(S_y^2 + v_i^2S_x^2 + 2\hat{\beta}_{(q)}v_iS_x^2 + \hat{\beta}_{(q)}^2S_x^2 - 2v_iS_{yx} - 2\hat{\beta}_{(q)}S_{yx}\right) \quad \ldots(08)$$

where $v_i = \frac{a\bar{X}}{a\bar{x}+b}$ for $i = 1,2,\ldots,8$.

RESULTS AND DISCUSSION

One notable limitation of established estimators, such as those proposed previously is their vulnerability to outliers/extreme observations (Irfan et al., 2019). Building upon this foundation, we introduce a novel family of robust estimators for the population mean in SRS when data is non-normal and contaminated

with outliers, using quantile regression approach. We also used non-conventional measures such as: quartile average, tri-mean, and Hodges-Lehmann estimator. These three measures are also resilient to outliers, and our proposed family of estimators leverages this robustness to provide improved estimates. Our proposed approach outperforms existing methods, particularly in cases where complete information of the auxiliary variable is available. Notably, this study employs specific quantiles, namely $q^{15th} = 0.15, q^{25th} = 0.25, q^{35th} = 0.35$ to develop the proposed estimators. By incorporating quantile regression coefficients based on these referenced quantiles, we significantly enhance the efficiency of our estimators. Utilizing the three referenced quantiles q^{15th}, q^{25th} and q^{35th}, the proposed family of estimators encompasses twenty-four distinct members. For the sake of conciseness and clarity, we present twenty-four members of the proposed family, along with their corresponding MSE values, in a compact and accessible format as this concise presentation facilitates easy reference and comparison of the estimators' performance, as given below:

$$\hat{\bar{Y}}_{Pi} = \alpha\bar{y}\left(\frac{a\bar{x}+b}{a\bar{x}+b}\right)^{\frac{a\bar{X}}{a\bar{X}+b}} + \hat{\beta}_{(q)}\,(\bar{X}-\bar{x}) \qquad ...(09)$$

where α is the selected appropriate constant whose value is determined later, $\hat{\beta}_{(q)}$ is the quantile regression coefficient, and "a" & "b" are the unknown constants, which are presented in Table 3.

This approach leverages the robustness of quantile regression to provide more accurate and reliable estimates, particularly in the presence of outliers and non-normality. A stream chart is presented in Figure 1 to visualize the appropriate selection of quantile regression versus OLS regression for the estimation of the true but unknown parameters of the population.

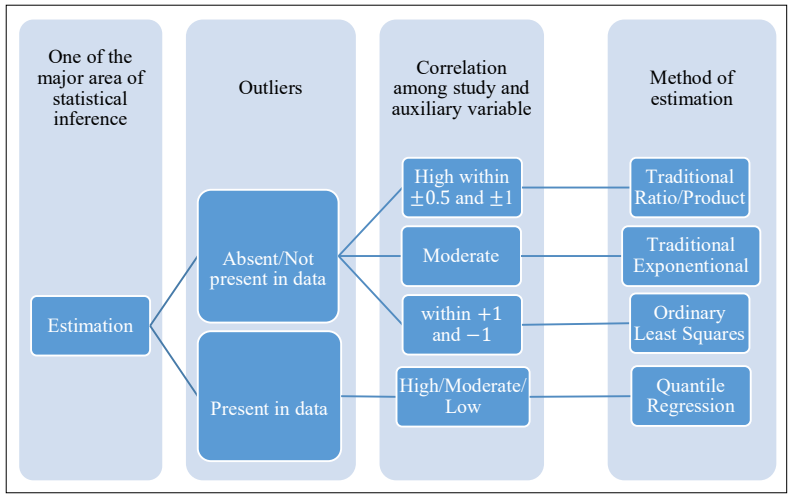

Figure 1: Quantile regression versus OLS regression

Equation (9) can be written as

$$\begin{cases} \hat{\bar{Y}}_{Pi} = \alpha\bar{y}\left(\frac{a\bar{x}+b}{(a\bar{x}+b)}\right)^{\frac{a\bar{X}}{a\bar{X}+b}} + \hat{\beta}_{(0.15)}\,(\bar{X}-\bar{x}) \\ \qquad \text{for } q^{15th}\ i = 1,2,\ldots,8 \\ \hat{\bar{Y}}_{Pi} = \alpha\bar{y}\left(\frac{a\bar{x}+b}{(a\bar{x}+b)}\right)^{\frac{a\bar{X}}{a\bar{X}+b}} + \hat{\beta}_{(0.25)}\,(\bar{X}-\bar{x}) \\ \qquad \text{for } q^{25th}\ i = 1,2,\ldots,8 \\ \hat{\bar{Y}}_{Pi} = \alpha\bar{y}\left(\frac{a\bar{x}+b}{(a\bar{x}+b)}\right)^{\frac{a\bar{X}}{a\bar{X}+b}} + \hat{\beta}_{(0.35)}\,(\bar{X}-\bar{x}) \\ \qquad \text{for } q^{35th}\ i = 1,2,\ldots,8 \end{cases} \qquad ...(10)$$

Expressing estimator "$\hat{\bar{Y}}_{Pi}$" in terms of relative error

$$\hat{\bar{Y}}_{Pi} = \alpha\bar{Y}\left[1 - v_i^2\zeta_1 + \frac{1}{2}v_i^3(v_i+1)\zeta_1^2 + \zeta_0 - v_i^2\zeta_0\zeta_1\right] - \hat{\beta}_{(q)}\bar{X}\zeta_1 \qquad ...(11)$$

Subtracting $\bar{Y}$ on both sides of Eq. (11), we get

$$\left(\hat{\bar{Y}}_{Pi} - \bar{Y}\right) = \alpha\bar{Y}\left[1 - v_i^2\zeta_1 + \frac{1}{2}v_i^3(v_i+1)\zeta_1^2 + \zeta_0 - v_i^2\zeta_0\zeta_1\right] - \hat{\beta}_{(q)}\bar{X}\zeta_1 - \bar{Y} \qquad ...(12)$$

$Bias\left(\hat{\bar{Y}}_{Pi}\right)$, up to first order of approximation, is defined as

$$\text{Bias}\left(\hat{\bar{Y}}_{Pi}\right) \cong E\left(\hat{\bar{Y}}_{Pi} - \bar{Y}\right)$$

Taking expectation on both side of the Equation (12), we get $\text{Bias}\left(\hat{\bar{Y}}_{Pi}\right)$

$$\text{Bias}\left(\hat{\bar{Y}}_{Pi}\right) \cong \bar{Y}(\alpha - 1) + \alpha\theta\bar{Y}\left[\frac{1}{2}v_i^3(v_i + 1)C_x^2 - v_i^2 C_{yx}\right] \quad ...(13)$$

Taking square on both sides of Equation (12), we get

$$\left(\hat{\bar{Y}}_{Pi} - \bar{Y}\right)^2 \cong (\alpha\bar{Y} - \bar{Y})^2 + \alpha^2[\bar{Y}^2 v_i^3(v_i + 1)\zeta_1^2 - 4\bar{Y}^2 v_i^2\zeta_0\zeta_1 + \bar{Y}^2 v_i^4\zeta_1^2 + \bar{Y}^2\zeta_0^2] + \alpha[2\bar{Y}^2 v_i^2\zeta_0\zeta_1 - \bar{Y}^2 v_i^3(v_i + 1)\zeta_1^2 - 2\bar{Y}\bar{X}\hat{\beta}_{(q)}\zeta_0\zeta_1 + 2\bar{Y}\bar{X}\hat{\beta}_{(q)}v_i^2\zeta_1^2] + \bar{X}^2\hat{\beta}_{(q)}^2\zeta_1^2 \quad ...(14)$$

$MSE\left(\hat{\bar{Y}}_{Pi}\right)$ is defined as

$$MSE\left(\hat{\bar{Y}}_{Pi}\right) \cong E\left(\hat{\bar{Y}}_{Pi} - \bar{Y}\right)^2$$

Taking expectation on both side of the Equation (14), we get $MSE\left(\hat{\bar{Y}}_{Pi}\right)$

$$MSE\left(\hat{\bar{Y}}_{Pi}\right) \cong (\alpha\bar{Y} - \bar{Y})^2 + \alpha^2\theta(\bar{Y}^2 C_y^2 + 2\bar{Y}^2 v_i^4 C_x^2 + \bar{Y}^2 v_i^3 C_x^2 - 4v_i^2\bar{Y}^2 C_{yx}) - \alpha\theta\left(v_i^4\bar{Y}^2 C_x^2 + v_i^3\bar{Y}^2 C_x^2 - 2v_i^2\bar{Y}^2 C_{yx} - 2\hat{\beta}_{(q)}v_i^2\bar{Y}\bar{X}C_x^2 + 2\hat{\beta}_{(q)}\bar{Y}\bar{X}C_{yx}\right) + \theta\hat{\beta}_{(q)}^2\bar{X}^2 C_x^2 \quad ...(15)$$

$$MSE\left(\hat{\bar{Y}}_{Pi}\right) \cong (\alpha\bar{Y} - \bar{Y})^2 + \alpha^2 A_1 - \alpha A_2 + \theta\hat{\beta}_{(q)}^2\bar{X}^2 C_x^2 \quad ...(16)$$

where

$$A_1 = \theta(\bar{Y}^2 C_y^2 + 2\bar{Y}^2 v_i^4 C_x^2 + \bar{Y}^2 v_i^3 C_x^2 - 4v_i^2\bar{Y}^2 C_{yx})$$

$$A_2 = \theta\left(v_i^4\bar{Y}^2 C_x^2 + v_i^3\bar{Y}^2 C_x^2 - 2v_i^2\bar{Y}^2 C_{yx} - 2\hat{\beta}_{(q)}v_i^2\bar{Y}\bar{X}C_x^2 + 2\hat{\beta}_{(q)}\bar{Y}\bar{X}C_{yx}\right)$$

To get the optimal value of α, differentiating Equation (16) with respect to α and equating to zero, we have:

$$\alpha = \frac{2\bar{Y}^2 + A_2}{2\bar{Y}^2 + 2A_1}$$

Putting the optimal value of α in Equation (16) and simplifying, we have the minimum MSE of $\hat{\bar{Y}}_{Pi}$

$$MSE_{min}\left(\hat{\bar{Y}}_{Pi}\right) \cong \left[\bar{Y}^2 - \frac{A_3^2}{2A_4}\right] \quad ...(17)$$

where

$A_3 = 2\bar{Y}^2 + A_2$ and $A_4 = 2\bar{Y}^2 + 2A_1$

Remark 3.1. Proposed class, *i.e.*, $\hat{\bar{Y}}_{Pi}$ reduces to the following existing estimators.

Values of $(\alpha, a, b, \hat{\beta}_{(q)})$	Proposed class reduces to
1) $(1,0,0,0)$	Usual unbiased estimator $\hat{\bar{Y}}$
2) $(1,1,0,0)$	Classical ratio estimator $\hat{\bar{Y}}_r$
3) $(1,0,0,\hat{\beta}_{(ols)})$	Classical regression estimator $\hat{\bar{Y}}_{Reg}$

Numerical illustration

In this section, the performance of the proposed estimators over the existing estimators is assessed using six real-life data sets. All real-life data sets are taken from different fields such as agriculture loan, cereal nutrition, population, agriculture, and school education. The different values of the correlation coefficient are assumed to be such that we can check the effectiveness of our proposed estimators over the existing estimators.

Population 1: [Agriculture loan data] We considered the data of Singh and Mangat (1996) to estimate the average "real estate farm loans during 1977". In this data, real estate farm loans during 1977 are considered as a study variable and non-real estate farm loans during 1977 as a helping / subsidiary / auxiliary variable. Important descriptive measures are:

$N = 50,\ n = 20,\ \bar{Y} = 555.440,\ \bar{X} = 878.162,$

$S_y = 584.830,\ S_x = 1084.680,\ S_{xy} = 509910.4,$

$C_y = 1.053,\ C_x = 1.235,\ H_L = 628.060$

$T_M = 536.40,\ Q_A = 620.3,\ \hat{\beta}_{(ols)} = 0.433,$

$\hat{\beta}_{(0.15)} = 0.345,\ \hat{\beta}_{(0.25)} = 0.354,\ \hat{\beta}_{(0.35)} = 0.357,$

$\rho_{yx} = 0.804.$

Population 2: [Cereal nutrition data] The data set provided by Venables and Ripley (1999) contain a lot of nutritional variables in their study to investigate the

average grams of potassium in breakfast cereals. In this population we use "grams of potassium" and "grams of fibre" as study and auxiliary variables, respectively. Important descriptive measures are:

$n = 20,\ \bar{Y} = 159.119,\ \bar{X} = 3.870,\ S_y = 180.280,$

$S_x = 6.133,\ S_{xy} = 1065.83,\ C_y = 1.133,\ C_x = 1.585,$

$T_M = 2.119,\ Q_A = 2.239,\ \hat{\beta}_{(ols)} = 28.332,\ \hat{\beta}_{(ols)} = 28.332,$

$\hat{\beta}_{(0.35)} = 27.727,\ \ \rho_{yx} = 0.964.$

Population 3: [Cereal nutrition data] To investigate the average number of calories in breakfast cereals, we used the data of Venables and Ripley (1999). In this population, "number of calories" and "grams of sodium" are considered as study and auxiliary variables, respectively. A moderate positive correlation between study and auxiliary variables has been found. Important descriptive measures are:

$N = 65,\ \ n = 20,\ \ \bar{Y} = 149.410,\ \ \bar{X} = 237.938,$

$S_y = 62.412, S_x = 130.630,\ S_{xy} = 4310.04,\ C_y = 0.417,$

$C_x = 0.544,\ \ H_L = 235.124,\ \ T_M = 233.50,\ \ Q_A = 235,$

$\hat{\beta}_{(ols)} = 0.252,\ \hat{\beta}_{(0.15)} = 0.198,\ \hat{\beta}_{(0.25)} = 0.173,$

$\hat{\beta}_{(0.35)} = 0.157,\ \ \rho_{yx} = 0.529.$

Population 4: [Decade of growth: Population 1920–1930] The data set is derived from Cochran (1977) to estimate the average number of inhabitants during 1930. We assumed the study variable y: number of inhabitants (in 1000's) during 1930, and the auxiliary variable x: number of inhabitants (in 1000's) in 1920. Important descriptive measures are:

$N = 49,\ n = 12,\ \bar{Y} = 127.790,\ \bar{X} = 103.143,\ S_y = 123.120,$

$S_x = 104.405,\ \ S_{xy} = 12619.23,\ \ C_y = 0.963,\ \ C_x = 1.012,$

$H_L = 77.250,\ T_M = 72.750,\ \ Q_A = 81.5,\ \ \bar{\beta}_{(ols)} = 1.158,$

$\bar{\beta}_{(0.15)} = 1.082,\ \ \bar{\beta}_{(0.25)} = 1.047,\ \ \hat{\beta}_{(0.35)} = 1.090,\ \ \rho_{yx} = 0.982$

Population 5: [Agriculture data] We considered the data from Singh and Mangat (1996). The objective was to estimate the average number of tube wells for 69 villages of the Doraha development block of Punjab, India. For this purpose, "number of tube wells" was considered as the study variable and "net irrigated area" is an auxiliary variable. Important descriptive measures are:

$N = 69,\ \ n = 15,\ \ \bar{Y} = 135.260,\ \ \bar{X} = 345.754,$
$S_y = 193.911,\ \ S_x = 293.160,\ \ S_{xy} = 30803.45,$
$C_y = 0.842,\ \ C_x = 0.847,\ \ H_L = 277,\ \ T_M = 274.50,$
$Q_A = 291,\ \beta_{(ols)} = 0.358,\ \ \beta_{(0.15)} = 0.238,\ \ \beta_{(0.25)} = 0.330,$
$\hat{\beta}_{(0.35)} = 0.343,\ \ \rho_{yx} = 0.922.$

Population 6: [School education data] To estimate the average number of teachers in both primary and secondary schools of Turkey, we used the data of Koyuncu and Kadilar (2009). The number of teachers in both primary and secondary schools was treated as the study variable and the number of students in both primary and secondary schools was considered as the auxiliary variable. Important descriptive measures are:

$N = 923,\ \ n = 220,\ \ \bar{Y} = 436.434,\ \ \bar{X} = 11440.5,$
$S_y = 749.939,\ \ S_x = 21331.13,\ \ S_{xy} = 15266040,$
$C_y = 1.718,\ \ C_x = 1.864,\ \ H_L = 5565.5,\ \ T_M = 4988.750,$
$Q_A = 5854.5,\ \ \hat{\beta}_{(ols)} = 0.033,\ \ \hat{\beta}_{(0.15)} = 0.026,$
$\hat{\beta}_{(0.25)} = 0.028,\ \hat{\beta}_{(0.35)} = 0.031,\ \ \rho_{yx} = 0.954.$

Figure 2 illustrates the scatter plot of the data sets to check the occurrence of outliers. It can be seen clearly from Figure 2. potential outliers exist in all real-life data sets. Histograms were also created to assess the normality of the data, which clearly indicate that all datasets are non-normal. Due to space constraints, sketches have not been provided here. The efficiency of the estimators is uncertain if we use the traditional OLS method and conventional measures of the auxiliary variable. Therefore, we used quantile regression and non-conventional measures related to the auxiliary variable. We calculated the values of bias and MSE for all existing and proposed estimators, MSE of traditional estimators $(\hat{\bar{Y}},\hat{\bar{Y}}_{Ree})$ under SRS without replacement, existing estimators $(\hat{\bar{Y}}_{USi})$ and proposed estimators $(\hat{\bar{Y}}_{Pi})$. In addition, percent relative efficiency (PRE) is calculated to check the proficiency of the proposed estimators over the traditional and existing estimators for all real populations under study. PRE is defined in Equation (18) as:

$$PRE = \frac{MSE(i)}{MSE(j)} \times 100 \qquad ...(18)$$

where $i = \hat{\bar{Y}}$ and $j = \hat{\bar{Y}}_{USi}$ and $\hat{\bar{Y}}_{Pi}$

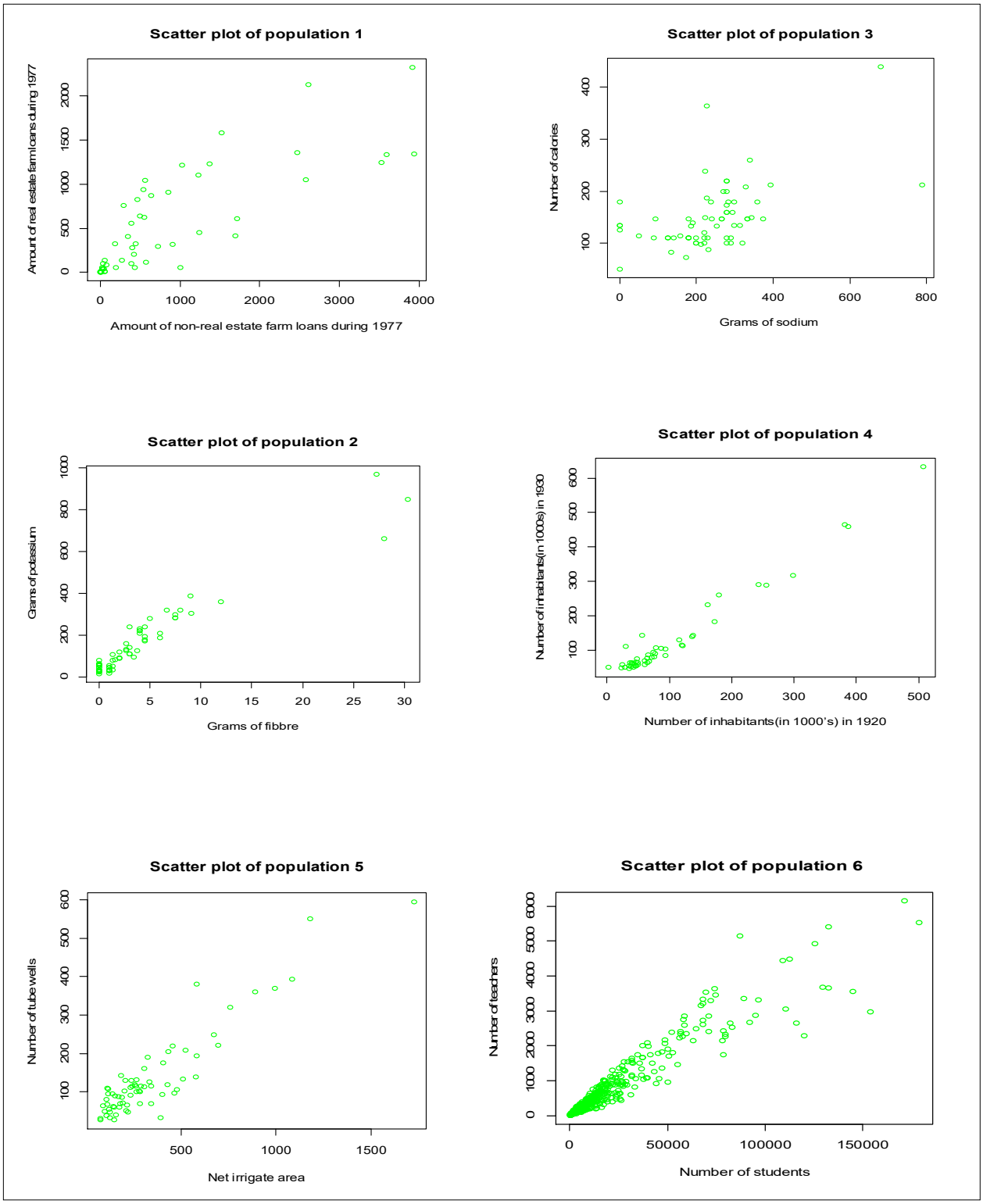

Figure 2: Scatter plot of six real-life applications

The following are some important findings observed in Tables 4-7:

- From Table 4, it is worth noting that $\hat{\bar{Y}}_{Reg}$ consistently outperforms $\hat{\bar{Y}}$ across all real-life applications considered in this study.
- It is also noteworthy from Table 4 that $\hat{\bar{Y}}_{Reg}$ performs best compared to the existing class of estimators proposed by Shahzad et al. (2022), namely $\hat{\bar{Y}}_{US1}$, $\hat{\bar{Y}}_{US2}$, $\hat{\bar{Y}}_{US3}$, $\hat{\bar{Y}}_{US4}$, $\hat{\bar{Y}}_{US5}$, $\hat{\bar{Y}}_{US6}$, $\hat{\bar{Y}}_{US7}$, $\hat{\bar{Y}}_{US8}$. $\hat{\bar{Y}}_{Reg}$ demonstrates superior performance primarily because it assigns equal weight to outliers. This finding highlights a key limitation of the traditional OLS method, which may yield unreliable results in the presence of outliers.
- The class of estimators proposed by Shahzad et al. (2022) demonstrates superior performance compared to the traditional estimator $\hat{\bar{Y}}$, particularly in terms of bias, mean squared error (MSE), and percentage relative efficiency (PRE). As a result, this class serves as the benchmark estimators in the present study.
- From Table 5, for all the listed populations, the proposed estimators $\hat{\bar{Y}}_{Pi}$ outperform the Shahzad estimators since their absolute bias is much closer to zero. This indicates that the proposed estimators introduce minimal systematic error, leading to more accurate and reliable estimates with reduced tendency to overestimate or underestimate the true value.
- It can be concluded from Table 6 that the proposed family of quantile regression-ratio-type estimators $\hat{\bar{Y}}_{Pi}$ exhibit higher efficiency, as they yield lower MSE values compared to the existing class of Shahzad et al. (2022), across all considered quantiles q^{15th}, q^{25th} and q^{35th}.
- From Table 6, it is important to note that as the quantile levels increase (*i.e.*, q^{15th},q^{25th} and q^{35th}), the MSE also shows an increasing trend for both the existing and proposed estimators.
- From Table 7, it is observed that the PRE values of both the existing and proposed estimators vary with different choices of "a" and "b". The corresponding configurations of "a" and "b" are presented in Table 3. Overall, the results indicate that the proposed family of quantile regression-ratio-type estimators $\hat{\bar{Y}}_{Pi}$ are more efficient, as they consistently yield higher PRE values than the existing estimators $\hat{\bar{Y}}_{USi}$.

A Simulation study

The numerical findings presented in Section 4 demonstrate that the proposed estimators consistently outperform their competing counterparts in terms of bias, MSE and PRE. In addition, a Monte Carlo simulation implemented in R software is carried out to further confirm the superiority of $\hat{\bar{Y}}_{Pi}$ over $\hat{\bar{Y}}_{USi}$. For this analysis, all real-life datasets described in Section 4, along with their corresponding summary statistics, are utilized. Different sample sizes are considered for the six populations, namely $(n = 14, 16), (n = 13, 16), (n = 13, 16), (n = 8, 10), (n = 10, 13)$ and $(n = 190, 210)$, respectively. The performance comparison is conducted as the 15th quantile level, $q^{15th} = 0.15$, to evaluate the effectiveness of $\hat{\bar{Y}}_{Pi}$ relative to $\hat{\bar{Y}}_{USi}$. Furthermore, Equation (19) is employed to compute the minimum MSE for all the existing and proposed estimators considered in this study.

$$MSE\left(\hat{\bar{Y}}_j\right) = \frac{\sum_{j=1}^{10000}\left(\hat{\bar{Y}}_j - \hat{\bar{Y}}\right)^2}{10000}. \text{where } j = USi \text{ and } Pi. \quad ...(19)$$

The following five steps are carried out to perform the simulation study:

1. Select a SRS without replacement of size n from a population of size N.
2. Calculate the minimum MSE for all estimators based on the sample obtained in Step 1.
3. Repeat Steps 1 and 2, a total of 10,000 times.
4. Obtain 10,000 minimum MSE values for each estimator, namely $\hat{\bar{Y}}, \hat{\bar{Y}}_{USi}$ and $\hat{\bar{Y}}_{Pi}$.
5. Using the results from Step 4, compute the average of the 10,000 MSE values to determine the minimum MSE for each estimator.

Tables 8 and 9 present the bias, minimum MSE, and PRE values for a range of sample sizes. The simulation results, which align closely with the outcomes obtained from real data applications, reveal the following:

- The MSE values of $\hat{\bar{Y}}$ for Populations 1 through 6, evaluated at different sample sizes, are reported as follows: (17589.682; 14535.914), (2000.095; 1531.322), (238.004; 182.891), (1585.495; 1206.519), (1109.088; 809.764) and (2349.807; 2068.007), respectively.
- The estimator $\hat{\bar{Y}}_{USi}$ attains a smaller minimum MSE than the traditional mean estimator $\hat{\bar{Y}}$.
- For all the listed populations, the proposed estimators $\hat{\bar{Y}}_{Pi}$ outperform the Shahzad et al. (2022) estimators since their absolute bias is much closer to zero.
- The bias of both estimators, $\hat{\bar{Y}}_{Pi}$ and $\hat{\bar{Y}}_{USi}$, decreases as the sample size increases.
- The proposed estimators $\hat{\bar{Y}}_{Pi}$ attain lower minimum MSE and higher PRE compared to $\hat{\bar{Y}}_{USi}$. Overall, the proposed family consistently exhibits superior performance relative to all competing estimators.

CONCLUSION

This study proposes a novel family of quantile regression-ratio-type estimators for estimating unknown population mean under simple random sampling. Mathematical properties of the proposed estimators including bias, mean squared error (MSE) and minimum MSE, are derived. To demonstrate the efficiency of the newly proposed estimators in the presence of extreme values/ outliers, six real-life applications taken from agriculture loan, cereal nutrition, population, agriculture, and school education are integrated into the study. The results show that the proposed estimators outperform existing estimators in terms of bias, MSE and percent relative efficiency (PRE). The proposed robust quantile regression-ratio-type estimators are highly recommended for future applications when dealing with data sets that may contain outlier(s). Future extensions of this study could include:

- Estimating population medians using non-conventional measures of auxiliary variables under SRS based on quantile regression coefficient.
- Estimating population means using non-conventional measures of auxiliary variables in the presence of non-sampling errors.
- Estimating population means, medians, and variances utilizing partial auxiliary information under different sampling schemes.

REFERENCES

Alomair, A. M., & Iftikhar, S. (2024). Dual-type quantile regression approach for mean estimation incorporating sampled and non-sampled data. *Heliyon*, *10*(10), Article e31034. https://doi.org/10.1016/j.heliyon.2024.e31034

Anas, M. M., Huang, Z., Shahzad, U., Zaman, T., & Shahzadi, S. (2024). Compromised imputation based mean estimators using robust quantile regression. *Communications in Statistics – Theory and Methods*, *53*(5), 1700–1715. https://doi.org/10.1080/03610926.2022.2108057

Cochran, W. G. (1977). *Sampling techniques*. Wiley.

Irfan, M., Javed, M., & Lin, Z. (2019). Improved estimation of population mean through known conventional and non-conventional measures of auxiliary variable. *Iranian Journal of Science and Technology, Transactions A: Science*, *43*, 1851–1862. https://doi.org/10.1007/s40995-018-0645-2

Khalid, M., Khana, H., & Shabbir, J. (2023). Exponentially quantile regression-ratio-type estimators for robust mean estimation. *Communications in Statistics – Theory and Methods*, 1–18. https://doi.org/10.1080/03610926.2023.2258426

Koc, T., & Koc, H. (2023). A new class of quantile regression ratio-type estimators for finite population mean in stratified random sampling. *Axioms*, *12*(7), 713. https://doi.org/10.3390/axioms12070713

Koç, H. (2021). Ratio-type estimators for improving mean estimation using Poisson regression method. *Communications in Statistics – Theory and Methods*, *50*(20), 4685–4691. https://doi.org/10.1080/03610926.2020.1777307

Koyuncu, N., & Kadilar, C. (2009). Efficient estimators for the population mean. *Hacettepe Journal of Mathematics and Statistics*, *38*(2), 217–225. https://doi.org/10.1080/03610920802562723

McClellan, M., McNeil, B. J., & Newhouse, J. P. (1994). Does more intensive treatment of acute myocardial infarction in the elderly reduce mortality? Analysis using instrumental variables. *JAMA*, *272*(11), 859–866. https://doi.org/10.1001/jama.1994.03520110039026

Shahzad, U., Ahmad, I., Al-Noor, N. H., Hanif, M., & Almanjahie, I. M. (2023). Robust estimation of the population mean using quantile regression under systematic sampling. *Mathematical Population Studies*, *30*(3), 195–207. https://doi.org/10.1080/08898480.2022.2139072

Shahzad, U., Al-Noor, N. H., Afshan, N., Alilah, D. A., Hanif, M., & Anas, M. M. (2021). Minimum covariance determinant-based quantile robust regression-type estimators for mean parameter. *Mathematical Problems in Engineering*, 5255839. https://doi.org/10.1155/2021/5255839

Shahzad, U., Hanif, M., Sajjad, I., & Anas, M. M. (2022). Quantile regression-ratio-type estimators for mean estimation under complete and partial auxiliary information. *Scientia Iranica*, *29*(3), 1705–1715.

Singh, R., & Mangat, N. S. (1996). *Elements of survey sampling*. Kluwer Academic Publishers. https://doi.org/10.1007/978-94-017-1404-4

Subhani, A., Irfan, M., & Javed, M. (2026). Quantile regression-based mean estimation in circular systematic sampling. *Maejo International Journal of Science and Technology*, *20*(1), 67–82.

Venables, W. N., & Ripley, B. D. (2009). *Modern applied statistics with S-PLUS*. Springer Science & Business Media.

Zaman, T. (2019). Improvement of modified ratio estimators using robust regression methods. *Applied Mathematics and Computation*, *348*, 627–631. https://doi.org/10.1016/j.amc.2018.12.037

Zaman, T., Ali, N., Ahmad, I., Hanif, M., & Shahzad, U. (2021). Robust-regression-type estimators for improving mean estimation of sensitive variables by using auxiliary information. *Communications in Statistics – Theory and Methods*, *50*(5), 979–992. https://doi.org/10.1080/03610926.2019.1645857

Zaman, T., Bulut, H., & Yadav, K. S. (2022). Robust ratio-type estimators for finite population mean in simple random sampling: A simulation study. *Concurrency and Computation: Practice and Experience*, *34*(15), Article e7273. https://doi.org/10.1002/cpe.7273

Zaman, T., & Sozen, C. (2026). Quantile-based neutrosophic

regression estimators under stratified random sampling. *Quality & Quantity*, 1–15. https://doi.org/10.1007/s11135-026-00000-0

Zaman, T., Shazad, U., & Yadav, K. V. (2024). An efficient Hartley-Ross type estimators of nonsensitive and sensitive variables using robust regression methods in sample surveys. *Journal of Computational and Applied Mathematics*, *440*, Article 115645. https://doi.org/10.1016/j.cam.2023.115645

Apendix

Table 1: Conventional and non-conventional measures

Conventional Measures	Non-conventional Measures	
Standard deviation: S_x	Quartile deviation:	$Q_D = \frac{Q_3 - Q_1}{2}$
Coefficient of variation: C_x	Mid-range:	$M_R = \frac{x_{(1)} + x_{(N)}}{2}$
Coefficient of skewness: $\beta_{1(x)}$	Inter-quartile range:	$Q_R = Q_3 - Q_1$
Coefficient of kurtosis: $\beta_{2(x)}$	Quartile average:	$Q_A = \frac{Q_3 + Q_1}{2}$
Coefficient of correlation: ρ_{yx}	Tri-mean:	$T_M = \frac{Q_1 + 2Q_2 + Q_3}{4}$
	Hodges Lehmann estimator:	$H_L = \text{Median}\left(\frac{x_j + x_k}{2}\right), 1 \le j \le k \le N$

Table 2: Family members of $\hat{\bar{Y}}_{USi}$

a	1	C_x	ρ_{yx}	1	C_x	1	C_x	ρ_{yx}
b	T_M	T_M	T_M	Q_A	Q_A	H_L	H_L	H_L
$\hat{\bar{Y}}_{USi}$	$\hat{\bar{Y}}_{US1}$	$\hat{\bar{Y}}_{US2}$	$\hat{\bar{Y}}_{US3}$	$\hat{\bar{Y}}_{US4}$	$\hat{\bar{Y}}_{US5}$	$\hat{\bar{Y}}_{US6}$	$\hat{\bar{Y}}_{US7}$	$\hat{\bar{Y}}_{US8}$

Table 3: Family members of $\hat{\bar{Y}}_{Pi}$

a	1	C_x	ρ_{yx}	1	C_x	1	C_x	ρ_{yx}
b	T_M	T_M	T_M	Q_A	Q_A	H_L	H_L	H_L
$\hat{\bar{Y}}_{Pi}$	$\hat{\bar{Y}}_{P1}$	$\hat{\bar{Y}}_{P2}$	$\hat{\bar{Y}}_{P3}$	$\hat{\bar{Y}}_{P4}$	$\hat{\bar{Y}}_{P5}$	$\hat{\bar{Y}}_{P6}$	$\hat{\bar{Y}}_{P7}$	$\hat{\bar{Y}}_{P8}$

Table 4: MSE of traditional estimators under SRS

Estima-tors	Pop-1	Pop-2	Pop-3	Pop-4	Pop-5	Pop-6
$\hat{\bar{Y}}$	10260.640	1125.138	134.835	953.872	677.004	1947.078
$\hat{\bar{Y}}_{Reg}$	3630.737	79.841	97.152	34.514	101.024	173.886

Table 5: Bias of $\hat{\bar{Y}}_{USi}$ and $\hat{\bar{Y}}_{Pi}$ estimators

Estimator	1	2	3	4	5	6	7	8
				Population-1				
$\hat{\bar{Y}}_{USi}$	9.797	11.381	8.208	8.731	10.288	8.641	10.196	7.119
$\hat{\bar{Y}}_{Pi}$	4.623	4.638	4.809	4.728	4.610	4.740	4.612	5.045
				Population-2				
$\hat{\bar{Y}}_{USi}$	5.776	7.641	5.623	5.551	7.424	5.105	6.982	4.959
$\hat{\bar{Y}}_{Pi}$	0.555	0.288	0.564	0.563	0.347	0.537	0.444	0.523
				Population-3				
$\hat{\bar{Y}}_{USi}$	0.797	0.898	0.791	0.895	0.897	0.794	0.797	0.889
$\hat{\bar{Y}}_{Pi}$	0.607	0.629	0.630	0.607	0.629	0.607	0.629	0.631
				Population-4				
$\hat{\bar{Y}}_{USi}$	2.833	2.861	2.790	2.571	2.598	2.694	2.722	2.651
$\hat{\bar{Y}}_{Pi}$	1.076	1.085	1.052	0.977	0.988	1.027	1.033	1.007
				Population-5				
$\hat{\bar{Y}}_{USi}$	1.576	1.353	1.465	1.495	1.277	1.563	1.341	1.452
$\hat{\bar{Y}}_{Pi}$	0.738	0.880	0.806	0.787	0.932	0.745	0.888	0.814
				Population-6				
$\hat{\bar{Y}}_{USi}$	2.547	3.450	2.474	2.298	3.233	2.377	3.304	2.305
$\hat{\bar{Y}}_{Pi}$	0.195	0.138	0.186	0.156	0.180	0.171	0.168	0.158

Table 6: MSE's of $\hat{\bar{Y}}_{USi}$ and $\hat{\bar{Y}}_{Pi}$ estimators

Estimator		1	2	3	4	5	6	7	8
					Population-1				
$q_{.15}$	$\hat{\bar{Y}}_{USi}$	6893.314	7582.030	6218.439	6442.900	7110.315	6400.697	7065.259	5767.998
	$\hat{\bar{Y}}_{Pi}$	4471.986	4956.287	4094.106	4208.502	4613.386	4186.404	4583.754	3897.674
$q_{.25}$	$\hat{\bar{Y}}_{USi}$	7100.573	7809.797	6403.370	6625.089	7312.653	6591.920	7277.827	5936.356
	$\hat{\bar{Y}}_{Pi}$	4579.947	5090.634	4175.655	4293.887	4723.300	4275.146	4698.352	3961.189
$q_{.35}$	$\hat{\bar{Y}}_{USi}$	7161.769	7876.931	6458.102	6687.090	7381.370	5986.289	7340.559	5986.289
	$\hat{\bar{Y}}_{Pi}$	4612.390	5130.718	4200.449	4323.613	4761.204	4302.024	4732.717	3980.759
					Population-2				
$q_{.15}$	$\hat{\bar{Y}}_{USi}$	654.820	893.707	635.916	626.432	865.227	571.266	808.388	553.086
	$\hat{\bar{Y}}_{Pi}$	253.420	462.718	240.063	233.519	434.029	198.129	379.600	187.397
$q_{.25}$	$\hat{\bar{Y}}_{USi}$	920.609	1205.160	897.716	886.286	1171.710	818.882	1104.41	796.548
	$\hat{\bar{Y}}_{Pi}$	410.238	684.038	391.673	382.588	647.880	331.803	578.158	315.993
$q_{.35}$	$\hat{\bar{Y}}_{USi}$	957.551	1247.837	934.156	922.459	1213.735	853.5418	1145.157	830.685
	$\hat{\bar{Y}}_{Pi}$	433.470	715.388	414.249	404.831	678.272	352.120	606.645	335.669
					Population-3				
$q_{.15}$	$\hat{\bar{Y}}_{USi}$	137.925	114.445	113.350	137.614	114.259	137.588	114.243	113.157
	$\hat{\bar{Y}}_{Pi}$	103.041	97.117	97.035	103.224	97.179	102.910	97.097	96.0184
$q_{.25}$	$\hat{\bar{Y}}_{USi}$	130.644	109.828	108.893	130.362	109.668	130.338	109.655	108.729
	$\hat{\bar{Y}}_{Pi}$	100.416	96.768	96.774	100.567	96.773	100.317	96.769	96.777
$q_{.35}$	$\hat{\bar{Y}}_{USi}$	126.342	107.238	106.406	126.079	107.096	126.057	107.084	106.261
	$\hat{\bar{Y}}_{Pi}$	99.100	96.916	96.977	99.2112	96.883	99.020	96.929	96.993
					Population-4				
$q_{.15}$	$\hat{\bar{Y}}_{USi}$	325.268	328.538	320.335	295.117	298.266	309.305	312.516	304.467
	$\hat{\bar{Y}}_{Pi}$	112.897	114.909	109.910	95.557	97.269	103.440	105.293	100.694
$q_{.25}$	$\hat{\bar{Y}}_{USi}$	295.159	298.256	290.490	266.362	269.333	280.057	283.093	275.484
	$\hat{\bar{Y}}_{Pi}$	97.706	99.515	95.027	82.111	83.624	89.245	90.898	86.800
$q_{.35}$	$\hat{\bar{Y}}_{USi}$	333.052	336.366	328.054	301.925	305.115	316.874	320.129	311.969
	$\hat{\bar{Y}}_{Pi}$	116.946	119.009	113.882	98.860	100.618	107.240	109.143	104.418
					Population-5				
$q_{.15}$	$\hat{\bar{Y}}_{USi}$	144.413	131.415	137.781	138.984	126.863	143.645	130.765	137.068
	$\hat{\bar{Y}}_{Pi}$	101.156	102.057	101.222	101.137	103.113	101.027	102.182	101.039
$q_{.25}$	$\hat{\bar{Y}}_{USi}$	262.347	236.212	249.302	252.845	227.443	260.861	234.836	247.867
	$\hat{\bar{Y}}_{Pi}$	139.389	126.518	132.650	134.427	122.771	138.590	125.910	131.947
$q_{.35}$	$\hat{\bar{Y}}_{USi}$	285.833	257.779	271.852	275.055	247.775	284.243	256.298	270.312
	$\hat{\bar{Y}}_{Pi}$	151.119	136.214	143.366	145.164	131.568	150.204	135.498	142.551
					Population-6				
$q_{.15}$	$\hat{\bar{Y}}_{USi}$	743.401	1034.01	720.822	666.528	963.0592	690.71	985.901	668.360
	$\hat{\bar{Y}}_{Pi}$	361.939	656.502	344.213	304.705	573.374	321.791	599.512	306.062
$q_{.25}$	$\hat{\bar{Y}}_{USi}$	916.628	1244.272	890.810	828.444	1164.940	856.273	1190.518	830.555
	$\hat{\bar{Y}}_{Pi}$	466.290	816.849	444.073	393.628	720.261	415.622	750.782	395.386
$q_{.35}$	$\hat{\bar{Y}}_{USi}$	1089.889	1450.448	1061.193	991.650	1363.671	1022.72	1391.684	994.016
	$\hat{\bar{Y}}_{Pi}$	578.298	978.657	552.087	491.909	870.093	518.273	904.517	494.028

Table 7: PRE's of $\hat{\bar{Y}}_{USi}$ and $\hat{\bar{Y}}_{Pi}$ estimators

Estimator		1	2	3	4	5	6	7	8
					Population-1				
$q_{.15}$	$\hat{\bar{Y}}_{USi}$	148.849	135.328	165.003	159.255	144.306	160.305	145.227	177.889
	$\hat{\bar{Y}}_{Pi}$	229.443	207.023	250.620	243.807	222.410	245.094	223.848	263.250
$q_{.25}$	$\hat{\bar{Y}}_{USi}$	144.504	131.382	160.238	154.876	140.314	155.655	140.985	172.844
	$\hat{\bar{Y}}_{Pi}$	224.034	201.559	245.725	238.959	217.235	240.007	218.388	259.029
$q_{.35}$	$\hat{\bar{Y}}_{USi}$	143.270	130.262	158.880	153.440	139.007	171.402	139.780	171.402
	$\hat{\bar{Y}}_{Pi}$	222.458	199.984	244.275	237.316	215.505	238.507	216.802	257.756
					Population-2				
$q_{.15}$	$\hat{\bar{Y}}_{USi}$	171.824	125.896	176.932	179.611	130.040	196.955	139.183	203.429
	$\hat{\bar{Y}}_{Pi}$	443.982	243.158	468.684	481.819	259.231	567.882	296.401	600.403
$q_{.25}$	$\hat{\bar{Y}}_{USi}$	122.217	93.360	125.333	126.950	96.025	137.399	101.877	141.252
	$\hat{\bar{Y}}_{Pi}$	274.265	164.485	287.265	294.086	173.665	339.098	194.607	356.064
$q_{.35}$	$\hat{\bar{Y}}_{USi}$	117.502	90.167	120.444	121.972	92.700	131.820	98.252	135.447
	$\hat{\bar{Y}}_{Pi}$	259.565	157.277	271.609	277.928	165.883	319.533	185.469	335.193
					Population-3				
$q_{.15}$	$\hat{\bar{Y}}_{USi}$	97.760	117.816	118.955	97.981	118.008	97.999	118.025	119.157
	$\hat{\bar{Y}}_{Pi}$	130.856	138.838	138.955	130.624	138.749	131.022	138.866	140.426
$q_{.25}$	$\hat{\bar{Y}}_{USi}$	103.208	122.769	123.823	103.431	122.948	103.450	122.963	124.010
	$\hat{\bar{Y}}_{Pi}$	134.276	139.338	139.330	134.075	139.331	134.409	139.337	139.325
$q_{.35}$	$\hat{\bar{Y}}_{USi}$	106.722	125.734	126.717	106.945	125.901	106.964	125.915	126.890
	$\hat{\bar{Y}}_{Pi}$	136.060	139.126	139.038	135.907	139.173	136.169	139.107	139.015
					Population-4				
$q_{.15}$	$\hat{\bar{Y}}_{USi}$	293.257	290.338	297.773	323.218	319.806	308.392	305.223	313.292
	$\hat{\bar{Y}}_{Pi}$	844.905	830.111	867.866	998.223	980.654	922.150	905.922	947.298
$q_{.25}$	$\hat{\bar{Y}}_{USi}$	323.172	319.817	328.367	358.111	354.161	340.599	336.947	346.253
	$\hat{\bar{Y}}_{Pi}$	976.268	958.521	1003.791	1161.686	1140.668	1068.824	1049.387	1098.931
$q_{.35}$	$\hat{\bar{Y}}_{USi}$	286.403	283.582	290.767	315.930	312.627	301.026	297.965	305.759
	$\hat{\bar{Y}}_{Pi}$	815.652	801.512	837.597	964.872	948.013	889.474	873.965	913.513
					Population-5				
$q_{.15}$	$\hat{\bar{Y}}_{USi}$	468.797	515.165	491.362	487.109	533.650	471.304	517.726	493.918
	$\hat{\bar{Y}}_{Pi}$	669.267	663.359	668.831	669.393	656.565	670.122	662.547	670.042
$q_{.25}$	$\hat{\bar{Y}}_{USi}$	258.057	286.609	271.560	267.755	297.659	259.527	288.288	273.132
	$\hat{\bar{Y}}_{Pi}$	485.694	535.105	510.369	503.622	551.436	488.494	537.689	513.088
$q_{.35}$	$\hat{\bar{Y}}_{USi}$	236.853	262.630	249.034	246.134	273.233	238.178	264.147	250.453
	$\hat{\bar{Y}}_{Pi}$	447.994	497.015	472.221	466.372	514.566	450.723	499.641	474.921
					Population-6				
$q_{.15}$	$\hat{\bar{Y}}_{USi}$	261.915	188.304	270.119	292.122	202.176	281.895	197.492	291.322
	$\hat{\bar{Y}}_{Pi}$	537.958	296.584	565.660	639.004	339.582	605.075	324.777	636.171
$q_{.25}$	$\hat{\bar{Y}}_{USi}$	212.417	156.483	218.574	235.028	167.140	227.390	163.549	234.431
	$\hat{\bar{Y}}_{Pi}$	417.568	238.364	438.459	494.649	270.329	468.473	259.340	492.450
$q_{.35}$	$\hat{\bar{Y}}_{USi}$	178.649	134.240	183.480	196.347	142.782	190.382	139.908	195.880
	$\hat{\bar{Y}}_{Pi}$	336.691	198.954	352.676	395.821	223.778	375.686	215.262	394.123

Table 8: Bias of $\hat{\bar{Y}}_{USi}$ and $\hat{\bar{Y}}_{Pi}$ estimators based on simulation studies

Sample size	Estimator	1	2	3	4	5	6	7	8
				Population-1					
$n = 16$	$\hat{\bar{Y}}_{USi}$	13.879	16.123	11.628	12.368	14.576	12.241	14.444	10.084
	$\hat{\bar{Y}}_{Pi}$	6.534	6.557	6.789	6.676	6.519	6.694	6.512	7.119
$n = 14$	$\hat{\bar{Y}}_{USi}$	16.795	19.511	14.070	14.967	17.638	14.813	17.478	12.204
	$\hat{\bar{Y}}_{Pi}$	7.897	7.902	8.195	8.068	7.867	8.089	7.861	8.581
				Population-2					
$n = 16$	$\hat{\bar{Y}}_{USi}$	7.862	10.400	7.658	7.556	10.104	6.949	9.503	6.750
	$\hat{\bar{Y}}_{Pi}$	0.753	0.390	0.752	0.750	0.468	0.713	0.598	0.693
$n = 13$	$\hat{\bar{Y}}_{USi}$	10.268	13.584	10.002	9.869	13.198	9.078	12.412	8.816
	$\hat{\bar{Y}}_{Pi}$	0.979	0.509	0.977	0.974	0.610	0.925	0.779	0.890
				Population-3					
$n = 16$	$\hat{\bar{Y}}_{USi}$	1.540	1.270	1.260	1.537	1.267	1.537	1.267	1.258
	$\hat{\bar{Y}}_{Pi}$	0.825	0.855	0.857	0.825	0.855	0.825	0.855	0.858
$n = 13$	$\hat{\bar{Y}}_{USi}$	1.706	1.352	1.340	1.701	1.350	1.701	1.349	1.337
	$\hat{\bar{Y}}_{Pi}$	1.076	1.115	1.117	1.076	1.115	1.076	1.115	1.118
				Population-4					
$n = 10$	$\hat{\bar{Y}}_{USi}$	3.584	3.169	3.529	3.252	3.287	3.407	3.442	3.354
	$\hat{\bar{Y}}_{Pi}$	1.344	1.355	1.325	1.220	1.237	1.281	1.294	1.262
$n = 8$	$\hat{\bar{Y}}_{USi}$	4.709	4.757	4.638	4.274	4.319	4.477	4.524	4.406
	$\hat{\bar{Y}}_{Pi}$	1.742	1.758	1.717	1.586	1.600	1.66o	1.677	1.634
				Population-5					
$n = 13$	$\hat{\bar{Y}}_{USi}$	1.886	1.619	1.753	1.789	1.528	1.871	1.604	1.738
	$\hat{\bar{Y}}_{Pi}$	0.883	1.053	0.965	0.942	1.115	0.892	1.063	0.974
$n = 10$	$\hat{\bar{Y}}_{USi}$	2.583	2.217	2.401	2.451	2.093	2.562	2.198	2.381
	$\hat{\bar{Y}}_{Pi}$	1.209	1.441	1.321	1.289	1.525	1.222	1.454	1.334
				Population-6					
$n = 210$	$\hat{\bar{Y}}_{USi}$	2.706	3.665	2.629	2.442	3.436	2.526	3.511	2.448
	$\hat{\bar{Y}}_{Pi}$	0.207	0.146	0.198	0.166	0.191	0.181	0.179	0.167
$n = 190$	$\hat{\bar{Y}}_{USi}$	3.075	4.165	2.987	2.770	3.904	2.870	3.988	2.782
	$\bar{Y}_p$	0.235	0.166	0.224	0.188	0.217	0.206	0.203	0.190

Table 9: MSE and PRE of $\hat{\bar{Y}}_{USi}$ and $\hat{\bar{Y}}_{Pi}$ estimators based on simulation studies

MSE/PRE	Estimator	1	2	3	4	5	6	7	8
					Population-1				
					$n = 16$				
MSE	$\hat{\bar{Y}}_{USi}$	9772.210	10748.550	8815.580	9127.450	10072.954	9073.720	10015.870	8176.820
	$\hat{\bar{Y}}_{Pi}$	6333.970	7019.670	5797.781	5957.390	6530.604	5928.848	6492.273	5518.170
PRE	$\hat{\bar{Y}}_{USi}$	148.750	135.240	164.890	159.250	144.319	160.209	145.138	177.774
	$\hat{\bar{Y}}_{Pi}$	229.490	207.070	250.720	244.000	222.587	245.174	223.904	263.427
					$n = 14$				
MSE	$\hat{\bar{Y}}_{USi}$	11825.194	13006.654	10667.607	11044.984	12189.126	10979.964	12120.055	9894.644
	$\hat{\bar{Y}}_{Pi}$	7660.524	8489.217	7011.695	7204.967	7898.268	7170.398	7851.929	6672.748
PRE	$\hat{\bar{Y}}_{USi}$	148.759	135.249	164.895	159.269	144.319	160.209	145.139	177.774
	$\hat{\bar{Y}}_{Pi}$	229.627	207.207	250.869	244.132	222.707	245.319	224.028	263.619
					Population-2				
					$n = 16$				
MSE	$\hat{\bar{Y}}_{USi}$	890.557	1215.94	864.971	852.178	1177.48	776.700	1099.67	752.095
	$\hat{\bar{Y}}_{Pi}$	343.309	629.431	325.177	316.362	590.434	267.809	515.772	253.276
PRE	$\hat{\bar{Y}}_{USi}$	171.951	125.937	177.037	179.695	130.051	197.157	139.253	203.608
	$\hat{\bar{Y}}_{Pi}$	446.048	243.287	470.920	484.041	259.355	571.796	296.899	604.606
					$n = 13$				
MSE	$\hat{\bar{Y}}_{USi}$	1163.188	1588.174	1129.756	1113.049	1537.928	1014.466	1436.311	982.328
	$\hat{\bar{Y}}_{Pi}$	446.795	821.843	423.044	411.502	770.826	347.981	672.899	328.990
PRE	$\hat{\bar{Y}}_{US}$	171.951	125.937	177.039	179.695	130.051	197.157	139.252	203.608
	$\hat{\bar{Y}}_{Pi}$	447.654	243.367	472.787	486.047	259.474	574.771	297.236	607.950
					Population-3				
					$n = 16$				
MSE	$\hat{\bar{Y}}_{USi}$	187.570	155.298	154.219	187.147	155.049	187.112	155.028	153.957
	$\hat{\bar{Y}}_{Pi}$	139.476	131.475	131.373	139.313	131.45	139.299	131.448	131.350
PRE	$\hat{\bar{Y}}_{USi}$	97.505	117.768	118.592	97.726	117.957	97.744	117.973	118.794
	$\hat{\bar{Y}}_{Pi}$	131.127	139.107	139.215	131.281	139.134	131.294	139.136	139.239
					$n = 13$				
MSE	$\hat{\bar{Y}}_{USi}$	244.994	202.839	201.429	244.437	202.512	244.392	202.486	201.087
	$\hat{\bar{Y}}_{Pi}$	181.910	171.459	171.324	181.698	171.427	181.681	171.424	171.295
PRE	$\hat{\bar{Y}}_{USi}$	97.147	117.334	118.156	97.367	117.524	97.385	117.539	118.357
	$\hat{\bar{Y}}_{Pi}$	130.834	138.809	138.918	130.987	138.835	130.999	138.837	138.942

(Continued -)

MSE/PRE	Estimator	1	2	3	4	5	6	7	8
				Population-4					
				$n = 10$					
MSE	$\hat{\bar{Y}}_{USi}$	411.137	415.272	404.900	373.284	377.267	390.954	395.014	384.837
	$\hat{\bar{Y}}_{Pi}$	140.683	143.204	136.943	119.123	121.263	128.847	131.165	125.413
PRE	$\hat{\bar{Y}}_{USi}$	293.459	290.537	297.979	323.217	319.805	308.608	305.437	313.514
	$\hat{\bar{Y}}_{Pi}$	857.615	842.517	881.037	1012.83	994.96	936.396	919.848	962.036
				n =8					
MSE	$\hat{\bar{Y}}_{USi}$	540.276	545.709	532.081	490.533	495.767	513.754	519.088	505.715
	$\hat{\bar{Y}}_{Pi}$	180.999	184.267	176.153	153.118	155.879	165.677	168.675	161.238
PRE	$\hat{\bar{Y}}_{USi}$	293.459	290.537	297.979	323.217	319.805	308.608	305.437	313.514
	$\hat{\bar{Y}}_{Pi}$	875.966	860.431	900.064	1035.469	1017.13	956.976	939.967	983.322
				Population-5					
				$n = 13$					
MSE	$\hat{\bar{Y}}_{USi}$	172.056	156.625	164.179	166.306	151.802	171.143	155.853	163.333
	$\hat{\bar{Y}}_{Pi}$	120.891	122.229	121.173	121.019	123.369	120.884	122.385	121.250
PRE	$\hat{\bar{Y}}_{USi}$	470.829	517.216	493.419	487.108	533.649	473.341	519.778	495.974
	$\hat{\bar{Y}}_{Pi}$	670.099	662.764	668.540	669.391	656.640	670.138	661.919	668.115
				$n = 10$					
MSE	$\hat{\bar{Y}}_{USi}$	235.656	214.521	224.8675	227.779	207.912	234.405	213.464	223.708
	$\hat{\bar{Y}}_{Pi}$	165.576	167.388	165.959	165.752	168.928	165.568	167.599	166.061
PRE	$\hat{\bar{Y}}_{USi}$	470.828	517.215	493.417	487.110	533.656	473.341	519.776	495.974
	$\hat{\bar{Y}}_{Pi}$	670.106	662.852	668.559	669.394	656.809	670.138	662.017	668.148
				Population-6					
				$n = 210$					
MSE	$\hat{\bar{Y}}_{USi}$	789.880	1098.66	765.889	798.200	1023.27	733.895	1047.54	710.148
	$\hat{\bar{Y}}_{Pi}$	384.381	697.284	365.553	323.699	609.184	341.738	636.744	325.032
PRE	$\hat{\bar{Y}}_{USi}$	261.915	188.303	270.119	259.185	202.177	281.895	197.492	291.321
	$\hat{\bar{Y}}_{Pi}$	538.219	296.696	565.940	639.116	339.604	605.380	324.905	636.495
				$n = 190$					
MSE	$\hat{\bar{Y}}_{USi}$	897.514	1248.38	870.704	804.704	1162.71	833.900	1190.29	806.917
	$\hat{\bar{Y}}_{Pi}$	436.606	792.228	415.213	367.662	692.094	388.155	723.418	369.176
PRE	$\hat{\bar{Y}}_{USi}$	261.915	188.302	269.979	292.122	202.176	281.895	197.491	291.321
	$\hat{\bar{Y}}_{Pi}$	538.408	296.723	566.148	639.370	339.653	605.614	324.946	636.748

Computational Procedure Based on R Software

```
N=;n=;bq=;qa=;tm=;hl=;
data=read.csv(file="pop 1.csv")                    #upload data file
x=data[,1]
y=data[,2]
f=n/N;lem=(1-f)/n;
xm=mean(x)
ym=mean(y)
sx=sd(x)
sy=sd(y)
cx=sx/xm
cy=sy/ym
cxx=cx^2
cyy=cy^2
l=cor(x,y)
cxy=cyx=l*cx*cy
sxy=l*sx*sy
# MSE of classical mean estimator
mse(c)=lem*ym^2*cyy
# MSE of Regression estimator
mse(r)=lem*ym^2*cyy(1-l^2)
# Usman Shahzad estimator
a=1;b=tm;
v=(a*ym)/(a*xm+b)
#MSE of Usman Shahzad estimator
mse(S1)=lem*(sy^2+v^2*sx^2+2*bq*v*sx^2+bq^2*sx^2-2*v*sxy-2*bq*sxy)
#Bias Usman Shahzad estimator
bi(S1)=(lem* sx^2*v^2)/ym
#Proposed estimator
a=1;b=tm;
v=(a*xm)/(a*xm+b)
A1=lem*(ym^2*cyy+2*v^4*ym^2*cxx +v^3*ym^2*cxx-4*v^2*ym^2*cyx)
A2=lem*(v^4*ym^2*cxx+v^3*ym^2*cxx-2*v^2*ym^2*cyx +2*bq*ym*xm*cyx-2*v^2*bq*xm*ym*cxx)
alf=(2*ym^2+A2)/(2*ym^2+2*A1)
# MSE of proposed estimator
mse(P1)=(alf*ym-ym)^2+alf^2*A1-alf*A2+ lem* bq^2*xm^2*cxx
#Bias of Proposed estimator
bi(P1)=(alf-1)*ym+lem*ym*alf*((0.5*v^3*(v+1)*cxx)-v^2*cxy)
#Results
mse(c);mse(r);mse(S1);bi(S1);mse(P1);bi(P1);
```

J.Natn.Sci.Foundation Sri Lanka 2026 54 (3): 425 - 437
DOI: http://dx.doi.org/10.4038/jnsfsr.v54i3.13051

RESEARCH ARTICLE

Meteorology

Sensitivity analysis of the simulation of tropical cyclone Amphan using the WRF model

TD Gamage[1,2*], U Sonnadara[2], S Jayasinghe[3] and S Basnayake[3]
[1] *Department of Electrical and Information Engineering, Faculty of Engineering, University of Ruhuna, Galle, Sri Lanka.*
[2] *Department of Physics, Faculty of Science, University of Colombo, Colombo, Sri Lanka.*
[3] *Climate Resilience Department, Asian Disaster Preparedness Center, Thailand.*

Submitted: 15 October 2025; Revised: 12 May 2026; Accepted: 24 July 2026

Abstract: The sensitivity of twenty-four physics option combinations in the Weather Research and Forecasting (WRF) model is investigated through simulations of the track, intensity, and landfall of tropical Cyclone Amphan. Simulation accuracy is evaluated using data from an international best track archive. Track performance is assessed using root mean square error (RMSE), while intensity is evaluated by comparing the minimum sea level pressure (MSLP) and the maximum wind speed measured at a height of 10 m above sea level. The results indicate that the combination of the New Tiedtke cumulus scheme, University of Washington planetary boundary layer scheme, Dudhia shortwave scheme, Rapid Radiative Transfer Model longwave scheme, and the WRF Single-Moment 6-Class microphysics scheme produces the most accurate track simulation, with an RMSE of 72 km, a mean absolute MSLP error of 27 hPa, and a mean absolute wind speed error of 22 ms^{-1}. Replacing the microphysics scheme with the Thompson microphysics scheme, while keeping the other physics options unchanged, results in a slightly higher track error but improves the landfall simulation, yielding the lowest landfall position error (43 km) and a time error of 1 hour and 32 minutes. These results indicate a trade-off between track and intensity accuracy and landfall prediction. Overall, the findings contribute to improved understanding of WRF physics configuration choices, support the development of more reliable cyclone forecasting frameworks, and highlight the need for better representation of intensity-related processes.

Keywords: Amphan, North Indian Ocean, tropical cyclone, WRF model.

INTRODUCTION

Tropical cyclones (TCs) are intense weather systems that develop over warm ocean waters, typically spanning hundreds to 1,000 km horizontally and extending through much of the troposphere (Wang, 2012). Depending on their location and intensity, they are referred to as hurricanes, typhoons, tropical storms, or tropical depressions. The formation and intensification of TCs are strongly influenced by ocean–atmosphere interactions, including sea surface temperature (SST) anomalies. For instance, in the case of Cyclone Amphan, a mean positive SST anomaly of approximately 0.8–1 °C was observed prior to cyclogenesis near the formation region (Singh et al., 2024), highlighting the role of environmental conditions in driving rapid intensification.

Cyclone Amphan, which developed over the Bay of Bengal in May 2020, was one of the most intense and costly cyclones recorded in the North Indian Ocean, causing approximately USD 13.2 billion in damages in West Bengal alone (Sud & Rajaram, 2020). The cyclone also affected several regions, including Bangladesh, Bhutan, parts of India such as Kerala, and Sri Lanka. Classified as a Category 5 storm on the Saffir–Simpson Hurricane Scale, Amphan exhibited rapid intensification and severe destructive potential. These characteristics

* Corresponding author (tharindu@eie.ruh.ac.lk; https://orcid.org/0000-0002-9770-7795)

This article is published under the Creative Commons CC-BY-ND License (http://creativecommons.org/licenses/by-nd/4.0/). This license permits use, distribution and reproduction, commercial and non-commercial, provided that the original work is properly cited and is not changed in anyway.

make the Cyclone Amphan a critical case study for understanding the challenges associated with accurately simulating high-impact cyclones, particularly in regions such as the Bay of Bengal, where forecasting remains complex.

Numerical weather prediction (NWP) models play a central role in simulating and forecasting TCs. Among these, the Weather Research and Forecasting (WRF) Model is widely used for both research and operational applications (Skamarock et al., 2019). The Advanced Research WRF (WRF-ARW) configuration incorporates a variety of physical parameterization schemes, numerical solvers, and data assimilation capabilities. However, the performance of WRF-ARW is highly sensitive to the selection of physical parameterization schemes, particularly those governing microphysics (MP), cumulus convection (CU), and planetary boundary layer (PBL) processes (Islam et al., 2015). Therefore, identifying suitable combinations of these schemes is important for improving the accuracy of TC simulations.

Several studies have explored the sensitivity of WRF simulations to different physics configurations. For example, Islam et al. (2015) examined the impact of MP, CU, and PBL schemes using multiple configurations and found that cumulus parameterization plays a significant role in intensity prediction, although no single optimal combination was identified. Similarly, Di et al. (2019) evaluated numerous physics combinations using an iterative optimization approach and reported consistent optimal CU and PBL schemes while identifying multiple viable MP options. Other studies have compared different dynamical cores and modelling approaches. Qi et al. (2018) showed that hydrostatic cores can produce stronger storm intensity and larger spatial structures compared to non-hydrostatic configurations. Litta et al. (2012) compared the performance of WRF model cores and found that the NMM core better captured certain storm characteristics. However, since the NMM core is no longer supported in recent WRF versions, the WRF-ARW configuration has become the standard choice for both research and operational applications and is therefore used in this study. Hon (2020) focused on cyclone track prediction by applying a vortex tracking algorithm to WRF outputs, while Shenoy et al. (2021) applied statistical methods to identify optimal combinations of physics schemes for multiple cyclones over the Bay of Bengal. Delfino et al. (2022) demonstrated the effectiveness of specific CU schemes in simulating cyclone tracks, achieving relatively low positional errors of 61 km and 94 km. More recently, there has been a growing shift toward advanced modelling strategies, including multi-physics ensemble approaches and machine learning-assisted frameworks for TC prediction.

Despite these efforts, there remains a lack of systematic investigation into the sensitivity of WRF physics parameterizations for high-impact cyclones affecting regions such as Sri Lanka. In particular, limited attention has been given to evaluating how different physics configurations influence the simulation of both the track and intensity of cyclones such as Amphan. Addressing this gap is important for improving regional forecasting capabilities and enhancing disaster preparedness.

This study focuses on the sensitivity analysis of Cyclone Amphan simulations using the WRF-ARW model. The objectives are twofold: (i) to evaluate the impact of various physical parameterization schemes on the simulation of the cyclone's track, intensity, and structure, and (ii) to identify suitable combinations of physics options that can improve forecasting performance for cyclones developing in the Bay of Bengal and affecting Sri Lanka.

MATERIALS AND METHODS

In this study, the sensitivity of the WRF model in simulating Cyclone Amphan is analyzed. The WRF model consists of two dynamical cores, namely ARW and NMM. The ARW dynamical core was selected for this work because it includes a large number of physical process schemes developed by the community over an extended period, making it a powerful NWP tool (Skamarock et al., 2019). Various physics options related to physical process schemes were tested to identify the most suitable combination for simulating Cyclone Amphan. The initial physics options selected for the experiments were based on those used in the literature.

Table 1 presents the MP, CU, PBL, shortwave (SW), and longwave (LW) physics options used in this work. The WRF Single-Moment 6-Class (WSM6) scheme and the Thompson scheme are used as the MP schemes. The Kain-Fritsch (KF), Tiedtke, and New Tiedtke schemes serve as the CU schemes. The PBL schemes considered are the Yonsei University (YSU) scheme and the University of Washington (UW) scheme. Radiation schemes include the Dudhia shortwave scheme, the Rapid Radiative transfer model (RRTM) longwave scheme, and the RRTMG shortwave and longwave schemes. In addition, the MM5 scheme is used as the surface layer option, and the Noah Land Surface Model is used as the land surface option.

Table 1: Selected physics options for the simulations

MP		CU		PBL		SW & LW	
Option	Scheme	Option	Scheme	Option	Scheme	Option	Scheme
6	WSM6	1	KF	1	YSU	1	Dudhia/RRTM
8	Thompson	6	Tiedtke	9	UW	4	RRTMG
		16	New Tiedtke				

The lateral boundary conditions for the selected domain are provided by the NCEP Final (FNL) Operational Global Analysis dataset. This dataset is produced operationally every six hours on 1° × 1° grids (National Centers for Environmental Prediction, National Weather Service, NOAA, U.S. Department of Commerce, 2000). It incorporates observational data from the Global Telecommunications system (GTS) and other sources. Furthermore, the dataset is generated approximately one hour after the initialization of the Global forecast system (GFS), allowing additional time to collect observational data. Despite this delay relative to the GFS, the FNL dataset is used in this study because the study focuses on sensitivity analysis rather than real-time forecasting. FNL represents a balanced choice for retrospective studies, as it incorporates additional observational data while maintaining consistency with operational NCEP products. Therefore, it is widely used for WRF-based cyclone simulations and is adopted in this study.

The model domain is centered at 17° N, 88° E, with 120 x 90 grid points and a grid spacing of 30 km, covering an area 3600 km x 2700 km. The selected domain encompasses the entire track of Cyclone Amphan. The terrain elevation of the simulation domain is shown in Figure 1. In the model configuration, the time step is set to 180 s, and the interval between radiation physics calls is set to 30 minutes. The simulations were initialized at 0000 UTC on May 15, 2020, using the FNL dataset. The total simulation length was 144 hours, with no explicit spin-up time applied. A total of 24 simulations were conducted, considering all combinations of the physics options shown in Table 1.

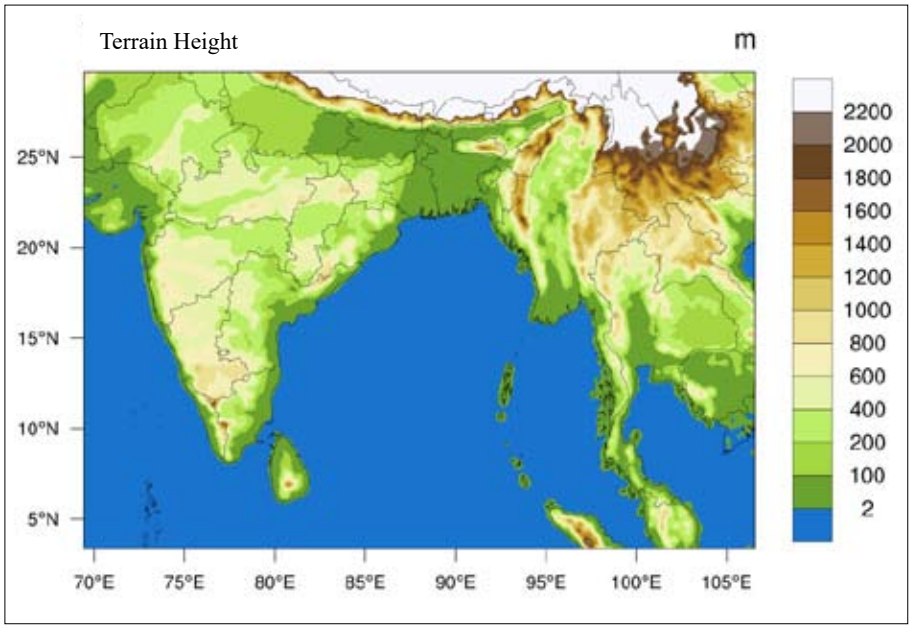

Figure 1: Terrain height of the selected simulation domain.

The accuracy of the simulations was evaluated using the International Best Track Archive for Climate Stewardship (IBTrACS) dataset (Knapp et al., 2010, 2018), as applied in Gamage et al., (2022). The root mean square error (RMSE) was calculated to evaluate the track error, with IBTrACS serving as the reference. The formula used for calculating RMSE is shown in Equation 1 (Britain, 2008). In this equation, N represents the number of cyclone positions recorded in the IBTrACS dataset. For Cyclone Amphan, 37 positions are available, spanning from 1200 UTC on May 16, 2020, to 0000 UTC on May 21, 2020, at 3-hour intervals.

$$RMSE = \sqrt{\frac{1}{N} x \sum_{n=1}^{N} d_n^2} \quad ...(1)$$

where d_n represents the great-circle distance between the observed track position from IBTrACS and the simulated track position.

The simulated intensity of Cyclone Amphan was evaluated by comparing sea level pressure and 10-m wind speed at the simulated track positions with the corresponding minimum sea level pressure (MSLP) and maximum sustained wind speed values from the IBTrACS dataset. The simulated cyclone position was defined as the location of minimum sea level pressure (MSLP) within the domain. The absolute MSLP error was calculated using these simulated values, with the IBTrACS data serving as reference. A search radius of 2° from the MSLP location was used to obtain the maximum simulated 10-m wind speed (Heming, 2017). The absolute wind speed error was then calculated using the maximum sustained wind speed from the IBTrACS dataset as the reference.

The landfall event of Cyclone Amphan was evaluated using landfall position error and landfall time error. Observed cyclone positions from the IBTrACS dataset were used to determine the actual landfall location and time. The latitude and longitude coordinates of cyclone positions before and after the landfall were used to define a straight-line trajectory. Terrain elevation at these coordinates was analyzed to distinguish land from sea, with the point of higher elevation identified as the landfall location.

The same procedure was applied to simulated cyclone positions to determine the simulated landfall location. The distance between the observed and simulated landfall locations is defined as the landfall position error.

Since the time interval between cyclone positions was three hours, the landfall time was estimated by assuming a constant cyclone speed between the positions before and after landfall. The timing was calculated based on the distance ratio between these positions and the landfall location. The landfall time error was defined as the difference between the simulated and observed landfall times.

RESULTS AND DISCUSSION

The sensitivity of physics options is evaluated based on the accuracy of track, intensity, and landfall. In this study, priority is given to the track RMSE, since the MSLP and wind speed are evaluated at the simulated cyclone positions. The following sections discuss the effects of different physics options on the simulation of cyclone track, intensity, and landfall.

Microphysics schemes

In this section, the sensitivity of the WSM6 and Thompson MP schemes is examined. These schemes are used in combination with CU, PBL, SW, and LW schemes. Table 2 presents the simulation results for all 24 combinations considered in this study, organized to compare the performance of the MP schemes while keeping the other physics options constant.

The WSM6 MP scheme produces lower track RMSE, mean absolute MSLP error, and mean absolute wind speed error in the first four experiments listed in Table 2. However, within these configurations, the Thompson MP scheme simulates the landfall event more accurately than WSM6. Beyond combination number 4, the track RMSE exceeds 100 km, and the landfall position error also exceeds 100 km. Additionally, 10 combinations failed to simulate landfall. Therefore, combinations beyond number 4 were excluded from further analysis.

Overall, the WSM6 MP scheme provides more accurate cyclone track simulations compared to the Thompson MP scheme. However, despite its higher track error, the Thompson MP scheme delivers improved landfall predictions, with lower positional and timing errors. The sensitivities of CU, PBL, SW, and LW schemes are further examined in combination with these two MP schemes.

Table 2: Track RMSE, mean absolute MSLP error, mean absolute wind speed error, landfall position error and landfall time error for each physics option combination.

#	MP	CU	PBL	LW & SW	Track RMSE (km)	Mean absolute MSLP error (hPa)	Mean absolute wind speed error (ms^{-1})	Landfall position error (km)	Landfall time error
1	6	16	9	1	72.1	27.05	22.21	83.2	3 h 02 m
2	8	16	9	1	78.9	29.62	23.16	42.9	1 h 32 m
3	6	16	1	1	81.0	30.78	23.00	91.2	6 h 02 m
4	8	16	1	1	94.5	32.85	24.11	13.5	4 h 32 m
5	6	6	9	1	177.1	36.73	26.12	n/a	n/a
6	8	6	9	1	173.0	38.61	28.72	325.8	4 h 32 m
7	6	1	1	1	216.5	25.08	18.58	309.3	-22 h 28 m
8	8	1	1	1	219.8	24.35	18.38	309.3	-22 h 28 m
9	6	1	9	1	230.2	22.59	18.47	344.9	-21 h 43 m
10	8	1	9	1	233.3	22.00	18.96	355.2	-23 h 13 m
11	6	6	1	1	370.4	38.56	25.84	n/a	n/a
12	8	6	1	1	260.6	36.46	24.91	284.8	8 h 40 m
13	6	1	1	4	326.3	25.91	17.75	575.7	- 18 h 43 m
14	8	1	1	4	265.7	25.49	17.65	540.2	- 20 h 13 m
15	6	1	9	4	361.2	21.84	17.02	657.9	-17 h 58 m
16	8	1	9	4	277.6	20.63	16.80	586.7	- 19 h 28 m
17	6	16	9	4	280.6	33.26	24.44	n/a	n/a
18	8	16	9	4	365.0	37.21	27.45	n/a	n/a
19	6	16	1	4	320.8	35.00	24.32	n/a	n/a
20	8	16	1	4	395.5	38.58	27.11	n/a	n/a
21	6	6	9	4	495.1	39.19	28.41	n/a	n/a
22	8	6	9	4	443.0	37.61	27.19	n/a	n/a
23	6	6	1	4	568.6	38.78	26.75	n/a	n/a
24	8	6	1	4	460.6	39.15	27.36	n/a	n/a

Cumulus schemes

This section evaluates the sensitivity of the KF, Tiedtke, and New Tiedtke CU schemes in combination with the WSM6 and Thompson MP schemes. The UW, Dudhia, and RRTM schemes are employed for the PBL, shortwave, and longwave radiation processes, respectively. Figure 2 shows the simulated cyclone tracks for these configurations compared with the IBTrACS reference track. In Figure 2a, the WSM6 MP scheme is used, whereas Figure 2b utilizes the Thompson MP scheme.

The results indicate that the New Tiedtke CU scheme, when combined with either MP scheme, produces more accurate track simulations than the other CU schemes. The corresponding track RMSE values are 72.1 km and 78.9 km, respectively (Table 2). These configurations also improve landfall predictions, with position errors of 83.2 km and 42.9 km, and landfall time errors of 3 h 02 min and 1 h 32 min, respectively.

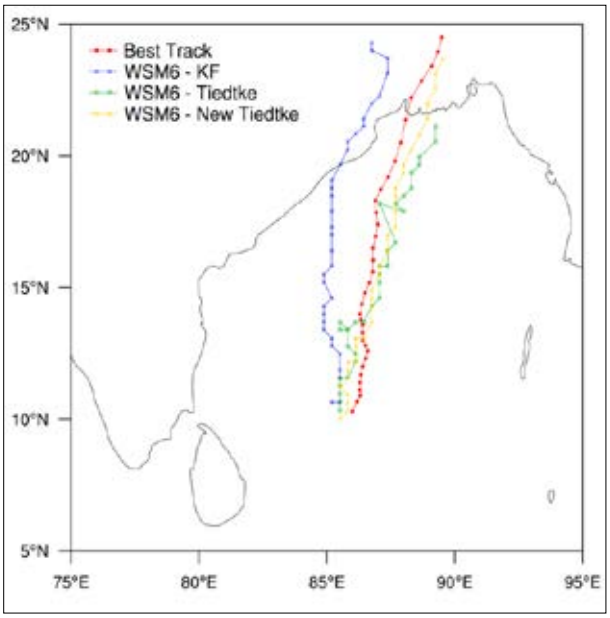

Figure 2(a): Simulated track of Cyclone Amphan using KF, Tiedtke and New Tiedtke CU schemes with the WSM6 MP scheme.

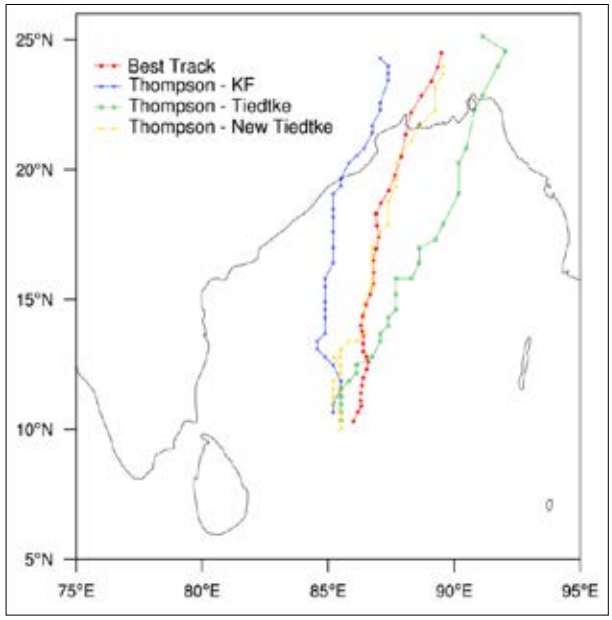

Figure 2(b): Simulated track of Cyclone Amphan using KF, Tiedtke and New Tiedtke CU schemes with Thompson MP scheme

The improved performance of the New Tiedtke CU scheme can be attributed to its mass-flux formulation, which explicitly represents convective updrafts and downdrafts, along with separate trigger functions for deep and shallow convection. This approach allows for a more realistic representation of convection and its interaction with the large-scale environment. Since cyclone tracks are strongly influenced by environmental steering flow, improved convection representation contributes to more accurate track simulations (Zhang et al., 2011).

In addition, the interaction between the CU and MP schemes plays a critical role. The WSM6 scheme provides a relatively stable representation of bulk microphysical processes, whereas the Thompson scheme includes a more detailed treatment of mixed-phase processes, such as cloud ice and graupel. These processes influence latent heat release within the cyclone, which in turn affects its vertical structure and coupling with the surrounding atmospheric flow (Mohan et al., 2019). The combination of the New Tiedtke CU scheme with these MP schemes results in a more physically consistent simulation of the cyclone system, leading to improved track prediction compared to other parameterization combinations.

Figure 3 illustrates the time evolution of simulated MSLP and 10-m wind speed for these configurations. The KF CU scheme produces lower MSLP and higher wind speeds during the initial stage compared to IBTrACS, with mean absolute MSLP errors of 22.59 hPa and 22.00 hPa, respectively, and wind speed errors of 18.47 ms^{-1} and 18.96 $ms^{-1,}$ respectively. However, these values correspond to tracks with high RMSE (230.2 km and 233.3 km), indicating poor track accuracy. Therefore, despite relatively lower intensity errors, the KF scheme is not considered suitable.

The Tiedtke and New Tiedtke schemes generally overestimate pressure and underestimate wind speed. Among these, the New Tiedtke scheme produces the lowest intensity errors while maintaining a low track RMSE, making it the most suitable CU scheme in this study.

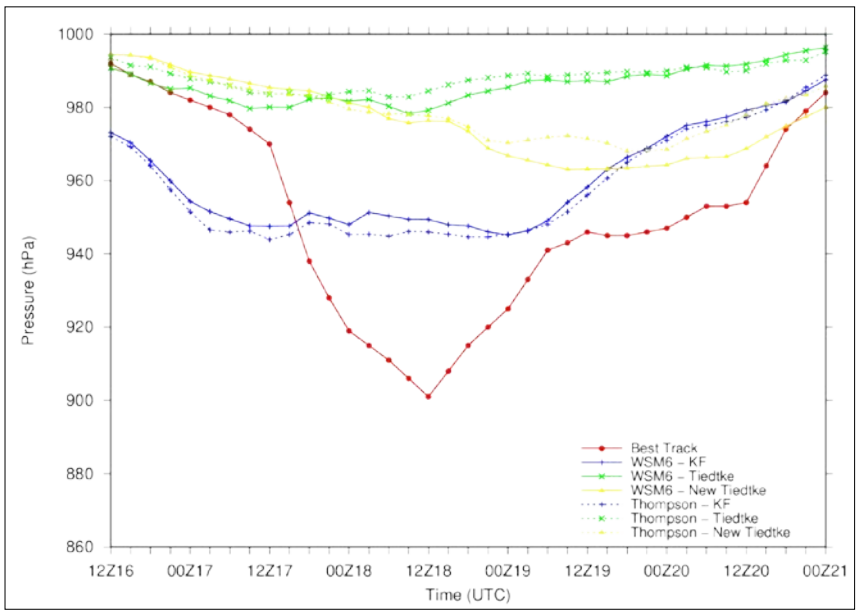

Figure 3(a): Minimum sea level pressure (MSLP) of Cyclone Amphan using KF, Tiedtke and New Tiedtke CU schemes with WSM6 and Thompson MP schemes.

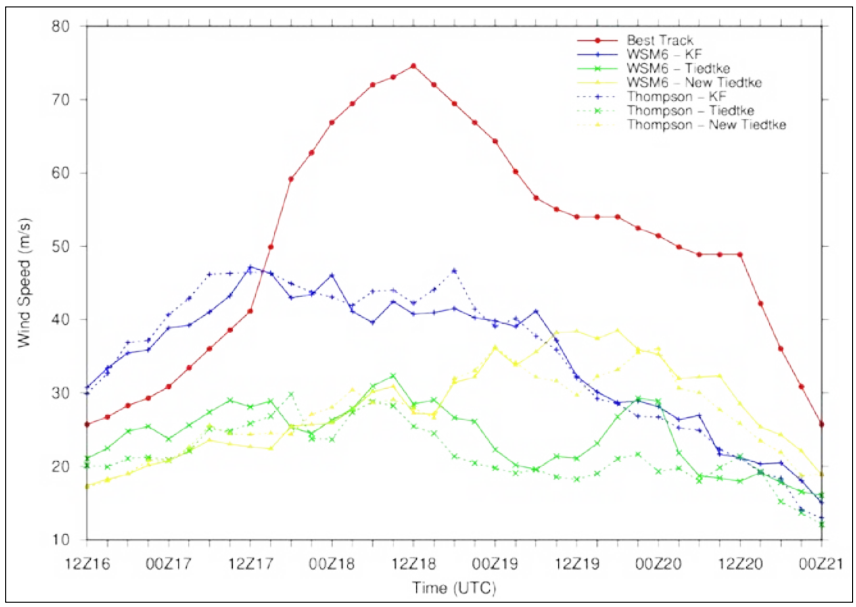

Figure 3(b): 10-m wind speed of Cyclone Amphan using KF, Tiedtke and New Tiedtke CU schemes with WSM6 and Thompson MP schemes.

PBL schemes

This section examines the sensitivity of the YSU and UW PBL schemes in combination with the WSM6 and Thompson MP schemes. The New Tiedtke, Dudhia, and RRTM schemes are employed for CU, SW, and LW parameterizations, respectively. Figure 4 presents the simulated tracks compared with the IBTrACS data. The WSM6 MP scheme is used in Figure 4a, while the Thompson MP scheme is applied in Figure 4b.

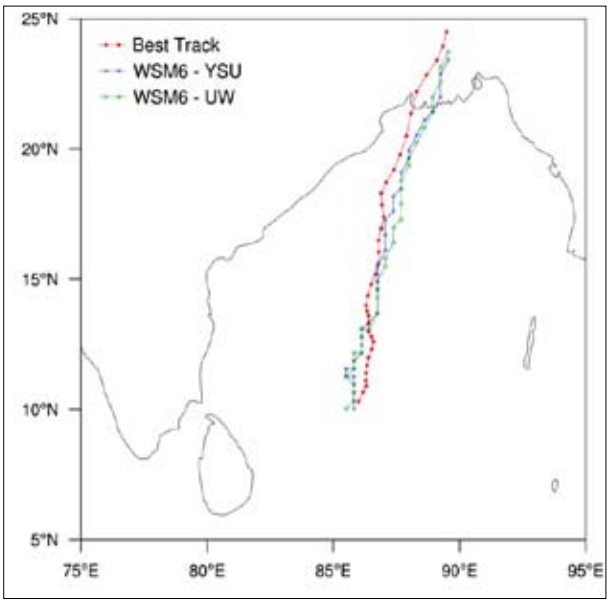

Figure 4(a): Simulated track of Cyclone Amphan with using YSU and UW PBL schemes with the WSM6 MP scheme.

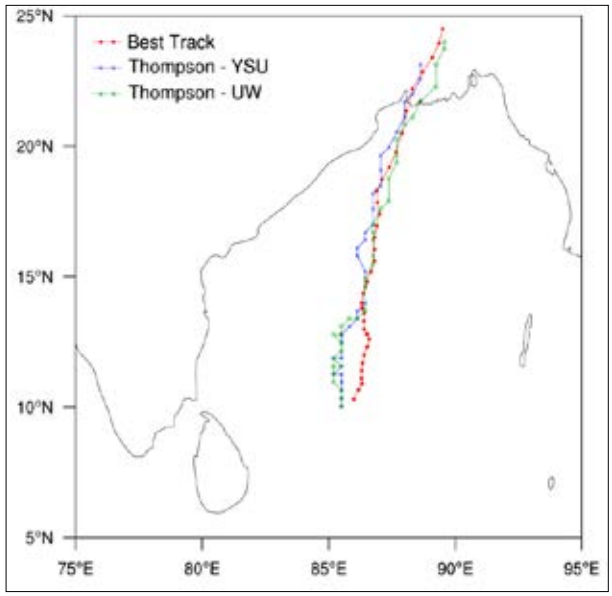

Figure 4(b): Simulated track of Cyclone Amphan using YSU and UW PBL schemes with Thompson MP scheme.

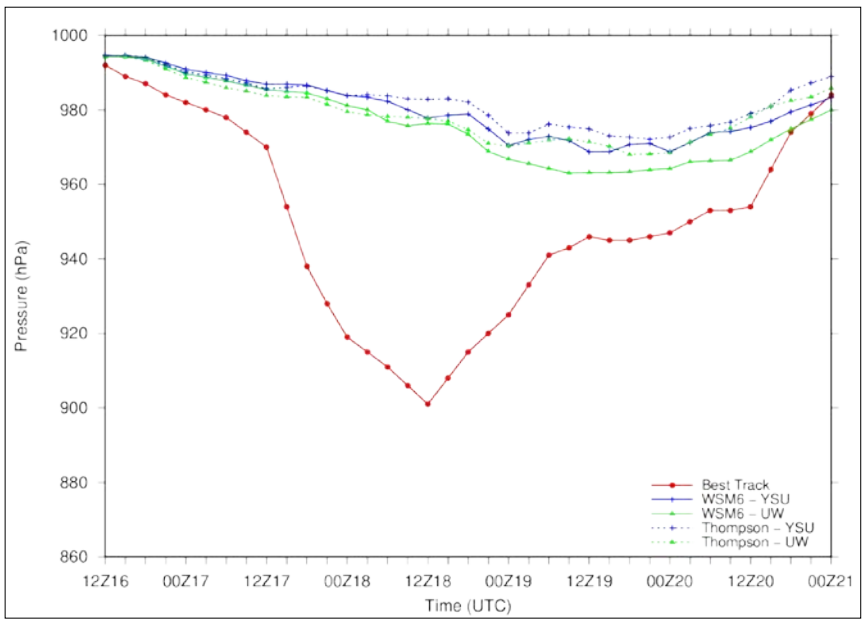

Figure 5(a): Minimum sea level pressure (MSLP) of Cyclone Amphan using YSU and UW PBL schemes with WSM6 and Thompson MP schemes.

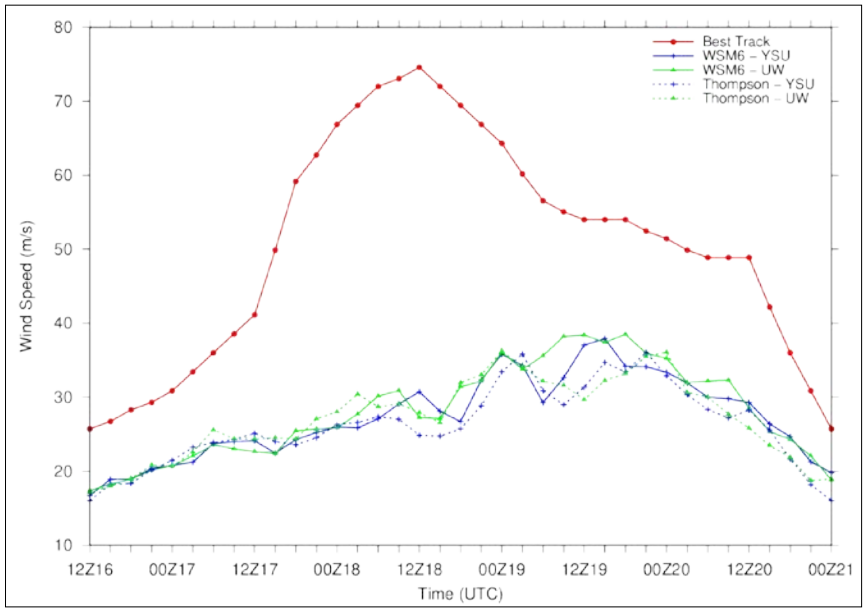

Figure 5(b): 10-m wind speed of Cyclone Amphan using YSU and UW PBL schemes with WSM6 and Thompson MP schemes.

All configurations produce track RMSE values below 94.5 km. Among these, the UW PBL scheme yields lower RMSE values of 72.1 km and 78.9 km. These configurations also simulate the landfall event with smaller position errors of 83.2 km and 42.9 km, and landfall time errors of 3 h 02 min and 1h 32 min, respectively.

Figure 5 shows the time evolution of simulated MSLP and 10-m wind speed. All configurations overestimate pressure and underestimate wind speed relative to IBTrACS observations. The UW PBL scheme produces the lowest mean absolute MSLP errors of 27.05 hPa and 29.62 hPa, as well as the lowest mean absolute wind speed errors of 22.21 ms^{-1} and 23.16 ms^{-1}.

SW and LW radiation schemes

This section evaluates the sensitivity of the Dudhia shortwave scheme, the RRTM longwave scheme, and the RRTMG shortwave and longwave schemes. These are tested in combination with the New Tiedtke CU scheme and UW PBL scheme, using both WSM6 and Thompson MP schemes. Figure 6 shows the simulated tracks of these combinations along with the IBTrACS reference track. The WSM6 MP scheme is used in Figure 6a, while the Thompson MP scheme is used in Figure 6b.

Simulations using the Dudhia shortwave and RRTM longwave schemes procedure lower track RMSE values of 72.1 km and 78.9 km. In contrast, the combinations using the RRTMG shortwave and longwave schemes show significant deviation from the IBTrACS track. Furthermore, landfall is only successfully simulated when using the Dudhia shortwave and RRTM longwave schemes, with position errors of 83.2 km and 42.9 km, and timing errors of 3 h 02 min and 1 h 32 min, respectively.

Figure 7 shows the time evolution of simulated minimum sea level pressure and 10-m wind speed for these radiation scheme combinations. All combinations overestimate MSLP and underestimate wind speed compared to the IBTrACS dataset. The Dudhia shortwave and RRTM longwave schemes produce the lowest mean absolute MSLP errors of 27.05 hPa and 29.62 hPa, respectively, and the lowest mean absolute wind speed errors of 22.21 ms^{-1} and 23.16 ms^{-1}.

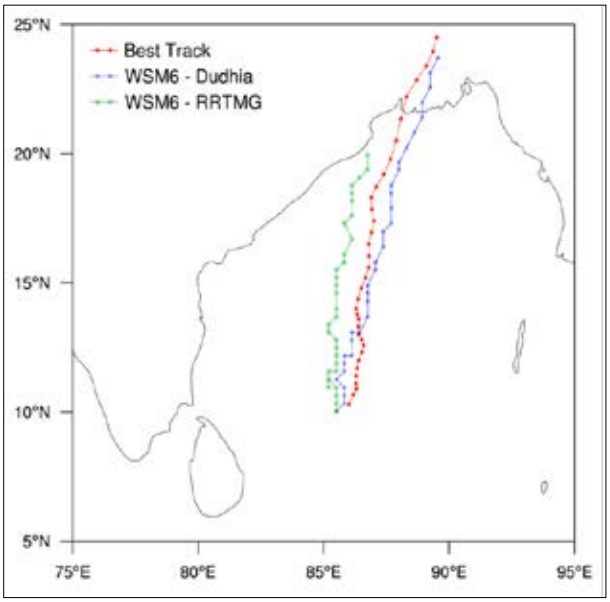

Figure 6(a): Simulated track of Cyclone Amphan using Dudhia shortwave scheme, RRTM longwave, and RRTMG radiation schemes with the WSM6 MP schemes.

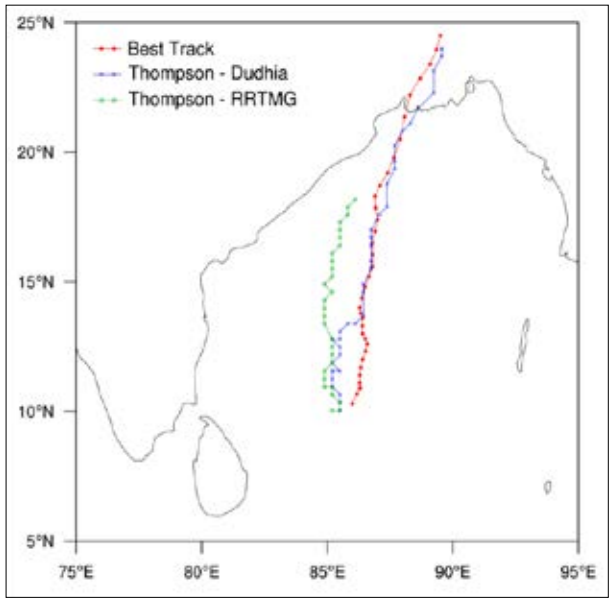

Figure 6(b): Simulated track of Cyclone Amphan using Dudhia shortwave scheme, RRTM longwave, and RRTMG radiation schemes with the Thompson MP schemes.

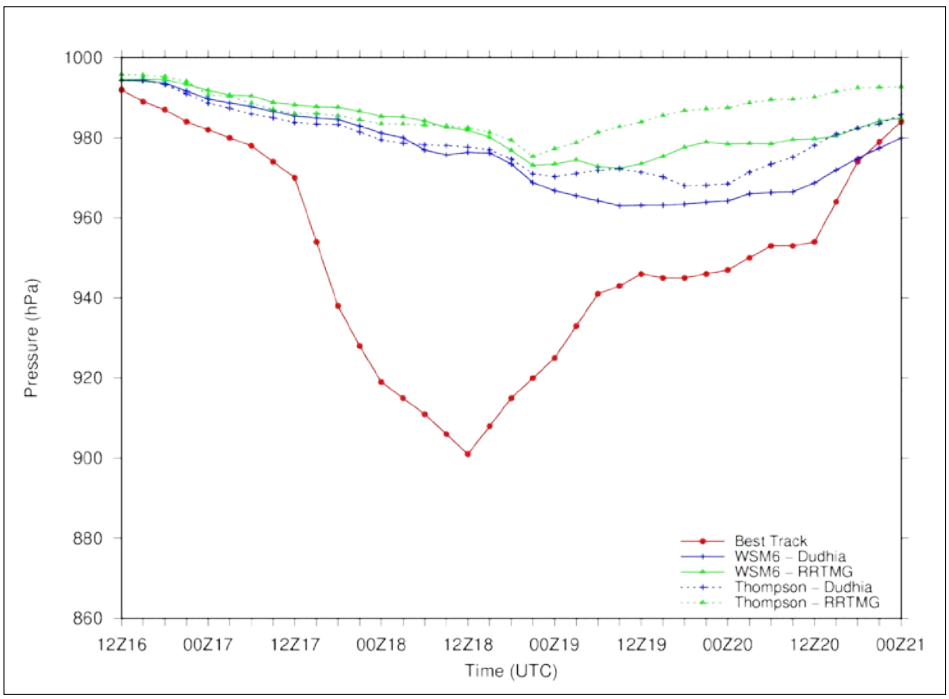

Figure 7(a): Minimum sea level pressure (MSLP) of Cyclone Amphan using Dudhia shortwave scheme RRTM longwave, and RRTMG radiation schemes with WSM6 and Thompson MP schemes.

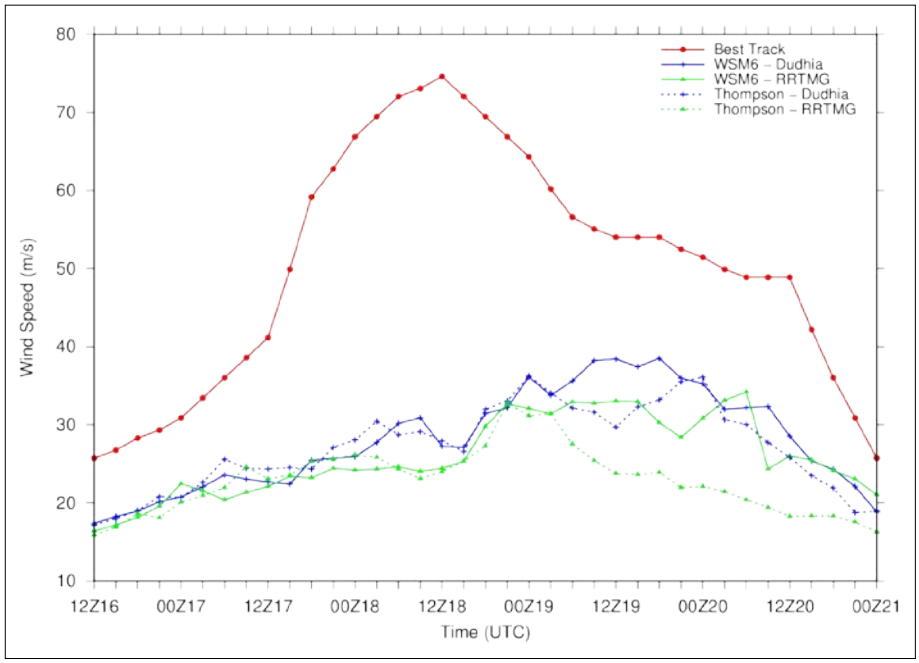

Figure 7(b): 10-m wind speed of Cyclone Amphan using Dudhia shortwave, RRTM longwave, and RRT-MG radiation schemes with WSM6 and Thompson MP schemes.

CONCLUSION

Cyclone Amphan caused severe damage across West Bengal, Bangladesh, Bhutan, Kerala, and Sri Lanka, highlighting the importance of accurately simulating both its track and intensity. This study investigated the sensitivity of different physical parameterization schemes within the WRF model through 24 simulations initialized at 0000 UTC on May 15, 2020, and integrated over 144 hours. The results demonstrate that model performance is highly dependent on the choice of physics configurations, with notable variations in both track and intensity predictions.

Among the schemes evaluated, the New Tiedtke CU scheme and the UW planetary boundary layer (PBL) scheme consistently produced lower track and intensity errors compared to other configurations. Similarly, the combination of the Dudhia shortwave and RRTM longwave radiation schemes resulted in improved simulation performance. For microphysics (MP), the WSM6 scheme provided better overall track and intensity representation, whereas the Thompson scheme showed improved accuracy in simulating landfall position and timing. These findings indicate that different physics schemes contribute uniquely to various aspects of TC simulation, emphasizing the need for balanced configuration selection based on the forecasting objective.

The optimal configuration – comprising the New Tiedtke CU scheme, UW PBL scheme, Dudhia shortwave scheme, RRTM longwave scheme, and WSM6 MP scheme – yielded the lowest track RMSE of 72 km, with a mean absolute MSLP error of 27 hPa and a mean absolute wind speed error of 22 ms^{-1}. This configuration simulated landfall with a positional error of 83 km and a timing error of 3 h 02 min. In comparison, replacing WSM6 with the Thompson MP scheme resulted in slightly higher track RMSE (79 km) and intensity errors but significantly improved landfall prediction, with a positional error of 43 km and a timing error of 1 h 32 min. These results highlight a clear trade-off between track and intensity accuracy and landfall prediction.

Despite improvements in track and landfall simulations, cyclone intensity was consistently underestimated. Although cyclone Amphan was observed as a Category 5 system, the best-performing configurations simulated it only as a Category 1 cyclone.

This discrepancy highlights limitations in representing the key processes that govern rapid intensification, including air-sea interactions and inner-core dynamics. The use of prescribed SST fields without fully coupled ocean–atmosphere interactions may limit the accurate representation of heat fluxes. In addition, initial conditions from global analysis datasets may not adequately capture the cyclone vortex structure. Furthermore, the choice of PBL, CU and MP schemes influences vertical transport processes and latent heat release, all of which are critical for cyclone intensification.

Overall, this study demonstrates that the careful selection of physics parameterizations can significantly improve the simulation of cyclone track and landfall characteristics. However, accurately capturing cyclone intensity remains a key challenge. Future work should focus on improving the representation of intensity-related processes, employing higher-resolution simulations, and utilizing advanced data assimilation techniques to enhance model performance.

Acknowledgements

The authors appreciate the assistance provided by the Faculty of Engineering, University of Ruhuna, Sri Lanka, and the Faculty of Science, University of Colombo, Sri Lanka.

REFERENCES

Delfino, R. J., Bagtasa, G., Hodges, K., & Vidale, P. L. (2022). Sensitivity of simulating Typhoon Haiyan (2013) using WRF: the role of cumulus convection, surface flux parameterizations, spectral nudging, and initial and boundary conditions. *Natural Hazards and Earth System Sciences*, *22*(10), 3285–3307. https://doi.org/10.5194/nhess-22-3285-2022

Di, Z., Gong, W., Gan, Y., Shen, C., & Duan, Q. (2019). Combinatorial Optimization for WRF Physical Parameterization Schemes A Case Study of Three-Day Typhoon Simulations over the Northwest Pacific Ocean. *Atmosphere*, *10*.

Gamage, T. D., Sonnadara, U., Jayasinghe, S., & Basnayake, S. (2022). Forecasting the track and the intensity of the cyclone Burevi using WRF. *Journal of the National Science Foundation of Sri Lanka*, *50*(3), 675. https://doi.org/10.4038/jnsfsr.v50i3.10761

Heming, J. T. (2017). Tropical cyclone tracking and verification techniques for Met Office numerical weather prediction models. *Meteorological Applications*, *24*(1), 1–8. https://doi.org/10.1002/met.1599

Hon, K.-K. (2020). Tropical cyclone track prediction using a large-area WRF model at the Hong Kong Observatory. *Tropical Cyclone Research and Review*, *9*(1), 67–74. https://doi.org/https://doi.org/10.1016/j.tcrr.2020.03.002

Islam, T., Srivastava, P., Rico-Ramirez, M., Dai, Q., Gupta, M., & Singh, S. (2015). Tracking a tropical cyclone through WRF–ARW simulation and sensitivity of model physics. *Natural Hazards*, *76*. https://doi.org/10.1007/s11069-014-1494-8

Knapp, K. R., Diamond, H. J., Kossin, J. P., Kruk, M. C., & Schreck, C. J. (2018). *International Best Track Archive for Climate Stewardship (IBTrACS) Project, Version 4*. NOAA National Centers for Environmental Information. https://doi.org/10.25921/82ty-9e16

Knapp, K. R., Kruk, M. C., Levinson, D. H., Diamond, H. J., & Neumann, C. J. (2010). The International Best Track Archive for Climate Stewardship (IBTrACS): Unifying Tropical Cyclone Data. *Bulletin of the American Meteorological Society*, *91*(3), 363–376. https://doi.org/10.1175/2009BAMS2755.1

Litta, A., Idideula, S. M., Mohanty, U., & Prasad, S. K. (2012). Comparison of Thunderstorm Simulations from WRF-NMM and WRF-ARW Models over East Indian Region. *The Scientific World Journal*, *2012*.

Mohan, P. R., Srinivas, C. V., Yesubabu, V., Baskaran, R., & Venkatraman, B. (2019). Tropical cyclone simulations over Bay of Bengal with ARW model: Sensitivity to cloud microphysics schemes. *Atmospheric Research*, *230*, 104651. https://doi.org/10.1016/j.atmosres.2019.104651

National Centers for Environmental Prediction, National Weather Service, NOAA, U.S. Department of Commerce. (2000). *NCEP FNL Operational Model Global Tropospheric Analyses, continuing from July 1999*. Research Data Archive at the National Center for Atmospheric Research, Computational and Information Systems Laboratory. https://doi.org/10.5065/D6M043C6

Qi, F., Fei, J., Ma, Z., Chen, J., Huang, X., & Cheng, X. (2018). Comparison of Simulated Tropical Cyclone Intensity and Structures Using the WRF with Hydrostatic and Nonhydrostatic Dynamical Cores. *Atmosphere*, *9*, 483. https://doi.org/10.3390/atmos9120483

Shenoy, M., Raju, P. V. S., & Prasad, J. (2021). Optimization of physical schemes in WRF model on cyclone simulations over Bay of Bengal using one-way ANOVA and Tukey's test. *Scientific Reports*, *11*(1), 24412. https://doi.org/10.1038/s41598-021-02723-z

Singh, V., Srivastava, A. K., Gupta, A., Konduru, R. T., Singh, A., Singh, S., Kumar, A., Bisht, D. S., & Singh, A. K. (2024). Intensification mechanisms and moisture dynamics of super cyclonic storm 'Amphan' over the Bay of Bengal: Implications for aerosol re-distribution. *Science of The Total Environment*, *951*, 175501. https://doi.org/https://doi.org/10.1016/j.scitotenv.2024.175501

Skamarock, W., Klemp, J., Dudhia, J., Gill, D., Liu, Z., Berner, J., Wang, W., Powers, J., Duda, M., Barker, D., & Huang, X.-Y. (2019). *A Description of the Advanced Research WRF Version 4*. NCAR Technical Notes.

Sud, V., & Rajaram, P. (2020). *Cyclone Amphan caused an*

estimated $13.2 billion in damage in India's West Bengal: Government source. https://edition.cnn.com/2020/05/22/weather/cyclone-amphan-damage-intl-hnk/index.html

Wang, Y. (2012). Recent Research Progress on Tropical Cyclone Structure and Intensity. *Tropical Cyclone Research and Review*, *1*(2), 254–275. https://doi.org/https://doi.org/10.6057/2012TCRR02.05

Zhang, C., Wang, Y., & Hamilton, K. (2011). Improved Representation of Boundary Layer Clouds over the Southeast Pacific in ARW-WRF Using a Modified Tiedtke Cumulus Parameterization Scheme*. *Monthly Weather Review*, *139*(11), 3489–3513. https://doi.org/10.1175/MWR-D-10-05091.1

J.Natn.Sci.Foundation Sri Lanka 2026 54 (3): 439 - 445
DOI: http://dx.doi.org/10.4038/jnsfsr.v54i3.12873

RESEARCH ARTICLE

Graph Theory

On the (*k,c*) – choosability of tri-partite graphs

GGBR Jayawardhana*, GS Wijesiri and SVA Almeida
Department of Mathematics, Faculty of Science, University of Kelaniya, Kelaniya, Sri Lanka.

Submitted: 27 November 2025; Revised: 06 July 2026; Accepted: 24 July 2026

Abstract: Graph colouring is a fundamental concept in graph theory with diverse real-world applications. List colouring is a key concept in graph colouring where vertices are coloured using an available list of possible colours. Proper list colouring guarantees that no two adjacent vertices share the same colour. If every vertex is assigned a list of k possible colours and the graph admits a proper list colouring, then the graph is said to be k −choosable. A graph $G = (V, E)$ is referred to as (k, c) − choosable $(k \geq c)$ if for each list assignment L satisfying $|L(v)| \geq k$ for each vertex v and $|L(x) \cap L(y)| \leq c$ for each edge xy. This research primarily investigates the (k, c) − choosability of tri-partite graphs, with a specific focus on $k_{1,q,r}$ graph which has significant applications, spanning multiple domains. The analysis begins by viewing the complete tripartite graph $k_{1,q,r}$ as a structure composed of three distinct levels where each level contain 1,q and r vertices respectively, each corresponding to one of the three independent partitions of the graph, and the assignment of colours is done in each level adhering to proper colouring with a given list of colours. This study proves that the complete tripartite graph $k_{1,q,r}$ is 3 − choosable by mathematical induction.

Keywords: Choosability; k −choosability; tri-partite graphs; (k, c) − choosability; proper colouring.

INTRODUCTION

Over two decades ago, M. Voigt conducted research on bi-partite graphs, which is a special case of *k*-partite graphs (Voigt, 1998). In general, a graph is said to be k − partite if its vertices can be partitioned into k independent sets such that no two vertices within the same set are adjacent. In this study we mainly focus on the field of graph colouring and it involves the process of assigning colours to the vertices of a graph. A proper colouring of a graph means that colours are assigned to the vertices so that no two adjacent vertices share the same colour and this principal is termed vertex colouring. For any graph $G = (V, E)$, each vertex $v \in V$ be associated with a list of possible colours $L(v)$ through a function L, referred to as list assignment and if the number of colours of this list is k, then this function is termed to be a k − list assignment. A graph is deemed L −colourable if this graph can be coloured from the colours in the given lists in such a way that no two adjacent vertices share the same colour and if there exist such a colouring for any k −list assignment, then the graph is considered as k −choosable. With the help of this definition, Kierstead studied the choosability of complete multipartite graphs with part size three (Kierstead, 2000) and motivated by this result , Kiani, Mohammadi, Moradi, and Rahamati, together with Akbari studied the choosability of some specific types of graphs (Akbari et al., 2015). This topic has been widely studied in the past few years (Zheng et al., 2010; Vetrik, 2012; Akbarim et al., 2006; Akbari et al., 2015; Kratochvil et al., 1998).

The concept of (k, c) −choosability can be defined based on the study presented by Kratochvil (Kratochvil et al., 1998). A graph $G = (V, E)$ is referred to as (k, c) − choosable $(k \geq c)$ if for each list assignment L satisfying $|L(v)| \geq k$ for each vertex v and $|L(x) \cap L(y)| \leq c$ for each edge xy.

* Corresponding author (binularasmitha@gmail.com; https://orcid.org/0009-0000-2426-7330)

This article is published under the Creative Commons CC-BY-ND License (http://creativecommons.org/licenses/by-nd/4.0/). This license permits use, distribution and reproduction, commercial and non-commercial, provided that the original work is properly cited and is not changed in anyway.

In 2018, Kumbhat, Moss and Stolee introduced a refinement of list colouring in which adjacent vertices are required to have sufficiently large unions of colour lists, generalizing classical choosability constraints (Kumbhat et al., 2018). In particular, they defined $(k, k+s)$ -choosability and investigated structural conditions under which graphs admit proper colourings under such restricted list assignments. Their work showed that planar graphs satisfy specific $(k, k+s)$-choosability bounds.

In 2020, Chen, Fan, Raspaud, Shiu and Wang extended list colouring by introducing separation constraints in which the overlap between colour lists of adjacent vertices is restricted (Chen et al., 2020). In particular, they investigated $(k, d)-$ choosability type conditions for planar graphs and established colouring results under forbidden cycle structures. Their work further demonstrated that planar graphs satisfy certain choosability bounds when additional structural restrictions such as the absence of prescribed cycles are imposed.

Vasudevan, Somasundaram and Narayanan, in "List-Colouring and Chromatic-Choosability: A Dynamic Survey", review recent developments in graph choosability. They note that many results are known for planar, toroidal and claw-free graphs. However, the complete characterization of complete multipartite graphs remains open. Only partial results are available for specific cases. (Vasudevan et al., 2026).

The (k, c) −choosability problem on tri-partite graphs is fundamental to many real-world applications and this method is flexible and adaptable, which makes it a strong tool for scheduling, task organization and resource distribution. This method makes it easy to work within specific limitations and still comes up with useful solutions that satisfy a range of requirements.

The main objective of this study is to determine values of k and c, so that the tri-partite graph is (k, c) − choosable.

MATERIALS AND METHODS

The concept of (k, c, r) −choosability, introduced by Kratochv´ıl in 1998, defines that a graph G is (k, c, r) − choosable if it admits a c −set colouring for every (k, r) −assignment and in particular he showed that when $r = 0$, the concept reduces to (k, c) − choosability which forms the basis for later studies (Kratochvil et al., 1998). Based on this result, several studies have been developed on generalized choosability under various structural restrictions and many related problems remain open for different classes of graphs.

In this section, we introduce some previous findings on (k, c) −choosability, that were used in our research (Sajeena et al., 2025).

Lemma 1. *If a graph G is k −choosable then it is k' − choosable for each $k' \geq k$.*

Lemma 2. *If a graph G is (k, c) −choosable then it is (k, c') −choosable for each $0 \leq c' \leq c$.*

Lemma 3. *When $k \geq ch(G)$ for a given graph G, it is (k, t) −choosable for all $t \leq k$, where $ch(G)$ is the choice number of G, defined as the minimum integer k such that G is $k-choosable$.*

Lemma 4. *A graph is (k, k) −choosable if and only if it is k −choosable.*

With the help of these previous findings, we analyzed the (k, c) −choosability of some special types of tri-partite graphs. After an extensive analysis, we were able to identify the values of k and c for which these graphs are (k, c) −choosable.

RESULTS AND DISCUSSION

This section contains the main findings of this study. Also this section provides detailed proofs of the key findings on the $(k, c)-$ choosability of several graph structures: $k_{1,2,r}$, $k_{1,3,r}$ and $k_{1,q,r}$, where q and r are positive integers representing the sizes of the corresponding partite sets.

Theorem 1. The complete graph $k_{1,2,r}$ is 3 −choosable.

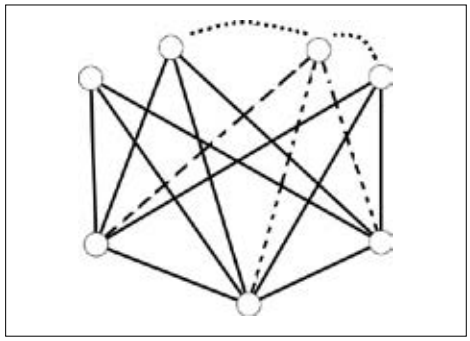

Figure 1: Illustration of the complete graph $k_{1,2,r}$

Proof:
To prove this theorem we divide the graph into three different levels and these levels represent the three partitions of the graph.

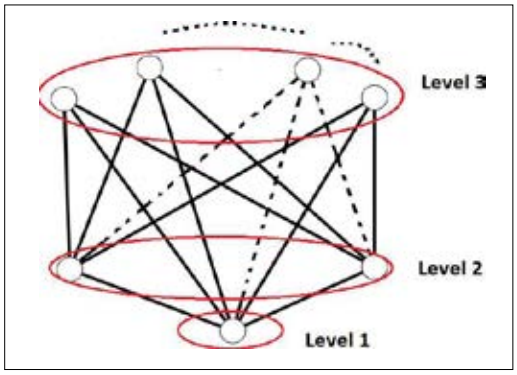

Figure 2: Illustration of the levels of the graph $k_{1,2,r}$

To accomplish our main goal, we consider the only possible cases how the graph can be coloured.

(1) Levels 1, 2, and 3 all have the same colour list.
(2) Levels 2 and 3 have colours entirely different from level 1.
(3) Only level 2 has at most two free colours.
(4) Only level 3 has at most two free colours.
(5) Some vertices of level 2 and some vertices of level 3 have at most two free colours.

To demonstrate the theorem, we need to prove it using all the cases mentioned above.

Case 1: Levels 1, 2, and 3 all have the same colour list.

Since $k_{1,2,r}$ is a tri partite graph the chromatic number is 3. If all the levels are assigned the same list of three colours, certainly it is 3 –choosable.

Case 2: Levels 2 and 3 have colours entirely different from level 1.

Let's assign colour sets to level 2 and 3 such that they are different from the colour set of 1. Since the subgraph induced by levels 2 and 3 is a bipartite graph, it can be properly coloured from any list of three colours. If we consider level 1 together with this bipartite graph, the whole graph is 3 –choosable because level 1 can be coloured with any colour in its list, that differ from the colours of 2 and 3. This is illustrated in figure 3.

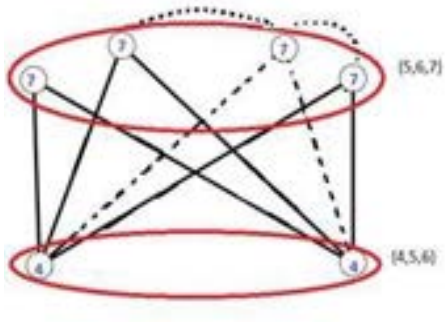

(a) An example illustrating that the bipartite graph induced by levels 2 and 3 is 3-choosable.

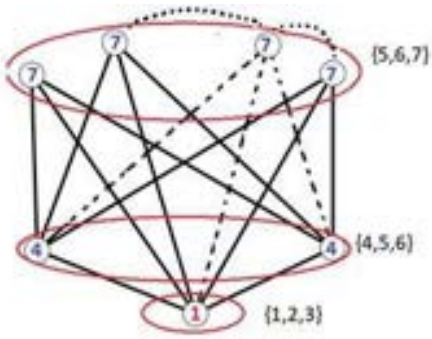

(b) An example illustrating that level 1 together with the above bipartite graph is 3-choosable.

Figure 3: Illustration of case 2

Case 3: Only level 2 has at most two free colours.

As in the previous case the bipartite graph induced by levels 1 and 3 is 3 –choosable. Now assign a list of three possible colours to the vertices of level 2, ensuring that two colours remain free. We can assign these free colours to the vertices of level 2, if only one colour is free, we can assign it to both vertices. Thus the above bipartite graph together with level 2, is 3 –choosable.

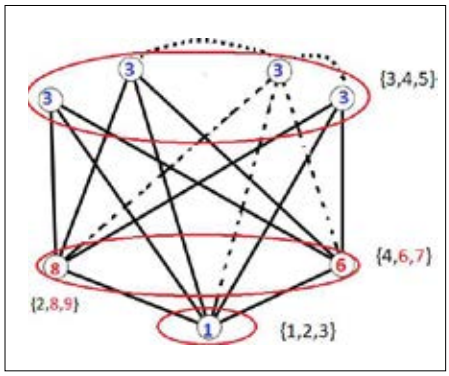

Figure 4: Illustration of case 3

Case 4: Only level 3 has at most two free colours.

A similar argument as in the above case can be applied to Case 4.

Case 5: Some vertices of level 2 and some vertices of level 3 have at most two free colours.

Let's assume some of the vertices in level 2 and level 3 have two free colours. We can colour these vertices using those colours. Since there is only one vertex in level 1, we can colour it using any colour from its list. In level 2, there is only one vertex that doesn't have any free colours in its list. We can colour this vertex using any colour from its list except the colour assigned to vertex 1. Since each vertex in level 3 has three colours in its lists and at most two of them can overlap with those of levels 1 and 2, there is always an extra colour available to colour the vertices in level 3. Thus, we may use those colours to colour the vertices in level 3.

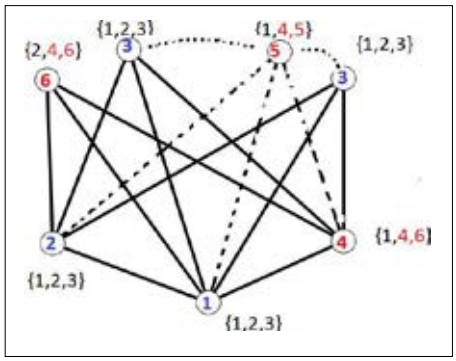

Figure 5: Illustration of case 5

If there is only one free colour in the lists of some vertices at level 2 and level 3, we can colour these vertices using those colours and colour the remaining vertices as in the case 3.

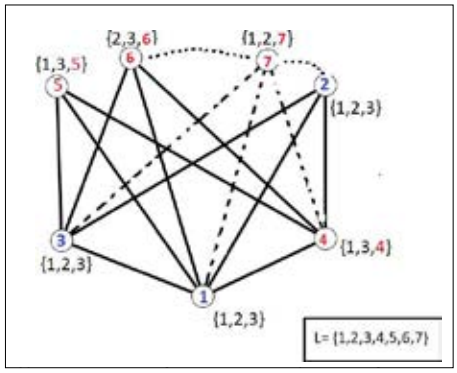

Figure 6: Illustration of case 5 with one free color

Since the graph is 3 –choosable for all the cases mentioned above, the graph $k_{1,2,r}$ is always 3 –choosable.

Corollary 2. The graph $k_{1,2,r}$ is $(k,3)$ –choosable for any $k \geq 3$.

Proof: The result is an immediate consequence of Lemmas 2.1– 2.4.

Corollary 3. The graph $k_{1,2,r}$ is $(3,c)$ –choosable for $c = 1,2,3$.

Proof: The result is an immediate consequence of Lemmas 1– 4.

Theorem 4. The complete tripartite graph $k_{1,3,r}$ is 3 – choosable.

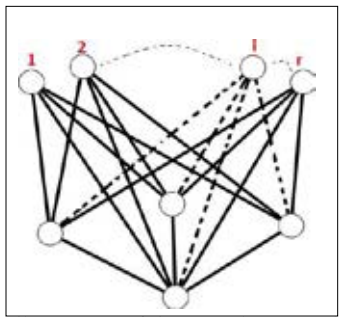

Figure 7: Illustration of the complete graph $k_{1,3,r}$

Proof:
The proof of the choosability of $k_{1,3,r}$ is very similar to the proof of $k_{1,2,r}$. Here, we also consider the same cases that we considered in **Theorem 1.** Since we consider the vertices level-wise and do not focus on any particular vertices in each level, we can extend the cases $1-4$ of the proof of $k_{1,2,r}$ to the proof of $k_{1,3,r}$.

Therefore, we only need to focus on case 5. i.e., some of the vertices in level 2 and 3 have at most two common colours. Let's assume that some of the vertices in level 3 have at most two free colours. Since some of the vertices in level 2, among the three vertices, have at most two free colours, there can either be one vertex with free colours or two such vertices. Consider the case where two vertices in level 2 have at most two free colours. For this case, a similar argument as in case 5 of Theorem 1 can be applied.

Now consider the case where only one vertex in level 2 of $k_{1,3,r}$ has at most two free colours.

Consider $k_{1,3,r}$ and assume one vertex in level 2 has a free colour. This vertex is connected to all vertices in level 3 and the single vertex in level 1. Since the new vertex has a free colour, we can assign that free colour to this vertex, as shown in the figure below. In this figure, vertex '3' in level 2 is the vertex that has one free colour.

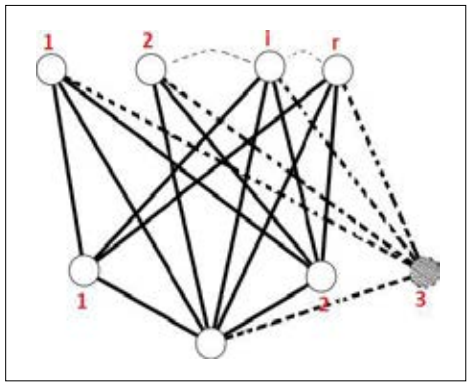

Figure 8: Illustration of the $k_{1,3,r}$ graph with free colours on one vertex in level 2.

We know that $k_{1,2,r}$ is 3 –choosable and the colouring of the new vertex does not affect the colouring of other vertices, as it uses a free colour. Thus, $k_{1,3,r}$ is also 3 –choosable.

We proved the choosability of the $k_{1,q,r}$ graph by applying the principle of mathematical induction. Using the choosability of $k_{1,2,r}$ graph and $k_{1,3,r}$ graph, we were able to prove that the $k_{1,q,r}$ graph is also 3 –choosable.

Theorem 3.5. The complete graph $k_{1,q,r}$ is 3 –choosable.

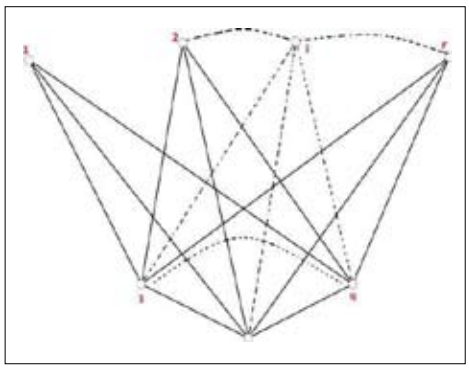

Figure 9: Illustration of the complete graph $k_{1,q,r}$

Proof:

We have proven that the $k_{1,2,r}$ graph, derived from $k_{1,q,r}$ when $q = 2$, is 3 – choosable; i.e. the result is true for the base case.

Assume that the graph $k_{1,q,r}$ is 3 –choosable when $q = n$. That is the graph $k_{1,n,r}$ is 3 –choosable.

Since we didn't consider any particular vertices in each level and only considered vertices level-wise, we can extend the cases $1-4$ of the proof of the Theorem 3.1 to the proof of $k_{1,q,r}$. Thus, we only need to consider case 5, as we consider each vertex at every level in this case. The method of mathematical induction is used to prove this case.

Consider the case $k_{1,n+1,r}$ which is formed by adding one vertex to level 2 in $k_{1,n,r}$, and connecting it to all vertices in level 1 and level 3. If the newly added vertex to level 2 has a free colour, then $k_{1,n+1,r}$ is 3 –choosable. This is because the new vertex, which can be coloured using its free colour does not affect the colouring of $k_{1,n,r}$ and $k_{1,n,r}$ is 3 –choosable by assumption. In other words, the new vertex at level 2 with a free colour does not affect the choosability of $k_{1,n,r}$.

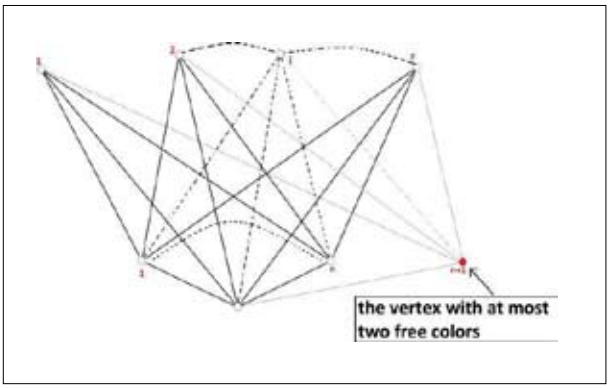

Figure 10: Illustration that a new level-2 vertex with a free colour does not affect the choosability of $k_{1,n,r}$

According to our 5th case, we consider that some of the vertices in level 2 and 3 have at most 2 free colours. Now, suppose the new vertex added to level 2 doesn't have a free colour. To prove this, let's interchange the position of this new vertex and any vertex which has a free colour in level 2 of $k_{1,q,r}$. Then level 2 of $k_{1,q,r}$ contains the new vertex without any free colours and the vertex which has a free colour in level 2 of $k_{1,q,r}$ is shifted to the place of the new vertex. Then again, this is similar to the above case. Thus, the graph $k_{1,n+1,r}$ is also 3 −choosable for this case.

The result assumed to be true for $q = n$ is also true for $q = n + 1$. By the method of mathematical induction, the result is true for any q. Thus, the graph $k_{1,q,r}$ is $3-$ choosable for any q and r with $q \leq r$.

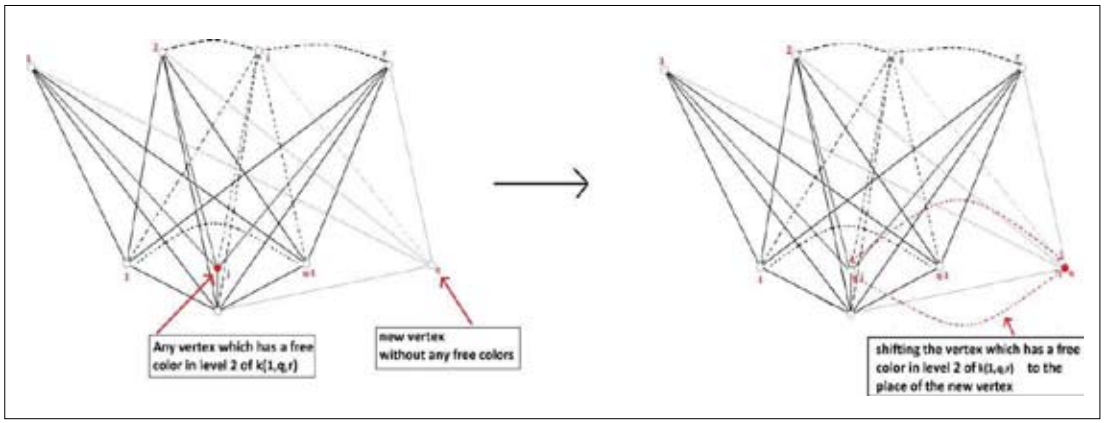

Figure 11: Illustration of proving $k_{1,n+1,r}$ is 3 −choosable

Corollary 3.6. The graph $k_{1,q,r}$ is $(k, 3)$ −choosable for any $k \geq 3$.

Proof: The result is an immediate consequence of Lemmas 2.1– 2.4.

Corollary 3.7. The graph $k_{1,q,r}$ is $(3, c)$ −choosable for $c = 1, 2, 3$.

Proof: The result is an immediate consequence of Lemmas 2.1– 2.4.

Discussion and Future Work

The present work establishes the (k, c) −choosability of several families of complete tripartite graphs, namely $k_{1,2,r}$, $k_{1,3,r}$ and $k_{1,q,r}$. These results extend the current understanding of list coloring in complete tripartite graphs and demonstrate how the relationship between $k-$ choosability and (k, c) −choosability can be effectively exploited to derive new choosability results. Although these graph families possess one singleton partition, the proofs illustrate techniques that may be applicable to more general tripartite structures.

A natural extension of this work is the study of graph families of the form $k_{2,q,r}$ and more generally, $k_{p,q,r}$. As an initial step in this direction, we established that $k_{2,2,4}$ is $3-$ choosable, consistent with the result of Enomoto, Ohba, Katsuhiro and Sakamoto who proved that the choice number of $k_{4,2,\ldots,2}$ is equal to the number of partitions when this number is odd (Enomoto et al., 2002).

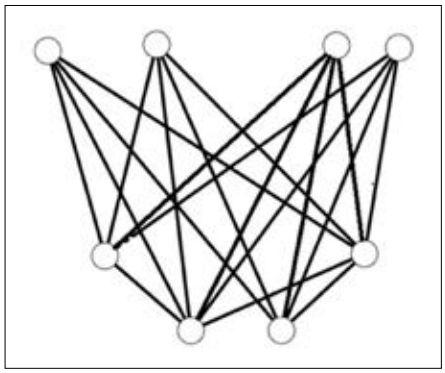

Figure 12: Illustration of $k_{2,2,4}$ graph

However, extending the present techniques to arbitrary values of q and r is considerably more challenging. Unlike the graph families considered in this paper, the interaction between larger partition sizes introduces substantially more complex list assignments and coloring configurations.

This increased complexity is reflected in known results. For example, while $k_{2,2,4}$ is 3 −choosable, Kierstead showed that $k_{3,3,3}$ is 4 −choosable (Kierstead, 2000). Although these graphs differ by only one vertex, the change in the partition structure increases the choice number, illustrating the sensitivity of choosability to relatively small structural modifications. Consequently, arguments that are successful for $k_{1,q,r}$ cannot be extended directly to the $k_{2,q,r}$ family without the development of additional techniques.

Establishing the choosability of $k_{2,2,5}$, followed by $k_{2,2,r}$, would provide an important intermediate step toward understanding the more general $k_{2,q,r}$ family. Developing such results, however, requires methods beyond those introduced in the present work and remains an interesting direction for future research.

CONCLUSION

There are numerous significant results in the field of graph colouring, particularly in the study of tri-partite graphs. Among these, the concept of (k, c) −choosability presents considerable theoretical challenges due to the additional constraints imposed on list colourings. Although several results concerning (k, c) −choosability have been established for bipartite graphs, comparatively limited attention has been devoted to the corresponding problem in tri-partite graphs. Consequently, a number of fundamental questions in this area remain unresolved.

Motivated by these challenges this study investigates the (k, c) −choosability of tri-partite graphs. The study establishes several significant results related to k − choosability and further characterizes the relationship between k −choosability and (k, c) −choosability in graphs. This relationship plays a central role in the development of the proofs of the main results presented in this work.

REFERENCES

Akbari, S., Kiani, D., Mohammadi, F., Moradi, S., & Rahmati, F. (2015). An algebraic criterion for the choosability of graphs. *Graphs and Combinatorics, 31*(3), 497–506. https://doi.org/10.1007/s00373-014-1411-7

Akbari, S., Mirrokni, V. S., & Sadjad, B. S. (2006). A relation between choosability and uniquely list colorability. *Journal of Combinatorial Theory, Series B, 96*(4), 577–583. https://doi.org/10.1016/j.jctb.2005.10.004

Kierstead, H. A. (2000). On the choosability of complete multipartite graphs with part size three. *Discrete Mathematics, 211*(1-3), 255–259. https://doi.org/10.1016/S0012-365X(99)00157-0

Kratochvíl, J., Tuza, Z., & Voigt, M. (1998). Complexity of choosing subsets from color sets. *Discrete Mathematics, 191*(1–3), 139–148. https://doi.org/10.1016/S0012-365X(98)00101-0

Sajeena, D., Almeida, K. V. A., Wijesiri, S. S., & Dencil, A. D. M. (202: k, c)-choosability of cycle graphs, wheel graphs, and –prism graphs. *Ceylon Journal of Science, 54*(3), 907–911. https://doi.org/10.4038/cjs.v54i3.8626

Vetrík, T. (2012). List coloring of complete multipartite graphs. *Discussiones Mathematicae Graph Theory, 32*(1), 31–37. https://doi.org/10.7151/dmgt.1583

Voigt, M. (1998). On list colourings and choosability of graphs. *Abilitationsschrift, TU Ilmenau.*

Zheng, G.-P., Shen, Y.-F., Chen, Z.-L., & Lv, J.-F. (2010). On choosability of complete multipartite graphs $k_{4,3t,2(k-2t-2),1(t+1)}$. *Discussiones Mathematicae Graph Theory, 30*(2), 237–244. https://doi.org/10.7151/dmgt.1489

Vasudevan, N. K., Somasundaram, K., & Narayanan, N. (2026). *List-coloring and chromatic-choosability: A dynamic survey*. arXiv. https://doi.org/10.48550/arXiv.2606.31702

Kumbhat, M., Moss, K., & Stolee, D. (2018). Choosability with union separation. *Discrete Mathematics*, *341*(3), 600-605. https://doi.org/10.1016/j.disc.2017.10.022

Chen, M., Fan, Y., Raspaud, A., Shiu, W. C., & Wang, W. (2020). *Choosability with separation of planar graphs without prescribed cycles*. Applied Mathematics and Computation, 367, 124781. https://doi.org/10.1016/j.amc.2019.124756

Enomoto, H., Ohba, K., Ota, K., & Sakamoto, J. (2002). Choice number of some complete multi-partite graphs. *Discrete mathematics*, *244*(1-3), 55-66. https://doi.org/10.1016/S0012-365X(01)00059-0

JOURNAL OF THE
NATIONAL SCIENCE FOUNDATION
OF SRI LANKA

GUIDANCE TO CONTRIBUTORS

GENERAL INFORMATION

Scope

The Journal of the National Science Foundation of Sri Lanka publishes the results of research in all aspects of Science and Technology. It is open for publication of Research Articles, Reviews, Research Communications and Correspondence.

Use of AI Tools in Manuscript Preparation

To ensure transparency and uphold scholarly standards, authors must disclose any use of Artificial Intelligence (AI) tools during the research and manuscript preparation process.
The use of AI tools (e.g., for language editing, summarization, data analysis, or figure generation) **must be declared in the manuscript, typically before the Acknowledgements**.
AI tools must not be credited as authors. Human authors remain fully responsible for the integrity, accuracy, and originality of the submitted work.
AI-generated content must be critically reviewed by the authors to ensure quality and ethical compliance, including data privacy and bias mitigation.
AI must not be used to fabricate or manipulate original research data, unless it is part of the approved research methodology and explicitly described.
Non-compliance with these guidelines may lead to rejection of the manuscript or post-publication corrective actions.

IT related and other non-empirical articles

The JNSF is a journal primarily devoted to natural sciences. It also considers for publication significant and novel contributions from formal sciences. Authors of emerging sub-disciplines of Computing and related areas such as Machine Learning, Artificial Intelligence and Data Sciences are requested to carefully adhere to the following guidelines when submitting manuscripts for this journal.

- Clear formulation of outcome-oriented **Research Objective/s** for targeted knowledge (sub)domain/s or (sub)discipline/s.
- Selection and comprehensive summarization of **appropriate Research Method/s** adopted to achieve the stated Research Objective/s.
- Reporting a sound **(Empirical) Evaluation** of the research finding/s thereby arguing reliability, validity, and generalizability of research claim/s.

Categories of manuscripts

Research Articles: Research Articles are papers that present complete descriptions of original research. Research Articles should include an Abstract, Keywords, Introduction, Methodology, Results and Discussion, Conclusion and Recommendations where relevant. References should be prepared according to the "Guidelines for the preparation of manuscripts". Maximum length of the article should be limited to 30 pages (Times New Roman, font size 12 , line space 1.5) with a word count less than 10,000 including references, figures and tables. Any articles above this limit will be returned. Please refer author guidelines for further details (https://jnsfsl.sljol.info/about/submissions#author-guidelines)

Reviews: Reviews are critical presentations on selected topics of Science or Technology. They should be well focused and organized and avoid general "textbook" style. As reviews are intended to be critical presentations on selected topics, the author (or the principal author in a multi-author review) need to have had substantial leadership in research supported by a publication track record in the areas covered by the review. A person/s wishing to submit a Review Article should obtain prior approval from the Editorial Board by submitting a concise summary of the intended article, along with a list of the author's publications in the related area (jnsf@nsf.gov.lk). Maximum length of the article should be limited to 40 pages (Times New Roman, font size 12 , line space 1.5) with a word count of 12,000 including references, figures and tables. Any articles beyond this limit will be returned.

Research Communications: Research Communications are intended to communicate important new findings in a specific area of limited scope that are worthy of rapid dissemination among the scientific community. Authors are required to provide a statement justifying the suitability of the submission for a Research Communication. The article should include an Abstract, Keywords, Introduction, Methodology, Results & Discussion, Conclusion and References. Maximum length of the article should be limited to 10 pages (Times New Roman, font size 12 , line space 1.5) with a word count of 2,500 including references, figures and tables. Any articles beyond this limit will be returned.

Correspondence: Correspondence will be accepted regarding one or more articles in the preceding four issues of the Journal, as well as Letters to the Editor. Articles covering important scientific events or any other news of interest to scientists, reviews of books of scientific nature, articles presenting views on issues related to science and scientific activity will also be considered. Publication will be made at the discretion of the Editor-in Chief. Maximum length of the article should be limited to 05 pages (Times New Roman, font size 12 , line space 1.5) with a word count of 1,500 including references, figures and tables. Any articles beyond this limit will be returned.

SUBMISSION OF MANUSCRIPT

Authors submitting articles to the JNSF should first create an account in the Sri Lanka Journals Online System (https://jnsfsl.sljol.info/). All manuscripts should be in MS Word format and must be submitted to the journal's online platform at https://jnsfsl.sljol.info/submit/start/. Submissions *via* emails are not encouraged. Please make sure that **no** author information is mentioned in the article submitted other than in the title page. Complete names and details of affiliations of all authors must be fed into the system during the online submission process. Authors are required to provide their personal, validated ORCID ID (by obtaining an ORCID ID from https:// orcid.org/) when submitting the manuscript. No change to the

authors or order of authors will be accepted after the submission. All those who have made significant contributions should be listed as co-authors. The corresponding author should ensure that all contributing co-authors are included in the author list and have approved the final version of the paper and have agreed to its submission for publication.

All submissions should be in English. If the manuscript conforms to the guidelines specified, the date received will be the date that the manuscript was submitted to the online system.

Submissions are accepted for processing on the understanding that they will be reviewed and that they have not been submitted for publication elsewhere (including publication as a full paper or extended abstract as a part of Conference Proceedings).

Suggesting potential reviewers by authors
The authors are requested to suggest three names of referees when submitting their manuscript, in the Cover Letter space provided at the bottom of the page in the first stage of online submission. Referees should not be from the institution where the work was carried out and should not have been co-authors in previous publications. The address, institutional affiliation and e-mail of the suggested referees should be provided. Please note that the JNSF is not bound to select all or any of the suggested referees for sending the manuscript for reviewing

Authorship
All authors designated as authors should be eligible for authorship. Those who have made a substantial contribution to the concept or design of the work; or acquisition, analysis or interpretation of data are recognized as Authors.
The corresponding author should be prompt and ensure adherence to timelines when responding to requests, queries and recommendation of reviewers conveyed by or on behalf of the Editor-in Chief and Editorial Board.

Avoiding predatory references in manuscripts

Authors of the manuscripts should identify and not include predatory journal articles in the reference list.
If any paper that is cited is published in an Open Access journal, the authors are advised to ensure that the journal is listed in the DOAJ (Directory of Open Access Journals) or by the COPE (Committee on Publication Ethics). Please note that authors should check with DOAJ and COPE by themselves, and not assume that the statements given in the journal websites are accurate.
If the journal is included either in DOAJ or COPE, it can be presumed as legitimate. If not, authors need to review the journal website and published articles for characteristics of predatory journals. At the same time, authors can check whether the journal or relevant publisher is included in the directory of predatory journals and publishers.
If it is revealed that the manuscript is supported by articles published in predatory journals, it could be rejected by the JNSF at any stage of the publication process.

Supplementary materials
Any experimental data necessary to evaluate the claims made in the paper but not included in the paper should be provided as supplementary materials. Supplementary materials will be sent to the reviewers and published online with the manuscript if accepted. The supplementary materials should conform to Journal guidelines and should be uploaded as separate files. Authors should number Supplementary Tables and Figures as, for example, 'Supplementary Table S1'. Refer to each piece of supplementary material at the appropriate point(s) in the main article. Supplementary Materials may include description of the materials and methods, controls, or tabulated data presented in Tables or Figures, and programming codes.

Peer review
The manuscripts submitted to the JNSF will initially be screened by the Editorial Board and, if suitable, will be referred to at least two subject experts in the relevant field. The peer-review process of the JNSF is double-blind.
When revision of a manuscript has been requested, the revised manuscript should be submitted on or before the stated deadline. The authors' response to the comments of referees should be tabulated with the comment and response. The decision of the Editorial Board shall be final.
Accepted papers are subject to editing. The date of acceptance will be the date the Editorial Board accept the paper for publication.

Article processing fee
Article processing fee of US$ 250 will be levied for each manuscript in two stages, except when the corresponding author is affiliated with a Sri Lankan institution,

- An initial processing fee of US$ 20 will be levied for each manuscript at the peer-review stage.
- The remaining US$ 230 will be charged for accepted articles at the time of publication.

Payments can be made online via NSF Payment Portal (http://pg.nsf.gov.lk/)

Authors' declaration
The authors are required to accept the conditions indicated in the online author declaration statement.

Copyright
Articles in JNSF are published under the Creative Commons License CC-BY-ND. This license permits use, distribution and reproduction of articles for commercial and non-commercial purposes, provided that the original work is properly cited and is not changed in anyway. The copyright of the article is with the National Science Foundation of Sri Lanka. Therefore, authors are requested to check with institution's copyright and publication policy before submitting an article to the JNSF. Authors secure the right to reproduce any material that has already been published or copyrighted elsewhere. When an article is accepted for publication, the authors are required to submit the Transfer of Copyright document signed by all the authors.

Post-publication corrections
The Editorial Board reserves the right to take action on publishing an erratum or corrigendum. If serious errors are identified in a published article, the Journal may consider a retraction or publishing a correction.

STRUCTURE OF MANUSCRIPT

Manuscript
The manuscript should be free of errors and prepared in single column, using 1.5 line spaced text of Times New Roman 12 font leaving 1 inch margins. Pages should be numbered consecutively.

a. Style
The paper should be written clearly and concisely. The style of writing should conform to scholarly writing. Slang, jargon, unauthorized abbreviations, abbreviated phrasings should not be used. In general, the impersonal form should be used. Poor usage of language will result in rejection of the manuscript during initial screening.

b. Layout
Manuscripts other than review articles should be generally organized as follows: Title, Abstract, Keywords, Introduction, Methodology, Results and Discussion, Conclusions and Recommendations (where relevant), Acknowledgements and References. Pages should be arranged in the following order:

First page should include the title of the manuscript and **complete names and affiliations** of all authors. **Author information should not be mentioned in other places of the manuscripts.** Any statement (including acknowledgment) which can reveal author identity should be removed. If a major part of the research has been published as an abstract in conference proceedings, it should be mentioned with citation in the space provided for "Comments for Editor". Authors must also indicate the **general and specific research area** of the manuscript in the title page.

***Title*:** Should accurately and concisely reflect the contents of the article.

***Running title*:** Should be a shortened title (limited to a maximum of 50 characters) that could be printed at the top of every other page of the Journal article.

***Abstract*:** Should be between 200 - 250 for research articles and 200 - 300 for reviews. It should not contain any references and should be able to stand on its own. It should outline objectives and methodology together with important results and conclusions.

***Keywords*:** Include a maximum of six keywords, which may include the names of organisms (common or scientific), methods or other important words or phrases specific to the study.

***Introduction*:** This should state the reasons for performing the work with a brief review of related research studies in the context of the work described in the paper. Objectives of the study should be clearly stated.

***Materials and Methods*:** This section should give the details of how you conducted your study. New methods may be described in detail with an indication of their limitations. Established methods can be mentioned with appropriate references. Sufficient details should be included to allow direct repetition of the work by others. Where human subjects are involved, they should be referred to by numbers or fictitious names. A paper reporting the results of investigations on human subjects or on animals must include a statement to the effect that the relevant national or other administrative and ethical guidelines have been adhered to, and a copy of the ethical clearance certificate should be submitted. Methods of statistical analyses used should be mentioned where relevant.

Results and Discussion
Results: the results should be concisely and logically presented. Repetition of the same results in figures, tables or text should be avoided.
Discussion: data essential for the conclusions emerging from the study should be discussed. Long, rambling discussions should be avoided. The discussion should deal with the interpretation of results. It should logically relate new findings to earlier ones. Unqualified statements and conclusions not completely supported by data should be avoided.
Molecular sequence data, such as gene or rDNA sequences, genome sequences, metagenomic sequences etc. must be deposited in a public molecular sequence repository, such as GenBank, that is part of the International Nucleotide Sequence Database Collaboration (INSDC). The accession numbers obtained must be cited in the text, Table or on Figures of phylogenetic trees of the manuscript.

***Conclusion*:** The conclusion should be brief, highlight the outcomes of the study and should be aligned with the objectives of the study. It should not contain references.

Competing Interest statement: The authors should include a statement on conflict of interest disclosing any financial or other substantive conflicts of interest that may influence the results or interpretation of the research in the space provided in the online article submission form. All sources of financial support for the project should also be disclosed.

***Acknowledgement*:** Should be brief and made for specific scientific, financial and technical assistance only. If a significant part of the research was performed in an institution other than the authors' affiliations should be acknowledged. All those who have made substantial contribution to the research but do not qualify to be authors should be acknowledged.

***References* :**
The JNSF uses APA (7th Edition) reference style
All research work of other authors, when used or referred to or cited, should be correctly acknowledged in the text and in the References.
All the references in the text should be in the list and vice versa

Citing references in the text:
- References to the literature must be indicated in the text and tables as per the Author-Year System, by the author's last name and year, in parenthesis (i.e. Able, 1997) or (Able & Thompson, 1998).
- Citation to work by more than two authors should be abbreviated with the use of et al. (i.e. Able *et al*., 1997).
- Multiple publications by the same first author in the same year should be coded by letters, (i.e. Thompson, 1991a, 1991b,1992,1993).
- Multiple citations of different authors should be made in chronological order and separated by a semicolon, (i.e. Zimmerman *et al*., 1986; Able *et al*., 1997).

Citing references in the List of references:
- The list of References should be arranged in alphabetical order based on the last name of the first author.
- In APA 7th ed., **up to 20 authors** should be included in a reference list entry. Write out the last name and first initial(s) for each contributor.

Example for 2–20 authors:

Wright, A., Komal, G., Siddharth, D., Boyd, G., Cayson, N., Beverley, K., Travers, K., Begum, A., Redmond, M., Mills, M., Cherry, D., Finley, B., Fox, M., Ferry, F., Almond, B., Howell, E., Gould, T., Berger, B., Bostock, T., & Fountain, A. (2020). Styling royalty. London Bridge Press.

- For references with more than 20 authors, after listing the 19th author replace any additional author names with an ellipsis (…) followed by the final listed author's last name and first initial(s).

Example for 21+ authors:

Kalnay, E., Kanamitsu, M., Kistler, R., Collins, W., Deaven, D., Gandin, L., Iredell, M., Saha, S., White, G., Woolen, J., Zhu, Y., Chelliah, M., Ebisuzaki, W., Higgins, W., Janowiak, J., Mo, K.C., Ropelewski, C., Wang, J., Leetmaa, A., … Joseph, D. (1996). The NCEP/NCAR 40-year reanalysis project. Bulletin of the American Meteorological Society, 77(3), 437-471. http://doi.org/fg6rf9

- All the initials of the author must be given after the last name and the year of publication should follow in parentheses.
- This should be followed by the full title of the referred publication.
- When journal articles are listed, the journal name should be given in full and in italics and followed by the volume number, issue number in parentheses and then the inclusive pages.
- Where there are several publications by the same author(s) and published in the same year they should be differentiated by adding a lower-case letter after the year.

Example

Clarke, P. N., & Fawcett, J. (2014a). Life as a mentor. *Nursing Science Quarterly*, 27(3), 213-215. https://doi.org/10.1177/0894318414534492

Clarke, P. N., & Fawcett, J. (2014b). Life as a nurse researcher. *Nursing Science Quarterly*, 27(1), 37-41. https://doi.org/10.1177/0894318413509708

- Digital object identifiers (DOIs) should be included for all references where available.

Details about this reference style can be obtained from below links

- https://apastyle.apa.org/style-grammar-guidelines/references
- https://apastyle.apa.org/style-grammar-guidelines/references/examples
- https://libguides.jcu.edu.au/apa

Abbreviations and Symbols: Unless common, these should be defined when first used, and not included in the abstract. The SI System of units should be used wherever possible. lf measurements were made in units other than SI, the data should be reported in the same units followed by SI units in brackets, e.g. 5290 ft (1610 m).

Formulae and Equations: Equations should be typewritten and quadruple spaced. They should be started on the left margin and the number placed in parentheses to the right of the equation.

Nomenclature: Scientific names of plants and animals should be printed in italics. In the first citation, genus, species and authority must be given. e.g. *Borassus flabellifer* Linn. In latter citations, the generic name may be abbreviated, for example, *B. flabellifer* L.

Tables and figures: Tables and Figures should be clear and intelligible and kept to a minimum, and should not repeat data available elsewhere in the paper. Any reproduction of illustrations, tabulations, pictures etc. in the manuscript should be acknowledged.

Tables: Tables should be numbered consecutively with Arabic numerals and placed at the appropriate position in the manuscript. If a Table must be continued, a second sheet should be used and all the headings repeated. The number of columns or rows in each Table should be minimized. Each Table should have a title, which makes its general meaning clear, without reference to the text. All Table columns should have explanatory headings. Units of measurement, if any, should be indicated in parentheses in the heading of each column. Vertical lines should not be used and horizontal lines should be used only in the heading and at the bottom of the table. Footnotes to Tables should be placed directly below the Table and should be indicated by superscript lower case italic letters (^{a}, ^{b}, ^{c}, etc.).

Figures: All illustrations are considered as figures, and each graph, drawing or photograph should be numbered consecutively with Arabic numerals and placed at the appropriate position in the manuscript. Any lettering to appear on the illustrations should be of a suitable size for reproduction and uniform lettering should be used in all the Figures of the manuscript. Scanned figures or photographs should be of high quality (**300 dpi**), to fit the proportions of the printed page (12 × 17 cm). Each figure should carry a legend so that the general meaning of the figure can be understood without reference to the text. Where magnifications are used, they should be stated.

Units of measurement

Length: km, m, mm, µm, nm
Area: ha, km^2, m^2
Capacity: kL, L, mL, µL
Volume: km^3, m^3, cm^3
Mass: t, kg, g, mg, µg

Time: year(s), month(s), week(s), day(s), hour(s), minute(s), second(s)
Concentration: M, mM, N, %, g/L, mg/L, ppm
Temperature: °C, K
Gravity: x g

Molecular weight: mol wt
Others: Radio-isotopes: 32P
Radiation dose: Bq
Oxidation-reduction potential: rH
Hydrogen ion concentration: pH